Fakultät für Maschinenwesen
Lehrstuhl für Carbon Composites LCC

Mechanical Performance of Pinned Composite/Metal Joints under Tension

Ludwig Maximilian Eberl

Vollständiger Abdruck der von der Fakultät für Maschinenwesen der Technischen Universität München zur Erlangung des akademischen Grades eines

Doktor-Ingenieurs

genehmigten Dissertation.

Vorsitzender:

Prof. Dr.-Ing. Dirk Weuster-Botz

Prüfer der Dissertation:

1. Prof. Dr.-Ing. Klaus Drechsler
2. Prof. Dr.-Ing. Horst Baier

Die Dissertation wurde am 15.01.2018 bei der Technischen Universität München eingereicht und durch die Fakultät für Maschinenwesen am 01.10.2018 angenommen.

Technische Universität München
Fakultät für Maschinenwesen
Lehrstuhl für Carbon Composites
Boltzmannstraße 15
D-85748 Garching bei München
Tel.: +49 (0) 89 / 289 – 15092
Fax.: +49 (0) 89 / 289 – 15097
Email: info@lcc.mw.tum.de
Web: www.lcc.mw.tum.de

ACKNOWLEDGEMENTS

I would like to express my gratitude to Prof. Klaus Drechsler and Dr. Elisabeth Ladstätter for providing me the opportunity to work on my PhD-topic at the Chair of Carbon Composites. In addition, I gratefully acknowledge Prof. Horst Baier for his contribution as the second committee member and Dr. Mathias Hartmann as well as Dr. Stephan Ucsnik for their helpful technical input. I also want to thank my group leader, Dr. Swen Zaremba, for our interesting technical discussions and his valuable advice, significantly contributing to the development of my work.

During my time at the Chair of Carbon Composites, I was incredibly lucky to work together with many great colleagues. I am thankful for numerous technical discussions and overall inspiration they gave me, but also for the deep friendships that were formed. I want to express my appreciation to my colleague, Luciano Avila Gray, who shared his excellent technical expertise and contributed to the outcome of the mechanical testing in this work. Many thanks also to my colleague, Ulrich Mandel, for his professional help regarding FEA and his valuable input.

I am very grateful to all my students who significantly contributed to this work by proposing solutions for different challenges that arose. I have always enjoyed supervising their student theses and working together with them in a team.

This research was made possible with the financial and technical support of the Composite Manufacturing Lab at GE Global Research Center in Munich. I therefore also want to thank my supervisor at GE aviation, Nick Kray, for his valuable advice.

I am eternally grateful to my parents, my brothers and my uncle. They always believed in me, supported and helped me throughout my entire life. Without their encouragement, this certainly would not have been possible.

Finally, I would like to thank my wonderful wife, Lauren. Thank you so much for your help and support during this thesis. I am so grateful for you always helping me through difficult times and sharing so many beautiful experiences with me.

KURZFASSUNG

Diese Dissertation beschäftigt sich mit der Analyse des Festigkeits- und Steifigkeitsverhaltens sowie der Versagensarten von gepinnten CFK/Metall-Verbindungen unter quasistatischer Zugbelastung. Anhand einer Vergleichsstudie auf Grundlage von zerstörenden Prüfverfahren wird zunächst ein geeignetes Verfahren zur Herstellung von gepinnten Metalleinlegern ausgewählt. Eine Optimierung von gepinnten CFK/Titan-Verbindungen erfolgt sowohl mithilfe numerischer Berechnungsmethodik als auch auf der Basis von mechanischen Prüfverfahren. Die Ermittlung des für die numerische Simulation benötigten Spannungs-Dehnungsverhaltens der eingesetzten Metalllegierungen, Faserverbundlaminate und Reinharze sowie interlaminaren Energiefreisetzungsraten ist ein weiterer Bestandteil dieser Arbeit. Zudem werden verschiedene Probengeometrien mit unterschiedlicher Pinanzahl sowie Pinanordnung untersucht. Eine Steigerung der übertragbaren Zuglast von 62% in Bezug auf in-situ geklebte zweischnittige Referenzproben ist möglich. Faserondulationen, welche durch das Eindrücken der Pins in das unausgehärtete Faserverbundlaminat entstehen, haben einen entscheidenden Einfluss auf die mechanischen Eigenschaften der gesamten Verbindung. Diese Faserondulationen werden zunächst anhand mikroskopischer Untersuchungen analysiert und anschließend in ein detailliertes Simulationsmodell implementiert. Die Analyse des Dehnungs- und Spannungsfeldes im Faserverbundfügepartner erfolgt sowohl anhand dieses Simulationsmodells als auch mithilfe von zerstörenden Prüfverfahren und digitaler Bildkorrelation. Gepinnte Laminate mit Faserondulationen zeichnen sich im Allgemeinen durch eine Homogenisierung des Dehnungs- und Spannungsfeldes in den lasttragenden 0°-Lagen gegenüber Laminaten mit Bohrungen aus. Lokale Spannungsspitzen im Nahbereich der Pins sind allerdings auch hier noch vorhanden. Ein Vergleich von gepinnten CFK-Metallverbindungen mit ondulierten Fasern gegenüber CFK-Metallverbindungen mit Bohrungen im Faserverbundlaminat zeigt, dass Festigkeitssteigerungen im Bereich von 30% möglich sind. Diese Festigkeitssteigerungen lassen sich vollständig auf einen geänderten Faserverlauf und den Wegfall von Fasertrennung aufgrund des Einfügens von Bohrungen zurückführen.

ABSTRACT

The main objective of this research is to analyze the mechanical response of pinned composite/metal joints under tensile loading. A comparative investigation based on mechanical testing reveals a suitable technology for pin creation. The optimization of pinned composite/titanium joints is conducted using numerical finite element analysis and destructive testing. Determination of the stress-strain behavior of the metallic alloys, carbon fiber laminates and neat resin as well as Mode I and Mode II fracture toughness is important for the implementation of material input data into the simulation model. Several joint geometries, differing in the amount and adjustment of the pins, are analyzed. Testing results show that an increase in joint strength up to 62% is possible, when compared to co-bonded reference joints. Fiber undulations, created by pin insertion into the uncured composite laminate, have a major impact on the mechanical response of the pinned composite/metal joint. Microscopy investigation is used to measure these undulations, which are then implemented into a detailed simulation model. Both numerical simulation and mechanical testing help to investigate the stress and strain distribution within the composite joint member. By utilizing digital image correlation techniques, it is proven that the presence of fiber undulations is responsible for a global homogenization of the strain field within the load carrying 0°-plies. However, local stress peaks close to the pins cannot be completely compensated. Pinned composite/metal joints with fiber undulations show joint strengths up to 30% greater than those of composite/metal joints with drilled holes in the composite joint member. The increase in joint strength is directly linked to the change of fiber course and the absence of fiber breakage caused by hole drilling.

List of contents

Glossary

Symbol	Unit	Description
a	mm	delamination length
b	mm	width
c	mm	length
C_i	N/mm², MPa	constant for calculation of thermal stress
$\boldsymbol{C}$	N/mm², MPa	elasticity matrix
d	mm	diameter
d	-	damage degradation value (scalar)
D	-	damage degradation vector
D_i	N/mm	constant value for calculation of thermal stress
$d_{86\%}$	µm	focus diameter of laser beam
E	N/mm², MPa	elastic modulus
e	mm	edge distance
F	N	force
G	N/mm², MPa	shear modulus
G_{Ic}, G_{IIc}	J/m²	fracture toughness, Mode I and Mode II
h	mm	height
K	m²	permeability
k_i	-	constant for calculation of thermal stress
l	mm	length
L	mm	length
P	N	load on single fastener or applied load
$p1$	mm	position 1
$p2$	mm	position 2

Symbol	Unit	Description
R	mm	characteristic radius
R	mm	radius
S	N/mm², MPa	shear strength
T	mm	thickness
$\boldsymbol{T}$	N/mm², MPa	nominal stress vector
T	°C	temperature
T_g	°C	glass transition temperature
ΔT	°C	temperature difference
U	mm	displacement
$u(t)$	m/s	flow front velocity
$v(t)$	m/s	darcy velocity
W	mm	width
X	mm	length, direction
X	N/mm², MPa	longitudinal strength
x_f	mm	flow front position
Y	mm	length, direction
Y	N/mm², MPa	transverse strength
Z	mm	length, direction
z_R	mm	Rayleigh length
A	°	in-plane angle
α_{jm_i}	1/°C	coefficient of thermal expansion at 20°C
B	1/mm	constant value
Γ	-	shear strain
Δ	mm	load point deflection, displacement
Δp	bar	pressure difference

Symbol	Unit	Description
ε	-	strain
η	mm	thickness of adhesive layer
Θ	°	out-of-plane angle
$\boldsymbol{\lambda}$	nm	wavelength
$\boldsymbol{\lambda}$	-	eigenvalue
$\mu(t,T)$	mPas	dynamic viscosity, dependent on time and temperature
ν	-	poisson's ratio
σ	N/mm², MPa	tensile or compressive stress
τ	N/mm², MPa	shear stress
ψ	°	tilting angle
$\boldsymbol{\varphi}$	-	fiber volume fraction

Indices	Description
$\bar{}$	average
+45-45	+45° and -45° direction
0	initial
0-90	0° and 90° direction
1	1-longitudinal (fiber) direction
2	2-transverse (fiber) direction
3	3-transverse (fiber) direction
avg	average
C	compressive
c	crack
co	composite
D	damage
eq	equivalent
f	failure
fc	fiber compression
ft	fiber tension
hole	hole
i	continuous index
I	Mode I or I-direction
II	Mode II or II-direction
j	continuous index
jm	joint member
k	continuous index
L	longitudinal
m	metal
max	maximum
mc	matrix compression
mean	mean value
Mises	von Mises

Indices	Description
mt	matrix tension
n	normal
nom	nominal
o	continuous index
p	continuous index
pl	plastic
q	continuous index
r	continuous index
red	reduced
s	symmetric or shear
s0	section 0 (for joint design 1)
s1	section 1 (for joint design 1)
service	service
Section1	Section 1 (for joint design 1)
Section2	Section 2 (for joint design 1)
shear	shear
stress free	stress free
t	continuous index or transverse
T	tensile
x	x-direction
y	y-direction
z	z-direction

List of abbreviations

Abbreviation	Description
ALM	Additive Layer Manufacturing
ASTM	American Society for Testing Materials
BK	Benzeggagh Kenane
BPP	Beam Parameter Product
CAE	Computer Aided Engineering
CFC	Carbon Fiber Composites
CFK	Carbonfaserverstärkter Kunststoff, carbon fiber reinforced plastics
CFRP	Carbon Fiber Reinforced Plastics
CLT	Classical Laminate Theory
CMC	Ceramic Matrix Composites
CMT	Cold Metal Transfer
CT	Computed Tomography
CTE	Coefficient of Thermal Expansion
DCB	Double Cantilever Beam
DIC	Digital Image Correlation
DIN	Deutsches Institut für Normung, German institute for standardization
DLS	Double Lap Shear
EN	European Norm
ENF	End Notched Flexural
FE	Finite Element
FEA	Finite Element Analysis
FEM	Finite Element Method
FFAD	Final Failure of ADhesive bond

Abbreviation	Description
FML	Fiber Metal Laminate
FTF	Fiber Tension Failure
FVF	Fiber Volume Fraction
GFRP	Glass Fiber Reinforced Plastic
GRP	Glass Reinforced Plastic
IFAD	Initial Failure of ADhesive bond
ISO	International Organization for Standardization
MCC	Modified Compliance Calibration
MMC	Metal Matrix Composite
NCF	Non-Crimp Fabric
QI	Quasi-Isotropic
RHEA	Redundant High Efficiency Assembly
RIFT	Resin Infusion under Flexible Tooling
RT	Room Temperature
RTM	Resin Transfer Molding
TC	Thermo-Couple
UD	UniDirectional
UF	Ultimate joint Failure
UC	Unit Cell
UPM 100	Hegewald & Peschke Inspect table 100 universal testing machine
UPM 250	Hegewald & Peschke Inspect 250 universal testing machine
VAP	Vacuum Assisted Process
VCCT	Virtual Crack Closure Technique

List of figures

List of tables

1 Introduction

Over the past few decades, composite structures have experienced continuous growth in industrial applications with high lightweight requirements, such as aerospace, motorsport, high performance sport equipment and automotive e-mobility. Due to their anisotropic material behavior, Carbon Fiber Reinforced Plastics (CFRP) specifically, are preferred wherever loading directions are well known. They are characterized by excellent strength and stiffness to density ratio. Therefore, CFRP replaced isotropic metals primarily in large sized surface structures like aircraft fuselages or wing shells. However, CFRP materials have several restrictions which exclude them from being used for particular fields of application. Due to their brittle nature and anisotropic behavior, CFRP materials are generally sensitive towards loading in the laminate's thickness direction, especially impact loading. Furthermore, their functional temperature range is limited, specifically with respect to the widely used thermoset resin systems.

New advances in metallurgy enable the production of high-performance alloys, which are characterized by a high strength while maintaining their isotropic material behavior. Furthermore, modern technologies, such as additive layer manufacturing, allow for further design freedom, enabling manufacturing of complex shaped parts with undercuts and intermediate spaces. Figure 1-1 illustrates the amount of aluminum, titanium and composites used in selected civil passenger aircrafts from the late 60's until today.

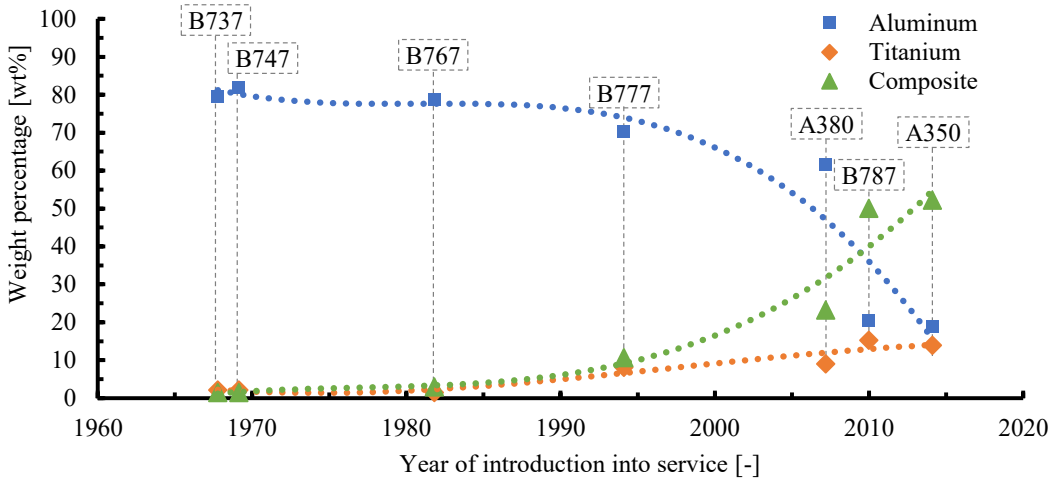

Figure 1-1: Amount of aluminum, titanium and composite materials used in civil passenger aircrafts over the last five decades

According to [1]; The term "composite" not only refers to carbon composites with polymeric matrices but also includes other types of composite materials such as Glass Fiber Reinforced Plastics (GFRP), Metal Matrix Composites (MMC), Ceramic Matrix Composites (CMC) or Fiber Metal Laminates (FML)

Whereas the use of aluminum declined over the last five decades, the amount of composite and titanium materials increased. Titanium materials are characterized by a greater stiffness and strength when compared to aluminum. However, due to their high raw material price and costs for manufacturing and machining, titanium materials are used rather hesitantly in civil passenger aircrafts. In the military sector, titanium materials are deployed more extensively. The Lockheed Martin F-22 Raptor stealth fighter, for example, consists of 33wt% titanium, 35wt% composite, 11wt% aluminum and 5wt% steel materials [1]. These examples, however, indicate that an optimized lightweight efficiency can only be achieved by using different material groups, primarily composite materials and metals.

1.1 Hybrid composite/metal structures

Whenever dissimilar materials are combined within highly loaded structures, the joining methods come into focus. Due to different manufacturing techniques, mechanical properties, thermal expansion and corrosion tendency, joining metallic to composite materials poses a major challenge. Joints should have a high joint efficiency; therefore, the joint strength should be close to the tensile strength of the joint members. Local thickening of the joint members should be reduced to a minimum in order to provide a high lightweight efficiency. Plastic deformation ensures strong energy absorption capacity, which is important for impact loading. Therefore, gradual damage degradation is usually preferred over sudden failure. In aerospace applications, joints are often designed in a way that a second load path is provided. This fail-safe design philosophy was already described by Leonardo da Vinci, 500 years ago:

“In constructing wings, one should make one cord to bear the strain and a looser one in the same position that if one breaks under strain the other is in position to serve the same function”

Leonardo da Vinci (1452-1519)

By using bonded/bolted joints or pure mechanically fastened joints with several fastener rows, several load paths are available.

1.2 Goal and structure of this work

The goal of this thesis is to investigate a novel technology for joining CFRP to metallic materials. Pinned CFRP/metal joints transfer loads between the CFRP and metallic joint member via adhesive joining and form closure mechanisms provided by a plurality of small pins. As pins are inserted into the fibrous composite material prior to curing, fibers are redirected around the pins. This thesis specifically focuses on the effect of these fiber undulations on the hybrid CFRP/titanium joint's mechanical performance under quasi-static tensile loading. It also aims to further increase the load carrying capability of

pinned CFRP/titanium joints beyond the state of the art. Based on the results of mechanical testing and finite element analysis, the joint's geometry is adjusted in order to obtain maximum lightweight efficiency.

Chapter 2 gives an overview of the state of the art regarding different types and corresponding design rules for composite[1]/metal joints. Chapter 3 provides fundamental information needed to understand the test and simulation results, such as explanations of the standards and challenges for mechanical testing, measurement techniques for analyzing fiber undulations around the pins and finite element modelling techniques. Specimen manufacturing for mechanical testing is then explained in Chapter 4. Chapter 5 analyzes testing results, including mechanical testing, fiber undulation measurements and simulation results derived by finite element analysis techniques. A comparison between co-bonded, Hi-lock riveted and pinned joints in terms of lightweight efficiency is presented in Chapter 6. In addition, Chapter 6 provides background information about influencing parameters for pinned composite/metal joints and includes design guidelines. A summary of the conducted work and outlook for future tasks is presented in Chapter 7. In addition, Appendix A provides additional testing data, data-sheets and material input parameters used for the finite element analysis.

[1] Within the scope of this thesis, only composite materials with either glass or carbon fibers and thermoset matrix materials are investigated

2 State of the art

This chapter provides an overview of several joining technologies applicable for hybrid composite/metal joints. Conventional adhesive bonding and mechanical fastening like riveting or bolting have been extensively researched and deployed on an industrial scale for decades. The hybrid composite/metal pinning technology represents a relatively new approach for joining isotropic metallic and anisotropic composite materials. Pinned composite/metal joints aim to combine several advantages of both, bonded and mechanically fastened joints.

2.1 Adhesive bonding

Adhesive bonding represents a joining method that does not affect the composite joint member's load carrying capacity. In order to obtain a high joint strength, an accurate surface preparation is essential and contaminations of the joining surfaces must be avoided prior to bonding [2–4]. Possible surface treatments for hybrid composite/metal joints include abrasion and solvent wipe, grit blasting, acid etching, peel or tear ply, sodium hydroxide anodization and laser treatment [5–9]. Furthermore, adhesive bonds are sensitive to environmental conditions such as temperature changes, moisture and corrosive media [10–12]. Adhesively bonded joints are generally prone towards Mode I peel stresses. Therefore, the specific design should be chosen in a way that Mode II shear is the dominant loading direction within the bonding area. Joint manufacturing usually takes place under elevated temperatures. As fibers, resins and metals possess different coefficients of thermal expansion (CTE), residual stresses cannot be prevented. Adhesive bonding is well suited for thin structures but also demands large joining areas. Due to a better shear stress distribution along the bond length, scarfed or stepped designs increase the joint strength for joints with thicker adherends, when compared to single- or double lap joints with adherends which are characterized by a constant thickness [13]. However, bondline length to adherend thickness ratios between 20:1 up to 60:1 [14] for scarfed joint designs still require large bond lengths.

Co-curing, co-bonding, bonding

Conventional adhesively bonded joints are usually manufactured using two cured or solid joint members and structural adhesive. The bondline thickness and ductility of the adhesive layer can be adjusted to improve the shear stress distribution within the adhesive layer and furthermore, the joint strength. This method is defined as "bonding". Another possibility is to use the resin as an adhesive between the two joint members. This

method reduces the overall manufacturing time, as curing and bonding of the joint members is done simultaneously. In literature, this method is often generally described as "co-curing". Within the scope of this thesis, the term "co-bonding" refers to a joint manufacturing method where one joint member is uncured and the other is either solid or already cured, prior to the joining step. Hence, RTM-processed hybrid composite/metal joints are co-bonded. "Co-curing", consequently describes a method for joint manufacturing, where both joint members are uncured when joining, i.e. joining of two subpreforms in a single RTM-cycle. Table 2-1 lists the different methods for joint manufacturing.

Table 2-1: Methods for joint manufacturing

Bonding technique	Joint member 1	Joint member 2	Adhesive type
Bonding	cured/solid	cured/solid	structural adhesive
Co-bonding	uncured	cured/solid	RTM or prepreg resin
Co-curing	uncured	uncured	RTM or prepreg resin

Volkersen law

Almost 80 years ago, in 1938, Olaf Volkersen described the shear strain and stress distribution for multi-row bolted single-lap joints in a linear elastic stress state [15]. Six years later, De Bryne [16] extended Volkersen's findings towards adhesively bonded double lap joints. Figure 2-1 exemplarily shows the shear strain distribution within the adhesive of a double lap shear (DLS) joint. This joint is designed in a way that the sum of the outer laps' stiffnesses is identical to the inner joint member.

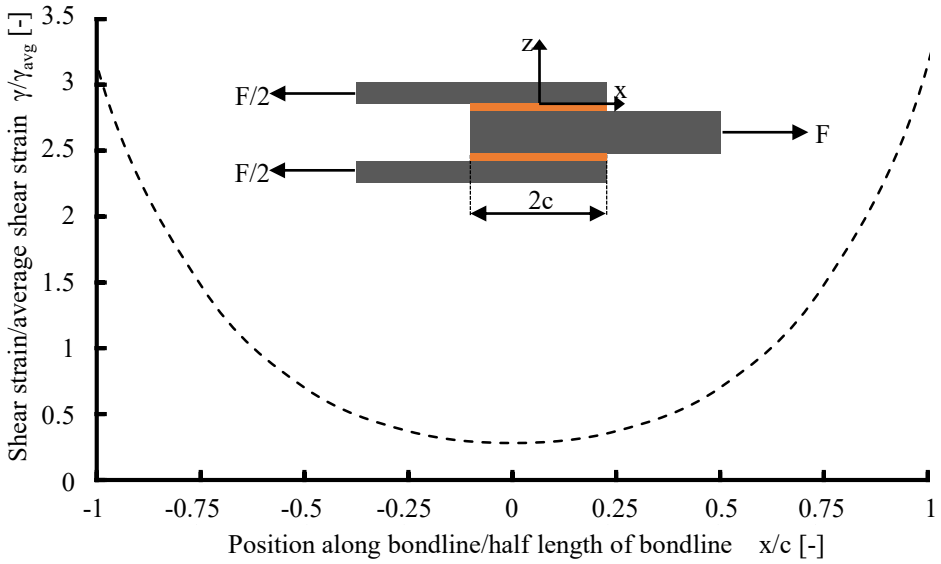

Figure 2-1: Shear strain distribution for a stiffness balanced DLS joint
According to [17]

In the case of double lap joints with constant adherend thickness, there is a definite limit for maximum tensile load capacity of the joint. Once a specific bondline length is reached, the bond strength can no longer be increased. Figure 2-2 shows the evolution of shear strain and stress with growing tensile load for a stiffness balanced DLS joint.

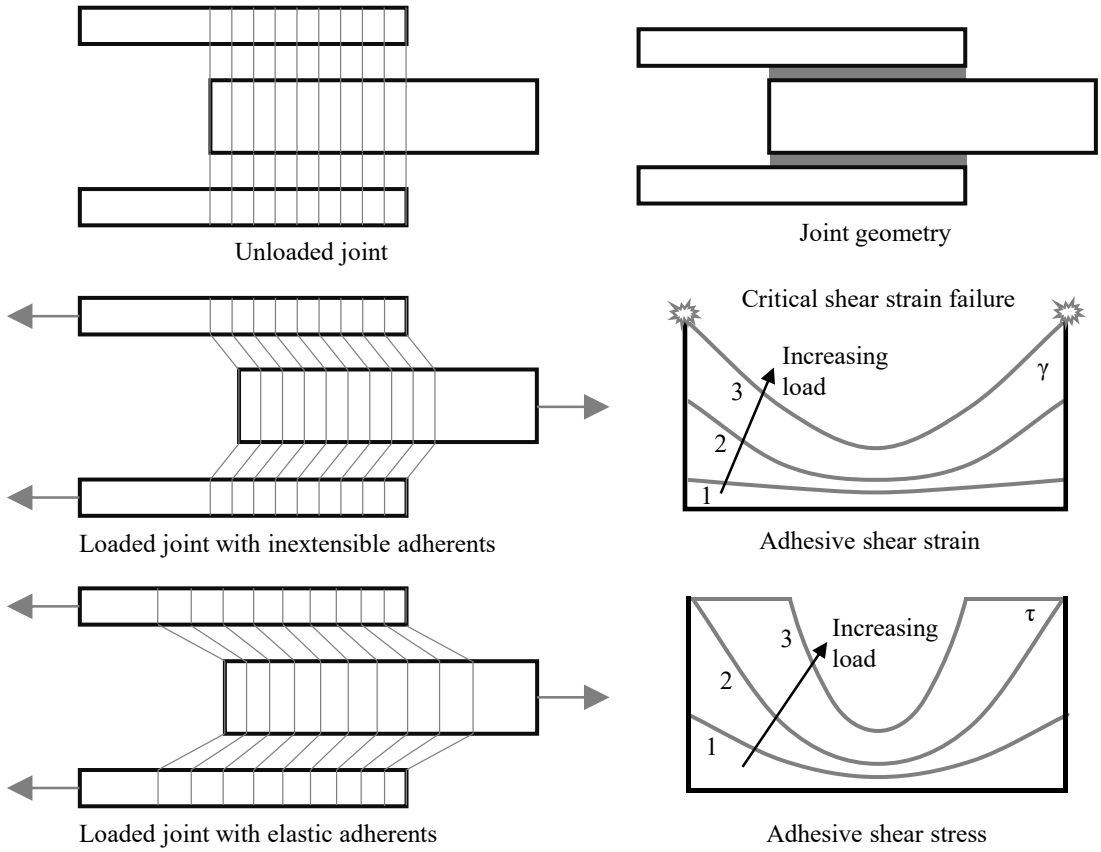

Figure 2-2: Schematic explanation of shearing in stiffness-balanced adhesive joints [11]

Conditions 1 and 2 represent random load states, whereas the tensile load is increased from state 1 to state 2. Load state 3 finally leads to joint failure, therefore slightly exceeds the maximum tensile load possible for this joint setup. Deformation of the elastic adherends leads to non-uniform strain and stress state within the adhesive layer. Strain and stress peaks occur at both ends of the bondline. Theoretically, a uniform stress and strain distribution can be achieved by using inextensible adherends. However, thickening the adherends and therefore increasing their stiffness does not necessarily lead to a greater bond strength. In practice, not only the tensile stiffness of the adherends affect the strain and stress distribution within the adhesive, but also the shear strength within the adhesive layer. In addition, thick adherends are prone to peel stresses [11]. Ductile adhesives and the correct adhesive thickness can have a positive effect on the stress distribution within the adhesive. The adhesive's ductile behavior leads to plastic deformation at both bondline ends. As a result, shear stress within the adhesive layer is distributed more towards the central section, leading to a homogenization throughout the entire bond length [18]. The adhesive's thickness should be adjusted in a way, that local roughness

peaks of both surfaces are not in physical contact with each other [18]. Very thick adhesive layers lead to manufacturing difficulties, often resulting in greater void content. In addition, cohesive failure (see page 12) becomes more probable.

Stiffness-imbalance

If possible, adhesive double-lap joints should be designed in a way that the stiffness of the adherends is balanced. The inner adherend should be twice as stiff as a single outer adherend [19]. The effect of a stiffness-imbalance on the shear stress distribution is shown in Figure 2-3.

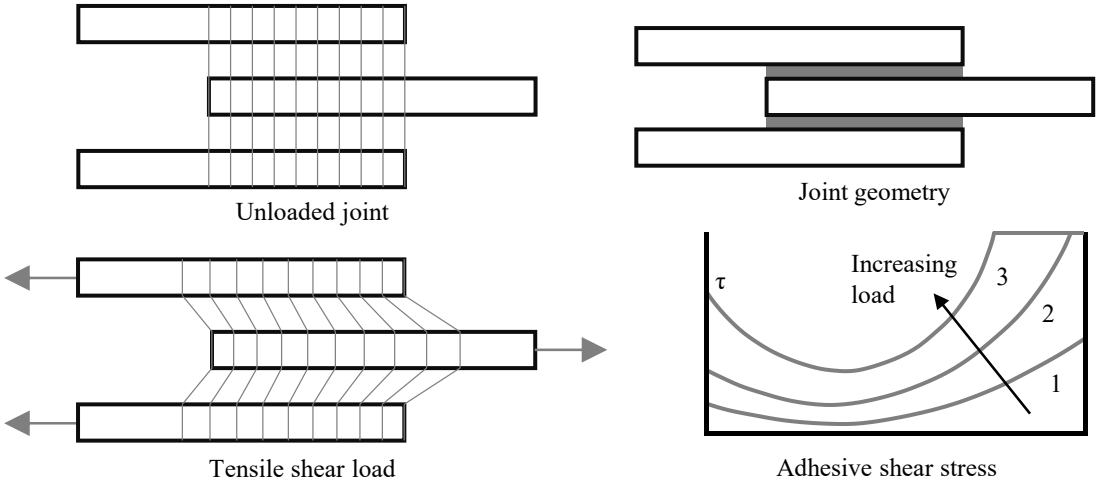

Figure 2-3: Deformations and adhesive shear strains in stiffness-imbalanced bonded joints [11]

If the inner adherend is characterized by a lower stiffness in comparison to the sum of both outer adherends, stress peaks are greater at the right end of the joining area, at the runouts of the outer adherends. The opposite happens if the inner adherend is stiffer than the sum of the outer ones. In this case, the highest stress peak would occur at the left end of the joining area [11]. These considerations emphasize the challenge when joining ductile metals and composite materials. As soon as the joint tensile load leads to stresses higher than the metallic yield strength, local softening, due to plastic deformation, occurs at the right end of the joining area, leading to joint failure due to critical shear strain within the adhesive layer.

Thermal mismatch

Structural adhesives and high-performance epoxy resin systems are usually cured under elevated temperatures up to 200°C. Different coefficients of thermal expansion compulsorily lead to residual stresses within the joint after cooling.

Table 2-2 lists values for CTE's of different metals, thermoset resin and carbon fibers.

Table 2-2: CTE-data for different materials [18, 20–22]

Material	Steel 1.4301	Ti6Al4V	PR520 RTM-resin	HM carbon fiber (longitudinal)	HM carbon fiber (transversal)
CTE at RT [10^{-6}/°C]	17.2	8.6	52.9	-1.08	31

Figure 2-4 shows the effect of different CTE's on the joint's stress and strain distribution.

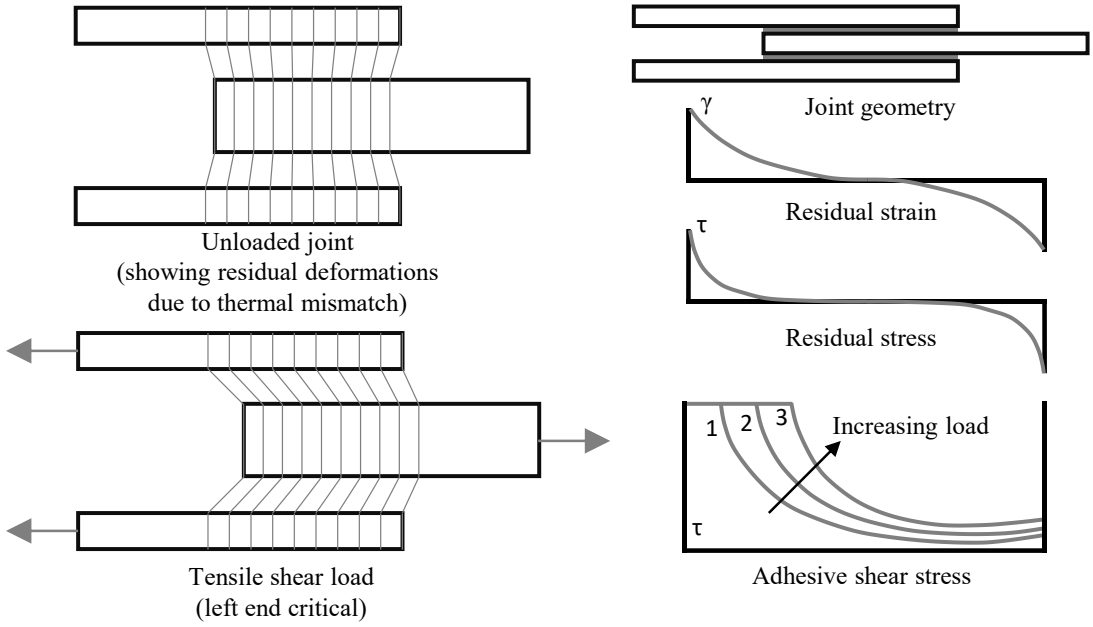

Figure 2-4: Deformations and adhesive shear strains in thermally-mismatched bonded joints [11]

The metallic adherend expands under heating whereas the CFRP adherends hardly change their geometry due to a low CTE and high stiffness of the carbon fibers in longitudinal direction. As the joint is manufactured under an elevated curing temperature, only small residual stresses are present at this state. However, the metallic adherend contracts when cooling to room temperature after curing, creating residual stresses within the adhesive layer. Due to a smaller CTE difference between titanium and CFRP laminates, this material combination is less critical than steel and CFRP.

Chen et al. [23] proposed a one-dimensional analytical approach to determine thermal stresses in between three elastic layers with two bonded joints for a case when no external loads are present. Plastic material behavior as well as thermal expansion within the adhesive layer are neglected. In addition, chemical crimp is not considered within this analytical approach. The shear stresses τ and τ' can be calculated with the following formulae:

$$\tau = C_1 \frac{\sinh \beta_1 x}{\cosh \beta_1 l} + C_2 \frac{\sinh \beta_2 x}{\cosh \beta_2 l} \tag{2-1}$$

$$\tau' = C_1 k_1 \frac{\sinh \beta_1 x}{\cosh \beta_1 l} + C_2 k_2 \frac{\sinh \beta_2 x}{\cosh \beta_2 l} \tag{2-2}$$

Where x denotes a specific position along the bondline and $x=0$ is located midway between both ends of the joint. The constants k_i, β_i and C_i are calculated in equation (2-3) to (2-6). In addition, l describes half of the bond length, see Figure 2-5.

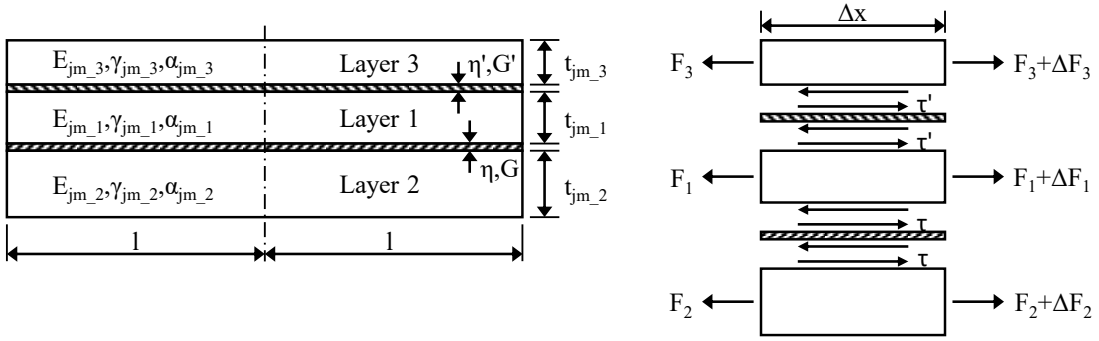

Figure 2-5: Calculation of residual stresses due to thermal mismatch
Notations on three joined layers (left), force balance on three joined layers for a section *dx* (right) [23][1]

The constants k_1, k_2 and C_1, C_2 are defined as:

$$k_i = E_{jm\_1} t_{jm\_1} \left[\left(\frac{1}{E_{jm\_1} t_{jm\_1}} + \frac{1}{E_{jm\_2} t_{jm\_2}} \right) - \frac{\beta_i^2 \eta}{G} \right] \tag{2-3}[1]$$

$$C_1 = \frac{G\beta_1 [D_2 k_2 + D_3]}{E_{jm\_1} t_{jm\_1} \eta (\beta_1^2 - \beta_2^2)} \tag{2-4}[1]$$

$$C_2 = \frac{G\beta_2 [D_2 k_1 + D_3]}{E_{jm\_1} t_{jm\_1} \eta (\beta_2^2 - \beta_1^2)} \tag{2-5}[1]$$

Where E_{jm_i} and t_{jm_i} denote the elastic moduli and thickness of each layer, respectively. The thickness of the adhesive layer is labelled by η and η'. G and G' describe the shear modulus of the adhesive layer. Furthermore, $\pm\beta_1$ and $\pm\beta_2$ can be calculated by solving the equation:

$$\begin{aligned} &\beta^4 - \frac{1}{E_{jm\_1} t_{jm\_1}} \left[\frac{G}{\eta} \left(1 + \frac{E_{jm\_1} t_{jm\_1}}{E_{jm\_2} t_{jm\_2}} \right) + \frac{G'}{\eta'} \left(1 + \frac{E_{jm\_1} t_{jm\_1}}{E_{jm\_3} t_{jm\_3}} \right) \right] \beta^2 \\ &+ \frac{GG'}{\left(E_{jm\_1} t_{jm\_1} \right)^2 \eta\eta'} \left[\left(1 + \frac{E_{jm\_1} t_{jm\_1}}{E_{jm\_2} t_{jm\_2}} \right) \left(1 + \frac{E_{jm\_1} t_{jm\_1}}{E_{jm\_3} t_{jm\_3}} \right) - 1 \right] = 0 \end{aligned} \tag{2-6}[1]$$

[1] E_i replaced by E_{jm_i}, t_i by t_{jm_i} due to ambiguity

And the constants D_1, D_2 and D_3 are defined by:

$$D_1 = \frac{E_{jm\_1}t_{jm\_1}\left[E_{jm\_3}t_{jm\_3}\left(\alpha_{jm\_3} - \alpha_{jm\_1}\right) + E_{jm\_2}t_{jm\_2}\left(\alpha_{jm\_2} - \alpha_{jm\_1}\right)\right]\Delta T}{E_{jm\_1}t_{jm\_1} + E_{jm\_2}t_{jm\_2} + E_{jm\_3}t_{jm\_3}} \quad (2\text{-}7)^2$$

$$D_2 = \frac{E_{jm\_2}t_{jm\_2}\left[E_{jm\_1}t_{jm\_1}\left(\alpha_{jm\_1} - \alpha_{jm\_2}\right) + E_{jm\_3}t_{jm\_3}\left(\alpha_{jm\_3} - \alpha_{jm\_2}\right)\right]\Delta T}{E_{jm\_1}t_{jm\_1} + E_{jm\_2}t_{jm\_2} + E_{jm\_3}t_{jm\_3}} \quad (2\text{-}8)^2$$

$$D_3 = \frac{E_{jm\_3}t_{jm\_3}\left[E_{jm\_1}t_{jm\_1}\left(\alpha_{jm\_1} - \alpha_{jm\_3}\right) + E_{jm\_2}t_{jm\_2}\left(\alpha_{jm\_2} - \alpha_{jm\_3}\right)\right]\Delta T}{E_{jm\_1}t_{jm\_1} + E_{jm\_2}t_{jm\_2} + E_{jm\_3}t_{jm\_3}} \quad (2\text{-}9)^2$$

Where α_{jm_1} to α_{jm_3} describe each layer's coefficient of thermal expansion and ΔT the temperature difference between the service temperature $T_{service}$ and stress-free temperature $T_{stressfree}$. According to Schürmann [24], the stress-free temperature can be estimated as follows:

$$T_{stressfree} = T_{g\_onset} - 20°C \quad (2\text{-}10)^3$$

Thus, ΔT calculates to:

$$\Delta T = T_{service} - \left(T_{g\_onset} - 20°C\right) \quad (2\text{-}11)$$

In the case of a symmetric double lap joint, the properties of layer 1 are similar to those of layer 3 and D_2 equals D_3. Based on the equations presented above, thermal shear stresses for hybrid CFRP/metal double lap joints can be estimated, see Chapter 5.3.2.

[2] E_i replaced by E_{jm_i}, t_i by t_{jm_i} and α_i by α_{jm_i} due to ambiguity

[3] T_{red} replaced by $T_{stressfree}$ due to ambiguity

Failure modes for bonded joints

Several failure modes are possible for bonded joints under tensile loading. These can be divided in two categories, adherend failure and failure of the bond. Figure 2-6 illustrates the different failure modes.

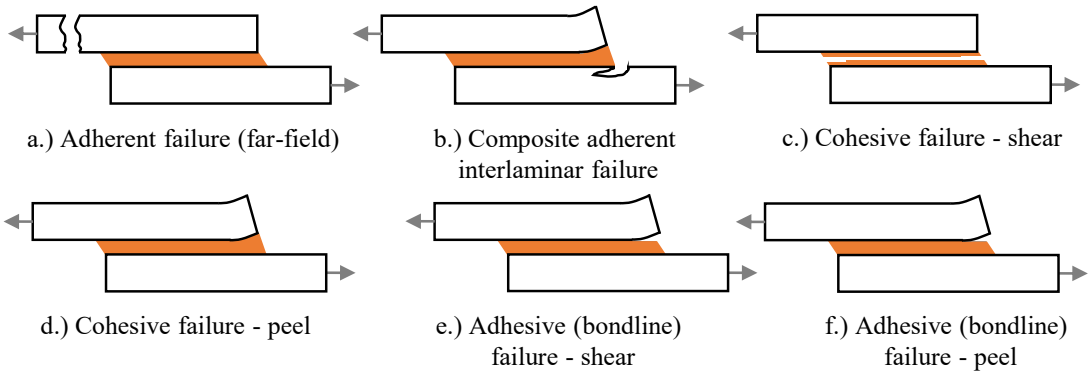

Figure 2-6: Failure modes in adhesively bonded joints under tension
According to [25]

Whereas adherend failure in the far-field of the joint often occurs for materials with a low tensile strength and/or low thickness, interlaminar failure within the adherend more likely happens for thick composite adherends or disadvantageous layups. Cohesive failure describes a shear or peel failure within the adhesive layer, whereas adhesive failure (shear or peel) is a result of de-bonding of the adhesive layer from the adherend. Poor surface treatment and manufacturing defects, like voids within the adhesive or processing variations, highly affect the quality of the bond. Therefore, adhesive joints should be ideally designed in a way that adherend failure in the far-field is present. As opposed to adhesive or cohesive failure, failure of the adherends in the far-field can be well predicted as tensile strength is the limiting factor. However, the thickness of the adherends has to be kept low and large sized joining areas are necessary [19].

2.2 Mechanical fastening

Mechanically fastened bolted and riveted composite/metal joints have been investigated for over 50 years [19]. Due to the composite's brittle material behavior, stress peaks cannot be decreased by plastic material behavior like this is the case for ductile metals. In addition, three-dimensional stress states around the holes demand for a laminate structure with a variety of fiber directions. As the composite is weakened by notch effects due to hole drilling, local thickening of the composite is necessary, leading to a reduction of lightweight efficiency [26, 27]. However, if sufficiently sealed, riveted and bolted joints are robust against environmental conditions. Fastener application is well established and joints can be disassembled. Predictability of joint strength is usually better for mechanically fastened joints than for adhesive joints as they are less prone to manu-

facturing defects. This is one of the reasons why bolted joints are still preferred in aerospace structures [28]. Due to plastic deformation of the fasteners and bearing within the adherends, the energy absorption capacity can be significantly higher in comparison to adhesive joints. For more detailed information regarding riveted and bolted joints, please refer to [19, 24, 29].

Failure modes

Several failure modes can occur in a mechanically fastened structure under tension, see Figure 2-7.

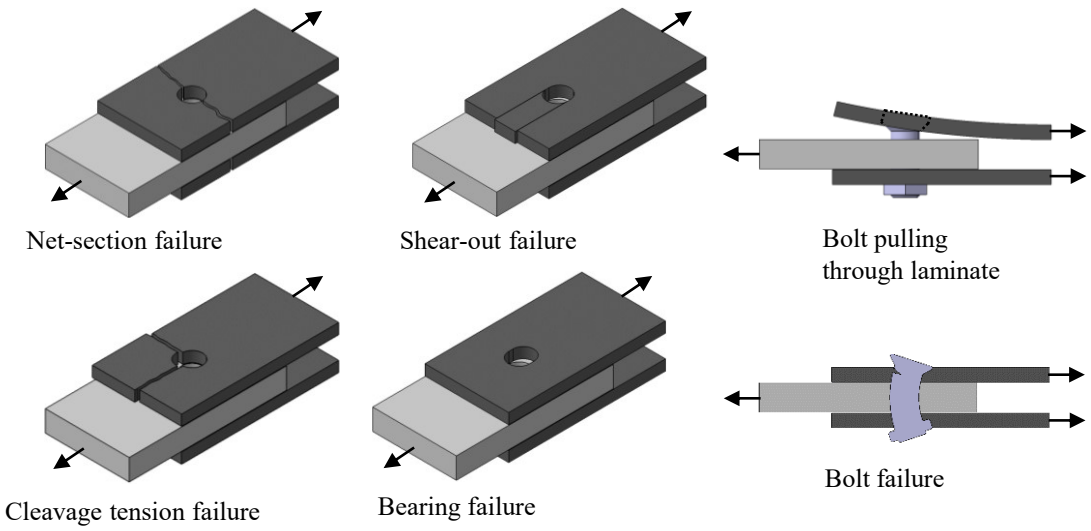

Figure 2-7: Failure modes for mechanically fastened joints under tension
According to [19]

Net-section failure is defined as tensile failure of the joint member next to the hole. It may occur if the amount of 0°-plies is too low or dimensions for hole spacing are insufficient. The reduction of hole diameter to specimen width ratio also leads to a greater resistance against net-section failure. Shear-out failure can be prevented by increasing the amount of ±45° plies or dimensions for edge distance. The right choice of fastener type with sufficient supporting surface between the washer or (countersunk) bolt head and the laminate limits the risk of a bolt pulling through the laminate. An increase of ±45° and 90° plies can inhibit cleavage tension failure. Edge distance, hole spacing and fastener diameter also have an influence on the probability that cleavage tension failure occurs. Whereas net-section, shear-out and cleavage tension failure modes are characterized by sudden failure, bearing failure does not lead to an abrupt failure of the entire structure and is therefore often the preferred failure mode. In addition, because of gradual failure propagation, the energy absorption capacity of a joint which fails due to bearing failure is higher in comparison to other failure modes. Adding 0°-plies and increasing the bolt diameter lead to a reduced bearing stress. Bolt failure can be prevented by

enlarging the bolt diameter or changing the bolt material. Further information regarding failure modes of mechanically fastened joints can be found in [19, 24, 30].

Stress concentrations

Stress concentrations around holes are more critical for composites in comparison to metals. Figure 2-8 shows the stress distribution along the width direction for a bolted plate in a tensile stress state.

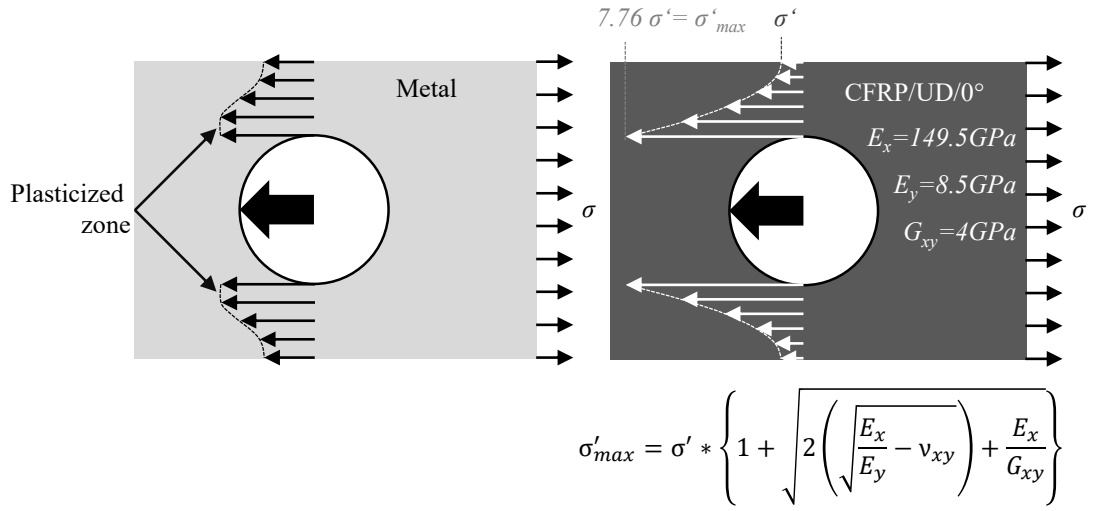

Figure 2-8: Stress concentrations around holes for metals and UD-CFRP
According to [31]

Whereas stress peaks within metallic structures can be reduced by plastic deformation, this redistribution of stress close to the hole is not possible within 0° composite plies. Especially in the case of CFRP materials with a great amount of 0°-plies, stress concentration factors reach high values, as the longitudinal linear-elastic behavior of the fibers dominates the stress-strain behavior in tensile direction [31]. These observations emphasize the need for a well-considered choice of ply-directions in a mechanically fastened composite structure. Quasi-isotropic laminates are recommended for bolted composite structures [32]. In order to maximize the bearing strength, 50/40/10-laminates are often used for aerospace applications. These laminates are characterized by a 50% content of 0°-plies, 40% of the plies have a fiber direction of ±45° and 10% are 90°-plies [28]. Through a local adaption of fiber direction within a ply, stress peaks can be significantly reduced [33].

Multi-row-joints

Mechanically fastened joints for highly loaded primary structures are usually designed as multi-row joints [19]. The load distribution on the different fastener rows is typically uneven, see Figure 2-9.

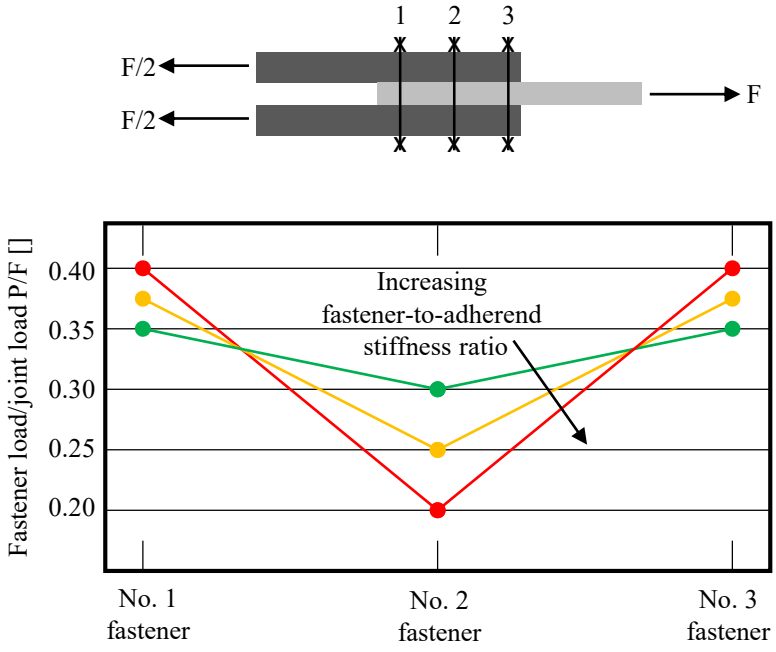

Figure 2-9: Load distribution on fastener rows for a stiffness balanced joint
According to [32]

Similar to adhesively bonded joints, stiffness balance of the adherends is beneficial for load distribution on the fastener rows. In addition, a high adherend stiffness in combination with a low fastener stiffness leads to a lower discrepancy of load *P* on the different fastener rows.

Softening inserts

Softening inserts are an efficient method to increase the load carrying capability of multi-row-joints as these inserts "simulate" a low fastener stiffness [34]. They are usually applied around the outer fasteners as these are exposed to the greatest loads, see Figure 2-10.

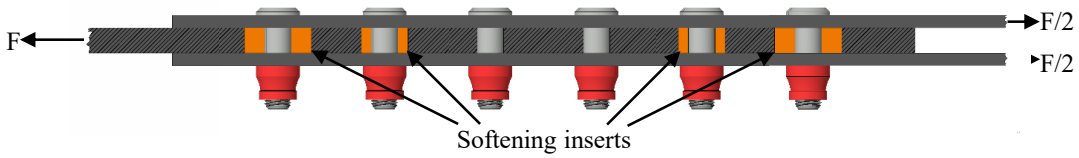

Figure 2-10: Multi-row-joint with softening inserts
According to [34]

Introducing softening inserts into composite laminates leads to a more even load distribution on the different fastener rows in the case of multi-row joints. It also significantly reduces stress peaks around holes, see Figure 2-11.

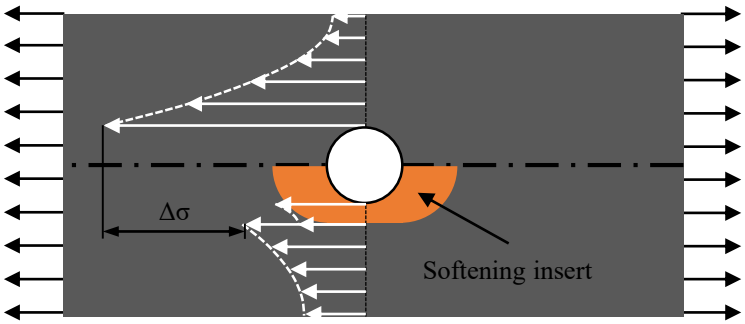

Figure 2-11: Stress distribution around hole with and without local softening
According to [34]

Softening inserts are characterized by a lower stiffness in comparison to the surrounding laminate. These inserts can be made from different materials, i.e. boron/epoxy-composite. For laminates under tensile loading, inserts with an elongated hole or ellipse shape are recommended to increase the load carrying capability of bolted composite joints [34].

Fiber metal-laminates

The substitution of single composite plies with thin metallic sheets can significantly increase the (non-weight-related) bearing strength of the laminate [34, 35]. Even though several material combinations exist, i.e. glass reinforced aluminum (GLARE), this chapter only refers to fiber-metal-laminates consisting of titanium and high-strength CFRP materials. Investigations on triple row bolted joints with adherends made from titanium sheets and 0°-plies indicate that the weight related joint tensile strength can be up to 26% greater in comparison to a joint consisting of pure CFRP 50/40/10-laminate [34]. Figure 2-12 shows a concept which includes local substitutions of CFRP plies with titanium sheets.

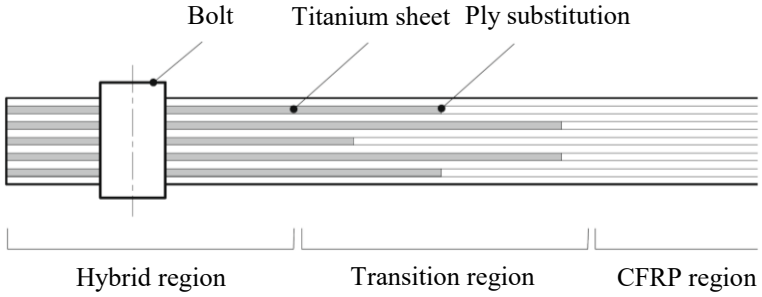

Figure 2-12: Hybrid composite/fiber-metal laminate for mechanically fastened joints [36]

This concept enables either composite/composite or composite/metal joining. Furthermore, the weight increase, caused by the higher density of titanium in comparison to CFRP, can be kept small as titanium sheets are only present around the holes. However, proper surface treatment of the metallic tab, leading to a greater manufacturing effort, is important for a high-quality laminate. In addition, different CTE's, resulting in residual stresses within the laminate, have to be taken into consideration. Further information regarding titanium-CFRP-laminates can be found in [28, 34–39].

Pin loaded strap

Pin loaded straps can be a lightweight efficient method to transfer high tensile loads into unidirectional composites. Typical designs are loops with parallel straps or waisted loops, see Figure 2-13.

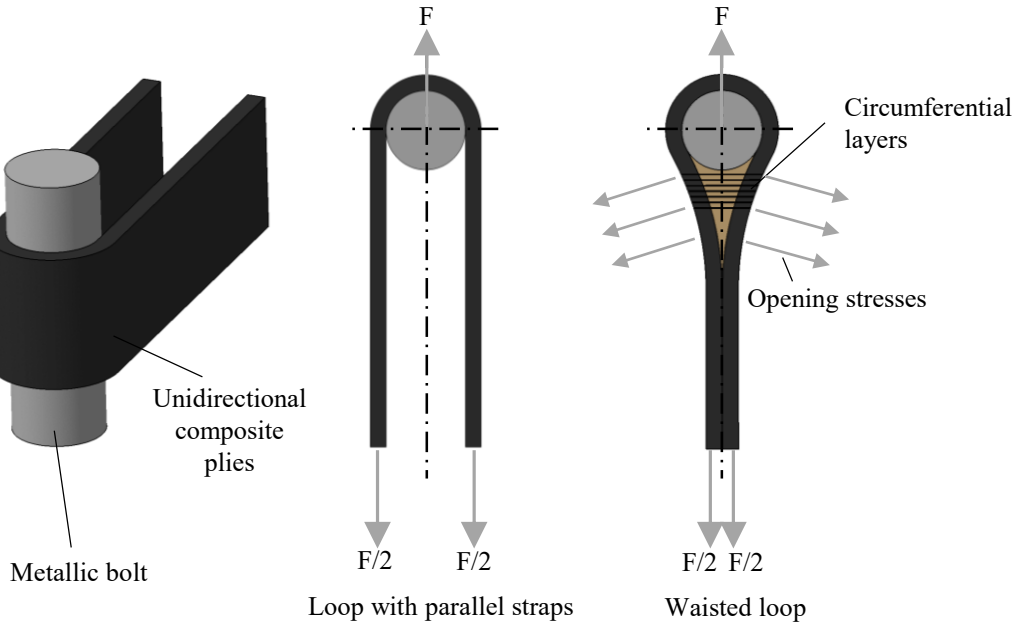

Figure 2-13: Forces and stresses on pin loaded straps
According to [24]

In the case of waisted loops, opening stresses have to be covered by either circumferential layers or 3D-reinforcements [40]. The manufacturing of these joints must be done with great care as wrinkles within the plies significantly weaken the joint. The stresses in tensile direction within the composite straps are not uniformly distributed. Therefore, the joint strength is lower than the tensile strength of both composite straps. Due to their complex manufacturing and unique design, pin loaded straps are limited to special areas of application such as root connections for helicopter rotor blades or trailing edge devices [24, 40].

2.3 Pinning

Pinning can be used to both increase the interlaminar strength and toughness of pure composite laminates or applied as a joining method for composite/composite or composite/metal joints. Pins represent thin fasteners which are inserted into an uncured prepreg material or dry fiber NCF or weave. They are either orientated in the laminate's thickness direction or tilted. Inserting the pins replaces the fibers, resulting in fiber undulations around the pins, see Chapter 2.3.3.

Pins, used within pure composite laminates, are made from composite rods or metal. Pinned laminates have proven to outperform conventional laminates in terms of Mode I and Mode II fracture toughness [41–47]. Tufting and stitching represent other technologies, which can also increase the interlaminar properties. Interleaving metallic sheets, containing a plurality of small pins are an effective method to reduce the risk of a composite structure to delaminate. Furthermore, this technique does not require complex sewing or stitching machinery.

2.3.1 Composite/composite joints

Interleaving metallic pinned sheets can also be used for composite/composite joints. Redundant High Efficiency Assembly (RHEA) joints represent a technology for composite/composite joining with the help of pins [48–51]. Through laser-cutting and successive local bending of the metallic sheet, pins with either spiky or hook-shaped heads are created. Tensile tested RHEA single-lap joints have proven to exceed adhesive joints in terms of tensile strength and energy absorption capacity [49]. Others use staple-like pins to enhance the tensile strength of composite/composite joints [52].

Another approach for pin creation uses a special arc-welding process, the "cold-metal-transfer" (CMT) process [53]. A welding wire is welded onto the metallic substrate's surface and teared off at a certain height via a high electrical current [54]. This technology also enables the pin head's shape to vary from cylindrical, to spiky and spherical or even a combination of the latter.

Stelzer et al. [55] investigated the load carrying capability of CFRP/CFRP joints with interleaving steel sheets equipped with CMT-pins in a quasi-static tensile stress state, see Figure 2-14.

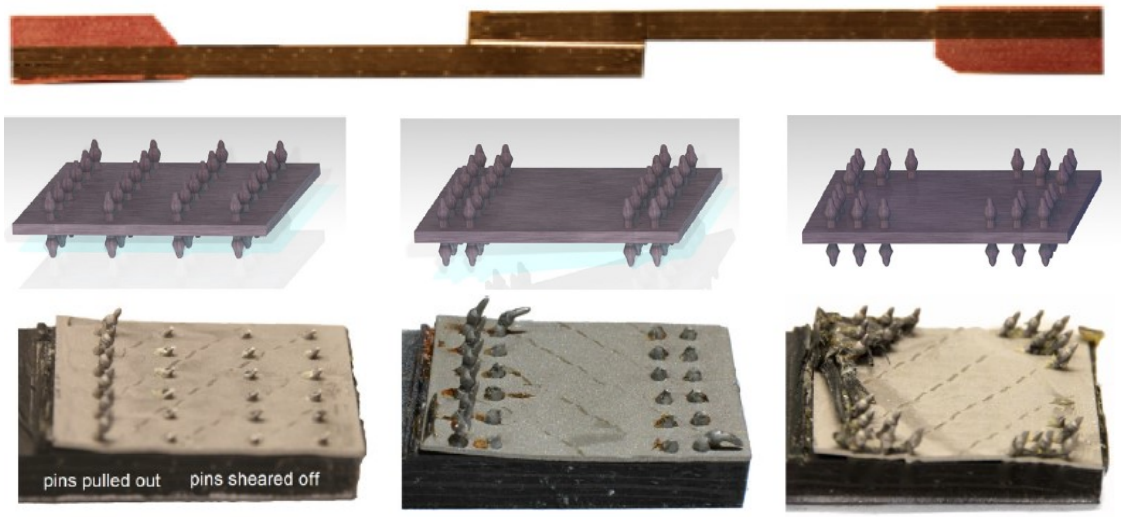

Figure 2-14: Composite-composite single lap joint with pinned metallic interleaving [55]

They found that the shear strength of the pinned configurations was similar to a co-cured reference joint, but outperformed adhesively bonded joints. The pin array had only little impact on the shear stress at ultimate failure. Failure modes were observed to be either pin shear or pull out. However, it turned out that due to plastic deformation of the pins, consequently higher joint failure strain, the total pinned joints' deformation energies were approximately 14 times greater than the co-cured reference joints' [55]. CFRP/CFRP joints with pinned interleaving steel sheets also outperform co-cured reference joints in terms of fatigue strength [56, 57]. As pins are highly loaded in shear direction, metallic pins are preferred over unidirectional composite pins for these applications.

2.3.2 Composite/metal joints

Pins are well suited to serve as fasteners for hybrid composite/metal joints. Several studies [54, 58–66] have been carried out to investigate the mechanical behavior of the joint under tensile loading. These studies mainly differ in the technology chosen for pin creation on the metallic surface. Pinned composite/metal joints can be designed as single lap shear (SLS) or DLS joints. However, DLS designs are preferred as the pins are primarily loaded in shear direction and Mode I loading is lower.

Surfi Sculpt™/Comeld™ Joints

The Surfi-Sculpt™ technology, developed by The Welding Institute (TWI), uses an electron beam to melt and displace metallic material, creating intrusions and protrusions on the surface of a metallic substrate [62, 63, 67]. A wide range of metallic materials

can be treated with this technology, including different titanium alloys. By adjusting the processing parameters, it is possible to vary the diameter, height and even the inclination of these protrusions. The term "Comeld™" describes a joint, made from a metallic sheet, treated with Surfi-Sculpt™, and CFRP, see Figure 2-15. As these protrusions serve as fasteners, they are designated as pins in the following chapters.

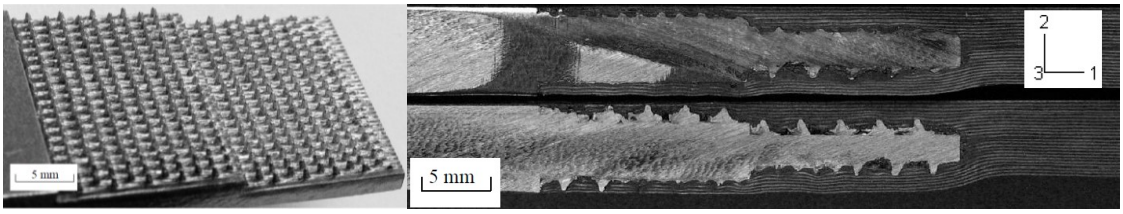

Figure 2-15: Image of a Surfi-Sculpt™/Comeld™ double lap joint [63]
Metallic surface, structured with Surfi-Sculpt™ (left), Comeld™ joint (right)

Tu [63] studied the mechanical behavior of Comeld™ joints, using quasi-static mechanical testing and a simulative approach. Tensile testing of the two-stepped titanium/prepreg specimens revealed that high stress concentrations in the composite close to the tops of the pins caused interlaminar delaminations, leading to final failure, see Figure 2-16.

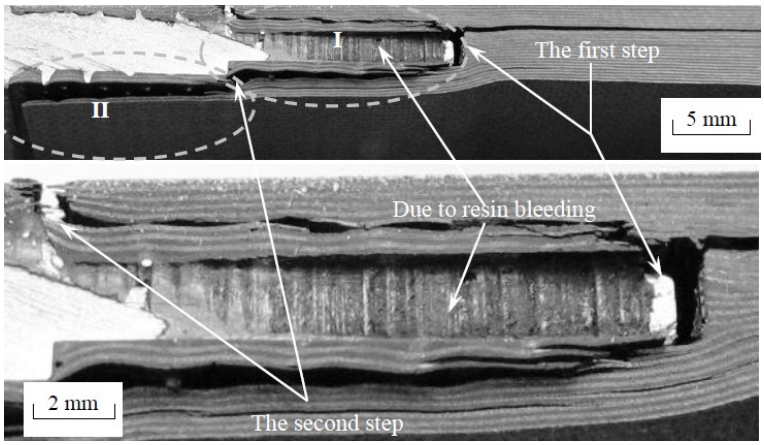

Figure 2-16: Illustration of failure modes for double-stepped Comeld™ joint [63]

Stress concentrations were found to be a combination of shear and peel stresses.

CMT pinning

Ucsnik et al. [54] studied CMT-pinned CFRP/steel DLS specimens under quasi-static tensile loading. Pins had a cylindrical shape with either flat or ball shaped heads. The pins' neck diameter (diameter of welding wire) was chosen to be 0.8mm and the pins were arranged in a 7x5 pattern. The average shear strength of the specimens with flat heads was measured to 15.9MPa. Specimens with ball head shaped pins were able to withstand an average shear strength of 21.9MPa. Due to pin bending, a load deflection

was present within the joining area between metallic and composite joint member, forcing the composite laps to move towards the specimens' thickness direction. The resulting peel stresses limited the load carrying capability of the entire joint. Ball-head shaped pins provided a form closure mechanism which was able to absorb these peel stresses. As a result, ball head shaped pins failed due to a combination of shear and tensile loading, whereas cylindrical pins with flat heads did undergo extensive pin bending, see Figure 2-17.

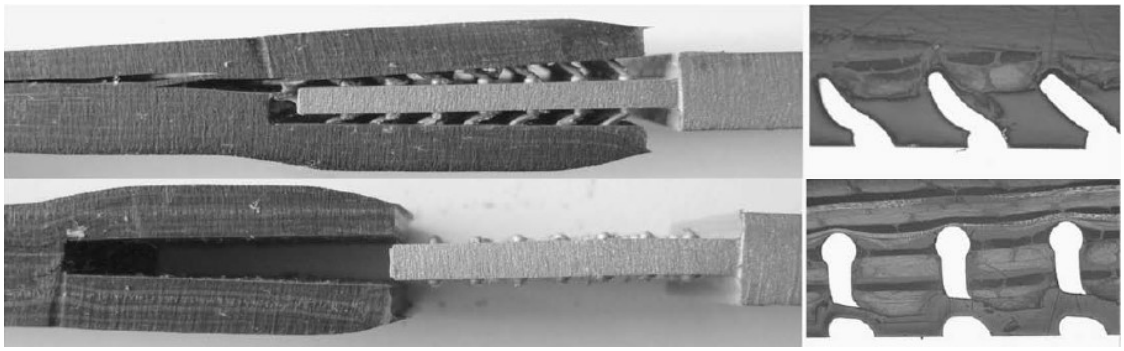

Figure 2-17: Failure modes for CMT-pinned double lap joints [54]

Ucsnik et al. [54] also found that the energy absorption capacity can be significantly increased when compared to a co-bonded reference joint. The absorbed energy until final failure was 27 (specimens with cylindrical pins and flat heads) and 30 (specimens with ball head shaped heads) times higher than for the co-bonded baseline joint.

Micro-machining

Di Giandomenico [58] investigated pinned hybrid CFRP/titanium joints under quasi-static tensile loading. He used double lap stepped and scarfed joints for his experimental research. Pins were created by either electron beam melting or micro machining and several pin geometries were tested. Scarfed specimens with micro-machined shark teeth pins showed the greatest loads at failure. The tensile strength of these specimens was measured to be 124% greater than those of the co-bonded reference joint.

The specimens finally failed due to pin shearing and peel stresses within the composite joint member, see Figure 2-18.

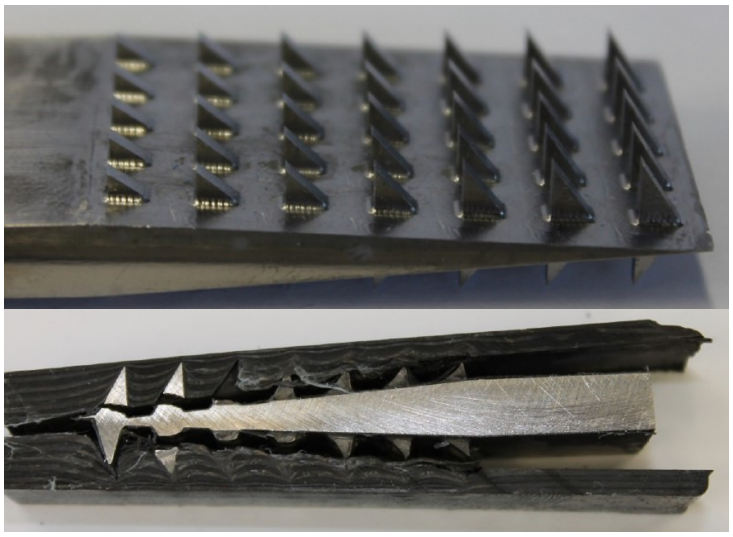

Figure 2-18: Failure mode for scarfed joint with micro-machined shark teeth pins [58]

However, it should be noted that optimizing the pin geometry towards one loading direction reduces the load carrying capability of the joint in the other loading directions, i.e. compressive or transversal loading.

Additive layer manufacturing

Graham et al. [59, 60] studied hybrid composite/metal DLS joints with pins created with the help of additive layer manufacturing techniques, see Figure 2-19.

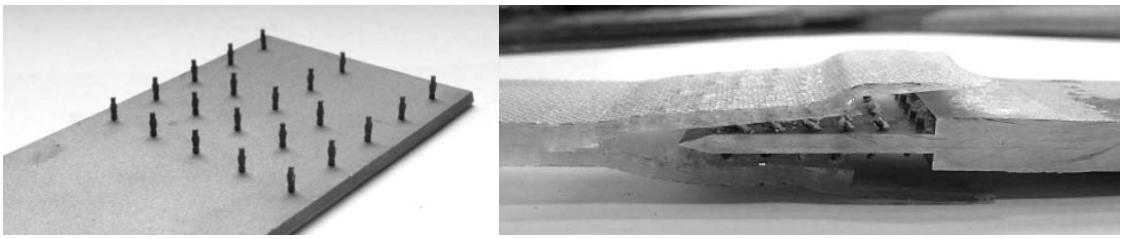

Figure 2-19: Failure mode for double lap joints with pins, produced via additive layer manufacturing techniques [60]

Besides quasi-static tensile testing they also investigated the joints in terms of hot/wet environmental degradation and drop weight impact. Depending on the pin density, pin distribution and stiffness mismatch between the adherends, improvements in ultimate strength for pinned joints were in the range 20-100% when compared to the co-bonded reference [59]. Environmental conditioning was found to be less critical for pinned joints than for co-bonded reference joints. Whereas the strength for the reference joints decreased by 21%, the strength of pinned joints only decreased by 17%. Due to a crack-stopping mechanism provided by the pins, pinned specimens also outperformed the reference joints in terms of impact loading. Even though the ALM-technology provides a

high level of freedom in designing the pin geometry, it has to be noted that this technique includes long process times as well as substantial investment and running costs [59].

2.3.3 Fiber undulation

As pins are inserted into an uncured laminate, filaments are replaced by the pins. This results in fiber undulation around the pins and resin rich zones or voids. Figure 2-20 shows a photograph of a laminate with inserted pins of 0.8mm diameter.

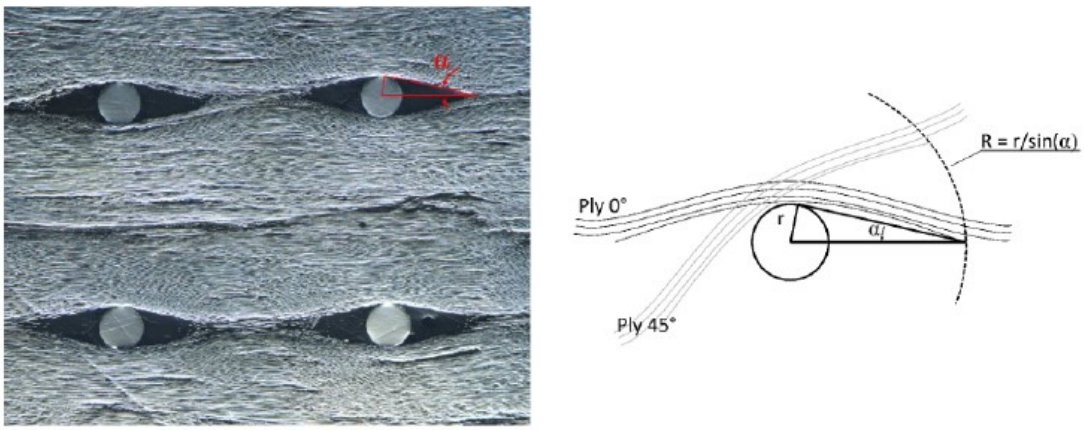

Figure 2-20: 2D microscopy inspection of fiber undulation around pins [66]

By analyzing the greyscale - the fibers are colored in light grey, resin in dark grey and voids in black - the fiber/resin and void ratio can be estimated. Figure 2-21 shows the fiber volume fraction, dependent on the radial distance from the pin.

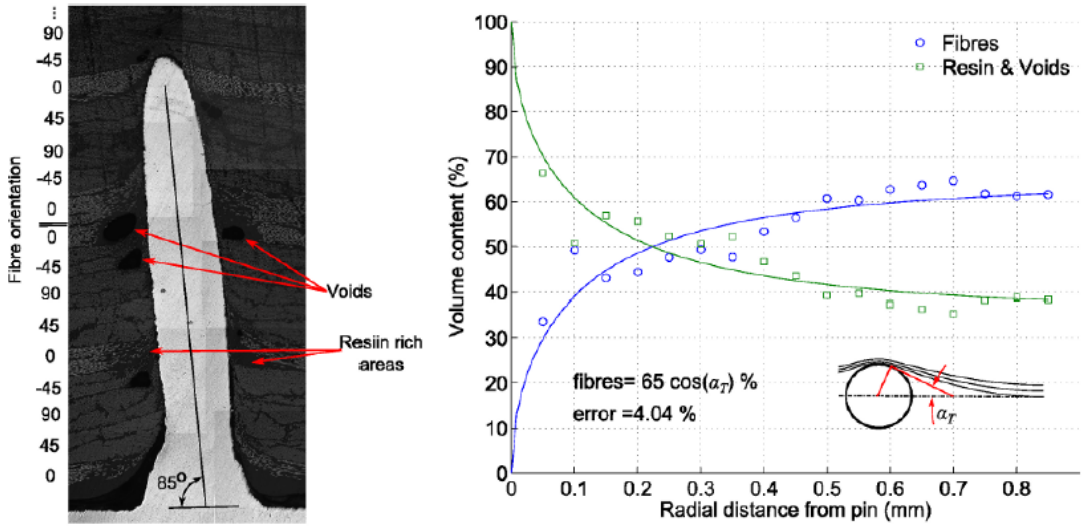

Figure 2-21: Analysis of resin rich areas and local fiber volume content [66]

Quantitative results are only valid for a specific spacing between the pins, pin geometry, type of NCF, Weave or prepreg material and stacking sequence. This measurement technique is not able to capture in-plane and out-of-plane fiber undulations in thickness direction.

Fiber undulations influence the in-plane properties of the composite material. Dickinson et al. [68] numerically studied the tensile stiffness of pinned CFRP laminates. They found that depending on the pin diameter, pin density and laminate stacking sequence, the stiffness reduction in tensile direction is smaller than 15%. The maximum pin density and pin diameter was 4.9% and 0.635mm, respectively. Grassi et al. [69] predicted an in-plane stiffness degradation of 7-10%. They used a pin diameter of 0.28mm and a pin density of 2% for their numerical studies. Experimental studies come to similar conclusions [44, 70, 71]. The compressive stiffness is also reduced by adding pins to CFRP laminates [72].

The strength of pinned composite laminates under tensile and compressive loading has been investigated by several authors [44, 70–76]. Steeves et al. [76] found that the presence of pins decreases the tensile strength of the CFRP-material by 27% and the compressive strength by 30%. The pin diameter and density were set to 0.28mm and 2%. They also found that adjusting the pin pattern so that the distance between the pins in loading direction is maximized, results in the lowest reduction of compressive strength.

Investigations regarding fiber undulations can also be found in research studies which are not directly related to the pinning technology explained above. Brown et al. [77] suggested a thermally assisted piercing process to create holes in thermoplastic fibrous material. This piercing process also creates fiber undulations around the holes which are qualitatively comparable to the fiber undulations caused by pin insertion. Seidlitz et al. [78] used a similar piercing process but added bushings in order to create holes in thermoplastic materials.

2.3.4 FE-modelling of pinned joints

Several authors numerically studied Mode I and Mode II interlaminar delamination in pinned laminates as well as tensile stiffness and strength of pinned composite/composite or composite/metal joints [63, 66, 79–82]. Interlaminar crack propagation was either described by using Virtual Crack Closure Technique (VCCT) or cohesive elements, see Chapter 3.4.1.2. Defining the material input data for the areas close to the pins represents a great challenge.

Tu [63] assumed the material properties to be homogeneous throughout the entire composite laminate. Therefore, no distinction was made between areas located close and far from the pins. Material input of the unidirectional prepreg material are implemented into the analysis.

Bianchi [66] proposed to locally homogenize the material properties for quasi-isotropic laminates. The region within one pin radius from the pin's surface was assumed to have

the properties of pure resin. In addition, an intermediate region was defined. This circular ring-shaped region was located outside the previously described area and limited by the boundary of the resin pockets. Material properties within this region were equal to 50% of the base laminate. All properties of the resin rich zone were considered as parameters of the model and were set over reference tests.

2.4 Intention of this work

After reviewing the state of the art for pinned composite/metal joints, several research questions arise. The following points highlight these questions, together with the intended strategies and methods to solve them:

- which load case is ideal for this study?
  Pinned composite joints should be able to withstand different mechanical loads, i.e. tension, compression, torsion.
  - ➢ Joint behavior of pinned composite/metal joints under tensile loading is not yet fully understood. In addition, tension is the main loading case for these joints. Therefore, this study focuses on tensile testing.
- how to provide optimal mechanical joint behavior for different load cases?
  Due to their asymmetric geometry, shark teeth pins [58] provide great bending stiffness and shear strength against tensile loading of the joint. However, a pin which is not axis symmetrical to its middle axis does not provide identical mechanical properties in all (in-plane) loading directions.
  - ➢ Within the scope of this thesis, the pin shape is kept symmetrical to its longitudinal axis.
- which technology should be used for pin creation?
  Several technologies exist to create pins on the metallic surface. However, due to different test methods and joint geometries presented in the corresponding studies, a direct comparison is not possible.
  - ➢ A comparative study is necessary to identify a suitable pinning technology.
- how can the fasteners be reinforced?
  Joints, tested in the studies presented above, partially failed due to pin failure.
  - ➢ By increasing the pin diameter, the risk of pin failure should be reduced.
- what is the preferred failure at ultimate load?
  Simultaneous adherend failure of both joint members outside the joining area indicates the maximum possible joint strength. If this occurs, the joint efficiency is at 100%.
  - ➢ Several adaptations are required to optimize pinned composite/titanium joints in order to reach high joint efficiencies.
- how can the strain during testing be investigated?
  In order to analyze the mechanical behavior of composite/metal joints, the local strain has to be known in detail.

  - Digital image correlation techniques are used to investigate the local deformation on the specimens' lateral and top surface and also to further analyze the strain state at different load levels.

- how can joint behavior be understood?
  Understanding the interaction between the joint members and fasteners is essential to improve the joint efficiency.
  - A simulation approach, using finite element methods, helps to estimate the joint stiffness and strength and additionally to optimize the joint geometry in terms of pin amount and adjustment.
- what are the correct input parameters for the simulation?
  Extensive material testing is necessary to derive material input data for the FE analysis.
  - Tensile, compressive, Mode I and Mode II fracture toughness testing of the single joint members are conducted. In addition, fiber undulation around the pins is measured and used as an input parameter for the simulation. As opposed to the measurements presented earlier, a specific 2.5D measurement technique enables the analysis of the fiber distortion not only of the top layer, but also of the underlying layers.
- what effect do fiber undulations have on the mechanical behavior of the entire joint?
  Pinned joints are characterized by a deflection of fibers around pins.
  - To investigate the impact of fiber undulation around the pins on the joint's mechanical performance, joints with holes, derived by hole drilling into the cured laminate, are compared to pinned joints with fiber undulations by means of mechanical testing and FE-analysis.

3 Fundamentals

This chapter provides insight into the methods and procedures that were utilized in this study. The basic requirements for pinned CFRP/metal joints are introduced, followed by a description of the testing standards, methods and equipment used for destructive testing along with the challenges that arose. The measurement of fiber undulation around the pins is explained and afterwards the fundamentals for FE-modelling of the CFRP/metal joints are described.

3.1 Basic requirements for pinned composite/metal joints

As described by several authors [54, 58, 63, 66], co-bonded pinned composite/metal joints transfer load both via an adhesive bond between the metallic and composite joint member as well as through a form fitting mechanism, provided by the pins. Whereas the adhesive bond has a high impact on the initial tensile stiffness and first failure, the form fit through pins can lead to a higher joint tensile strength and strain at ultimate failure, compared to co-bonded reference joints.

In order to obtain a greater joint tensile stiffness and strength for first failure, it is crucial that proper surface pretreatment is applied especially for the metallic joint member [5–9]. In addition, the geometrical design of the joining area has a high impact on the joint tensile strength of pure adhesive joints. Tapered step joints, stepped lap joints and scarfed joints can provide greater joint strength than single- or double lap joints. They have been investigated extensively [11, 32, 58, 83]. The bond-line thickness also influences the joint tensile strength of pure adhesive joints [84].

To achieve a greater joint strength at ultimate failure, the pinned composite/metal joint must fulfill several requirements. The pins should be characterized by an overall shear strength, which needs to exceed the shear strength of the adhesive bond. It is to be noted, that the load introduction into the different pins is typically unevenly distributed. The pin's flexural strength is also important for a great ultimate joint strength, as pins can also fail due to excessive bending (see Chapter 5.4.2.5). Furthermore, both metallic and composite joint members must provide a high tensile strength to prevent net section failure. Also, the hole bearing stiffness and strength significantly impact the load distribution on the different pin rows, influencing the ultimate joint strength.

Bending of the composite layers towards the z-direction (see Chapter 5.1.1) is a major challenge for pinned composite/metal joints in a single or double lap configuration, as

described in [54, 58, 63]. This drawback can be reduced by undercuts caused by special pin head geometries and/or by increasing the bending stiffness of the composite joint member. Moreover, an adjusted joint design (see Chapter 5.4.1.1) can minimize bending of the composite layers towards the z-direction.

The research presented in this thesis exclusively focuses on the mechanical behavior of pinned CFRP/metal joints under a pure quasi-static tensile load. The main goal of the research is to investigate form fitting mechanisms provided by the pins. Proper surface pretreatments were only conducted for the co-bonded reference joints, which serve as a baseline for the comparison of co-bonded reference joints and pinned joints.

3.2 Mechanical testing

This chapter outlines the standards, methods and equipment that were used for destructive testing. The testing plan provides an overview of the tests performed, followed by a description of the measuring equipment. Afterwards, each method is explained in further detail. The test results can be found in Chapter 5.

3.2.1 Testing plan

Within the scope of this thesis, several destructive tests were carried out, either on coupon level or on element level. Figure 3-1 shows a testing pyramid for both mechanical testing and simulation.

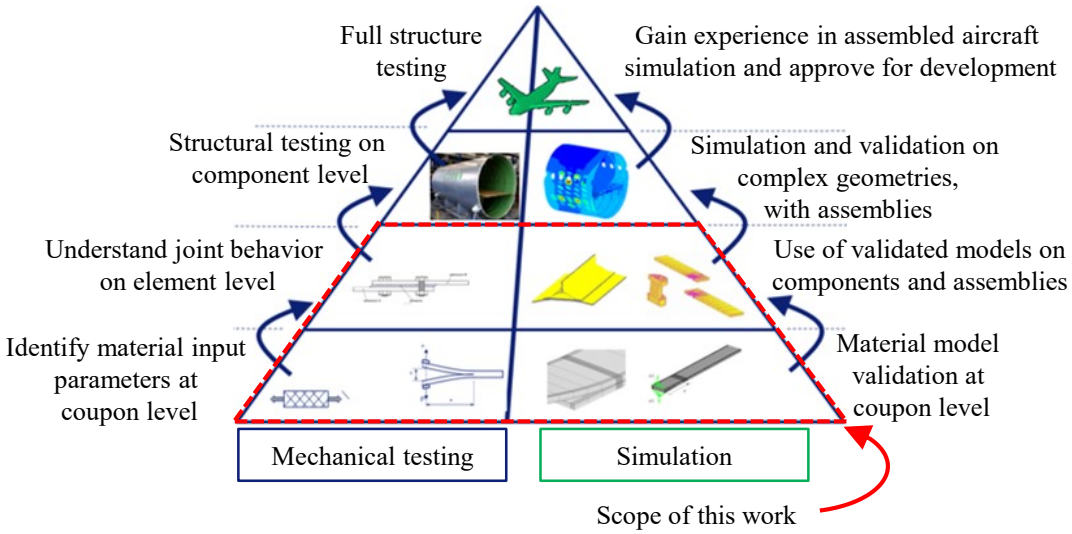

Figure 3-1: Test pyramid including mechanical testing and simulation
According to [85]

Mechanical tests on coupon level were used to identify material input data for the FE-Analysis. Tests on coupon level were also simulated to validate the material models. Mechanical testing of the entire joint aimed to help evaluate the mechanical behavior of pinned CFRP/metal joints. In addition, it served to validate a FE-Analysis of the entire

joint. A simulation approach on element level enables a specific analysis of stress states and mechanical interaction between metal and composite joint members and pins. Furthermore, a validated FE-Analysis is a less cost intensive method to vary specimen design and geometry, as opposed to destructive mechanical testing. The mechanical testing carried out in the scope of this work can be divided into four test series, see Table 3-1.

Table 3-1: Testing plan for destructive mechanical testing

Test series	Description	Standard	Materials	Purpose
1	CFRP/steel joint design 1	ASTM D 3528-96	Steel 1.4301 ST15 + NCF	Selection of pinning technology
2	Tension Metal	DIN EN ISO 6892-1 / DIN 50125	Steel 1.4301 Ti6Al4V	Material characterization
2	Tension CFRP	ASTM D 3039/D 3039M-00	PR520 + NCF	Material characterization
2	Mode I fracture toughness	ASTM D 5528-01	PR520 + NCF Ti6Al4V 5320-1 Prepreg	Material characterization
2	Mode II fracture toughness	DIN EN 6034	PR520 + NCF Ti6Al4V 5320-1 Prepreg	Material characterization
2	Tension neat resin	DIN EN ISO 527-1	PR520	Material characterization
2	Compression neat resin	DIN EN ISO 604	PR520	Material characterization
3	CFRP/titanium joint design 1	ASTM D 3528-96	Ti6Al4V PR520 + NCF	Variation of pin quantity and adjustment
4	CFRP/titanium joint design 2	ASTM D 3528-96	Ti6Al4V 5320-1 Prepreg	Impact of fiber undulation on joint mechanical behavior

Whereas test series 1, 3 and 4 were performed on element level, test series 2 was used to obtain material input parameters for FE-analysis. Each mechanical testing method and setup is described in detail within Chapter 3.2.3 to Chapter 3.2.5.

3.2.2 Measuring equipment

Depending on the testing method, different measuring equipment was used for data acquisition. The two main measures required were tensile/compressive force and 2- or 3-dimensional deformation state of the specimen's surface. Stress and strain measures can be computed from these by taking into account the specimen's geometry. Whereas the force can be directly measured by a load cell, the displacement of the universal testing machine's crosshead is not necessarily indicative for the specimen's actual strain state. Possible reasons for this discrepancy are slip effects between the grips and the specimen, as well as structural compliance of the testing machine. Techniques used to capture the specimen's deformation state were Digital Image Correlation, Video-extensometer and strain gauges.

3.2.2.1 Universal testing machines

Two electro mechanical universal testing machines were utilized to perform the mechanical tests for series 1 through 4. The first testing machine, the Hegewald & Peschke Inspect 250 (UPM 250), is able to provide a maximum tensile and compressive force of 250kN. Hydraulic grips were used in combination with this testing machine, see Figure 3-2.

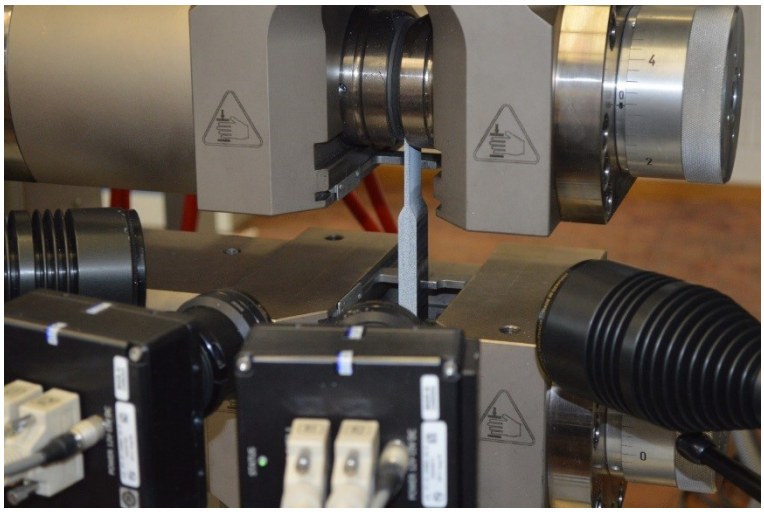

Figure 3-2: Universal testing machine and Aramis DIC-Correlation equipment

The second testing machine, the Hegewald & Peschke Inspect table 100 (UPM 100), is a 100kN testing machine for tensile and compressive testing. Mechanical wedge type grips were used in combination with this machine.

Four class 1 load cells were available for acquisition of tensile and compressive forces with nominal loads of 250kN, 100kN, 10kN and 1kN.

3.2.2.2 Digital Image Correlation

To analyze the mechanical behavior of pinned CFRP/metal joints, it is necessary to capture the strain field of the joining area. Therefore, full-field Digital Image Correlation technique was applied for all tests on element level and for some tests on coupon level. A GOM ARAMIS 4M system in a stereoscopic configuration was used.

3D Analysis

Two cameras in a stereoscopic configuration using four-megapixel sensors (2358 x 1728) and endocentric Titanar objectives with 50 mm focal length simultaneously captured pictures of the specimens. The stereoscopic configuration was chosen to avoid the apparent deformation that occurs when the distance between the specimen and the camera changes while measuring on a 2D configuration with just one camera. Since magnification is a function of working distance for regular endocentric objectives, the system would interpret specimen movement toward or away from the camera as expansion or contraction [86, 87, 87].

The cameras were positioned in a manner, that they form an angle of around 25° relative to the normal axis of the inspected surface. The distance of the cameras from the specimen was adjusted to around 295 - 355mm, depending on the test series. This configuration achieved a field of view of about 50 - 60mm width and 37.5 - 45mm height. Each picture was dived into correlation templates or "facets" of 15 x 15 pixels with an overlap of three pixels between neighboring facets. Prior to the measurements, the DIC system was calibrated according to the manufacturer's instructions. The calibration consisted of 13 captures with the calibration object placed in front of the camera in different positions and orientations. After calibration, the system could calculate the position and orientation of the cameras relative to each other to triangulate the location in space of the facets' center. Figure 3-3 exemplary shows noise caused by the DIC measurement and the testing machine for a specimen of test series 4, at an unloaded state.

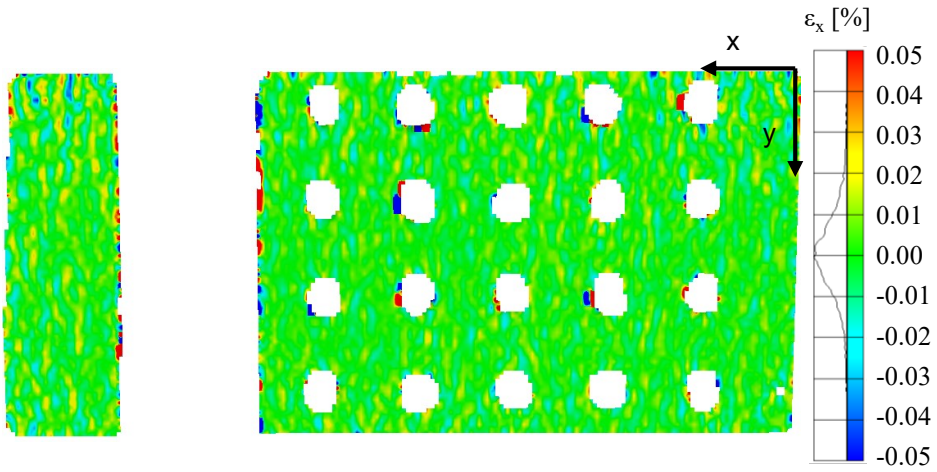

Figure 3-3: Visualization of noise caused by DIC and testing machine

The typical local strain precision rounds to ±0.02%. Similar results for measurement inaccuracies were also found for the other tests conducted by the help of 3D DIC-measurement technique.

3.2.3 Test series 1 and test series 3: CFRP/steel joint and CFRP/titanium joint design 1

Test series 1 and 3 were performed on element level. A double lap shear geometry was chosen for quasi-static tensile testing. The main goal of test series 1 is to identify an appropriate pinning technology, whereas test series 3 aims to optimize the specimen design in terms of amount and adjustment of pins. Maximum joint tensile strength is the primary design criterion for both test series. The same testing standard and specimen geometry are used for test series 1 and test series 3, described below.

3.2.3.1 Testing standard

Tests were performed, following ASTM D3529-96 [88] as this standard is suitable for determining the strength properties of DLS adhesive joints by tension loading. For pinned composite/metal joints, such a standard for tensile testing does not exist. Nevertheless, this standard is also used for pinned joints as co-bonded reference joints serve as a baseline for comparison of mechanical properties between the two types of joints.

According to ASTM D3529-96, specimens were loaded with a constant free crosshead speed of 1.3mm/min until ultimate failure. However, ultimate failure is not always characterized by a sudden drop, but by a gradual load decrease, see Chapter 5.1.3 and 5.4.1. In these cases, a load drop of 90% in relation to maximum tensile load was used as a condition to stop free crosshead movement.

3.2.3.2 Specimen geometry

ASTM D3529-96 defines the specimen geometry in detail. It is recommended to cut the specimens from test panels [88]. In order to use this standard for pinned composite/metal joints, the geometry of the specimens had to be slightly adjusted. Based on Ucsnik's work [54], the thickness of the composite joint member was set to 11mm, see Figure 3-4.

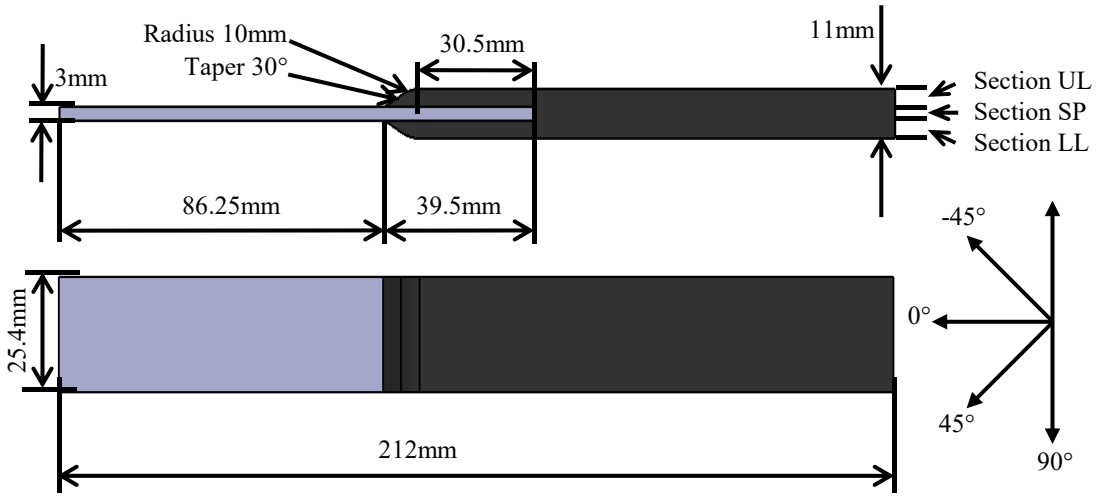

Figure 3-4: Dimensions for double lap joint design 1

Furthermore, a taper of 30° was applied to the front edge of the composite joint member to decrease free edge effects and increase the strength properties of the adhesive bond. Whereas the specimen geometry is similar for test series 1 and test series 3, the selected material differs significantly. The materials and layups for the composite joint member can be viewed in Table 3-2.

Table 3-2: Material selection and fiber architecture for composite joint member

CFRP joint member	Test series 1	Test series 3
Filament type	IMS65 E23 24K 830tex	IMS60 E13 24K 830tex
Semi-finished product	NCF triax 0°/0°/90° 596g/m²	NCF biax 0°/90° 552g/m² NCF biax +45°/-45° 552g/m²
Resin	ST15 RTM-resin	PR520 RTM-resin
Binder material	Cycom 7720 & TEC WEB: ABE 003	TEC WEB: ABE 003
Fiber architecture		
• Section UL	$[0_2/90_3/0/45_2/-45_3/45]_2$	$[0/90/-45/45]_4$
• Section SP	$[0_2/90_3/0/45_2/-45]_s$	$[0/90/-45/45/0/90]_s$
• Section LL	$[45/-45_3/45_2/0/90_3/0_2]_2$	$[45/-45/90/0]_4$
Nominal FVF outside joining area [-]	0.65	0.60

Binder web was placed between every NCF-layer, but not in the joining area between metallic and CFRP joint member. The fiber volume fraction increases in the joining area for pinned specimens as fibers are dislocated by the pins, but not removed, see Chapter 3.3 and Chapter 4.2.2.

3.2.3.3 Data acquisition

As stated in Chapter 3.2.2, the deformation state has to be measured directly from the specimen's surface and cannot be computed by taking into account the displacement of the testing machine's crosshead. In the case of test series 1 and 3, the DIC-system GOM Aramis was used for measuring the deformation state, whereas the applied tensile force was recorded by the 250kN load cell. In order to evaluate the performance of the joint, it is recommended to analyze the joining area instead of the entire joint [54, 58, 62, 64, 65]. Therefore, stress-strain curves were generated for all specimens of test series 1 and 3. The nominal joint stress, normalized in relation to the metallic joint member, σ_{x_nom} is defined as follows:

$$\sigma_{x\_nom} = \frac{F_x}{w_m * t_m} \tag{3-1}$$

Where F_x is the applied load and w_m and t_m are the width and thickness of the metallic joint member. The nominal strain ε_{x_nom} is computed by taking into account the displacement of two characteristic lines in the direction of the specimen's thickness, named Section 0 and Section 1, see Figure 3-5.

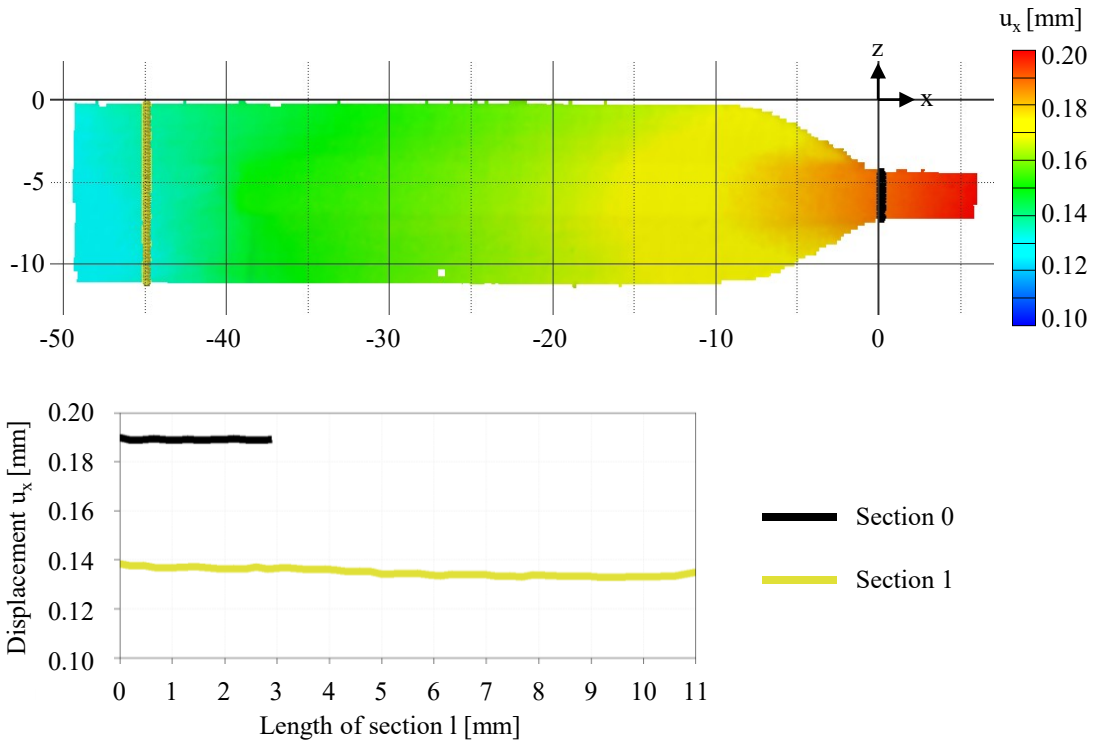

Figure 3-5: Determination of nominal strain ε_{x_nom} for joint design 1
Dimensions in [mm]

Whereas Section 0 is placed at the front edge of the taper of the composite joint member, Section 1 is located 50mm (test series 1) or 45mm (test series 3) behind Section 0 in a non-deformed state. Both sections are located in a manner that approximately uniform

displacement values u_x along these sections can be expected throughout the entire test, see Figure 3-5. The discrepancy of the location of Section 1 between test series 1 and test series 3 results from the measurement field adaption. The measurement field's reduced size leads to a higher resolution in the joining area. However, test series 1 and test series 3 are not directly compared to each other.

The nominal strain ε_{x_nom} is computed by taking into account the local displacement values u_x along these sections:

$$\varepsilon_{x\_nom} = \frac{\left(\bar{u}_{x\_s0} - \bar{u}_{x\_s1}\right)}{l_0} \tag{3-2}$$

with:

$$\bar{u}_{x\_s0} = \sum_{p=1}^{r-1} \frac{\left(u_{x\_s0_{p+1}} - u_{x\_s0_p}\right) * \left(z_{s0_{p+1}} - z_{s0_p}\right)}{2 * \left(z_{s0_r} - z_{s0_1}\right)}$$

and:

$$\bar{u}_{x\_s1} = \sum_{t=1}^{q-1} \frac{\left(u_{x\_s1_{t+1}} - u_{x\_s1_t}\right) * \left(z_{s1_{t+1}} - z_{s1_t}\right)}{2 * \left(z_{s1_q} - z_{s1_1}\right)}$$

Where r and q describe the amount of measuring points along both sections. The corresponding positions of the local displacement values u_{x_s0} and u_{x_s1} in z-direction are defined as z_{s1} and z_{s2}. In addition, l_0 is the initial distance between Section 0 and Section 1 at an unloaded state.

3.2.4 Test series 2: Material characterization

The main goal of test series 2 is to identify material input parameters for the FE-Analysis. Therefore, tensile testing was performed for the metallic and composite joint member. The investigation of interlaminar properties is also of great importance for the FE-analysis. Specifically, Mode I and Mode II fracture toughness between the NCF-layers as well as between composite and metallic joint member were measured. Neat resin testing, tension and compression, are also necessary in order to model the area close to the pins.

3.2.4.1 Tension metal

Tensile testing for specimens made from stainless steel 1.4301 and Ti6Al4V were performed according to standard DIN EN ISO 6892-1 [89] and DIN 50125 [90]. Whereas DIN EN ISO 6892-1 describes all requirements for metal tensile testing, DIN 50125 represents a supplement containing alternative specimen geometries applicable in connection with DIN EN ISO 6892-1.

According to DIN 50125, dog-bone shaped specimens of form E3x8x30 were cut from metal plates of 3mm thickness. The tests were carried out using the UPM100 testing machine in combination with the 100kN load cell and the displacement was measured by the video-extensometer. Preliminary tests indicated that there is a significant strain-

rate dependency for stainless steel 1.4301 and Ti6Al4V specimens. The standard defines a three-stepped adjustment of free crosshead velocity. However, as this test aimed to identify material parameters applicable for the simulation of full joint tests on element level, it was reasonable to use a free crosshead velocity of 1.3mm/min, identical to the velocity for test series 1, 3 and 4.

3.2.4.2 Tension CFRP

In addition to tensile testing of the metallic joint member, input parameters for the composite joint member were also required. These tests were performed based on standard ASTM D 3039/D 3039M [91]. Therefore, flat panels of 3mm thickness with a FVF of 60% were manufactured using an RTM-process. Two different panels with a $[0/90]_{3s}$ and $[+45/-45]_{3s}$ layup were produced containing IMS60 NCF-material in combination with PR520 RTM-resin, see Table 3-2. As biaxial NCF-material was used, a unidirectional layup was not possible. Single specimens were then cut from the panels.

Because of high expected tensile loads for the $[0/90]_{3s}$ specimens, all CFRP tensile tests were performed on the UPM250 testing machine in combination with the 250kN load cell. As deformation in tensile(x)-direction and transverse(y)-direction had to be captured, the Aramis DIC-system was used for these tests. According to test ASTM D 3039/D 3039M, the specimens have a rectangular shape, width of 25mm and an overall length of 250mm. Deviating from ASTM D 3039/D 3039M, glass-fiber fiber tabs were bonded onto the specimens at both ends in order to prevent slip effects between the grips and specimens as well as to avoid damage of the specimen's surface. The standard suggests to solely apply emery cloth instead of tabs for balanced and symmetric layups. However, testing results indicated that the free length between the tabs was sufficient and tabs had no influence on the stress-strain behavior of the coupons. Longitudinal ε_{x_nom} and transversal ε_{y_nom} strain measures were evaluated using a similar method as described in Chapter 3.2.3.3. The measurement field was defined to be 30mm in length and 15mm in width, see Figure 3-6.

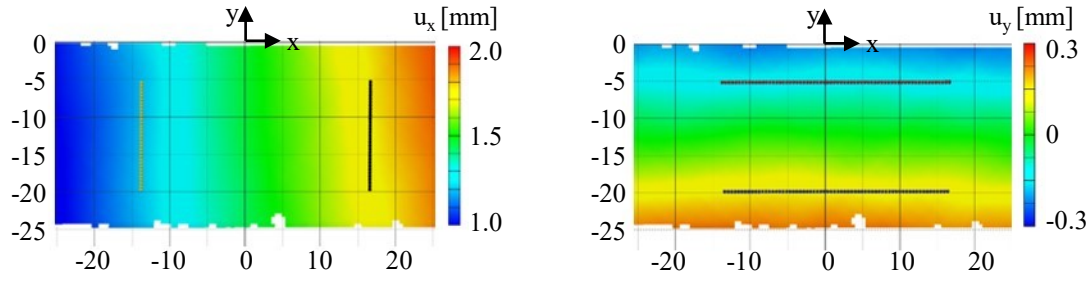

Figure 3-6: Determination of nominal strain ε_{x_nom} and ε_{y_nom} for CFRP tensile testing
Dimensions in [mm]

By taking into account the classical laminate theory and assuming transversely isotropic material behavior, both strain measures in combination with the applied stress are sufficient to calculate the elastic tensile moduli E_1, E_2 and E_3, poisson's ratios v_{12} and v_{13} and shear moduli G_{12}, G_{13} and G_{23}, according to ASTM D 3039/D 3039M [91] and ASTM D 3518/D 3518M [92]. However, the poisson's ratio v_{23} cannot be computed by using the measurement data available and therefore has to be estimated. Tensile strength values for the $[0/90]_{3s}$ and $[+45/-45]_{3s}$ setup are calculated directly from the maximum applied force and specimen's cross section.

3.2.4.3 Mode I fracture toughness

Evaluating Mode I and Mode II fracture toughness is essential in order to predict delamination with the help of cohesive elements (see Chapter 3.4.1.2). Delamination within the CFRP/metal joint can occur within the CFRP joint member. Alternatively, it can occur at the interface between composite and metallic joint member. Both cases were tested with the material combinations NCF/PR520, Prepreg 5320-1 and hybrid titanium-composite Ti6Al4V/NCF/PR520.

Testing standard ASTM D 5528 - 01 [93] is the basis for these tests. Rectangular shaped Double Cantilever Beam (DCB) specimens with a length of 125mm and a width of 25mm were tested for the three material combinations mentioned above.

In the case of NCF/PR520 specimens, test panels of 3mm thickness were manufactured in a RTM-process, containing a $[90/0]_{3s}$ layup. Single specimens were cut from these panels. Standard ASTM D 5528 - 01 is limited to unidirectional composites. However, as mentioned, the production of unidirectional specimens is not possible with bidirectional NCF-material. To guarantee in-plane crack propagation along the mid-plane, two 0°-plies were placed in the middle of the DCB-specimen. In between these two 0°-plies, a release foil was positioned, see Figure 3-7.

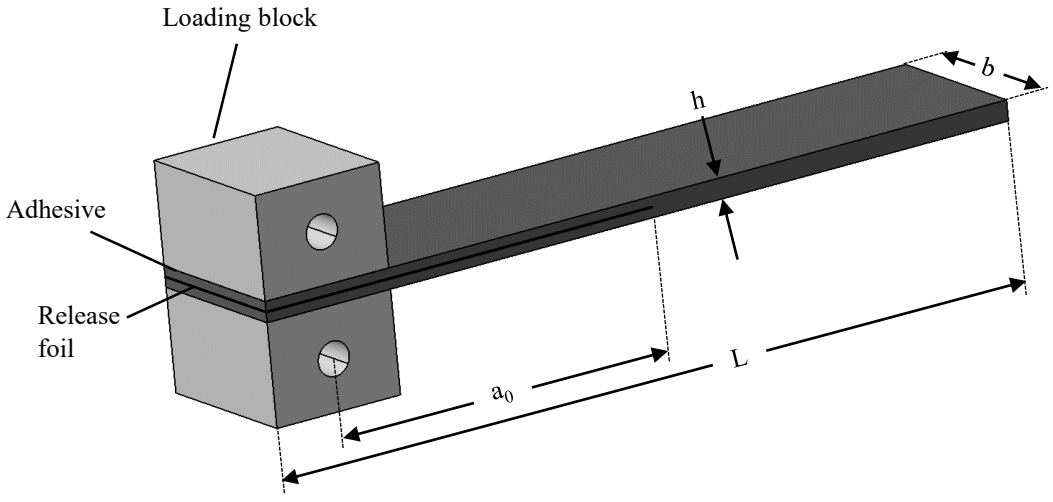

Figure 3-7: Specimen geometry for Mode I fracture toughness
According to [93]

In addition, two loading blocks, which serve as load input elements, were adhesively bonded onto the composite. The initial delamination length a_0 was adjusted to 50mm. The tests were performed using the UPM100 testing machine with a constant free cross-head speed of 5mm/min. Load was recorded by the 1kN load cell and images of the specimen's front face were taken with a frequency 2/s. The standard requires loading the specimen until a first delamination crack growth of 3 to 5 mm, followed by unloading. Then the tip of the precrack was marked. Afterwards, the specimen was reloaded until crack propagation occurred throughout the entire bond length and both beams were separated from each other. Finally, the images were used to measure the position of the crack tip for several load points. By using the Modified Compliance Calibration (MCC) Method, the Mode I interlaminar fracture toughness G_{Ic} was computed. For further information regarding testing procedure and calculation of the G_{Ic}-value, please refer to ASTM D 5528 - 01 [93].

Deviating from this standard, tests were also performed using alternative loading blocks which were clamped laterally onto both beams, see Figure 3-8.

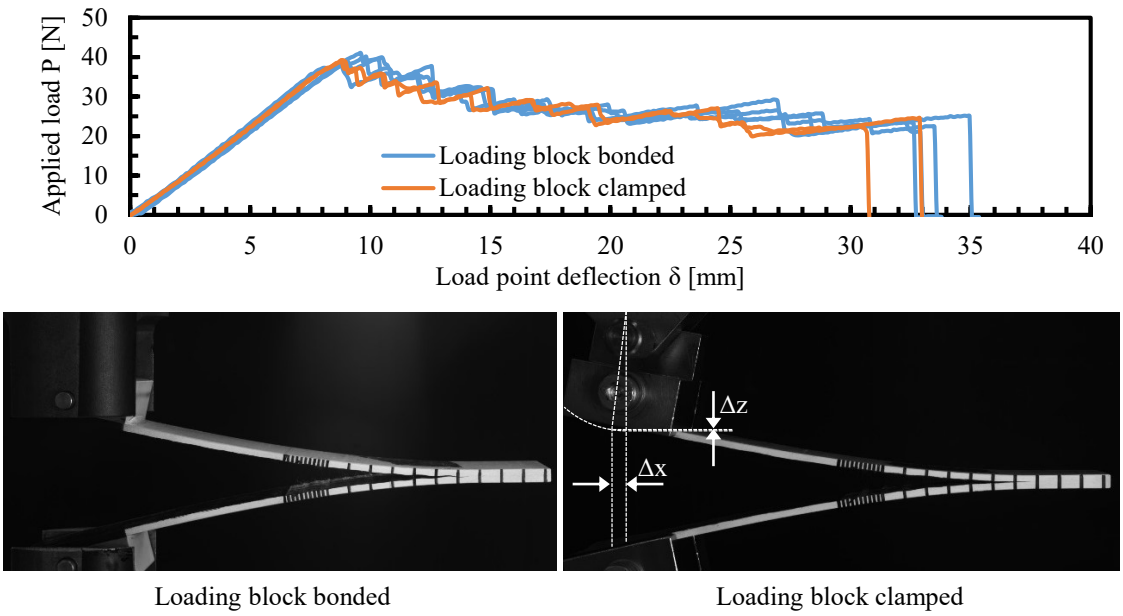

Figure 3-8: Comparison of load introduction for Mode I fracture toughness

The clamped loading blocks reduce the specimen's production time significantly. It was found that these loading blocks have a negligible influence on the applied load - load point deflection behavior for NCF/PR520 specimens. Care was taken to ensure that only specimens with an identical precrack length are compared. It should be noted that due to the greater distance between the load introduction point and the specimen's surfaces, delamination length can no longer be referenced to the longitudinal axis of the testing machine, see Figure 3-8. The error regarding load point deflection, indicated as Δz, is negligible as tilting angles of the loading blocks stay small throughout the entire test. In

order to account for this issue, ASTM D 5528 - 01 provides two correction factors, explained in Annex A1 of this standard.

Test specimens made of Prepreg 5320-1 were cut from 3mm thick panels with a FVF of 60%, produced in a press. These panels consisted of 22 unidirectional prepreg plies and no binder material was placed between the plies.

Hybrid Ti6Al4V/NCF/PR520 specimens were tested to evaluate the Mode I fracture toughness of the interface between titanium and composite joint members. As the materials for the two beams of the DCB-specimens are not identical, the thickness of both joint members had to be adjusted, in order to assure the same bending stiffness for both laps. This was done with the help of a FE-analysis. Care was taken to ensure a horizontal orientation of the bonded part of the DCB-specimen to enable the measurement of delamination length. The delamination length serves as an input parameter for the calculation of the G_{Ic}-value by the MCC Method, described in ASTM D5528-01 [93]. Furthermore, the specimen was designed to avoid plastic deformation within the titanium. By estimating a G_{Ic}-value of 1000J/m², taken from the PR520 data sheet, a thickness of 1.5mm for the titanium beam and 2mm for the biaxial $[90/0]_4$ composite beam led to positive results. For a more detailed explanation of the FE-analysis, please refer to Chapter 3.4 and Chapter 5.2.3.2. For the Mode I fracture toughness tests of material combination Ti6Al4V/NCF/PR520, a hybrid titanium-composite plate was produced in a RTM-process. A titanium sheet of 1.5mm thickness was treated with sandpaper grit 180 and cleaned with isopropanol. Afterwards, this sheet was positioned in a mold. The release foil and dry fiber biaxial NCF-material with a $[90/0]_4$ layup was placed on top of the titanium plate. A "TEC WEB: ABE 003" binder web was inserted between the NCF-layers, but not between the titanium and composite. Subsequently, the NCF was injected with PR520 RTM-resin and the plate was cured for two hours. The process is similar to the RTM-process, explained in Chapter 4.3. Finally, the specimens were cut from the 3.5mm thick plate using a waterjet cutting machine. The specimen's edges were then grinded in order to reduce roughness caused by the cutting process.

All test specimens of the three material combinations were dried in an oven at 50°C under around +10mbar above vacuum for 12 hours prior to testing. Overall, Mode I fracture toughness testing involves several challenges and the evaluation is especially critical. Chapter 5.2.3 presents the testing results and analyzes the different challenges in further detail.

3.2.4.4 Mode II fracture toughness

The determination of interlaminar fracture toughness energy Mode II was performed according to standard DIN EN 6034 [94].

This test is based on a 3-point bending test setup, see Figure 3-9.

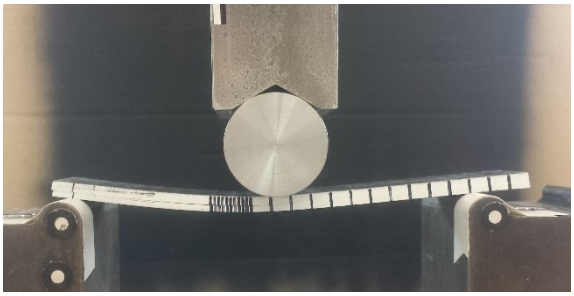

Figure 3-9: Mode II fracture toughness testing, three-point bending test setup

The production of specimens for Mode II testing is almost identical to those of Mode I testing. However, the specimen length was changed from 125mm to 120mm and the length of the inserted release foil, which served as the crack initiator, was reduced from 62.5mm (Mode I testing) to 40mm (Mode II testing). Loading blocks are not necessary for Mode II testing.

Tests were performed on the UPM100 testing machine in combination with the 10kN load cell. The span length between the two supports on the bottom side of the specimen was adjusted to 100mm. Furthermore, the free crosshead velocity was set to 1mm/min. The critical load at delamination crack onset was recorded and as soon as a small load drop occurred, loading of the specimen was stopped.

According to standard DIN EN 6034, the G_{IIc} Mode II fracture toughness can be calculated by taking into account the crosshead displacement at crack delamination onset, the critical load to start the crack, the initial crack length, specimen width and the span length. For further details regarding the testing procedure and calculation of the G_{IIc}-value, please refer to DIN EN 6034 [94].

3.2.4.5 Tension and compression neat resin

Knowledge of neat resin's mechanical properties is essential for the FE modelling of resin pockets for pinned composite laminates. Therefore, tension and compression testing were performed for PR520 RTM-resin. Even though linear elastic mechanical properties and strength values for tensile and compressive loading are given in the datasheet, the exact plastic behavior is unknown.

Tensile neat resin testing was carried out according to DIN EN 527-1/DIN EN 527-2 [95, 96]. For this purpose, dog-bone shaped specimens of shape 1A were cut from a 4mm thick plate, see Figure 3-10.

Figure 3-10: Dog-bone specimen for neat resin tensile testing

The plate was manufactured using a RTM-process. Therefore, the resin was injected into the empty mold with a pressure difference of 0.5bar. In regard to porosity, applying ambient pressure at the resin outlet and excessive pressure at the inlet lead to the best results. However, the porosity content was not measured by ultrasonic inspection. Instead it was visibly analyzed after cutting out the specimens.

For tensile testing, the UPM100 testing machine in combination with the 100kN load cell was used and the deformation state was captured by the Aramis DIC-system. Specimens were clamped between the mechanical grips and loaded at a constant free crosshead velocity of 1mm/min until final failure.

The nominal stress σ_{x_nom} can be calculated by taking into account the applied load and the specimen's cross section. Longitudinal ε_{x_nom} and transverse ε_{y_nom} strain measures are computed by the method described in Chapter 3.2.4.2. However, in contrast to tensile testing for CFRP, the measurement area is significantly smaller with a length of 20mm and a width of 6mm. Under the assumption of isotropic material behavior, the poisson's ratio v can be calculated as well.

Besides tensile testing, compression testing was also conducted for neat PR520 RTM-resin. DIN EN ISO 604 [97] served as a basis for these tests. Two different specimen geometries are described in this standard. In order to determine the compressive modulus, rectangular shaped specimens with a length of 50mm, a width of 10mm and thickness of 4mm are required. For the measurement of compressive strength, specimens should be rectangular shaped with the dimensions of 10mm*10mm*4mm (length*width*thickness). Due to the fact that the thickness for all neat resin specimen's testing is identical, the specimens for compression testing could also be cut from the plate mentioned earlier.

The UPM100 testing machine in combination with a plate-to-plate configuration was used for both types of specimens. Furthermore, the applied load was recorded with the help of the 100kN load cell. The specimens were tested by loading them with a constant free crosshead velocity of 1mm/min. While the specimens of 50mm length were only tested until plastic deformation occurred, the specimens of 10mm length were loaded until final failure.

By applying strain gauges to both sides, the deformation on the specimen's surface could be measured, see Figure 3-11.

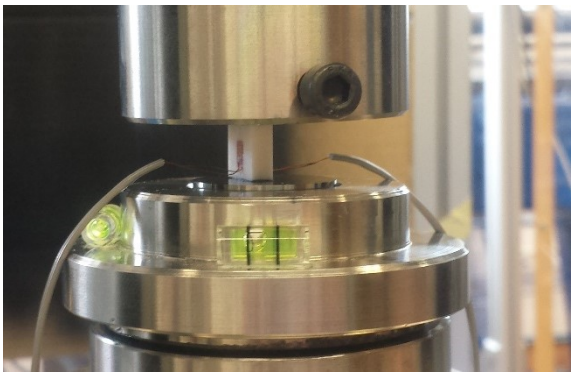

Figure 3-11: Plate-plate testing setup for neat resin compression testing

However, de-bonding of the strain gauges from the specimen's surface took place for those with 10mm length. This was caused by buckling at a nominal compressive stress of around 135MPa. As a consequence, the strain cannot be measured at loads beyond approximately 135MPa. The mechanical behavior for neat resin at high load states can only be evaluated by means of load-displacement instead of stress-strain curves.

3.2.5 Test series 4: CFRP/titanium joint design 2

The main goal of test series 4 is to evaluate the composite joint member's load carrying capability of the pinned composite/metal joint. Therefore, a DLS specimen design was chosen to minimize mode I loading in between the composite and metallic joint member. In order to allow for an isolated investigation of the composite joint member, the influence of the metallic joint member and pins needs to be reduced to a minimum. Hence, plastic deformation of metals has to be avoided and materials with high yield strength are preferred. Therefore, Ti6Al4V was chosen for the metallic joint member and pins made of spring steel were used. However, opposed to test series 1 and 3, the composite joint member was made of Cycom 5320-1 prepreg tape instead of NCF and PR520 RTM-resin.

Contrary to conventional bolted or riveted joints, pinned joints are characterized by fiber undulations, caused by the pin insertion into the dry NCF, weave or uncured prepreg. In order to investigate the impact of these undulations on the mechanical properties of the joint, joints with drilled holes in the composite joint member were also tested. Further information, regarding production of these joints and fiber undulation can be found in Chapter 4.4 and Chapter 5.5, respectively.

3.2.5.1 Testing standard

In accordance with test series 1 and 3, ASTM D 3528-96 [88] is also suitable for these tests. Tests were performed after the same principle as already described in 3.2.3.

3.2.5.2 Specimen geometry

The basic dimensions for the specimens of test series 4 are illustrated in Figure 3-12.

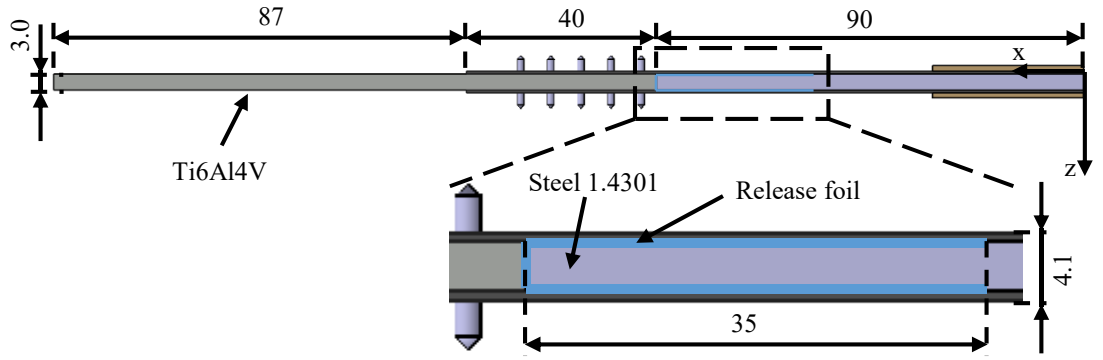

Figure 3-12: Geometry and dimensions for double lap joint design 2
Dimensions in [mm]

A metallic plate made of stainless steel 1.4301 serves as the spacer between the composite laps. A thin release foil is placed at the front edge of the spacer to prevent adhesion between the spacer and the composite, which could possibly influence the joint's mechanical behavior. Prepreg material is chosen in this case, as undulations around pins are more defined in comparison to pinned joints with NCF, see Chapter 3.3.1.1. The desired failure mode for these specimens is hole bearing. For this purpose, Kelly et al. [98] proposes a width to hole diameter ratio (*w/d*) of 4 or higher and an edge distance to hole diameter ratio (*e/d*) of 3 or higher. For this study, *w/d*-ratios of 4.23 and *e/d*-ratios of 7.62 are implemented, see Figure 3-13.

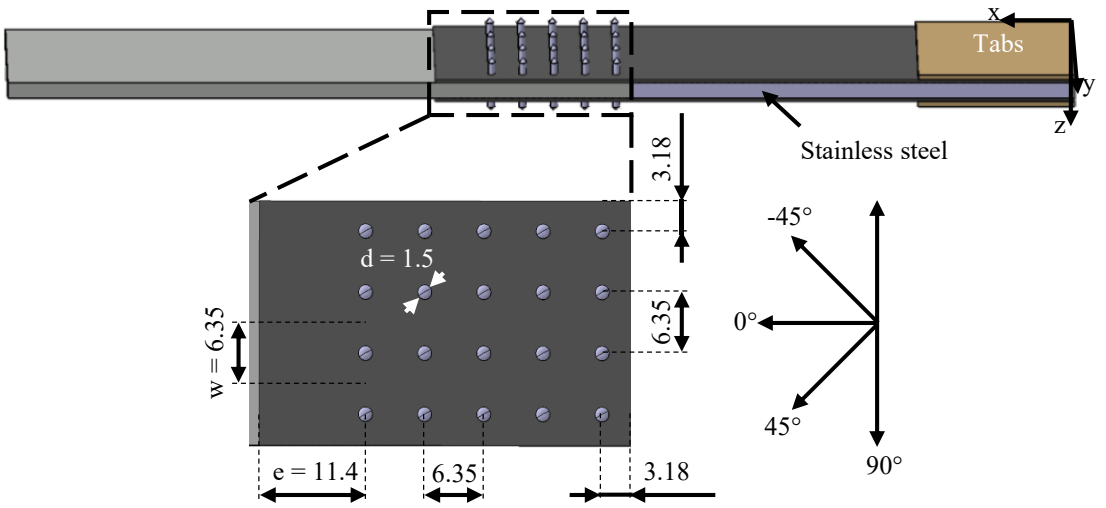

Figure 3-13: Fastener arrangement for double lap joint design 2
Dimensions in [mm]

Furthermore, the distance between the fasteners in tensile (x)-direction is designed to be identical to the distance between the pins in y-direction. Tabs made of glass fiber reinforced plastics, which are bonded onto the composite joint member, ensure that there is no slippage between the specimen and the grips of the testing machine. Three different layups were tested to investigate the influence of fiber direction on the mechanical performance of the joint. One single prepreg ply is defined by a nominal thickness of 0.137mm at 60% FVF and each composite lap consists of 4 single prepreg plies. The laminates created for these tests have a $[\pm 45]_2$, $[0/90]_2$ and quasi-isotropic [0/90/-45/+45] layup.

3.2.5.3 Data acquisition

Similar to series 1 and 3, tests for series 4 were performed using the UPM250 in combination with the 250kN load cell. However, for these tests, the Aramis system was set so that the deformation state on the specimen's surface in the x-y plane could be captured, see Figure 3-14 on the left.

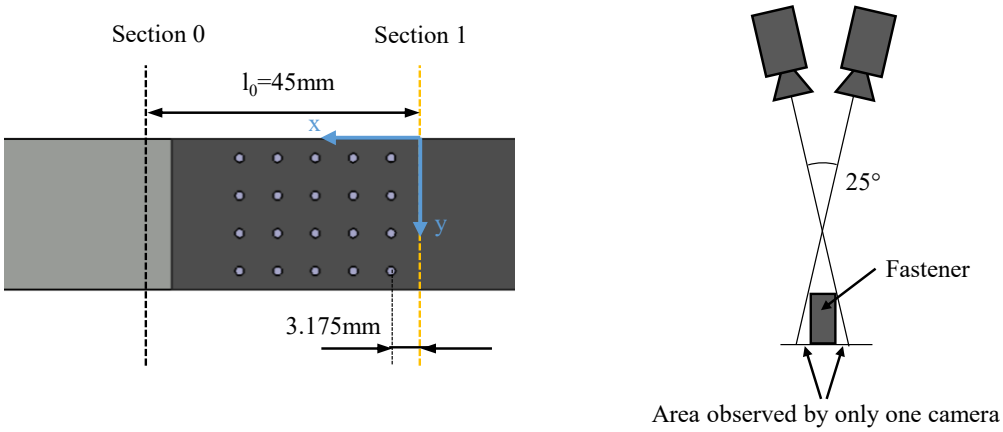

Figure 3-14: Determination of nominal strain ε_{x_nom} for joint design 2 and shadowing effect

This type of Aramis setup allows for a precise analysis of the strain distribution on the surface of the composite joint member's outer plies. Hence, for the $[0/90]_2$ and quasi-isotropic laminate the (outer) 0°-ply and for the $[\pm 45]_2$ laminate, the -45°-ply can be investigated. The nominal strain ε_{x_nom} is calculated identically to the method described in Chapter 3.2.3.3. However, the metallic joint member's deformation within the joining area cannot be analyzed by using this type of Aramis setup. Due to the fact that only a very small deformation is expected for the titanium joint member and pins, this setup is more suitable for test series 4. Furthermore, as a 3-dimensional Aramis measurement technique was used, deformation in thickness (z)-direction can also be captured. Thus, potential warping of the specimen in z-direction can be analyzed.

In the case of test series 4, the fasteners protrude 3mm at an angle of 90° relative to the specimen's surface. The fact that the cameras observe the surface at a 12.5° angle prevents a specific area around the fasteners from being investigated, as only one camera observes it, see Figure 3-14 on the right. The area around the pins suffers from edge

effects in addition to the shadowing effect already mentioned. At the edges, part of the facet could be covering the composite's surface and part of the fastener.

Since the part of the facet covering the fastener does not deform together with that covering the surface and simultaneously forms a very steep angle with the cameras, the facet is often either lost or inaccurately measured. This situation engenders erroneous strain measurement in these areas, which are therefore excluded from further investigation.

3.3 Fiber undulation

As already stated in Chapter 2.3.3, fiber undulations have a major impact on the stress distribution of pinned composite structures. Several authors [43, 44, 66, 68, 72] investigated fiber undulations around pins. However, the pin diameters they used for their studies were in a range from 0.254 to 1.0mm.

In order to improve bending stiffness of the pins, it is advantageous to increase the diameter of the pins, as the geometrical moment of inertia, referred to the longitudinal axis of the pin grows by r^4, whereas the cross section of the pin only grows by r^2. Chapter 5.4.2.5 provides a more detailed insight into the issue of pin bending. However, greater pin diameters also lead to greater fiber undulations. Furthermore, the insertion process becomes more challenging with growing pin diameters. Based on literature and preliminary testing, the pin diameter is set to 1.5mm. This pin diameter still enables the insertion into dry fiber NCF and uncured prepreg. It also provides a good bending stiffness. Figure 3-15 demonstrates the fiber undulation around the pins.

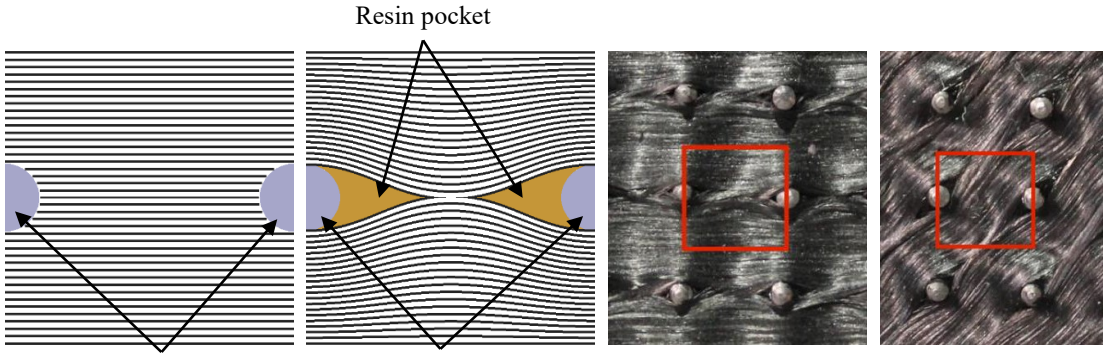

Figure 3-15: Illustration of fiber undulation around pins

The schematic a) on the left shows a unidirectional laminate. Two holes are drilled into the cured laminate. As the fibers are cut, the fiber direction remains unchanged. Schematic b) presents the fiber undulation caused by the pin insertion, which leads to a displacement of single fibers and therefore to fiber undulation around the pin. Furthermore, cavities form in front of and behind the pin, which are filled with resin, either by resin

injection (in the case of dry semi-finished products and RTM-processing) or by the surrounding resin in the state of low viscosity at an elevated temperature (in the case of prepreg material). The two photographs of an uncured pinned prepreg c) and d) show the fiber undulation for a 90° principal fiber direction and +45° principal direction. As the distance between the pins in 0° and 90° principal direction is equal, it is assumed that fiber undulations are identical for 0° and 90° principal direction. The same applies to +45° and -45° principal fiber direction. However, the distance between the pins in regards to principal fiber direction is not identical for 0° (90°) and +45° (-45°) pinned composite plies. In this case, pins are placed in a quadratic pattern, therefore the distance between the pins in the principal fiber direction is 1.41 times higher for +45° (-45°) plies, compared to 0° (90°) plies. This feature has a high impact on the fiber undulation, thus both directions have to be analyzed. Other fiber directions are not investigated in the scope of this thesis. The red boxes in Figure 3-15 are defined as unit cells and mark the area that is analyzed within fiber undulation measurements.

3.3.1 Measurement of fiber undulations

The fiber undulations around the pins were measured on a single filament level. Two measuring methods, Micro CT and Microscopy were taken into consideration. The advantage of the Micro CT-techniques is that a real 3D-image can be generated, whereas with microscopy inspection only a single polished surface can be inspected. However, available Micro CT devices could not offer the required resolution in combination with the object size of 6.35mm x 6.35mm x 0.55mm. Therefore, microscopy inspection was used for the analysis of fiber undulation. A special procedure of specimen preparation and image analysis of several planes enabled the creation of a 2.5D-image of the measurement field. Furthermore, a very fine resolution of 0.064 µm/pixel could be implemented by microscopy inspection techniques.

3.3.1.1 NCF versus prepreg

Preliminary pin insertion tests at room temperature were conducted, using NCF and prepreg material, see Figure 3-16.

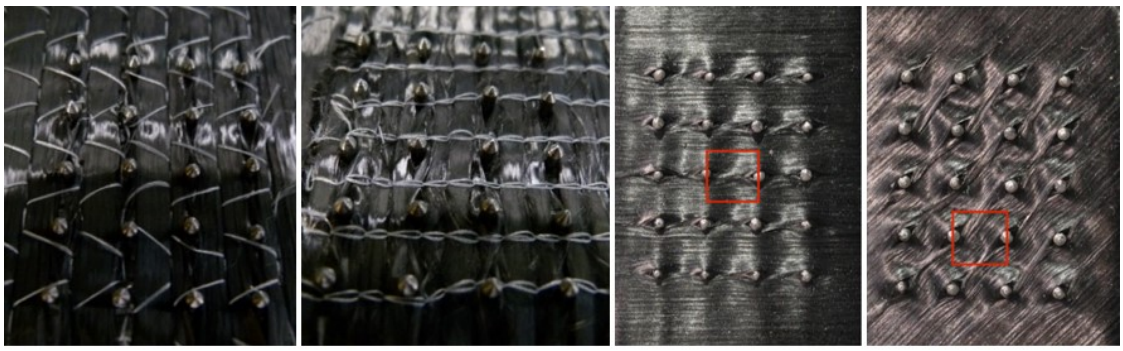

a) NCF stitching pattern 1 b) NCF stitching pattern 2 c) Prepreg 90° d) Prepreg +45°

Figure 3-16: Effect of stitching on fiber undulation around pins

Reviewing images a) and b), it can be concluded that the NCF-material's stitching pattern significantly influences the fiber undulation. Furthermore, a comparison of different unit cells indicates that, in the case of NCF material, results from the analysis of a single unit cell are not necessarily transferrable to other unit cells. For prepreg materials however, no stitching thread is present. Due to the tack between prepreg plies, it can be assumed that the stacking sequence also has an influence on the fiber undulations. It could be observed that for unidirectional prepreg stacks, resin pockets turn out to be significantly bigger than for cross-ply $[0°/90]_2$-stacks or quasi-isotropic [0/90/-45/+45]-stacks.

3.3.1.2 Measurement procedure

As 0°/90° plies and +45°/-45° plies had to be analyzed, four prepreg stacks with different stacking sequences were produced. These consisted of a $[+45/-45]_2$ (two stacks), a [0/90] and a [+45/-45] layup. The first $[+45/-45]_2$ stack was draped onto a 5x4 pattern of spiky pins which were inserted into holes in a metallic plate. Coating the pins and metal plate with release agent prevented adhesion between the prepreg, metal and pins. By pushing the stack downwards, the pins penetrated the prepreg stack and moved the fibers around the pins. The same procedure was repeated for the [0/90], [+45/-45] and $[+45/-45]_2$ stacks. Whereas the two outer $[+45/-45]_2$ stacks served as protection, the inner plies were the basis for the fiber undulation analysis. Subsequently, another steel plate with inserted holes was placed on top of the prepreg stacks and the entire setup was embedded in a vacuum foil. Finally, curing of the prepreg took place based on a curing cycle which was similar to the cycle explained in Chapter 4.4.

Figure 3-17 illustrates the entire procedure for the measurement of fiber undulation.

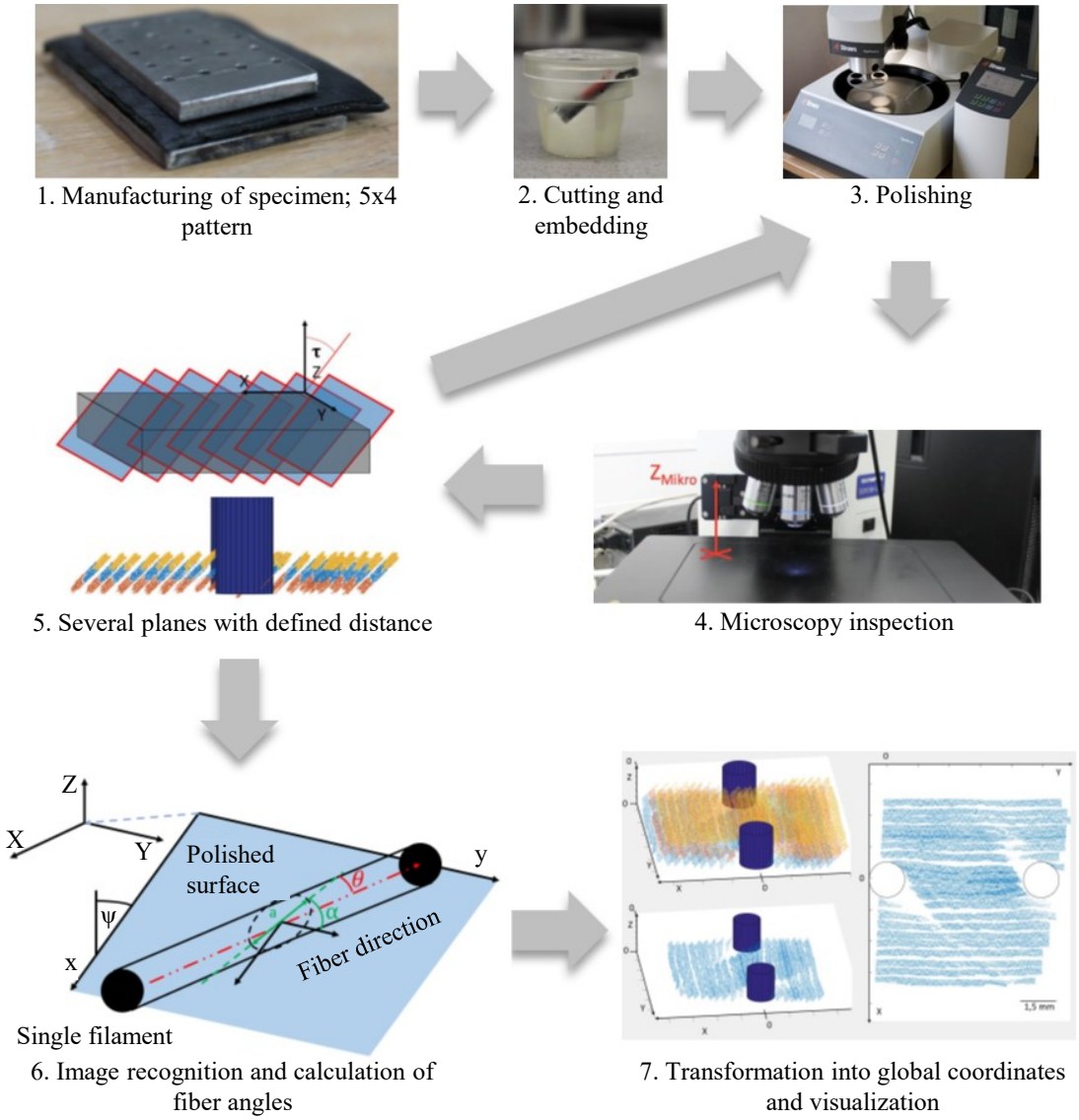

Figure 3-17: Procedure for measurement of fiber undulation

After curing (1), the metal plates and pins were removed and the cured prepreg was cropped and embedded in resin in a tilted position (2). Subsequently, the specimen was polished with the help of a Struers TegraForce-5 polishing machine (3), followed by microscopy inspection using an Olympus BX41M-LED microscope with integrated camera and microscope table with automated drive system (4). Afterwards, the specimen was polished and the above cycle was repeated. Through this process, 22 single planes with a defined distance of 0.3mm were investigated (5). The images of these planes were evaluated with the help of image recognition software. For this purpose, a matlab image recognition algorithm was developed, which was able to detect the elliptical cross section of the cut filaments and further calculate the in- and out-of-plane fiber angles (6). Finally, in order to obtain a 2.5D image of the unit cell's fiber undulations, the angles

and positions for each cross section were transferred into the global coordinate system (7).

3.3.1.3 Tilting angle and measurement precision

The titling angle mentioned above has a major impact on the accuracy for measuring fiber angles. Figure 3-18 describes the geometrical parameters for the analysis of fiber angles, derived from the elliptical cross section of a single filament.

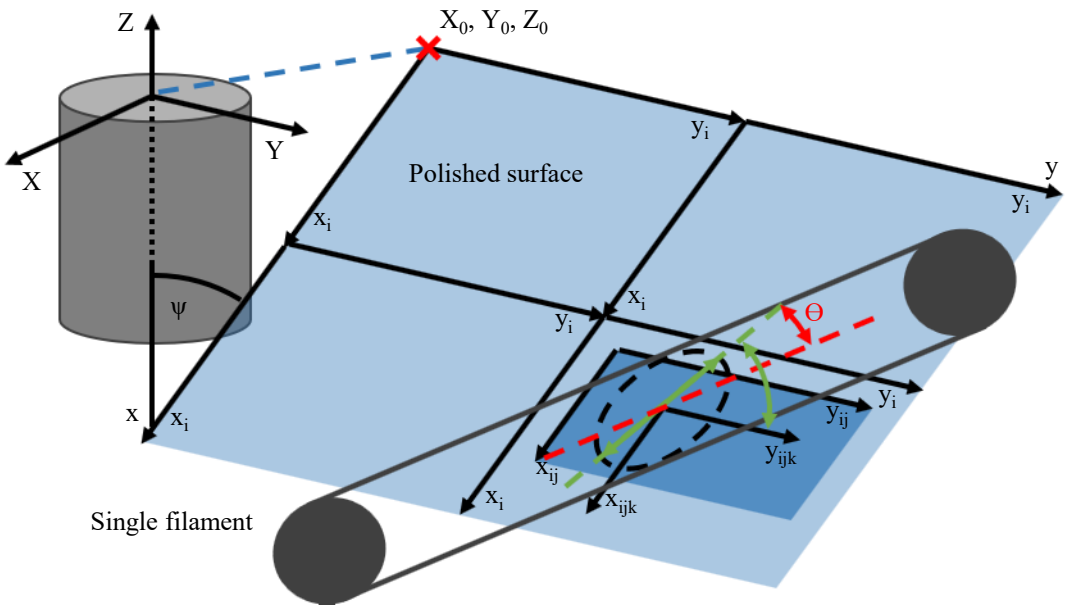

Figure 3-18: Trigonometric relations and adjustment of tilting angle ψ

The tilting angle ψ is defined as the angle between the *Y-Z* plane of the global coordinate system and the polished surface. Therefore, the polished surface is not parallel to the CFRP layers and also not perpendicular to the stacking direction. The angle between the *X-Z* plane and the polished surface is kept constant at 90°. In addition, the in-plane angle is defined as α and the out-of-plane angle as Θ. Both angles are referenced to the polished surface and not to the global coordinate system.

Figure 3-19 illustrates ambiguities that arise by applying high tilting angles ψ.

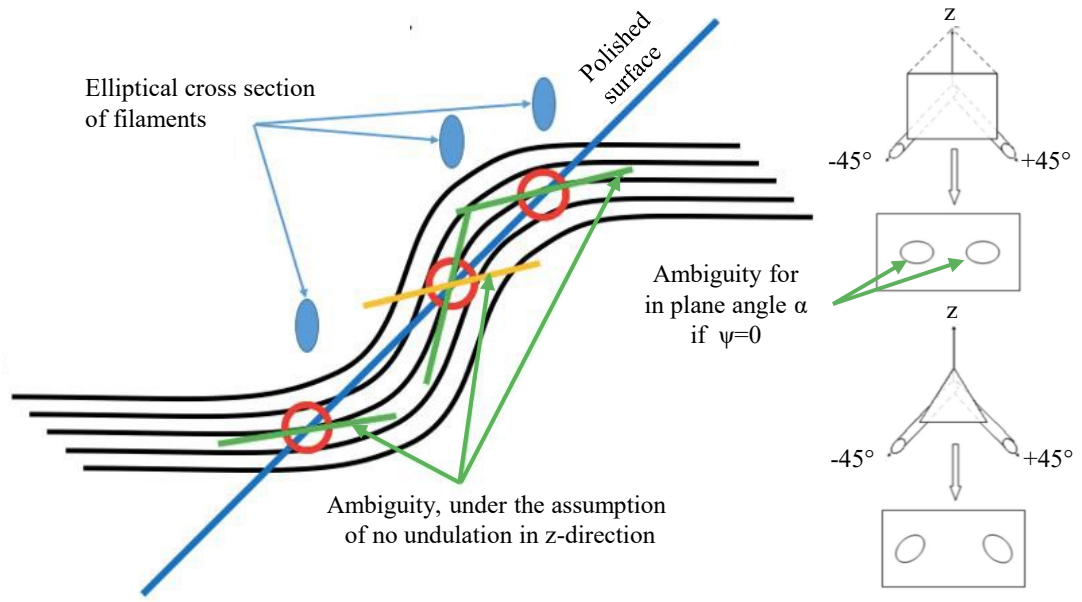

Figure 3-19: Illustration of ambiguity for low and high tilting angles ψ
According to [99]

Undulations in z-direction, typically caused by pin insertion, are primarily present in the areas close to the pins [44]. If single filaments are highly deflected in z-direction, ambiguities are likely as the filament is detected more than once. In addition, for low tilting angles it is not possible to distinguish between two filaments which are symmetrical to an axis normal to the polished surface. The major and minor main axis of the ellipse are defined as a and b. Figure 3-20 shows the progress of the ratio a/b of the ellipse in relation to the out-of-plane angle Θ under the assumption that no z-undulation is present.

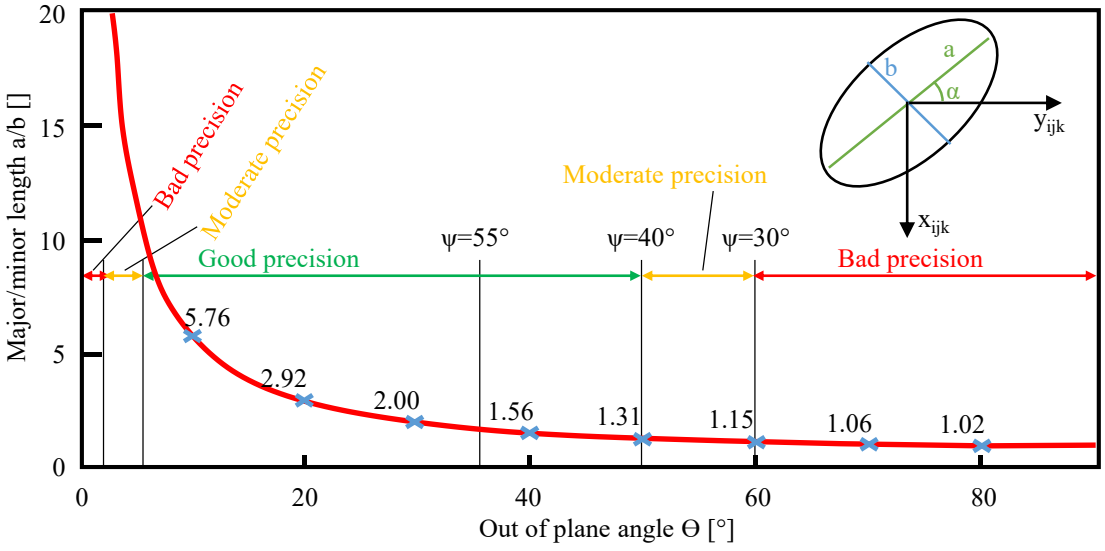

Figure 3-20: Estimation of measurement precision, dependent on tilting angle ψ

Low precision for fiber angle measurement can be expected with either very small or very large tilting angles ψ. On the one hand, high tilting angles ψ (low out-of-plane angles Θ) lead to high *a/b* ratios. The algorithm has difficulties detecting cross sections with very high *a/b* ratios. On the other hand, low tilting angles ψ lead to low *a/b* ratios. As inaccuracies while measuring the major and minor axis cannot be prevented due to the limited image resolution, low *a/b* ratios also result in low precision. In addition, low precision is also caused by poor quality of the polished surface. After polishing filaments perpendicular to their longitudinal axis, several craters could be observed.

This analysis method of the fiber direction is only valid if the roundness of fibers equals 1.0. Preliminary tests showed that this is approximately the case for the IM7 fibers used for these investigations. Based on the assumption that fiber undulations in *z*-direction are only present in small areas very close to the pins, and the majority of filaments are undulated in the *x*-*y* plane, a tilting angle of +45° was chosen.

In addition to fiber direction measurement, this method also allows for an estimation of the fiber volume fraction. The fiber area content can be calculated by dividing the fibers' cross section by the size of the measurement plane. It can be determined locally and as an average value over the entire measurement plane. Theoretically, in the case of a homogenous unidirectional ply without fiber undulations, the fiber area content equals the fiber volume fraction. However, it has to be noted that this method can lead to measurement inaccuracies. The size of a single fiber's cross section is highly dependent on the chosen greyscale threshold to detect the fiber's edge. To validate the fiber volume fraction estimated via microscopy inspection, other measurement techniques, i.e. acid digestion or resin burning-off methods should be carried out additionally. As these measurements are beyond the scope of this thesis, the fiber volume fraction is only plotted qualitatively within Chapter 5.5.

The matlab image recognition code is responsible for data processing and graphical visualization. This code is not explained in this thesis. However, the interested reader should refer to the Bachelor's thesis “Ermittlung der Faserondulation bei gestifteten CFK/Metallverbindungen” which is incorporated in the scope of this research project.

3.4 Finite element modelling

The main goal of the Finite Element Analysis is to study the stress state within the pinned composite/metal joint and further optimize the joint's geometry. Digital Image Correlation technique, explained in Chapter 3.2.2.2, provides detailed information of the specimen's strain state on its surface. However, if non-linear material behavior (i.e. plastic deformation) is present, strain can no longer be directly transferred into stress with the help of the elastic material properties. As stress and strain distributions strongly depends on the fiber direction, inspecting only the surface of the specimen is not sufficient to analyze the joint's mechanical behavior in detail. Furthermore, FEA allows for the in-

vestigation of the mechanical interaction between metallic joint member, pins and composite joint member. FEA was conducted on coupon and on element level and each FE-model was validated by testing. The software used for the entire analysis, including pre- and post-processing was Abaqus 6.14 [100]. Whenever complex geometries were applied, the geometry was created in Catia V5R21 and subsequently transferred to Abaqus 6.14.

3.4.1 Basics

This chapter provides an overview of the most important modelling techniques used in the scope of this thesis. Proper modelling of the interactions between metallic joint member, pins and composite joint member is essential for the reasonable FE-modelling of pinned joints. Furthermore, elastic-plastic behavior of pins and the metallic joint member has to be taken into account. In order to predict failure, several failure criteria have to be implemented as well.

3.4.1.1 Elements

Different element types are used for FE modelling. C3D8R, 8-node linear brick elements are assigned for the metallic joint member, pins, neat resin and composite joint member if Hashin damage (see Chapter 3.4.1.2) is not applied. In some cases, C3D6, 6-node linear triangular prism elements have to be utilized in order to enable a uniform mesh geometry. For the models which are used in conjunction with a Hashin damage criterion, SC8R 8-node hexadron continuum shell elements are utilized. Abaqus 6.14 only provides a function for the usage of the Hashin criterion in combination with continuum shell elements. The creation of an Abaqus subroutine goes beyond the scope of this thesis. For the cohesive zones, COH3D8, 8-node three dimensional cohesive elements are used.

3.4.1.2 Material models

Elasticity

Linear elastic behavior is assumed for all materials in an elastic stress state. For the metallic joint member, pins and neat resin, this behavior applies for stresses which are lower than the elastic limit. In the case of composite joint member and cohesive zones, linear elastic material behavior was implemented for conditions prior to damage initiation. Metallic joint member, pins and neat resin are assumed to be isotropic elastic. Transversal isotropic elastic material behavior is defined for the composite joint member.

Plasticity

For the FEA, two plasticity models are applied. Perfect plasticity in combination with a von Mises yield criterion was implemented for the metallic joint member and the pins. A cast iron plasticity model is used to model the mechanical response for neat resin.

Perfect plasticity models assume that the yield stress does not change with plastic strain [100]. Therefore, hardening effects are excluded from the simulation. Furthermore, strain rate dependency is neglected. In the case of the metallic joint member and pins, material input parameters are identical for tensile and compressive stress states.

However, in the case of neat resin, a differentiation between tension and compression is necessary, see testing results in Chapter 5.2.5. Abaqus/CAE allows different material input for compression and tension by applying a cast iron plasticity model [100]. Therefore, a plastic poison's ratio has to be defined. This value is computed as the ratio of the transverse to the longitudinal plastic strain under uniaxial tension. The plastic poisson's ratio is considered to be constant for all plastic strain states. For further information regarding cast iron plasticity, please refer to [100].

Explicit FEA requires true/logarithmic instead of nominal strain and stress values. Hence, the nominal stress/strain measures, derived from material testing on coupon level, have to be transferred into true stress/strain values. The relationship between true strain and nominal strain can be expressed as:

$$\varepsilon = \ln(1 + \varepsilon_{nom}) \tag{3-3}$$

Where ε and ε_{nom} are defined as true and nominal stress, respectively. True stress σ can be computed from the nominal stress σ_{nom} and nominal stress ε_{nom} by using the following equation:

$$\sigma = \sigma_{nom}(1 + \varepsilon_{nom}) \tag{3-4}$$

However, equations (3-3) and (3-4) are only valid prior to necking [100]. A comparison of FE- and testing results on coupon level can be found in Chapter 5.2.1.

Damage for ductile metals

All failure models applied for FEA require a damage initiation and a damage evolution criterion. In the case of damage for ductile metals, which is used for the metallic joint member and pins, the equivalent plastic strain at the onset of damage $\bar{\varepsilon}_D^{pl}$ defines the value of plastic strain for damage initiation [100]. After damage initiation occurred in an element, its stiffness gradually decreases. This decrease in stiffness depends on the damage degradation value d and the stress $\bar{\sigma}$ that would exist in the element if no damage was present. The actual stress σ in the element can be computed, according to equation (3-5):

$$\sigma = (1 - d)\bar{\sigma} \tag{3-5}$$

A linear damage evolution law of type "displacement" was chosen in this case. Therefore, the damage degradation value *d* increases linearly with the equivalent plastic displacement $\bar{u}^{pl}$ until it equals the value 1.0. However, Abaqus removes the affected element once the damage degradation value *d* reaches the value 0.99 [100]. Figure 3-21 illustrates progressive damage degradation and linear damage evolution.

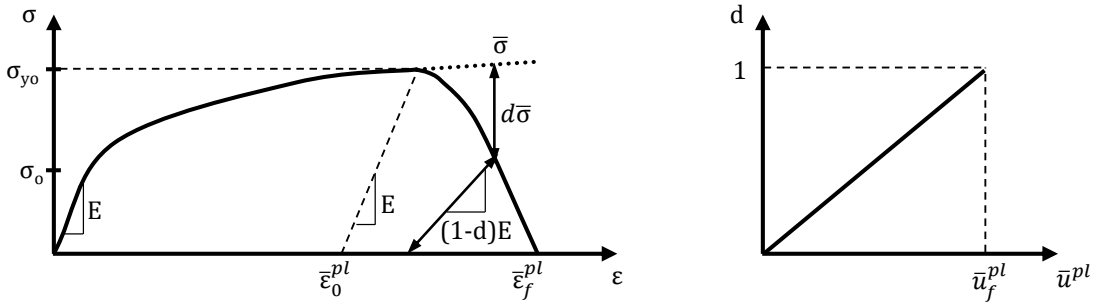

Figure 3-21: Damage formulation for ductile metals
σ/ε-curve with progressive damage degradation (left), linear damage evolution (right), according to [100]

Constitutive models are usually based on stress-strain relations. Due to strain localization, caused by strain-softening behavior after damage initiation, the mesh size strongly influences the dissipated energy in the element. Abaqus accounts for this issue by introducing a characteristic length which is internally computed, dependent on the specific type and size of the element. Therefore, the damage evolution law is not expressed as a damage degradation value to strain, rather damage degradation value to displacement relation. The dissipated energy is computed based on a unit area instead of a unit volume. This approach minimizes the mesh size dependency for these types of progressive damage degradation models. Due to simplification reasons, the above presented relations are explained for a one-dimensional case, but can be extended to two- or three-dimensional cases as well. For further information regarding mesh size dependency, please refer to [100].

Hashin damage for CFRP

In order to model damage in the composite joint member for the simulation related to test series 3, a Hashin failure criterion is applied. Similar to the damage modelling of ductile metal explained above, the Hashin criterion also requires input for damage initiation. Due to the composite material's anisotropic behavior, several values for damage initiation have to be implemented. Depending on the stress state within the elements, they can be damaged by fiber tension, fiber compression, matrix tension and matrix compression. The following strength values determine the onset of damage:

- X^T: longitudinal tensile strength
- X^C: longitudinal compressive strength
- Y^T: transverse tensile strength

- Y^C: transverse compressive strength
- S^L: longitudinal shear strength
- S^T: transverse shear strength

An energy-based formulation is used for damage progression of fiber-reinforced plastics. The stress in each element can be calculated by:

$$\sigma = \mathbf{C}_d * \varepsilon \tag{3-6}$$

where $\boldsymbol{C}_d$ describes the damage elasticity matrix which contains elastic material parameters as well as damage degradation values. The basic principle for damage propagation after damage initiation for a one-dimensional case is illustrated in Figure 3-22.

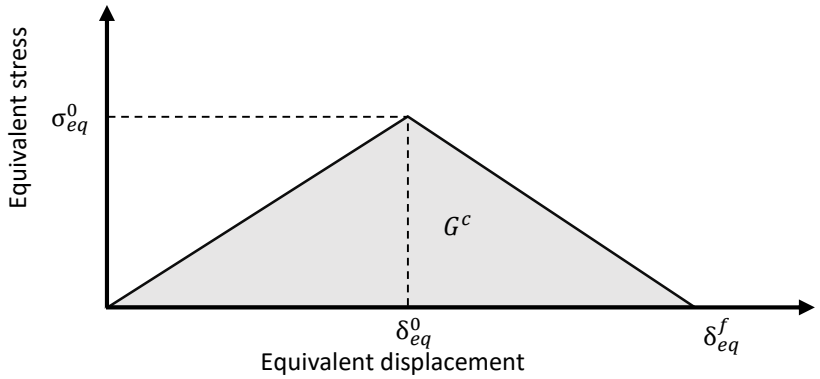

Figure 3-22: Basic principle for energy-based linear damage propagation
According to [100]

The equivalent stress at damage initiation σ^0_{eq} is defined by the strength values mentioned above (failure index = 1.0), whereas the equivalent displacement δ^f_{eq} is a function of the dissipated energy G^c. The four values G^c_{ft}, G^c_{mt}, G^c_{fc} and G^c_{mc} describe the dissipated energy during damage for fiber tension, fiber compression, matrix tension and matrix compression, respectively. Once the equivalent displacement δ^f_{eq} is reached, the equivalent stress is set to zero and the element is deleted. For further information regarding the computation of damage initiation and progression, please refer to [101, 102] and [103].

Cohesive zone modelling

Cohesive element zones are used to describe delamination behavior between the NCF-layers and between the composite and metallic joint member. In case of test series 4, they are also used to describe intra-laminar delamination. A traction-separation law was chosen to describe their constitutive response. Similar to the material model for Hashin damage, described above, a linear elastic material behavior is assumed until the damage initiation criterion is met. In a three-dimensional case, the nominal stress vector $\boldsymbol{t}$ consists of three components. These components, t_n and t_s, t_t describe the nominal and two

shear directions, respectively. The values δ_n, δ_s and δ_t represent the corresponding separations. A typical traction-separation response for cohesive elements is presented in Figure 3-23.

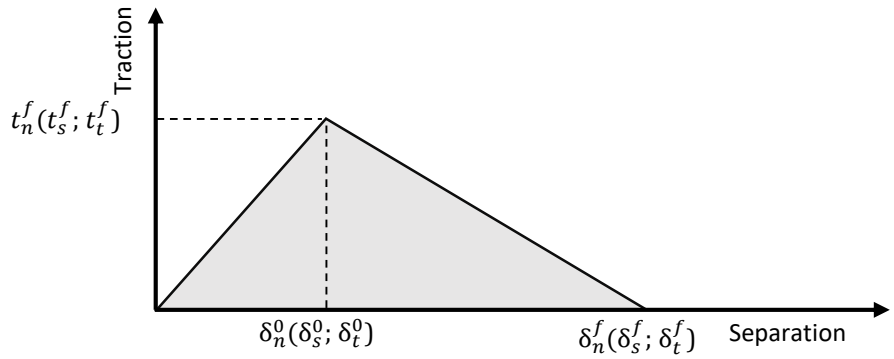

Figure 3-23: Illustration of traction-separation law for cohesive elements
According to [100]

A maximum nominal stress criterion is used for damage initiation. An energy based Benzeggagh-Kenane (BK) fracture criterion with a mixed mode damage evolution and linear softening was chosen. For further information on mixed-mode damage evolution for cohesive elements please refer to [104] and [105].

3.4.1.3 Contacts

Contact interactions were generally applied for all adjacent parts. For this purpose, a "hard contact" formulation is utilized for contact in normal direction. Penetration of one part into another is not possible. Tangential contact behavior is covered with the application of a friction coefficient. This friction coefficient was adapted, depending on the material pairings composite/composite, composite/metal and metal/metal. Chosen values for friction coefficients are listed in Table 3-3.

Table 3-3: Friction coefficients for finite element simulation

Material pairing	Composite/composite	Composite/metal	Metal/metal
Friction coefficient [-]	0.2	0.2	0.05

Whenever cohesive zones are utilized in the interfaces, contact interactions only take effect after failure of the cohesive elements.

3.4.2 CFRP/titanium joint design 1

The main goal of the FE analysis for the Titanium-CFRP joint of specimen design 1 (relating to test series 3) is to optimize the joint's geometry in terms of total pin number and pin pattern.

Model setup

Based on the joint design 1, introduced in Chapter 3.2.3.2, several FE-models were created. The metallic joint member and pins are modelled as solids, whereas the composite joint member consists of 11 single parts containing continuum shell elements (see also Chapter 3.4.1.1). Each single part of the composite joint member represents one layer of NCF, including two fiber directions (0°/90° or +45°/-45°). In order to simplify the model setup and reduce computational effort, fiber undulations are neglected and the fiber volume fraction is kept at a constant value of 60% for the entire composite joint member. To account for in-plane failure inside the composite joint member, a Hashin failure criterion is implemented. Figure 3-24 exemplarily illustrates a CAE-model for a 5x4 pin adjustment.

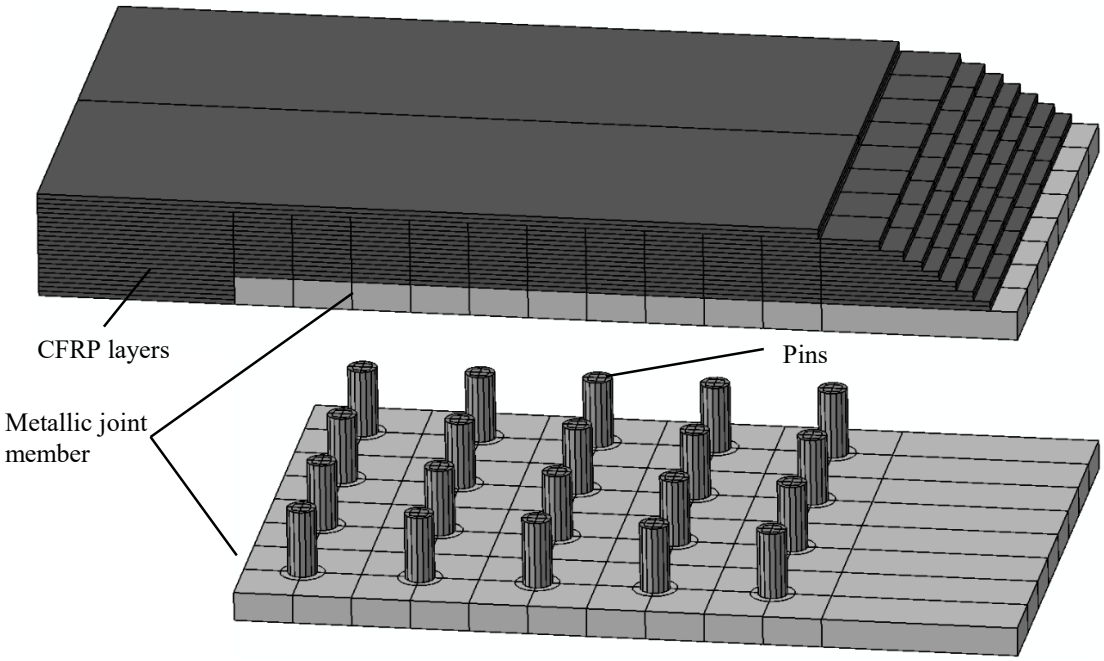

Figure 3-24: Abaqus CAE-model for double lap joint design 1

By integrating cohesive zones between two NCF-layers, interlaminar delamination behavior within the composite joint member can be analyzed. The interface between the composite joint member and metallic joint member is also modeled with the help of a cohesive zone. Two cohesive sections were defined, which differ in material input data. The first section is applied to all cohesive zones within the composite joint member, whereas the second section is assigned to the cohesive zone at the interface between the composite joint member and metallic joint member.

The cohesive zones are shown in Figure 3-25.

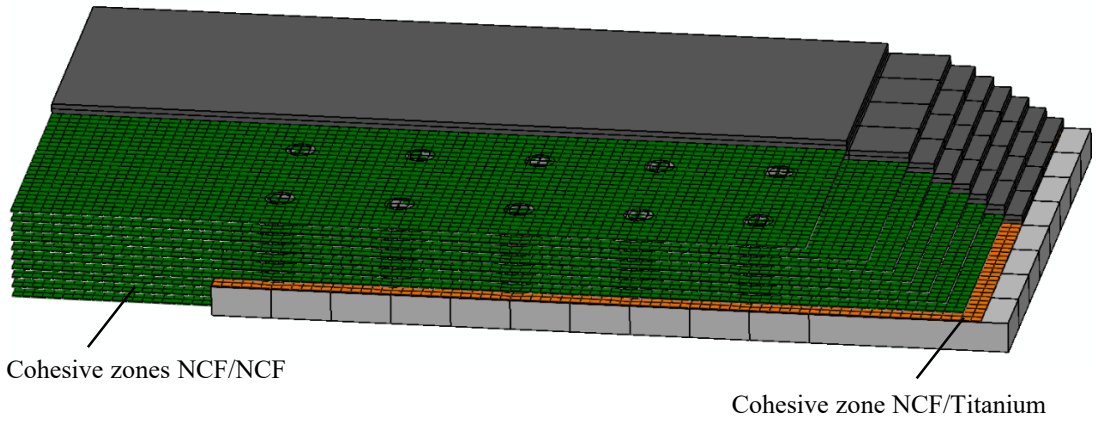

Figure 3-25: Cohesive zones for double lap joint design 1

Pins are modelled with solid elements and have a cylindrical shape, regardless of the actual pin head geometry (flat or spiky).

Boundary conditions

Several boundary conditions are applied to the FE-model for joint design 1. As the specimen is symmetrical to the mid-plane in thickness direction, the computational effort is significantly reduced by analyzing only the upper half of the DLS joint. Furthermore, the FE-model is geometrically limited to the joining area. The displacement in tensile (x)-direction of all nodes associated with the lateral face of the composite joint member is set to zero, see Figure 3-26.

Figure 3-26: Boundary conditions for double lap joint design 1

In addition, the velocity in tensile (x)-direction of all nodes associated with the lateral face of the metallic joint member is set to a constant speed of 1000mm/s after an initial time period of constant acceleration. The application of a constant acceleration is essential for an explicit FE-analysis in order to minimize undesired dynamic effects.

3.4.3 CFRP/titanium joint design 2

The mechanical testing and FE-analysis of the composite/titanium joint design 2 aims to analyze the impact of fiber undulation on the entire joint's mechanical behavior. Therefore, a special focus is put on the detailed modelling of the undulations within the composite joint member.

Implementation of fiber undulation

Based on the measurement of fiber undulation, see also Chapter 3.3 and Chapter 5.5, several parts representing the actual fiber course within the prepreg plies were created. Figure 3-27 exemplary illustrates the model set up for a 0°-ply.

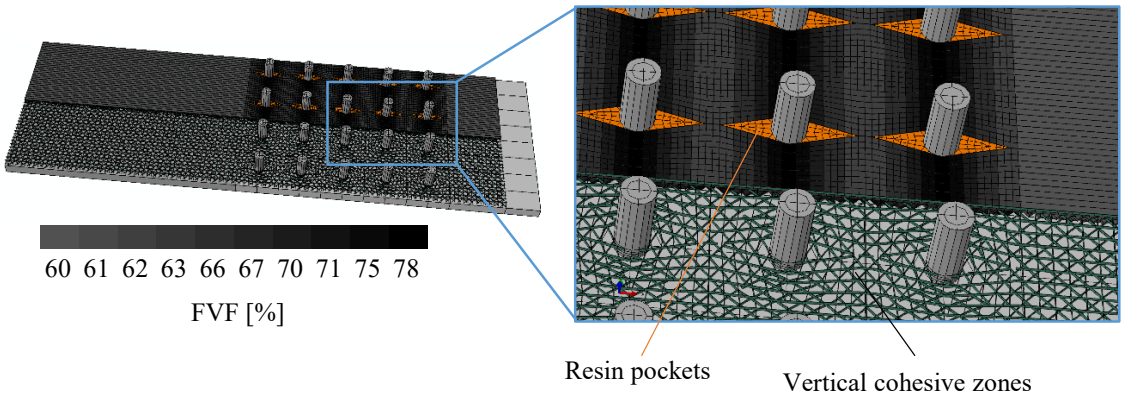

Figure 3-27: Abaqus CAE-model double lap joint design 2 (0°-layer)

The resin pockets are also modeled in each single ply. All parts are connected to each other by means of vertical cohesive zones in order to cover intra-laminar delamination. A -45°-ply is shown in Figure 3-28. In order to account for inter-laminar delamination, all plies are connected by horizontal cohesive zones. Input parameters for the vertical cohesive zones are identical to those of the horizontal cohesive zones.

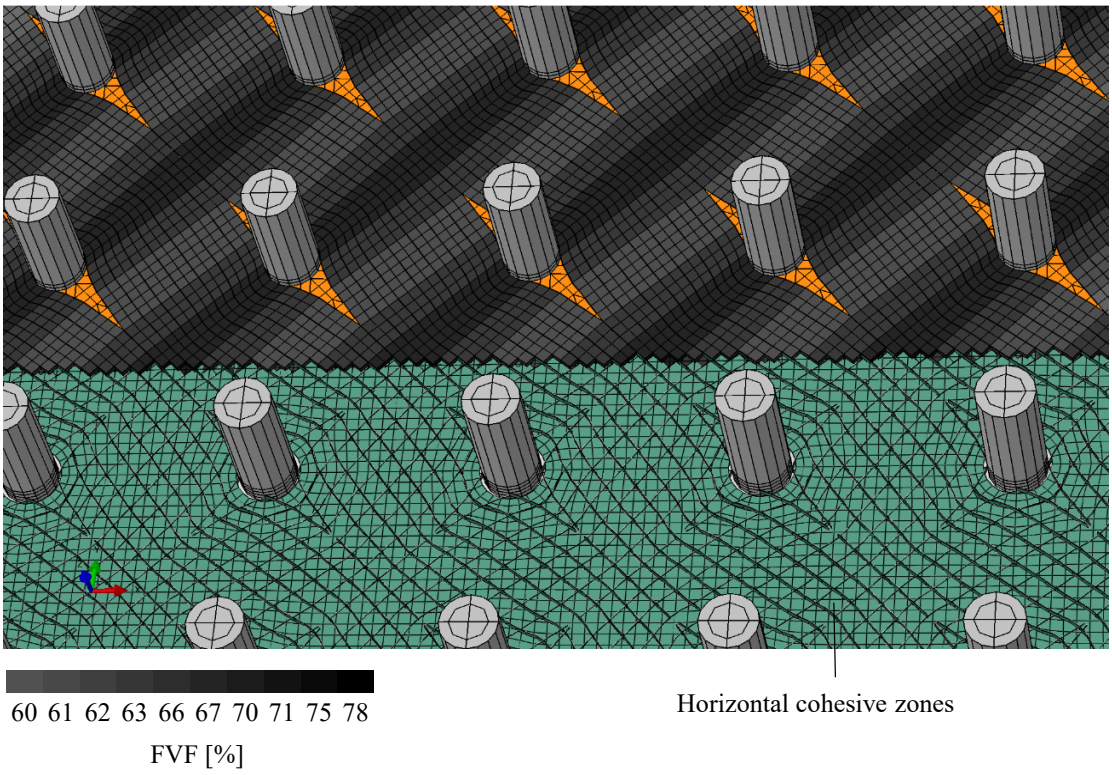

Figure 3-28: Abaqus CAE-model double lap joint design 2 (-45°-layer)

Material input

The pin insertion not only causes fiber undulations around the pins, but also locally influences the fiber volume fraction. Therefore, material properties also change throughout the entire ply. The elastic properties for all sections were calculated with the help of the axial and inverse rule of mixture. The material data for a fiber volume fraction of 60%, taken from the Cycom 5320-1 prepreg data sheet served as the basis. It should be noted that the determination of this material data is subject to many assumptions, yet still represents a more detailed modeling of the composite joint member in comparison to the modelling technique applied for joint design 1. Table A-7 in the Appendix lists all input parameters, utilized for the composite joint member.

4 Specimen manufacturing

This chapter describes the manufacturing of DLS-specimens for test series 1, 3 and 4 in detail. First, the pinning technologies used in this thesis, namely laser pinning, CMT pinning and inserted pinning, are explained. Afterwards, preforming and RTM-processing for the specimens of test series 1 and 3 is examined. Chapter 4.4 describes the stacking of prepreg plies, pin insertion and cure cycle for the DLS-specimens of test series 4. The process used for manufacturing of the different test specimens for test series 2 on coupon level are similar to those used for the DLS-specimens for test series 1, 3 and 4. Therefore, Chapter 4.5 provides a short summary for manufacturing of the test series 2 specimens.

4.1 Pinning technology

Pin creation is always the first step in the production chain of pinned composite/metal joints. As stated in Chapter 3.1, pins should provide a good shear strength and bending/tensile strength in order to ensure a high overall joint tensile strength. Furthermore, bending of the composite layers towards the z-direction (see Chapter 5.1.1) can be limited by a great bending stiffness of the pins. The pinning technology, geometry and material of the pins have a major impact on the pins' mechanical properties and consequently on the overall joint strength. The pin pattern for test series 1 was chosen based on Ucsnik et al. [54]. Therefore, a rectangular pin pattern with 7 pin rows in tensile direction and 5 pins in each row is used for the pinned configurations.

4.1.1 Laser pinning

Laser pinning is a technology for pin creation onto a metallic substrate, which is comparable to the Surfi-Sculpt^{TM} technology [62, 63, 67, 106], described in Chapter 2.3.2. A 3kW single-mode fiber laser at a wavelength of λ=1070nm was used within the scope of this thesis. Therefore, the beam was focused on the metallic substrate made by scanning optics. The focus diameter of the laser beam was $d_{86\%}$=48µm and the Rayleigh length was adjusted to z_R=1.1mm, with a resulting beam parameter product BPP of 0.5mm*rad. For further information regarding laser pinning technology, please refer to [107].

Figure 4-1 illustrates the setup for the laser pinning process.

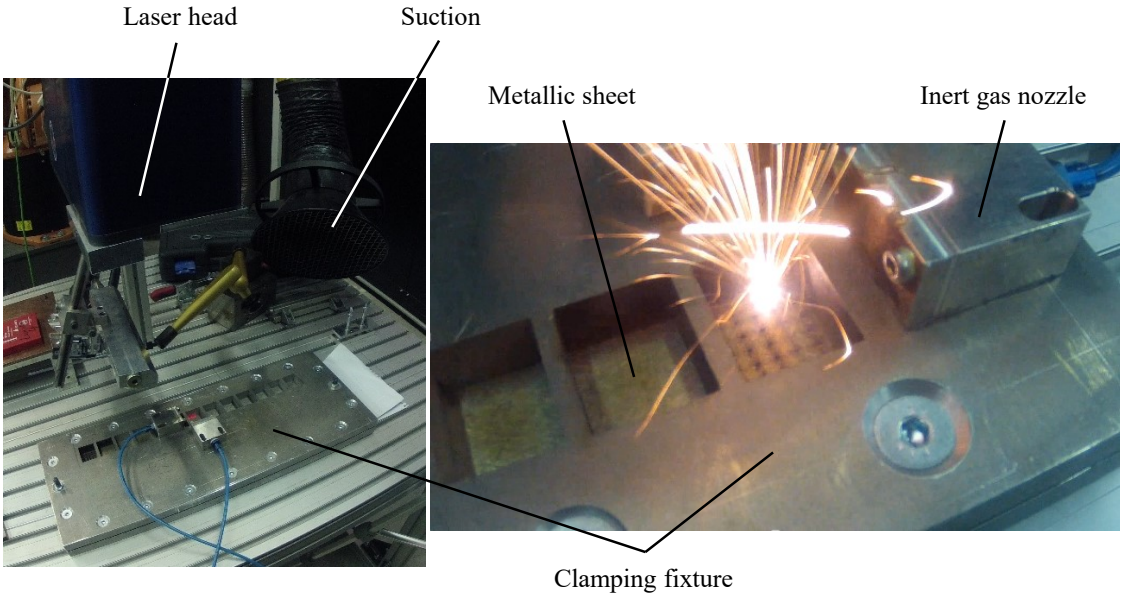

Figure 4-1: Setup for the laser pinning process

By clamping the metallic substrate (steel 1.4301) in between a clamping fixture made of aluminum, heat can be more evenly distributed. This results in lower residual stresses after cooling of the metallic substrate. Figure 4-2 shows a 7x5 pattern of pins on the metallic substrate.

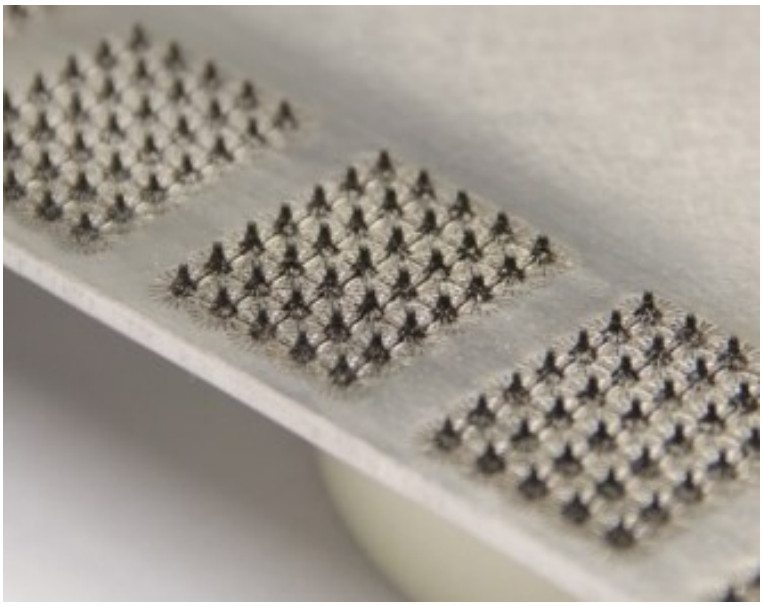

Figure 4-2: Image of a laser pinned metallic sheet with a 7x5 pin pattern

Cylindrical pins cannot be created by the laser pinning technology. The pin has a conical shape and is characterized by a pin root diameter of around 1.9mm and a height of

2.7mm. These values represent the maximum size of a single pin in combination with a field of 7x5 pins and a field length and width of 30.5mm and 25.4mm, respectively. Pins were created on both sides of the 3mm thick metallic sheet.

4.1.2 CMT pinning

Two metallic sheets, made of steel 1.4301, were equipped with CMT-pins. A 7x5 pin pattern with cylindrical pins is used for both sheets, see Figure 4-3.

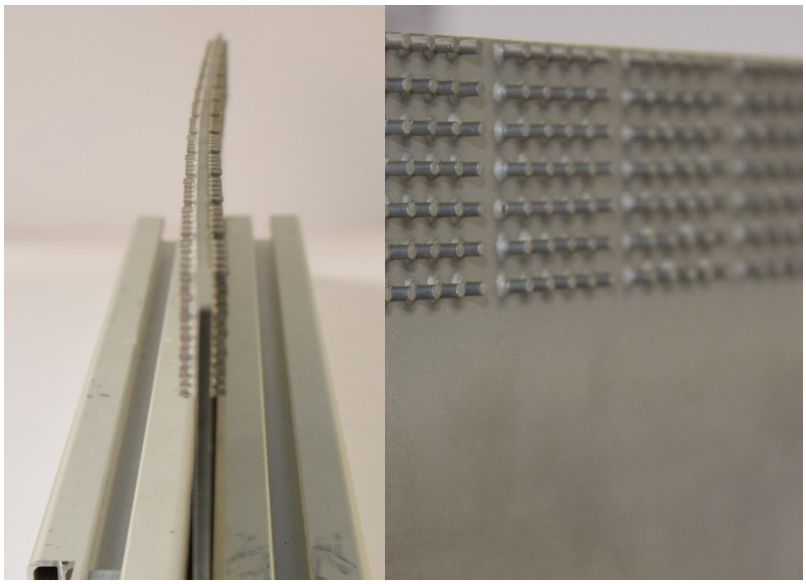

Figure 4-3: Image of a CMT-pinned metallic sheet with a 7x5 pin pattern

The pin diameter is 1.2mm for the first sheet and 1.6mm for the second sheet, as a pin diameter of 1.5mm was not available. CMT pins are characterized by a distinct root zone which ensures the connection of the pin to the metallic sheet. The pin height for both diameters is 3.5mm. The pin root diameter was measured at the bottom of the pin root on the surface of the metallic sheet. For the 1.2mm pins, the root diameter ranges from 2.5-2.9mm and for the 1.6mm pins from 3.3-3.9mm. The CMT pinning-process [53] is also explained in Chapter 2.3.1 and Chapter 2.3.2.

4.1.3 Inserted pinning

The third method of pin creation is referred to as inserted pinning. Several holes were drilled into the metallic sheet and pins were pushed through these holes so that there was equal distance between the pin heads and the corresponding metallic surfaces. The pins are connected to the metallic sheet by means of a press fit connection. This method allows for the use of spring steel pins which are characterized by a great elastic limit, high bending stiffness and shear strength. However, their field of application is limited to double lap joints with a symmetrical load distribution on both sides of the metallic sheet. Only the press fit connection restricts the movement of the pins along their longitudinal axis. In addition, hole drilling, leading to a reduced cross section and notch effects, results in a reduction of tensile and compressive stiffness and strength of the metallic joint member. Figure 4-4 shows a 7x5 and 6x4 pin pattern with cylindrical and spiky pins.

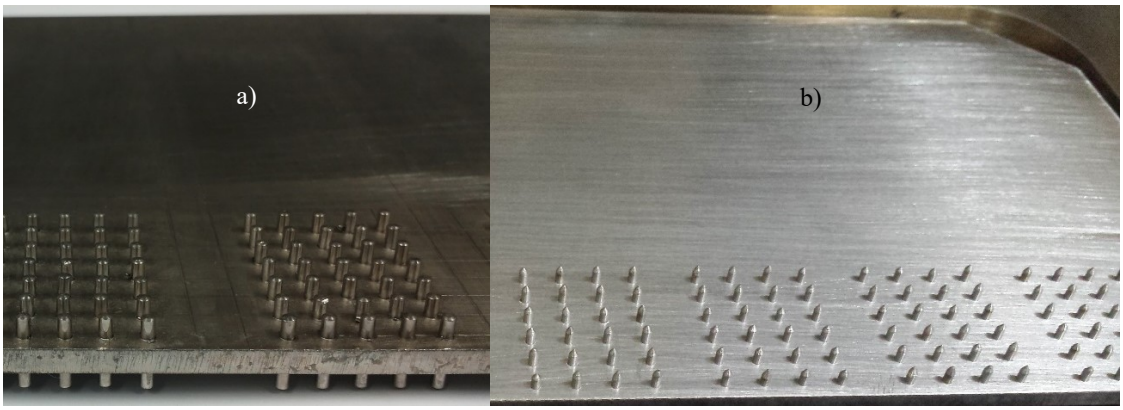

Figure 4-4: Image of metallic sheets with inserted pins and different pin patterns
a) 7x5 pattern - cylindrical pins; b) 6x4 pattern - spiky pins

The inserted pins are characterized by a pin diameter of 1.5mm and an overall length of 10mm. The combination of a 3mm thick metallic sheet with the 10mm pin length leads to a pin height of 3.5mm on both sides of the metallic sheet. Whereas the 7x5 pin pattern with cylindrical pins is investigated in test series 1, the spiky pins are used for the DLS-specimens of test series 3 and 4.

4.1.4 Pin geometries for test series 1

The dimensions of the pins, which are dependent on the pinning technology, are listed in Table 4-1.

Table 4-1: Geometrical parameters for single pin

Pinning technology	Pin shape [-]	Pin height [mm]	Pin neck diameter [mm]	Pin root diameter [mm]	Pin material [-]
Laser	conical	2.7	-	1.9	Steel 1.4301
CMT (CMT1)	cylindrical	3.5	1.2	2.5 - 2.9	Steel 1.4301
CMT (CMT2)	cylindrical	3.5	1.6	3.3 - 3.9	Steel 1.4301
Inserted	cylindrical	3.5	1.5	1.5	Spring steel 1.1231

The thickness of one composite lap is set to 4mm. Due to limitations of the specific pinning technologies, pin geometries and applicable materials are not identical for different setups. Therefore, the comparison criterion for the different setups must be independent from the pinning technology or pin geometry/material. Hence, the joint strength, defined as the applied tensile load, divided by the cross section of the metallic joint member at an unloaded state, is used to assess the mechanical performance of the joint.

4.2 Preforming for joint design 1

The composite joint member of joint design 1 for test series 1 and 3 consists of non-crimp-fabric, binder material and RTM-resin. The specific materials used are mentioned in Table 3-2 in Chapter 3.2.3.2. The layups for test series 1 and 3 are not identical. However, the basic preforming steps are the same for test series 1 and 3.

4.2.1 Composite layup

The pre-cut NCF-layers of Section LL, see Figure 4-5, were first placed into a mold.

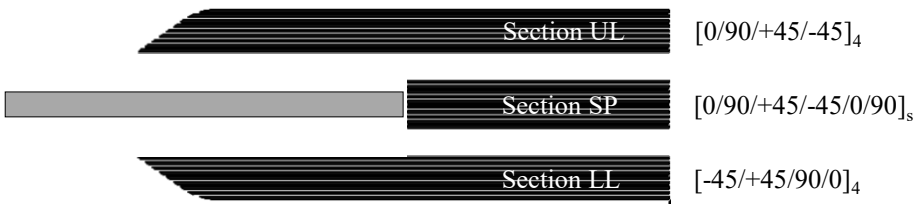

Figure 4-5: Schematic explanation of the composite layup for joint design 1/ test series 3

Afterwards, the NCF-layers of Section SP, together with a flat metallic sheet, were stacked on top of Section LL, followed by Section UL. Binder web was applied in between the NCF-layers, but not in the interface region between the metallic joint member and NCF-layers as well as in between Section SP and Section UL. With the help of compression and heating of the preform, the binder was activated. After cooling the entire setup, the binder material's adhesive properties prevented the disintegration of the stacks.

Surface treatment of the metallic joint member was only applied for the co-bonded composite/titanium reference joints without pins of test series 3 which serves as a baseline. In this case, the titanium sheets were acid etched and treated with a primer. The metallic surfaces of all of the other setups of test series 1 and test series 3 were only grinded with sandpaper grit 180 and cleaned with isopropanol. For testing results, please refer to Chapter 5.1.2 and Chapter 5.4.1.1.

4.2.2 Penetration of pins through dry fabric

The pins were inserted into the dry fabric with the help of a press. Accurate positioning of the composite preform to the pinned metallic sheet is a major challenge, see Figure 4-6.

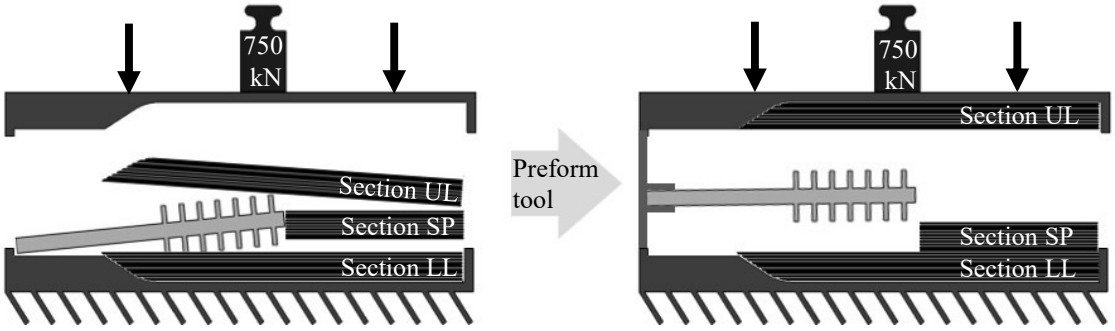

Figure 4-6: Illustration of the pin insertion process for joint design 1

As pins should penetrate the preform in thickness direction, the metallic sheet must be kept in a horizontal position when closing the press. Therefore, Section UL was fixed to the upper mold and a guide unit was developed, which ensures correct positioning of the pinned metallic sheet throughout the pin insertion process. Prior to closing the press, binder web was applied in between Section UL and Section SP. The press was then closed and heated to activate the binder. After cooling the press, all three sections were joined with the pinned metallic sheet via the integrated binder material.

4.3 RTM-processing for joint design 1

A closed mold RTM-process was chosen to manufacture the specimens for test series 1 and 3. Pinned composite/metal structures produced in a closed mold RTM-process lead

to several advantages in comparison to a RIFT-process (Resin Infusion under Flexible Tooling).

- lower cycle times → no vacuum bagging required
- higher compaction pressure → Clamping pressure of press vs. autoclave pressure
- higher injection pressure possible
- accurate adjustment of fiber volume fraction → Mold geometry defines dimensions of part
- lower geometric tolerances and higher surface qualities

However, in order to ensure a high-quality part with low porosity, a suitable tool design and adapted process management is crucial.

4.3.1 Tool design

The tool consists of a top and bottom tool part, several sealing gaskets and two metallic inserts, see Figure 4-7.

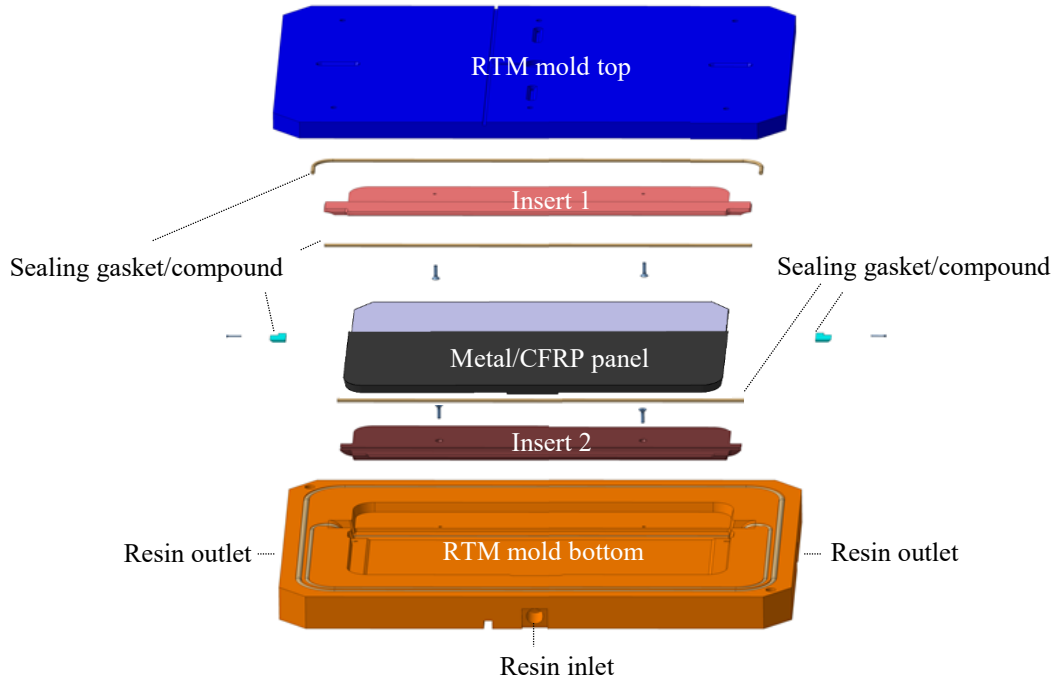

Figure 4-7: CAD-image of the tool design

Whereas the outer rectangular sealing gasket in the bottom half of the tool ensures vacuum tightness, the other sealing gaskets and compounds prevents undesired resin flow into areas where no preform is present. Furthermore, insert 1 and 2 are fixed with screws to the top and bottom molds.

4.3.2 Infiltration

Infiltration of the dry preform with liquid RTM-resin is the most critical step within the production cycle of the test panel. Accurate temperature and pressure control are essential to assure a high-quality part. In order to determine the required injection pressure, the filling time of the preform was calculated for different pressure differences between inlet and outlet, on the basis of the one-dimensional Darcy's law.

$$v(t) = u(t)(1-\varphi) = -\frac{K}{\mu(t,T)}\frac{\Delta p}{x_f} \tag{4-1}$$

$$\frac{dx}{dt} = -\frac{K}{(1-\varphi)\mu(t,T)}\frac{\Delta p}{x_f}$$

$$\int x_f dx = -\frac{K\Delta p}{(1-\varphi)}\int \frac{1}{\mu(t,T)}dt + C$$

with: $x_f(t=0) = 0 \rightarrow C = 0$

$$\Delta p = -\frac{x_f^2}{2}\frac{(1-\varphi)}{K}\frac{1}{\frac{1}{\mu(t,T)}dt} \tag{4-2}$$

Where *v(t)* is the Darcy velocity, *u(t)* the flow front velocity, φ the fiber volume fraction, *K* the 1D permeability, $\mu(t,T)$ the dynamic viscosity, Δp the pressure difference between inlet and outlet and x_f the flow front position. In order to solve equation (4-2), the viscosity profile of the PR520 RTM-resin at a temperature of 160°C had to be approximated for three time periods, see Figure 4-8.

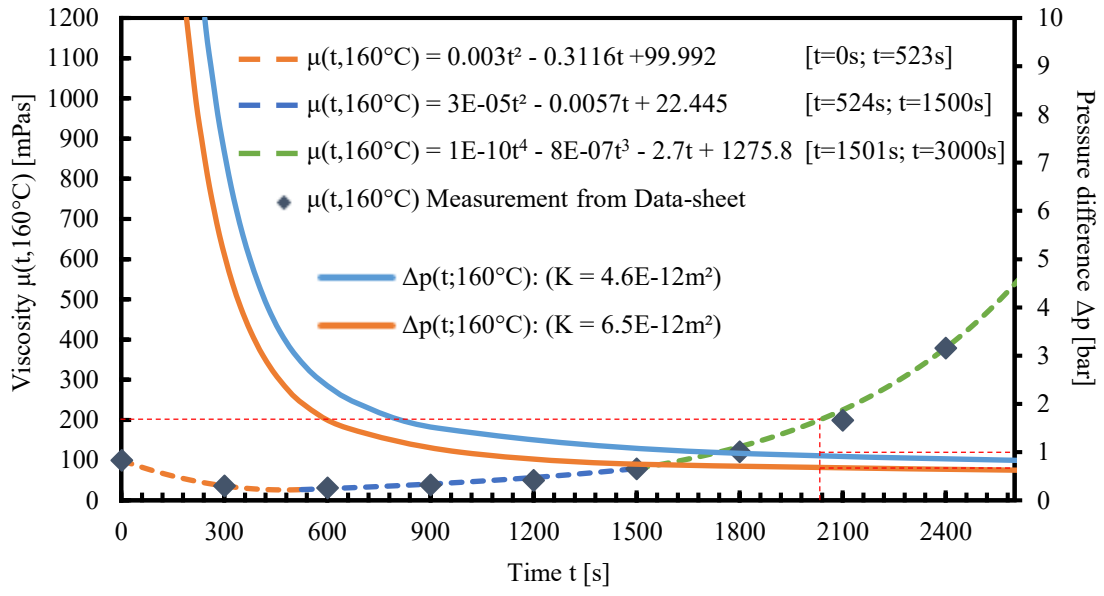

Figure 4-8: Viscosity and pressure difference over injection time

To calculate the filling time, x_f is equated with the distance between the inlet and outlet. After solving this equation, the required pressure difference to fill the preform within a specific time can be taken from Figure 4-8 for two different permeability values. A viscosity of 200mPas was set as the maximum tolerable viscosity for the injection step. The value of 200mPas for the maximum tolerable viscosity during infiltration is chosen based on preliminary testing for this setup. The maximum time period for the infiltration is 2000s. The minimum pressure difference to ensure preform filling within this time range is 1bar and 0.7bar for a permeability of 4.6E-12m² and 6.5E-12m², respectively. Even though the suggested injection temperature of the resin is 165°C [20], these calculations were performed for a resin temperature of 160°C as the PR520 data sheet only provides isothermal viscosity data for 160°C and 179°C. Several authors describe both experimental and simulative approaches to prevent undesired resin flow. They also evaluate tools in terms of resin inlet and outlet design [108–112].

The PR520 RTM-resin is a toughened epoxy resin system which provides high tolerance to impact damage and good strain to failure. It is recommended for primary aircraft structures which require superior toughness like engine blades, outer guide vanes, hinges and fittings or containment cases [20]. Small additive thermoplastic particles are mostly responsible for the resin system's increased impact tolerance in comparison to non-toughened epoxy resin systems. However, these particles only resolve within the epoxy resin at temperatures of around 165°C and above. Therefore, in order to prevent preform filtration of these particles, controlled heating of the resin to the required temperature is crucial. Heating the resin in the reservoir (resin pot) to 165°C is not suitable for proper injection. This would lead to a chemical cross-linking reaction during the time-consuming heating of the entire resin reservoir. As a result, the resin viscosity would be too high for successful infiltration of the preform. Therefore, the reservoir was kept at a temperature of around 105°C. The 60°C temperature difference between the reservoir and preform have to be overcome with the help of an electrical heated hose, a heating tool and the RTM-tool. The heating tool is made of aluminum and consists of a thin heat exchange area with the dimensions 300mm*50mm*0.5mm (length*width*thickness). The heating tool reduces the resin to a liquid film and therefore enables a very effective heat input into the resin. By placing the heating tool on top of the heated plate of the press, heat can be introduced by thermal conduction. De-gassing took place before the injection at a pressure of around +15mbar above vacuum and a temperature of 105°C for 15 min.

The first infiltration trials indicated that complete infiltration of the preform is not possible by a single-stepped infiltration process, with one resin inlet and two resin outlets as shown in Figure 4-7.

In order to guarantee complete filling of the preform, the infiltration process was extended by two additional steps, see Figure 4-9.

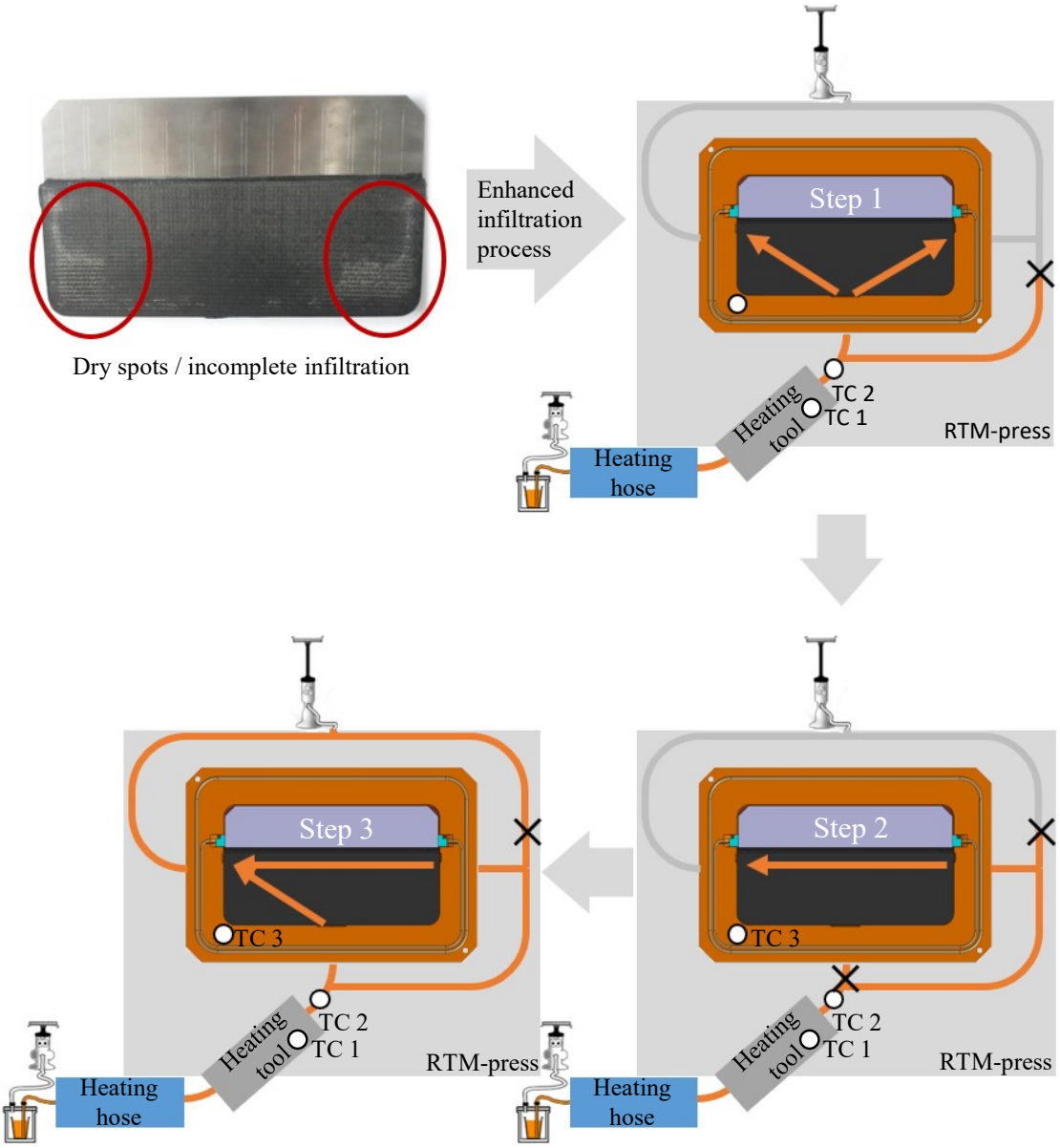

Figure 4-9: Different processing steps for RTM-infiltration

Once the resin reached the outlet on the right side of the tool, this resin outlet was converted into an inlet and the original inlet was closed. In a third step, the original resin inlet was opened again. After the resin reached the trap in front of the vacuum pump, the pipe in front of the trap was closed.

4.3.3 Temperature and pressure cycle

Three thermocouples were used to control the temperature on top of the heating tool (TC1), the temperature of the resin prior to entering the tool (TC2) and the temperature

of the tool (TC3). Figure 4-10 shows the temperature profiles throughout the entire injection step and successive cure cycle of a hybrid composite/titanium panel.

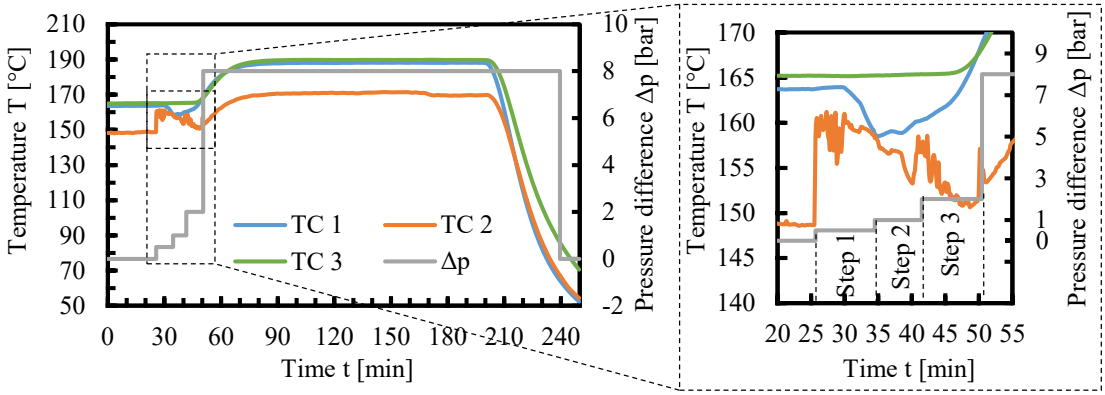

Figure 4-10: Temperature and pressure cycle over time for RTM-processing

For the injection step, the plates of the press and the electrical heating hose were heated to around 165°C. Even though the resin temperature in front of the resin inlet was slightly below the required injection temperature of 165°C, it is assumed that conductive heating between the tool and resin ensured the correct resin temperature when entering the preform. Several infiltration trials indicated that a stepped pressure cycle performs better when compared to a uniform pressure difference between inlet and outlet. In order to minimize the amount of entrapped air in the final part, vacuum was applied at the outlet throughout the entire injection step. During step 1, the pressure difference was adjusted to 0.5bar due to low resin viscosity. Within step 2, the pressure difference was increased to 1 bar and finally set to 2 bars in step 3. After around 25 minutes of infiltration, the resin pipe in front of the trap was closed and a pressure difference of 8bars was applied to minimize the size of potentially existing air inclusions. Afterwards, the tool was heated to 185°C, followed by a dwell phase of two hours. Finally, the press was cooled and the part was demolded at 60°C.

4.3.4 Cutting and trimming

The hybrid composite/metal panels were cut with a waterjet cutting machine. 13 single specimens were cut from one panel, see Figure 4-11.

Figure 4-11: Image of a trimmed hybrid composite/metal panel of joint design 1

As a closed mold RTM-process was used for manufacturing the panels, the specimen's thickness was uniformly distributed throughout the entire panel. Trimming was done with a grinding machine.

4.4 Prepreg-processing for joint design 2

The main goal of test series 4 is to evaluate the load carrying capability of the composite joint member for the pinned composite/metal joint, see Chapter 3.2.5. Two different joining methods were used for this purpose. For configuration "dh" (drilled holes), holes were drilled into the cured laminate and titanium. The spring steel pins were then inserted into the holes. Configuration "fh" (formed holes) was manufactured by inserting the pins into the uncured prepreg, leading to fiber undulations around the pins.

4.4.1 Specimen arrangement and treatment of metallic joint member

Three test panels with the layups $[\pm 45]_2$, [0/90/-45/+45] and $[0/90]_2$ were manufactured. Each panel contained specimens of both configurations, see Figure 4-12.

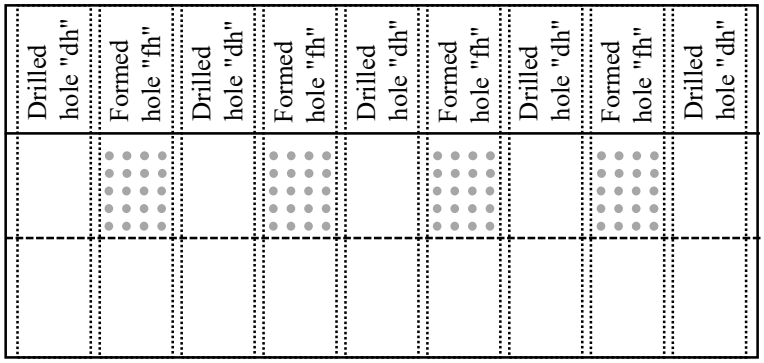

Figure 4-12: Specimen arrangement for hybrid CFRP/titanium panels of joint design 2

First, four unidirectional prepreg plies were joined to one stack by hand-layup. Afterwards, holes of 1.50mm diameter for the pinned specimens were drilled into the titanium sheet, followed by a cleaning step and the application of a release agent to suppress adhesive bonding between the titanium and composite joint member.

4.4.2 Insertion of pins

For pin insertion, a quasi-isotropic dry fiber stack of NCF material, which served as a supporting material, one prepreg stack, the titanium sheet and the spacer were placed inside a clamping fixture, see Figure 4-13.

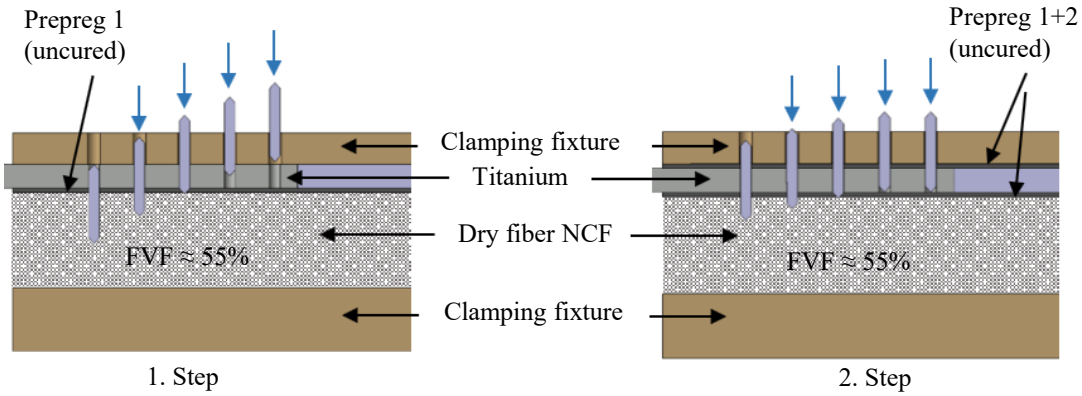

Figure 4-13: Pin insertion into uncured prepreg material for joint design 2

Preliminary tests showed that a fiber volume fraction of approximately 55% of the dry fiber NCF material represents strong support for the pin insertion, leading to minimum fiber breakage within the prepreg material. In step 1, the pins were pushed through the titanium sheet and the first prepreg stack. Then, after rotating the panel 180° and adding the second prepreg stack, the pins were also pushed through the second stack so that the free length of the pins on both sides of the DLS-joint was identical. Release foil was placed between the prepreg stack and the supporting NCF-material. In addition, the clamping fixture was treated with a release agent to suppress tackiness between all components.

4.4.3 Consolidation and curing

The processing took place inside the tool. In order to avoid damage of the pins while closing the press and to ensure correct positioning of the panel in the tool, two metal plates with perforations were treated with release agent. Release agent was also applied between the panel and both the bottom and top mold of the tool, see Figure 4-14.

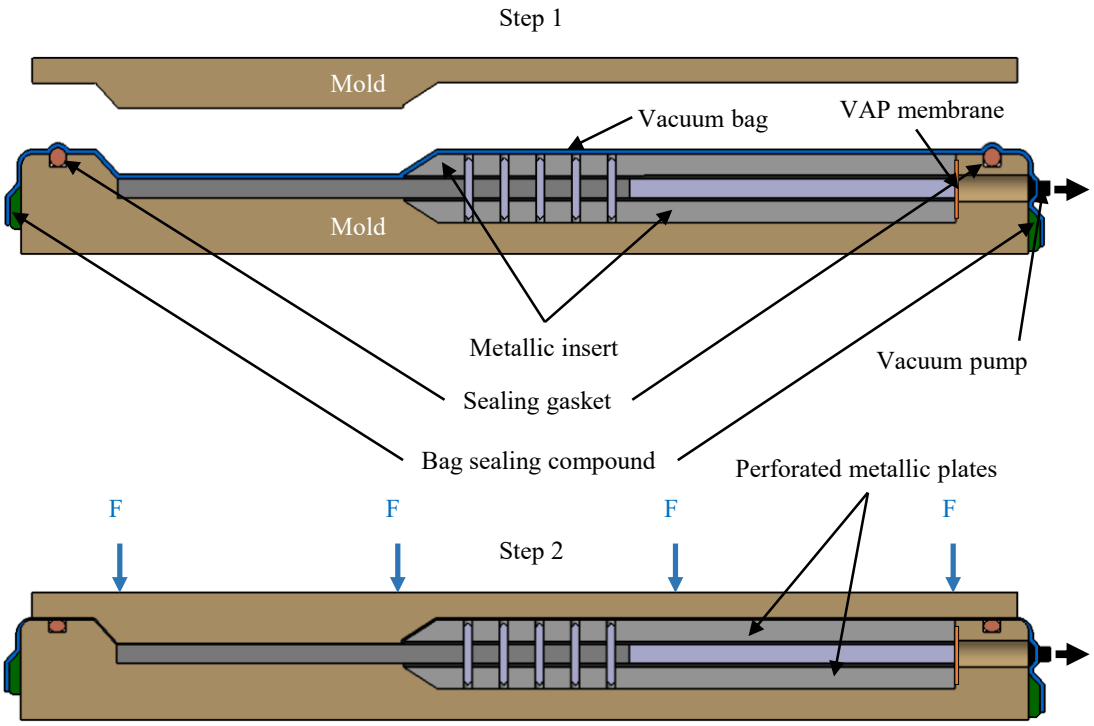

Figure 4-14: Tooling for prepreg processing - joint design 2

The VAP-membrane suppressed the resin flow from the prepreg material into the air evacuation duct of the mold. A vacuum bag was placed on the bottom mold, covering the panel and the perforated plates. Subsequently, vacuum was applied and the temperature of the mold was adjusted to 60°C, followed by a heating ramp and a dwell phase at 120°C for two hours, see Figure 4-15.

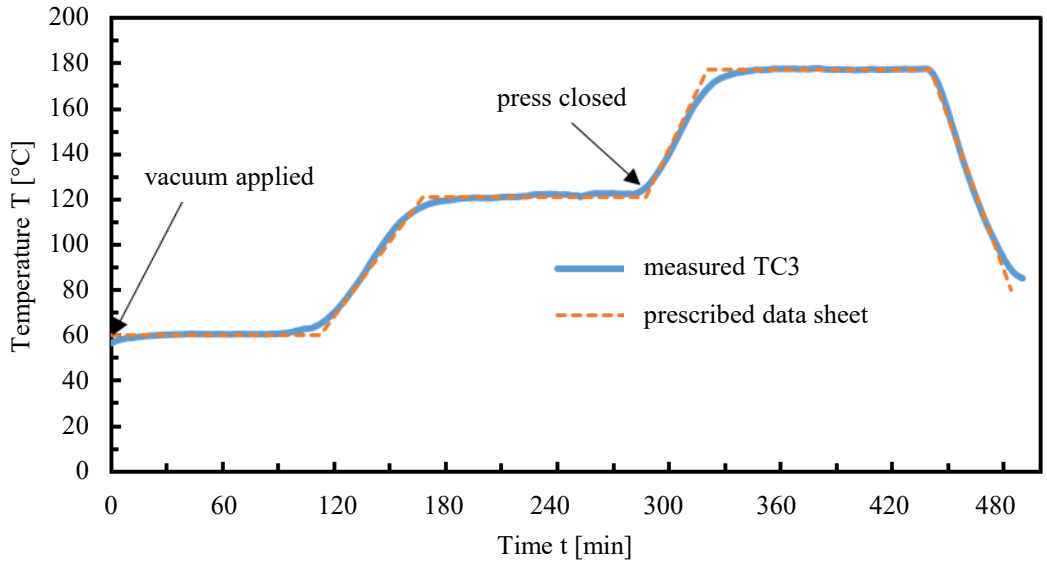

Figure 4-15: Prepreg cure cycle for double lap joint design 2

Prior to the second heating ramp, the press was closed and a force of 750kN was applied, leading to a compression of the prepreg stacks to its nominal thickness. Curing took place at a temperature of 177°C for another two hours, followed by cooling to 60°C and demolding. Single specimens were cut from the panel with a waterjet cutting machine.

In order to equip the specimens of configuration "dh" with fasteners, holes of 1.50mm diameter were drilled into the cured laminate and titanium joint member separately. Microscopy inspection of eight machined holes per stacking sequence revealed that the average diameter was equal to 1508 µm with a standard deviation of 10 µm. To allow for the inspection of hole edges, flash was removed using sandpaper grit 4000. Large sized ply breakouts were not observed, see Figure 4-16.

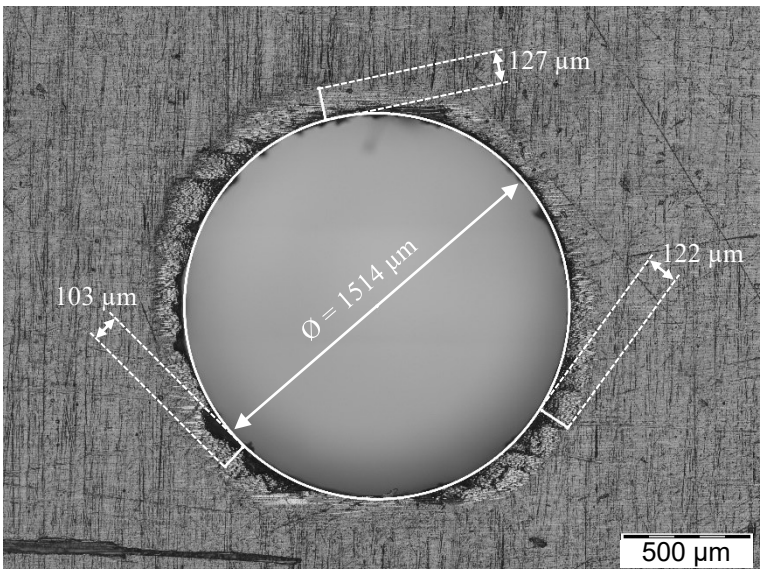

Figure 4-16: Microscopy inspection of a drilled hole

Due to the absence of an adhesive bond between the titanium and composite joint member, the joint could be easily disassembled. Finally, the joints of configuration "dh" were assembled and fasteners were inserted into the holes and kept in position by a press fit.

4.5 Specimens for test series 2

The specimen manufacturing for test series 2 was performed using similar production technologies as described previously. The specimens for CFRP-tension, Mode I, Mode II fracture toughness of configuration NCF/PR520 and Ti6Al4V/NCF/PR520 and neat resin were produced in an RTM-process with different rectangular tools. Specimens made from Prepreg Cycom 5320-1 for Mode I and Mode II fracture toughness were manufactured using vacuum bagging and the press by applying a cure cycle, similar to the one shown in Figure 4-15. Table 3-1 in Chapter 3.2.1 summarizes all of the tests performed within the scope of this thesis.

5 Results

This chapter describes testing and FE results for test series 1 through 4. Test series 1 on element level aims to compare the mechanical performance of pinned composite/metal joints with different pinning technologies in order to identify a suitable pinning technology for further joint testing. The goal of test series 2 is to determine the material parameters needed as an input for the FE analysis of the CFRP/titanium joints of test series 3 and 4. In order to validate the FE results, comprehensive testing is also included into test series 3 and 4. Whereas the goal of test series 3 is to optimize the tensile strength of the joint, test series 4 aims to identify the impact of fiber undulations around the pins with respect to the joint's mechanical behavior. For further information regarding test setup, methodology and setup of the FE-model including material models, please refer to Chapter 3.

5.1 Test series 1: CFRP/steel joint design 1

Three different pinning technologies - laser pinning, CMT pinning and inserted pinning are applied for the double lap shear test specimens of test series 1. A co-bonded reference joint without pins serves as a baseline for the comparison to the pinned configurations, see Figure 5-1.

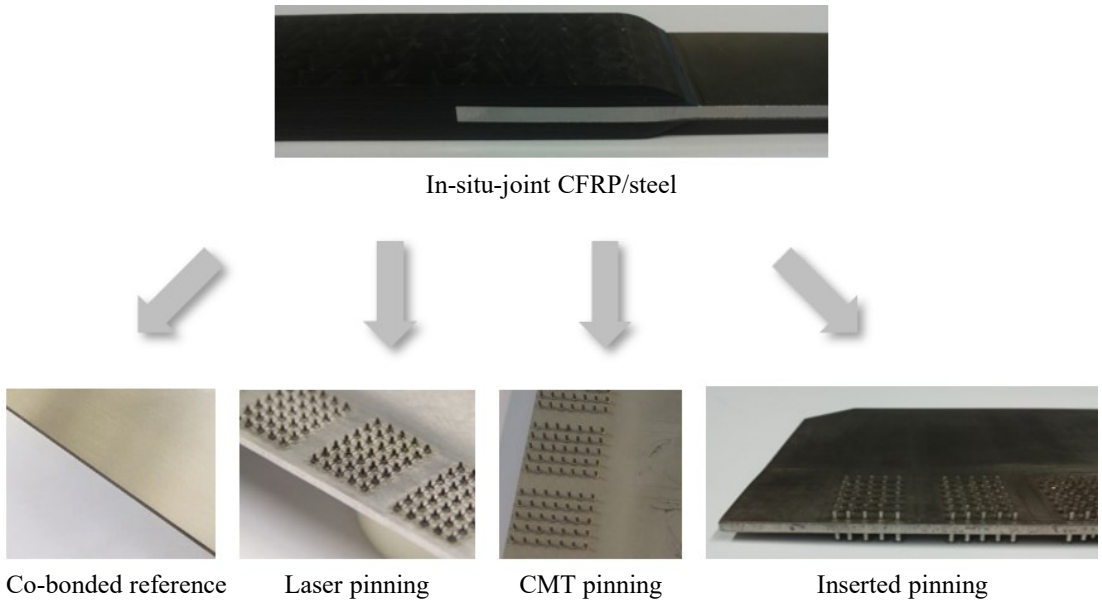

Figure 5-1: Different pinning technologies, applied for CFRP/steel joints

5.1.1 Failure modes

The failure modes for different setups of test series 1 are illustrated in Figure 5-2.

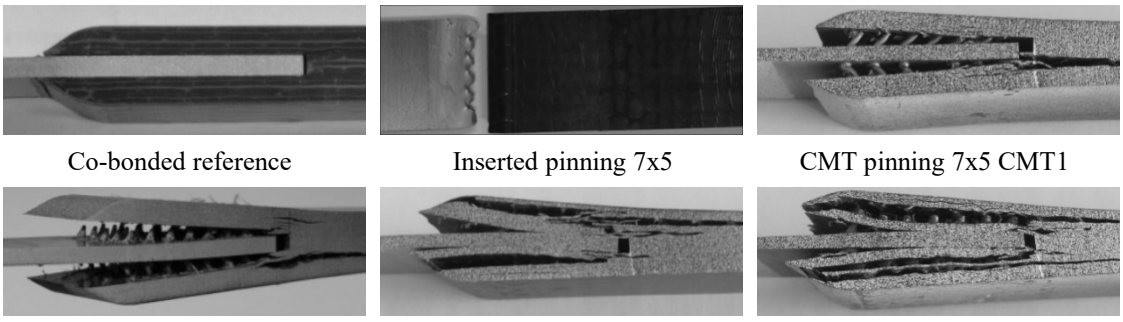

Figure 5-2: Failure modes for CFRP/steel joints

Debonding between the metallic and composite joint members occurred for the co-bonded reference joints. Due to bending of the laser pins, a deflection of the composite laps in z-direction could be observed for the laser pinned specimens. In addition, some pins failed due to shear at their root zones. CMT-pinned specimens with a pin diameter of 1.2mm ("CMT1") failed similarly to the laser pinned specimens. However, a different failure mode could be observed for the CMT-pinned specimens with a pin diameter of 1.6mm. Delamination between the NCF-layers occurred in an area located close to the pin tops, followed by a net section failure of the NCF-layers in between the delamination zone and metallic joint member.

The pinned specimens with inserted pins and a 7x5 pin pattern failed due to net section failure within the metallic joint member. Therefore, in order to reduce notch effects in the first pin rows, an alternative pin pattern was tested for the inserted pins, see Figure 5-3.

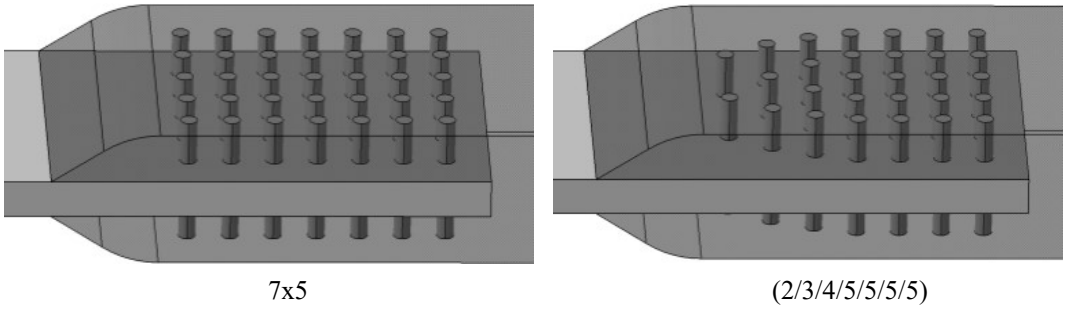

Figure 5-3: Pin patterns for pinned CFRP/steel joints

The configurations with inserted pins and the alternative pin pattern showed a failure mode, comparable to the "CMT2" configuration with a pin diameter of 1.6mm.

5.1.2 Joint strength

The joint strength is defined as the maximum applied load, divided by the metallic joint member's cross section outside the joining area at an unloaded state. The metallic joint member's cross section outside the joining area (3mm x 25.4mm) is identical for all configurations. The shear strength is defined as the maximum applied load, divided by the joining area (2 x 39.5mm x 25.4mm), which is also identical for all configurations. Results for tensile testing in terms of nominal joint strength and shear strength for all configurations of test series 1 are displayed in Figure 5-4.

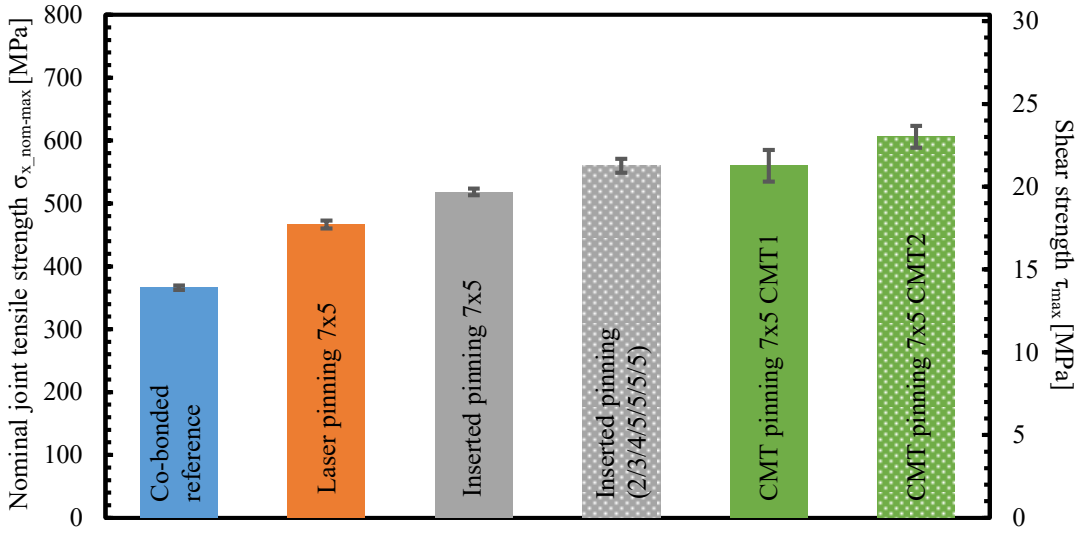

Figure 5-4: Joint tensile strength for CFRP/steel joints, co-bonded reference vs. pinned joints

The co-bonded reference joint shows the lowest joint strength of all setups, followed by the laser pinned specimens and specimens with inserted pins and the 7x5 pin pattern. The joint strength of the specimens with inserted pins and 2/3/4/5/5/5/5 pin pattern is comparable to the specimens of configuration "CMT1". However, the standard deviation for configuration "CMT1" is as twice as high as those of the configuration with inserted pins and 2/3/4/5/5/5/5 pattern. The highest joint strength can be observed for configuration "CMT2". Five specimens of each configuration were tested with an exception for configuration "inserted pinning 7x5" (2 specimens).

5.1.3 Stress-strain behavior

In order to evaluate the mechanical performance in a tensile stress state, the stress-strain behavior should be analyzed in more detail.

Figure 5-5 displays representative stress-strain curves for the configurations of test series 1 with an exception of configuration "inserted pinning 7x5".

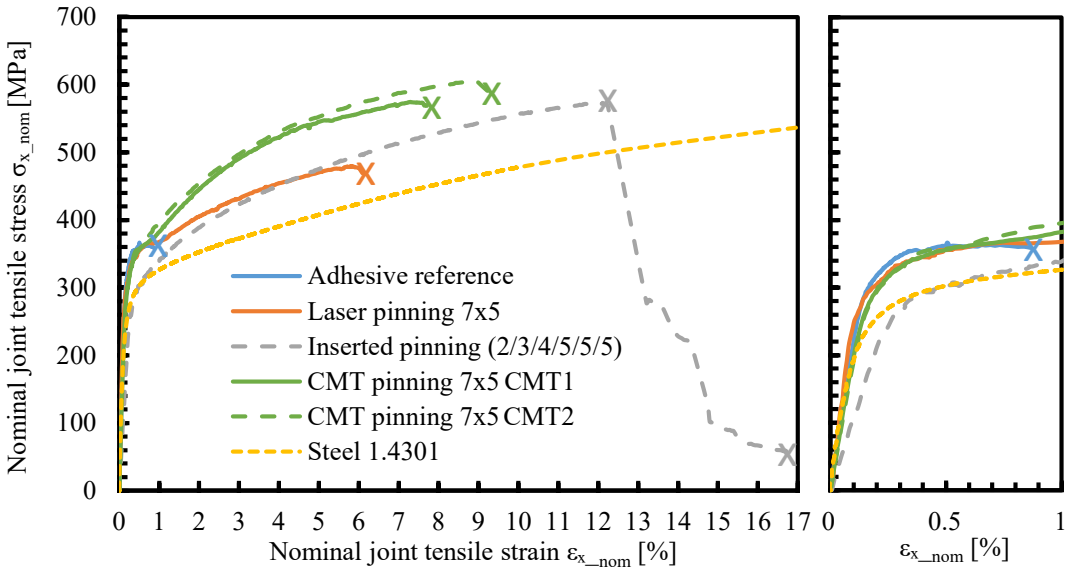

Figure 5-5: Stress-strain behavior for CFRP/steel joints, co-bonded reference vs. pinned joints

According to the determination of nominal strain, explained in Chapter 3.2.3.3, the area of measurement is limited to the joining area. Figure 5-5 indicates that the initial stiffness in the linear elastic state is comparable for all configurations with an exception for the joint with inserted pins. In this case, the reduction of cross section of the metallic tab, due to hole drilling, results in a reduced initial stiffness. Because of local elongation of the metallic tab for nominal stresses above its yield point, debonding in the interface between metallic and composite joint member is initiated at the front edge of the joining area for all configurations. The stress-strain behavior for nominal joint strains above 0.3% for all pinned configurations is strongly driven by the plasticity of the metallic components.

Premature bending of the laser pins lead to a decrease of joint stiffness and sudden failure. CMT pins are characterized by a higher bending stiffness in comparison to laser pins. The first section of plastic joint behavior until a nominal strain of around 4% is dominated by the material behavior of the metallic joint member. A significant decrease of joint stiffness can be observed for "CMT1" configuration with pin diameters of 1.2mm for nominal strain values above 4%. In this case, pin bending and deflection of the composite laps towards thickness direction are responsible for this degradation in joint stiffness. The pins of configuration "CMT2" with diameters of 1.6mm were able to withstand the highest tensile loads, due to their high bending stiffness. The reduced cross section for configuration "inserted pinning (2/3/4/5/5/5/5)" significantly decreases the overall joint stiffness. However, extensive pin bending could not be observed until a nominal joint strain of 12%, even though the total amount of pins is 17% lower in comparison to the other pinned configurations. A gradual failure behavior could be observed

for this configuration. The first load drop is caused by the two pins bending in the first pin row, resulting in a deflection of the composite joint member towards thickness direction. As pin bending is low within the last 5 pin rows, these pins are able to act as a crack stopper for the inter-ply delamination.

5.1.4 Microscopy of cross section

In order to evaluate fiber undulations in the *x*-*z* plane and the material structure of metallic joint member and pins, microscopy images were utilized. The images of non-tested specimens were created for the laser pinned configuration with cone shaped pins and "inserted pinning 7x5" with cylindrical pins. Figure 5-6 shows a cross section of the mid-plane through the laser pins.

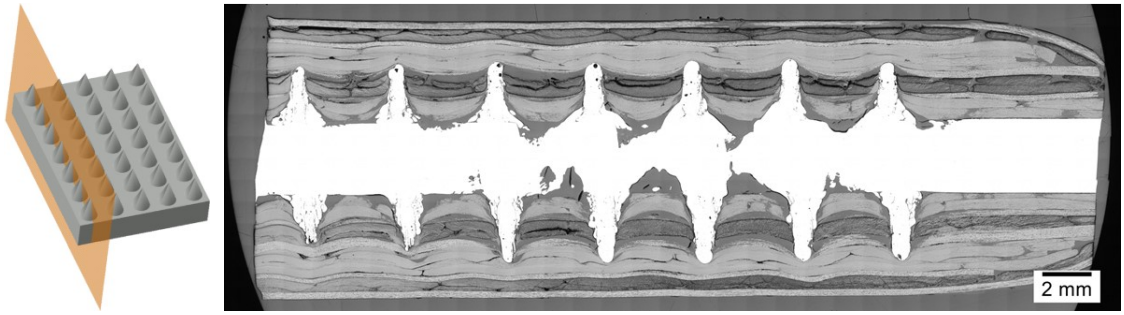

Figure 5-6: Microscopy image of laser pinned CFRP/steel joint - Section 1

Due to local melting of the metallic substrate, cavities and porosities occur primarily in the third, fourth and fifth pin row. It is assumed that heat transfer from the metallic substrate into the clamping fixture, see Chapter 4.1.1, is more efficient in the peripheral regions of the joining area. Due to the fact that material is transferred from the regions around the pins into the pin itself, see Chapter 2.3.2, the intrusions and cavities are present throughout the entire joining area. Figure 5-7 displays the cross section in between the pins.

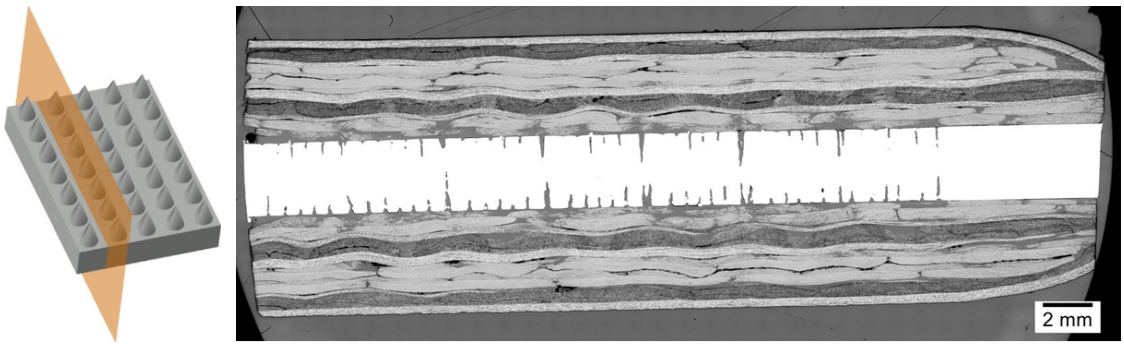

Figure 5-7: Microscopy image of laser pinned CFRP/steel joint - Section 2

According to Figure 5-6, defects within the metallic substrate occur primarily in a region close to pin rows 3, 4 and 5. However, both microscopic images indicate that because of the conical shape of the pins, fiber undulations in thickness direction are low for laser

pinned specimens. Figure 5-8 shows a microscopy image of a cross section through a specimen with cylindrical inserted pins.

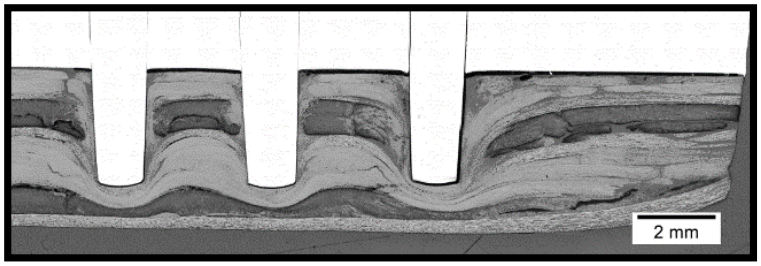

Figure 5-8: Microscopy image of inserted pinned CFRP/steel joint

Significant out-of-plane undulations can be observed in areas close to the pin heads, whereas extensive resin pockets are present around the pins near the metallic joint member. However, in order to reduce pin bending, load should rather be introduced into the pin at locations close to the metallic joint member. Therefore, undulations in thickness direction should be reduced to a minimum.

5.1.5 Selection of pinning technology

In order to choose a suitable pinning technology for test series 3, both advantages and disadvantages of each joining technology have to be weighed against each other.

Local melting of the metallic substrate caused by the laser pinning process results in a significant weakening of the metallic joint member. Furthermore, cavities and porosity within the pins leads to a reduced bending stiffness and shear strength in comparison to the other pinning technologies. However, it should be noted that process parameters, i.e. laser power or translation speed have a significant impact on the size and quality of the pins. Wang et al. [65] have found that the joint tensile strength of CFRP/titanium joints with pins created by the Surfi-Sculpt^{TM} technology can be significantly improved by an optimization of the pin geometry. Therefore, they created a linear triangular pin geometry with an improved bending stiffness and shear strength in tensile load direction. It can be reasonably assumed that, because of the non-axis-symmetrical pin design, the joint strength for compressive or transverse loading is reduced. Even though the specimens are only loaded in tensile direction within the scope of this thesis, the pin geometry is kept symmetrical to its longitudinal axis in order to provide identical pin stiffness and strength in all in-plane loading directions. Due to their limited mechanical properties, the laser pins are excluded from the selection process.

CMT-pinned specimens reach the highest values for joint tensile strength. Especially pins with 1.6mm are characterized by a high shear strength and bending stiffness. Furthermore, it is the only pinning technology, investigated within the scope of this work, which does not result in a reduction of the cross section of the metallic joint member. However, a distinct root zone in combination with a high pin diameter leads to high local fiber volume fractions within the composite joint member. Based on Table 4-1, the mean

fiber volume fractions for a single unit cell (UC; 4.36*5.08*4.1 mm³)) and a 7x5 pin pattern can be calculated for the different configurations, see Table 5-1.

Table 5-1: Averaged fiber volume fractions for unit cell

Configuration	Volume of fibers (UC) [mm³]	Volume of pin [mm³]	Volume of composite (UC) [mm³]	FVF (UC) [-]
Laser 7x5	57.54	2.55	88.20	0.65
CMT1 7x5	57.54	5.46	85.29	0.67
CMT2 7x5	57.54	10.60	80.15	0.72
Inserted 7x5	57.54	6.19	84.57	0.68

As opposed to Figure 3-4 which states that the nominal specimen thickness is 11.0mm, thickness measurements of the specimens after demolding indicated that the real specimen thickness is 11.2mm. This results in a real FVF of 0.634 outside the joining area.

High fiber volume fractions can be critical due to an increased susceptibility to intra-ply delamination [24]. Because of the lack of space for the matrix component, it cannot sufficiently enable load transfer in between the fibers. Therefore, in order to strengthen the composite joint member, either the fiber volume fraction outside the joining area, the pin diameter, or the number of pins has to be decreased. Reducing the fiber volume fraction outside the joining area may be critical as this impacts the design of the entire part and further decreases the mechanical in-plane properties outside the joining area. A lower pin diameter or number of pins results in a lower load carrying capability of the pins.

Pins made of spring steel offer a high yield and tensile strength. The cylindrical shape without a conical root zone furthermore enables an efficient load introduction into the pin close to the metallic joint member.

Figure 5-9 illustrates the load introduction into pins for the different geometries prior to pin bending.

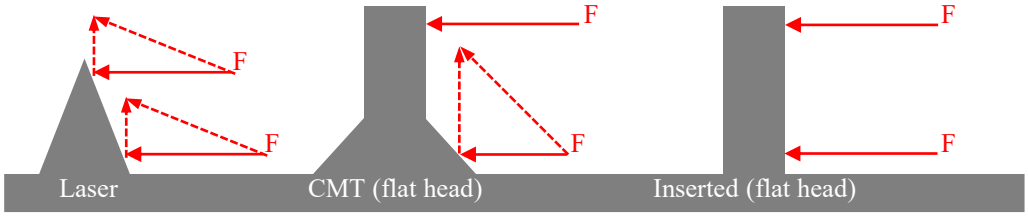

Figure 5-9: Schematic explanation of load introduction into pins, dependent on pin geometry

A force deflection towards the specimen's thickness direction leads to premature debonding of the composite from the metallic joint member and therefore should be reduced to a minimum. These considerations also emphasize the importance of low pin bending, thus high bending stiffness. Once pin bending occurs, a force deflection towards thickness direction also takes place for the inserted pins. Another advantage of inserted pinning towards CMT-pinning is the lower variation in joint tensile strength, see Figure 5-4. However, the metallic tab's degradation of mechanical properties through hole drilling is a major drawback for inserted pinned specimens. It should be noted that the CMT-pinning process offers the possibility to change the geometry of the pin head [54].

Pin head geometries which exceed the pin neck in diameter are able to absorb load in the pinned composite/metal joint's thickness direction. As a result, the pin is additionally loaded in longitudinal direction. However, in order to still enable pin insertion into the uncured composite, the possible diameter of the pin head is limited. Furthermore, the pin neck diameter must be substantially smaller than the pin head diameter, which reduces pin bending stiffness and shear strength.

Both pinning technologies, CMT-pinning and inserted pinning are promising in terms of high joint tensile strength for CFRP/steel joints. As opposed to test series 1, Ti6Al4V was used for the metallic joint member for test series 3. Due to an increase of the metallic joint member's tensile and yield strength from test series 1 to 3, see Chapter 5.2.1, net section failure of the metallic joint member becomes less likely. The variation coefficient in regards to joint tensile strength was observed to be smaller for the joints with inserted pins in comparison to configuration "CMT1". In addition, the fiber volume content for a unit cell (7x5 adjustment) with 1.5mm inserted pins and 1.2mm CMT pins ("CMT1") is similar. As a result, fiber undulations, hence degradation of tensile stiffness and strength of the composite joint member should be comparable. Therefore, inserted pins were selected for further investigation within test series 3. Based on the results found in test series 1, it was decided to decrease the pin density to obtain a lower fiber volume fraction within the joining area. Furthermore, a spiky pin head should reduce the fiber undulations in *z*-direction, see Figure 4-4 in Chapter 4.1.3.

5.2 Test series 2: Materials characterization

This chapter presents the results of all tests performed on coupon level. Tensile testing was carried out for Ti6Al4V, steel 1.4301 and CFRP, ±45° and 0/90 fiber direction. Testing results for Mode I and Mode II fracture toughness are analyzed in Chapter 5.2.3 and 5.2.4. Furthermore, neat resin was tested in a tensile and compressive stress state, see Chapter 5.2.5.

5.2.1 Tensile testing metal

Tensile testing of the metal types used for the metallic joint member of the hybrid composite/metal joints were performed under a free crosshead speed, identical to ASTM D3528 - 96 [88]. This was used as the basis for testing of the hybrid composite/metal joints. Therefore, a transfer from coupon to element level can be guaranteed as strain rate dependencies are minimized. Figure 5-10 shows testing results for tensile strength and two representative stress-strain curves for steel 1.4301 and titanium Ti6Al4V specimens.

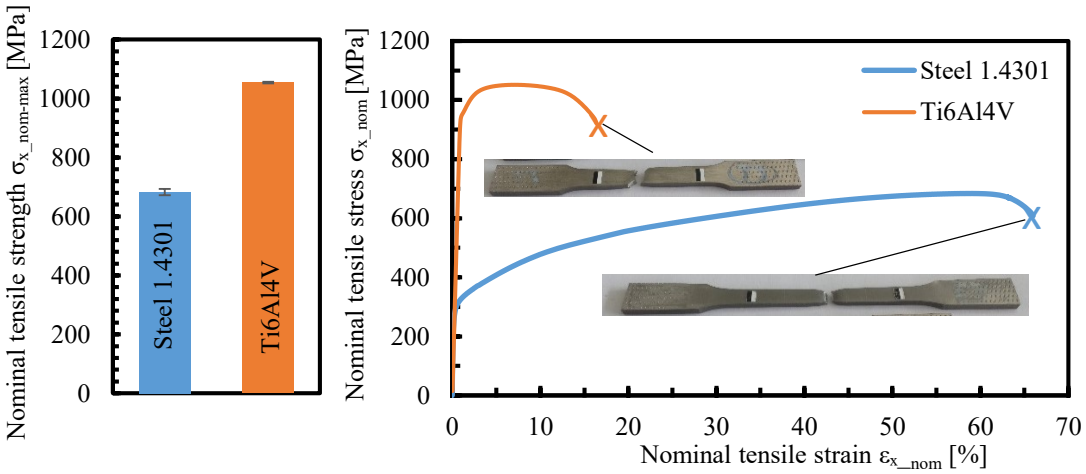

Figure 5-10: Tensile strength and stress-strain behavior for steel and titanium

These results emphasize the importance of a precise knowledge of the entire stress-strain behavior until failure. Plastic yielding has a significant impact on the mechanical behavior of the hybrid composite/metal joint. The elastic modulus of steel 1.4301 (225GPa) was measured to be 80% higher than those of Ti6Al4V (124.5GPa). In order to validate the plasticity and damage model described in Chapter 3.4.1.2, a FE-simulation was set up.

A comparison of stress-strain curves for testing and FE-results of Ti6Al4V are illustrated in Figure 5-11.

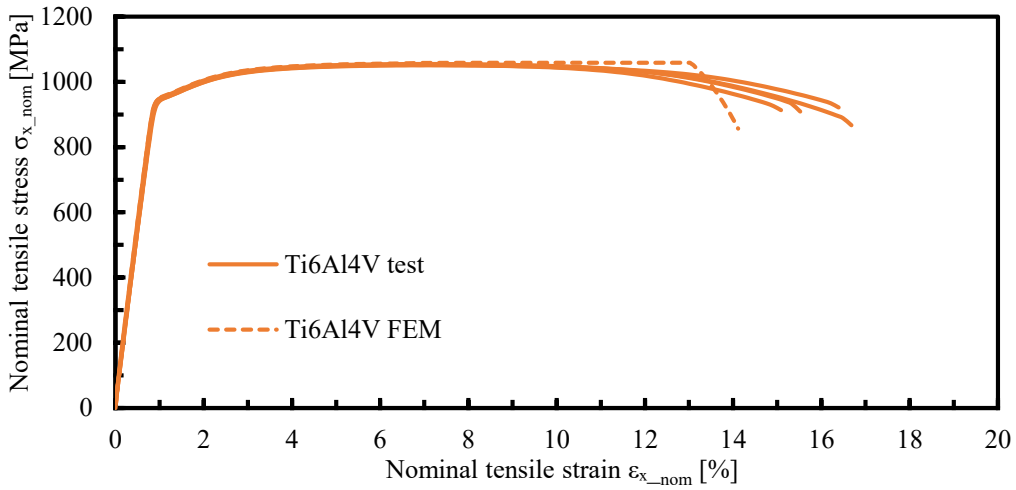

Figure 5-11: Stress-strain behavior, mechanical testing vs. FEA for titanium

FEA and testing show similar results until necking occurs. The damage degradation model used for this FE analysis is not able to fully analyze metallic necking. However, these results were found to be sufficient for numerical modelling of the hybrid composite/metal joint.

5.2.2 Tensile testing CFRP

Tensile testing of CFRP was performed for two different layups, $[\pm 45]_{3s}$ and $[0/90]_{3s}$. As bidirectional NCF-material was used, testing of unidirectional layups was not possible. Figure 5-12 shows testing results of both layups for tensile strength and two representative stress-strain curves.

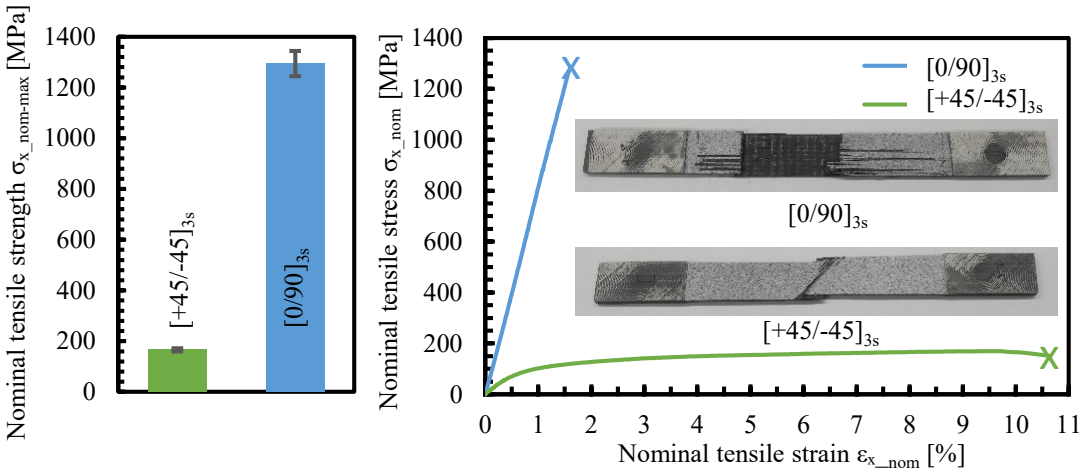

Figure 5-12: Tensile strength and stress-strain behavior for a CFRP $[0/90]_{3s}$ and $[\pm 45]_{3s}$ layup

Whereas the $[0/90]_{3s}$-specimens failed due to fiber tension of the 0°-fibers, matrix dominated shear failure was found to be the failure mode for the $[\pm45]_{3s}$-specimens. Figure 5-12 furthermore emphasizes the plastic behavior of the ±45°-layers. According to Chapter 3.2.4.2 a bidirectional NCF-material containing IMS60 fiber was used in combination with PR520 RTM-resin and a FVF of 60%.

5.2.3 Mode I testing

Mode I interlaminar fracture toughness testing was performed to identify the energy-based material input parameter G_{Ic}, which is needed for cohesive zone FE-modelling. Interlaminar delamination can either occur within the composite joint member or the interface between the metallic and composite joint member. The NCF/PR520 and Ti6Al4V/NCF/PR520 material combinations were tested for test series 3 and Prepreg 5320-1 for test series 4. As no adhesive bond is present between the titanium and composite joint member in test series 4, the Ti6Al4V/Prepreg 5320-1 material combination can be excluded from testing. Figure 5-13 shows testing results for the averaged G_{Ic_mean}-value for different material combinations.

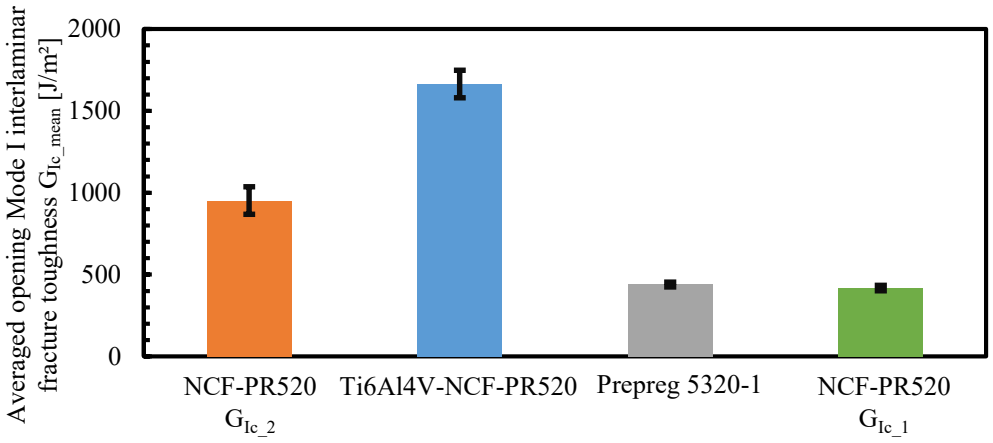

Figure 5-13: Mode I fracture toughness, comparison of G_{Ic_mean}-values for different material combinations

The G_{Ic}-value can be calculated individually for every state during testing of one specimen. The G_{Ic_mean}-value represents the averaged G_{Ic}-value for one specific test specimen. Highest G_{Ic_mean}-values could be measured for the CFRP/titanium interface. Two configurations were tested for the NCF/PR520 combination which differ only in the stitching pattern of the NCF in the mid-plane of the DCB-specimen, where crack propagation occurs. Testing results indicate that the stitching pattern has a high influence on the Mode I fracture toughness. Specimens made from Prepreg 5320-1 show a comparably low G_{Ic_mean}-value. A minimum of four specimens were tested for each setup. Each material combination is analyzed in further detail in the following two chapters.

5.2.3.1 NCF+PR520 and Prepreg 5320-1

A $[90/0]_{3s}$ layup was used for the NCF/PR520 specimens and binder web was applied in between the NCF-layers. In order to ensure crack propagation within the mid-plane of the DCB-specimen, it is essential to place the 0°-layers adjacent to the release foil which acts as a crack initiator. However, the stitching pattern is not identical on both sides of the NCF-layer. Therefore, two different configurations are possible for the same type of NCF-material and a $[90/0]_{3s}$ layup. Figure 5-14 shows representative load-load point deflection curves for both NCF/PR520 configurations and the DCB-specimens made from Prepreg 5320-1.

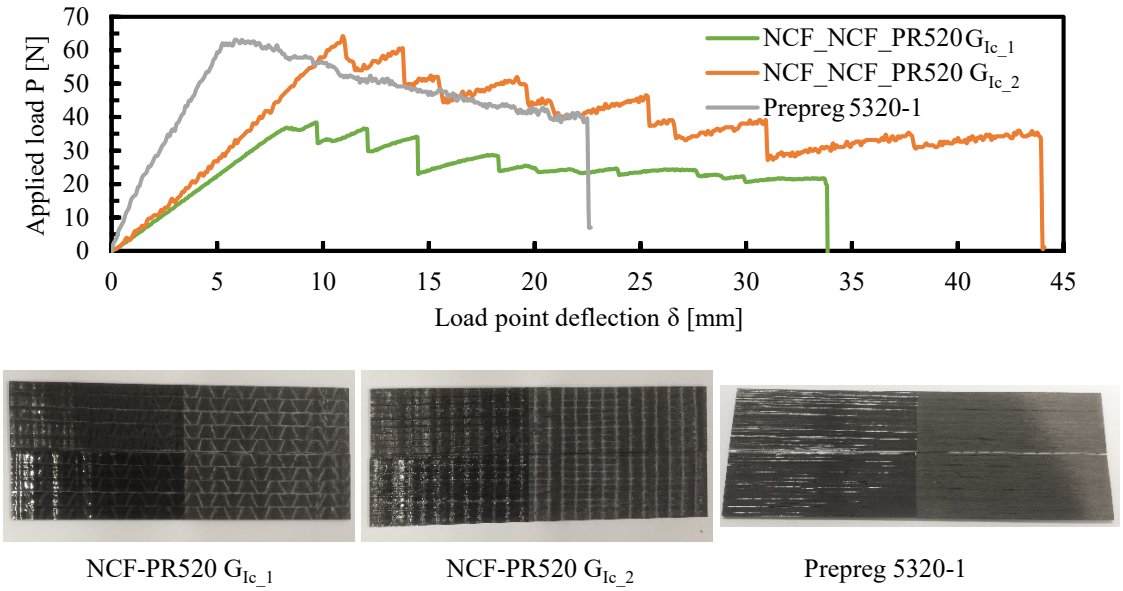

Figure 5-14: Mode I fracture toughness, load-load point deflection

A direct comparison of the load-load point deflection curves for DCB-specimens is only valid if three basic requirements are met:

- the layup and type of material are identical
- specimens are characterized by the same thickness
- the length of the precrack coincides

Therefore, two NCF/PR520 DCB-specimens were chosen for Figure 5-14, which satisfy these requirements. Two important findings result from these tests. First, the required load for crack initiation significantly increases if the stitching pattern is orientated perpendicular to the direction of crack propagation instead of 45°. Second, the stitching thread leads to interruption of crack propagation. After a critical load is reached, the crack propagates, resulting in a sudden drop of the load-load point deflection curve. This crack stopping mechanism is more effective for stitching patterns, which are oriented perpendicular to the direction of crack propagation. The DCB-specimens made of Prepreg 5320-1 consist of a unidirectional 0°-layup, as this layup is recommended in ASTM

D 3518 [92]. Therefore, the bending stiffness is higher in comparison to the NCF/PR520 DCB-specimens, which are made from bidirectional NCF and consist of a 0/90°-layup. Furthermore, as no stitching threads are present in the delamination area of the prepreg specimen, crack propagation is expressed as a smooth load drop in the load-load point deflection curve.

These tests emphasize the difficulty in choosing a suitable G_{Ic}-value for the FE analysis. Calculation of the G_{Ic}-value is only valid for in-plane crack propagation. In the case of composite/composite DCB-specimens this can only be guaranteed in between two 0°-layers with continuous unidirectional fibers. However, specimens of test series 3 and 4 contain different fiber directions. Furthermore, the orientation and type of stitching pattern depends on the fiber direction. Chapter 5.4.2.2 further explains the impact of the G_{Ic}-value on the joint behavior and highlights the difficulty in choosing a proper G_{Ic}-value as an input for FE-simulation.

5.2.3.2 CFRP/titanium

In order to identify the Mode I fracture toughness in the interface between the CFRP and titanium joint member, hybrid CFRP/titanium DCB-specimens were manufactured in a RTM-process. A preliminary design study using FEA helped to define the thickness of the CFRP and titanium joint member, see Chapter 3.2.4.3. According to the FE-results, a 2mm thick $[90/0]_4$ -layup was used for the CFRP joint member, whereas the thickness of the titanium joint member was adjusted to 1.5mm. The surface of the titanium joint member was grinded with sandpaper grit 180 and cleaned prior to co-bonding in the RTM-process.

Mode I fracture toughness testing of the CFRP/titanium DCB-specimens indicated that extensive fiber bridging occurred within the delamination zone. Figure 5-15 illustrates the evolution of the G_{Ic}-value with load point deflection and the principle of fiber bridging.

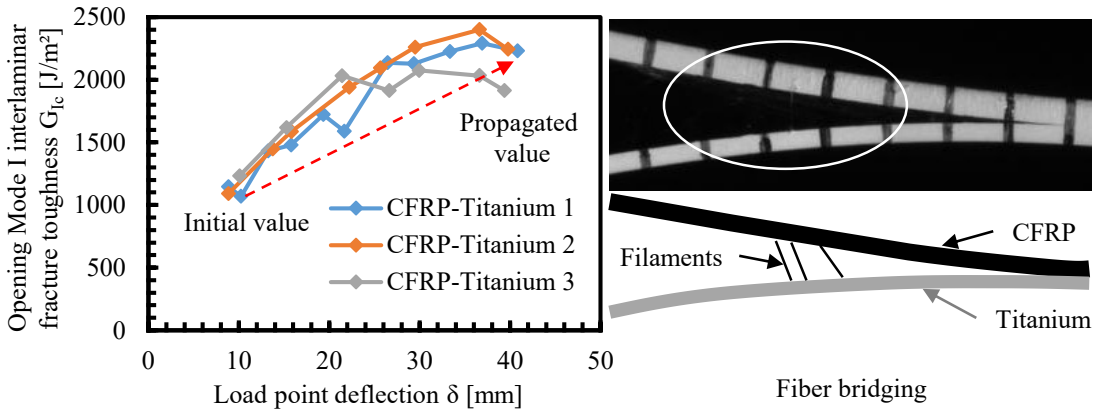

Figure 5-15: Mode I fracture toughness, fiber bridging

Fiber bridging usually occurs for high G_{Ic}-values if single filaments de-bond from the surrounding matrix material due to intra- instead of inter-ply delamination. As a result, the single filaments built a bridging mechanism between both beams and significantly increase the G_{Ic}-value.

This bridging mechanism becomes more effective with the increase of load point deflection as the orientation of the bridging filaments converges with the direction of crosshead movement. ASTM D5528-01 states that in case of fiber bridging, the first value for G_{Ic} with minimum load point deflection should be used. Therefore, the initial value for G_{Ic} of 1100J/m² is used as an input parameter for the validation of the cohesive material model. Figure 5-16 illustrates the comparison of load-load point deflection behavior between testing and FEA.

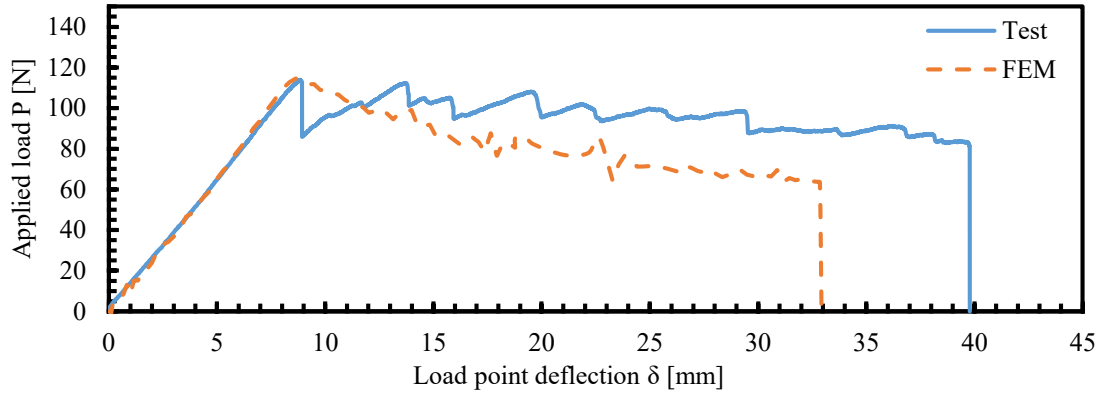

Figure 5-16: Mode I fracture toughness, CFRP/titanium DCB specimens - testing vs. FEM

Testing and simulation show a strong match in terms of bending stiffness and applied load which leads to crack initiation. However, crack propagation cannot be fully described by cohesive elements and one material model underlying a linear traction-separation law. Fiber bridging and interruption of crack propagation caused by the stitching thread of the NCF-material can only be covered by applying a plurality of cohesive zones with different material properties. However, this would lead to a very high complexity and was therefore not implemented in the FE-model.

Figure 5-17 shows FE-results for von Mises stress for the titanium joint member and the damage degradation value D within the cohesive zone.

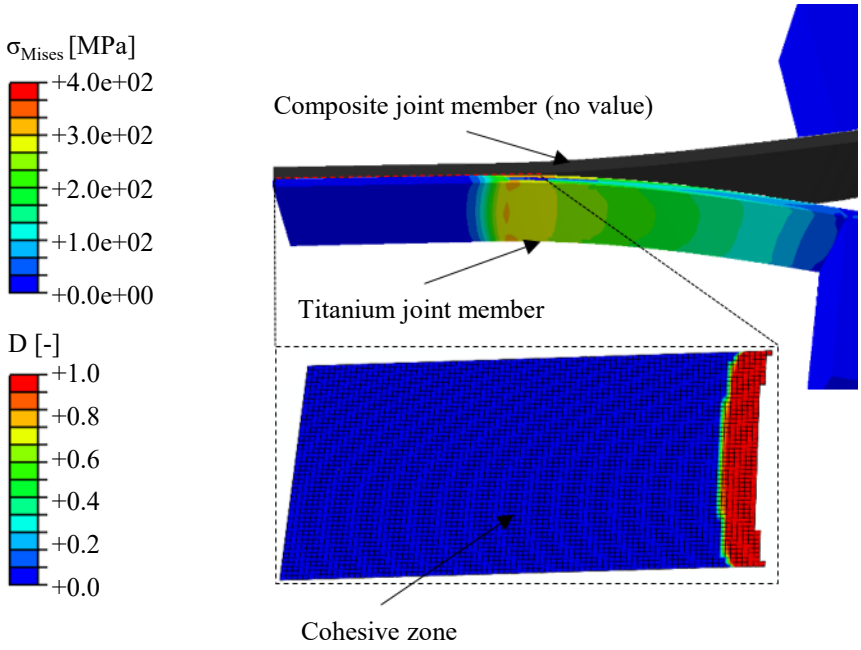

Figure 5-17: Mode I fracture toughness, CFRP/titanium DCB specimen - plasticity FEM

FE-results show that the von Mises stress σ_{Mises} never exceeds 400MPa. Taking into account the yield point of Ti6Al4V (~900MPa), it can be reasonably assumed that plastic deformation of the titanium beam is negligible during testing. The visualization of damage degradation value D indicates that several rows of cohesive elements degrade simultaneously. This is an important demand for cohesive zone damage degradation [105]. Analyzing the mechanically tested specimens, it was observed that the titanium beam, which was separated completely from the composite beam, did not show permanent deformation.

5.2.4 Mode II testing

Mode II fracture toughness testing was performed for the same material combinations as described in Chapter 5.2.3. However, only one configuration of the NCF/PR520 material combination was tested. The configuration "G_{IIc_2}" has a layup and stitching pattern identical to configuration "G_{Ic_2}". The Mode II fracture toughness test is based on a three-point bending setup, see Chapter 3.2.4.4. A minimum of four specimens were tested for each configuration.

The averaged G_{IIc}-values are shown in Figure 5-18.

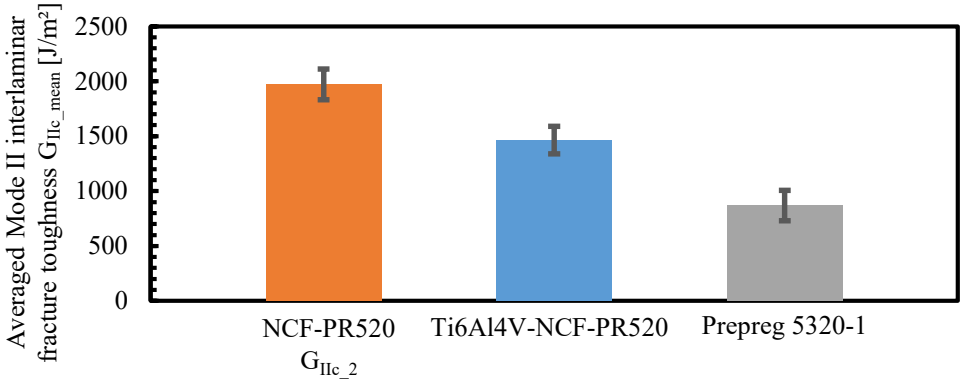

Figure 5-18: Mode II fracture toughness, comparison of G_{IIc}-values for different material combinations

High shear stresses τ_{xz} cause the delamination within the mid-plane of the End Notched Flexural (ENF)-specimen, where the release foil for crack initiation is located. As opposed to Mode I fracture toughness testing with DLS-specimens both joint members, located below and on top of the release foil, do not move apart from each other. Therefore, fiber bridging may occur, but is significantly less effective in comparison to Mode I fracture toughness testing.

5.2.5 Neat resin testing

In order to obtain extensive material input parameters for the FE-analysis of test series 4, neat resin testing had to be performed. The resin system used for these tests (Cycom PR520 RTM-resin) is similar, but not identical to the Cycom 5320-1 Prepreg resin system. Both systems are characterized as toughened epoxy systems. The wet T_g (161°C for PR520; 163°C for 5320-1) and cured density (1.25g/m³ for PR520; 1.31g/m³ for 5320-1) is comparable. Furthermore, both systems are cured at an almost identical temperature (180±5°C for PR520; 177±5°C for 5320-1) for two hours. Only PR520 RTM-resin was tested and these results are used as an input for test series 4. Figure 5-19 illustrates test results for tension and compression testing in comparison to FE-results.

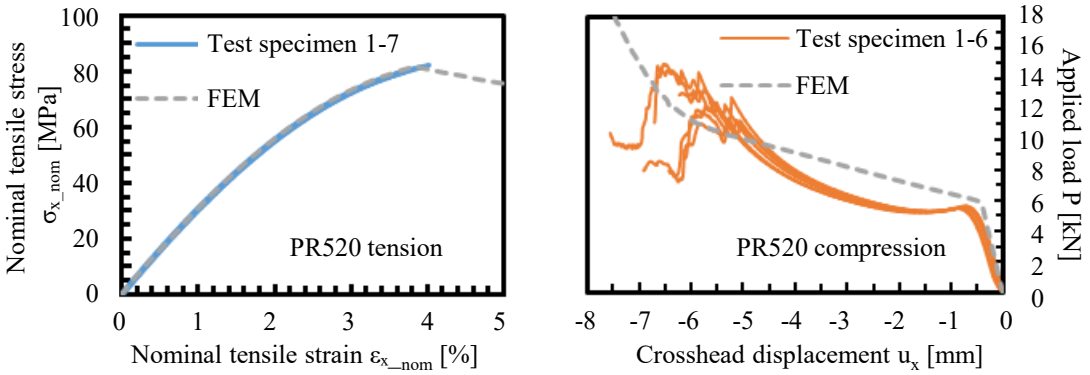

Figure 5-19: Neat resin tension and compression testing, stress-strain and load-displacement behavior

Dog-bone shaped specimens were tested in a tensile stress state. By using the Aramis DIC-system, tensile and transverse strain can be measured. Two different types of specimens were tested for compression testing, see Chapter 3.2.4.5. While specimens of 50mm length were used for the evaluation of elastic properties, measurement of compressive strength was done by loading the specimens of 10mm length until final failure. However, buckling led to a de-bonding of the strain gauges from the specimen's surface after the compressive yield point was reached.

Therefore, compressive stress-strain behavior could only be captured within the linear elastic state. A FE-analysis was set up in order to validate the material input parameters in a tensile and compressive stress state. The material model covers plasticity but no damage. Similar behavior between testing and FEA could be found for tension testing. For compressive testing, the prediction of stiffness within the linear elastic stress state is accurate. However, compressive plasticity is not represented accurately with the plasticity model chosen. The importance of an accurate material model for neat resin under compression can only be evaluated after analyzing the entire pinned joint, see Chapter 5.6.2. An explanation of the material model can be found in Chapter 3.4. All input parameters are listed in the Appendix.

5.3 Stresses within the adhesive layer

This chapter provides results of an analytical approach for the calculation of stresses within the double lap joint's adhesive layer of joint design 1. Besides the stiffness imbalance between the joint members, thermal mismatch and resulting residual stresses affect the load carrying capability of the joint.

5.3.1 Stiffness relation for joint design 1

When considering the testing results for the metallic and CFRP joint member, the stiffness relation for the pure adhesive DLS-joint of joint design 1 in an elastic stress state

can finally be computed. In the case of a metallic joint member made of steel 1.4301 it calculates to:

$$\frac{E_m t_m}{2E_{co}t_{co}} = \frac{E_m t_m}{(E_{co\_0-90} + E_{co\_+45-45})t_{co}} = \frac{225.0GPa * 3mm}{(79.0GPa + 14.6GPa) * 4mm} = 1.803 \qquad (5\text{-}1)$$

and in the case of a titanium joint member to:

$$\frac{E_m t_m}{2E_{co}t_{co}} = \frac{E_m t_m}{(E_{co\_0-90} + E_{co\_+45-45})t_{co}} = \frac{124.5GPa * 3mm}{(79.0GPa + 14.6GPa) * 4mm} = 0.998 \qquad (5\text{-}2)$$

where E_m and E_{co} denote the elastic tensile modulus for the metallic and composite joint member, respectively. The thickness of the metallic insert and one single composite lap are described by t_m and t_{co}. The indices $_{0\text{-}90}$ and $_{+45\text{-}45}$ label the fiber direction. As described in Chapter 2.1, stiffness balanced joints are preferred over unbalanced joints in terms of shear stress distribution along the bondline.

In the case of test series 1, the steel joint member is 1.8 times stiffer than the quasi-isotropic composite laminate. However, tensile stiffness of steel 1.4301 rapidly decreases once plastic deformation occurs. Therefore, the co-bonded baseline joint of test series 1 failed due to a stiffness mismatch at a joint stress slightly above the yield strength of the steel insert.

For test series 3, titanium and composite joint members are characterized by an identical tensile stiffness. In addition, Ti6Al4V shows a linear elastic behavior until a tensile stress of around 900MPa. It can therefore be stated that the chosen joint design is suitable for co-bonded pure adhesive DLS-joints of test series 3, as long as the joint strength stays below 900MPa.

5.3.2 Thermal mismatch for joint design 1

According to formulae (2-1) to (2-11), presented in Chapter 2.1, residual stresses due to thermal mismatch of the composite and metallic joint members can be estimated. Material parameter, used for this estimation are listed in Table 5-2.

Table 5-2: Material input parameter for estimation of thermal residual stresses

Material combination	E_{jm_1} [GPa]	t_{jm_1} [mm]	E_{jm_2} (=E_{jm_3}) [GPa]	t_{jm_2} (=t_{jm_3}) [mm]	α_{jm_1} [10^{-6}/°C]	α_{jm_2} (=α_{jm_3}) [10^{-6}/°C]	G (= G')[1] [MPa]	l [mm]	T_{g_onset}[2] [°C]
CFRP – Steel 1.4301	225.0	3	46.8	4	17.2	1.55	1268.1	19.75	150
CFRP – Ti6Al4V	124.46	3	46.8	4	8.6	1.55	1268.1	19.75	161

In the case of symmetric double lap joints, the following relation between shear stresses τ and τ' is valid:

$$\tau = -\tau' \tag{5-3}$$

According to formulae (2-1) and (2-2) in Chapter 2.1, the distribution of residual shear stress due to thermal mismatch τ along the bondline in x-direction can be calculated for several bondline thicknesses. Figure 5-20 shows the results for the material pairings CFRP/Ti6Al4V and CFRP/Steel 1.4301:

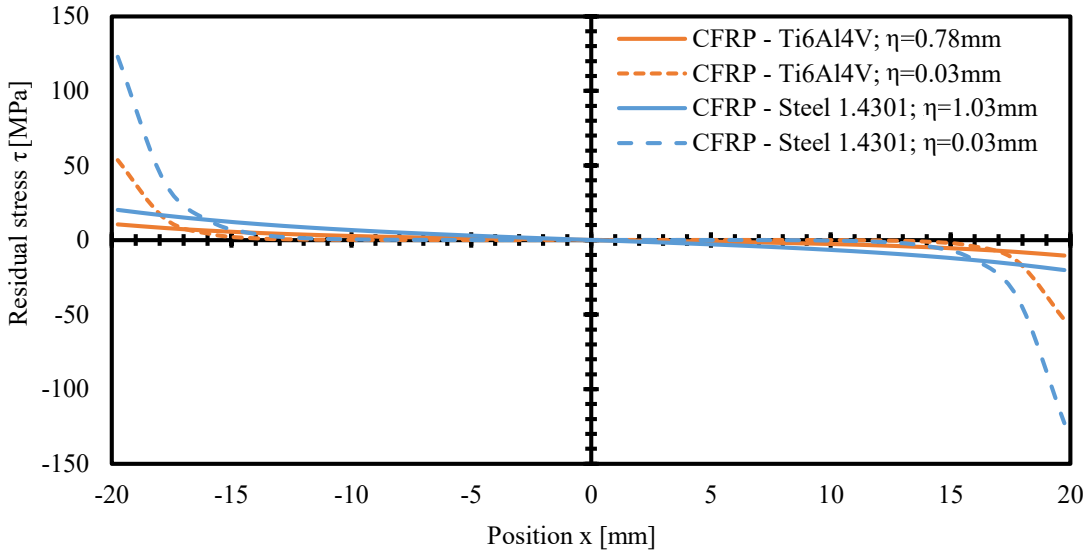

Figure 5-20: Residual stresses due to thermal mismatch for different η
Along the bondline in tensile direction for several values of bondline thickness η (no external loads, service temperature $T_{service}$=20°C)

Three main findings emerge from these results. First, stress peaks generally occur at the edges of the bondline. Second, due to steel's greater coefficient of thermal expansion in comparison to titanium, stresses are greater for the material combination CFRP/Steel

[1] Shear modulus considered to be similar for PR520 and ST15 resin

[2] T_{g_onset} differs for ST15 resin [113] (CFRP – Steel 1.4301) and PR520 resin [20] (CFRP – Ti6Al4V)

1.4301 than for CFRP/Ti6Al4V. Third, stress peaks grow as the adhesive layer's (or bondline's) thickness η decreases. The distribution of residual stresses is plotted exemplarily for three different adhesive layer's thicknesses. The value η=30µm represents the averaged distance between the metallic joint member's surface and outer surface of the CFRP joint member's +45°-layer, measured by microscopy inspection. The distance between the steel joint member's surface and outer surface of the CFRP joint member's 0°-layer (7^{th} ply) equals η=1.03mm. In the case of CFRP/Ti6Al4 joints, the distance between the titanium joint member's surface and outer surface of the CFRP joint member's 0°-layer (4^{th} ply) equals η=0.78mm. A smeared approach is used which considers the in-plane stiffness to be identical for all CFRP plies, regardless of their fiber direction. In fact, ±45°-layers and 90°-layers are characterized by a lower stiffness in x-direction, in comparison to the smeared approach's stiffness (46.8GPa). The stiffness reduction of one joint member decreases the peak stresses. The graphs in Figure 5-20 represent the maximum (η=30µm) and minimum (η=1.03mm; η=0.78mm) peak stresses for both material combinations. Figure 5-21 displays the distribution of residual thermal stress due to thermal mismatch for CFRP/Ti6Al4V double lap joints, three different service temperatures $T_{service}$ and an adhesive layer's thickness of η=30µm.

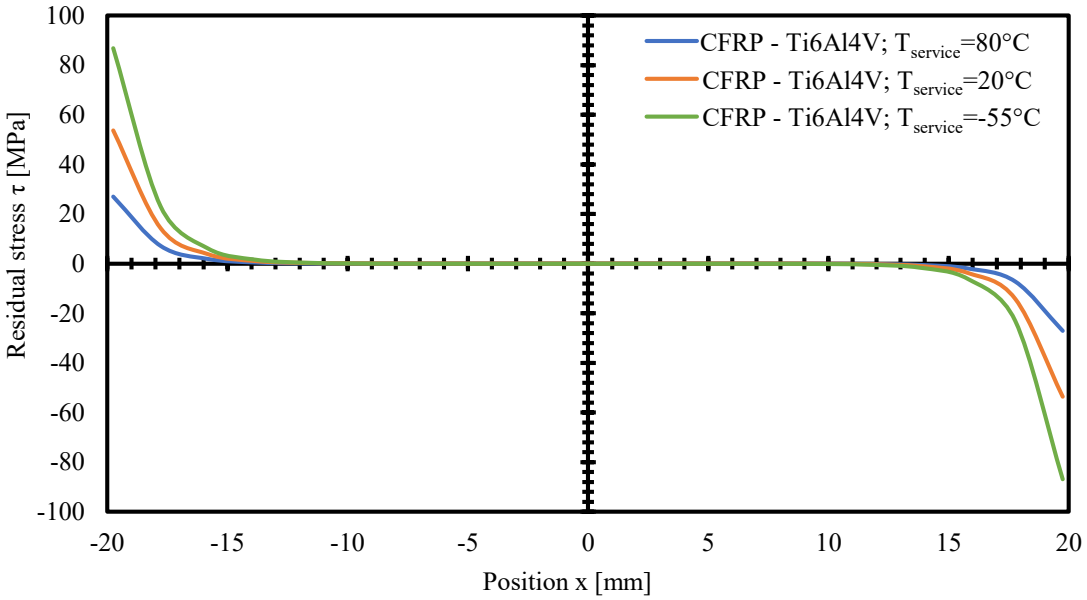

Figure 5-21: Residual stresses due to thermal mismatch for different $T_{service}$
Along the bondline in tensile direction for different service temperatures $T_{service}$ (no external loads, adhesive bondline thickness η=30µm)

Smaller values for $T_{service}$ (= greater values for ΔT) result in greater peak stresses. The maximum peak stress for the CFRP/Ti6Al4V joint can be calculated to τ=86.9MPa. These values are comparable to those of i.e. CFRP/Titanium hybrid laminates [39]. However, the taper of 30° at the runouts of the CFRP joint members, see Figure 3-4,

reduces peak stresses in this area. These runouts are not considered in the analysis presented above. In addition, plasticity and creep within the adhesive layer, which also lead to reduction of peak stresses, are neglected.

5.4 Test series 3: CFRP/titanium joint design 1

Test series 3 was performed to optimize the joint tensile strength of the pinned composite/metal joint. In order to strengthen the metallic joint member, Ti6Al4V was used instead of steel 1.4301. Chapter 5.4.1 presents the testing results, whereas Chapter 5.4.2 further analyzes the interaction between the joint members and pins with the help of FE-analysis.

5.4.1 Tensile testing

This chapter describes testing results for hybrid co-bonded reference and pinned CFRP/titanium joints as well as the corresponding failure modes. Whereas Chapter 5.4.1.1 compares a joint with a pinned 6x4 setup to the co-bonded reference joint, the impact of the pin pattern variation on the joint's tensile strength is analyzed in Chapter 5.4.1.3. Chapter 5.4.1.2 explains the damage progression for hybrid CFRP/titanium DLS-specimens by using results from DIC-measurements.

5.4.1.1 Co-bonded reference vs. pinned joint

Co-bonded reference joints without pins are intended to serve as a baseline for the comparison to pinned joints. Prior to co-bonding with the help of the RTM-process, described in Chapter 4.3, the titanium surface was acid etched and treated with a primer to enhance the bond strength between the CFRP and titanium joint member. The analysis of the failure mode shows that delamination occurred between the composite layers but not in the interface between titanium and CFRP joint member, see Figure 5-22.

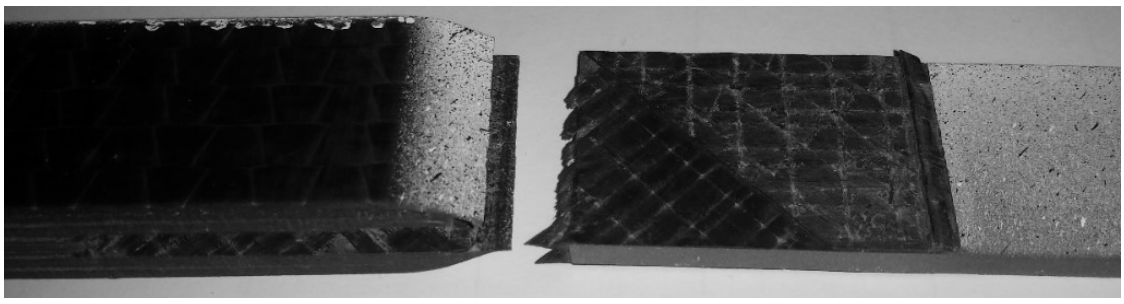

Figure 5-22: Failure mode for a tensile tested co-bonded reference joint

These observations emphasize the effectiveness of proper surface treatment. Furthermore, it can be stated that the mismatch in CTE between the titanium and CFRP joint member is not critical as the joint did not fail due to adhesive or cohesive failure, rather inter-ply delamination. A pinned joint with a 6x4 pin pattern and spiky spring steel pins

with a pin diameter of 1.5mm is used as the basic configuration for pinned CFRP/titanium joints of joint design 1. This configuration was found by FEA-simulation to result in the greatest joint strength. A deflection of the composite laps towards thickness direction is responsible for final failure, see Figure 5-23.

Pinned 6x4

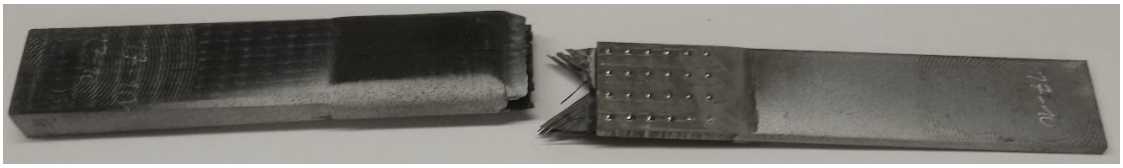

Pinned 6x4 circ. layers

Figure 5-23: Failure mode for tensile tested pinned CFRP/titanium joints with a 6x4 pin pattern

In order to prevent this failure mode, circumferential unidirectional prepreg layers were added to the joint and cured in a second processing step in an oven under vacuum. Mechanical testing of these joints show that the failure mode can be changed. Furthermore, the application of circumferential prepreg layers has an impact on the joint tensile strength, see Figure 5-24.

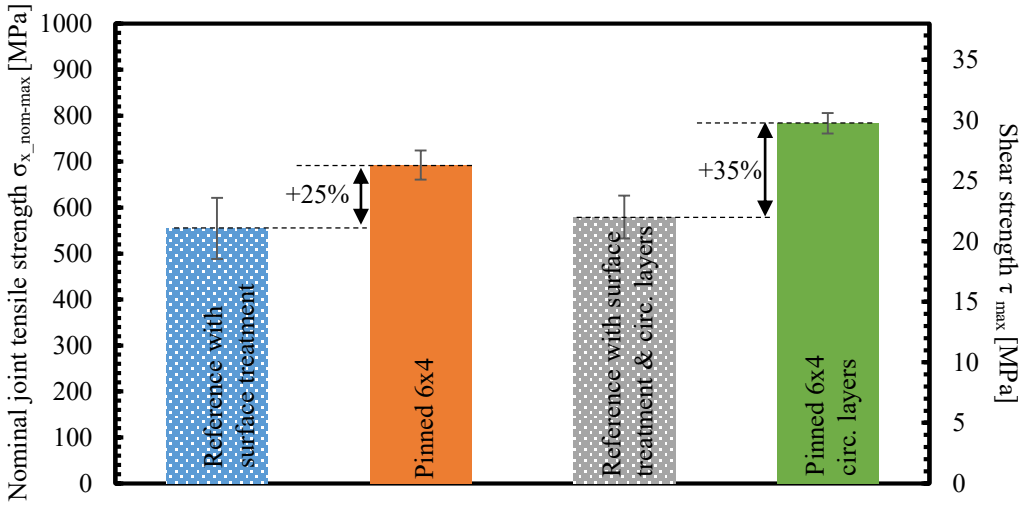

Figure 5-24: Comparison of joint tensile strength for CFRP/titanium joints, reference joint vs. pinned joint with a 6x4 pin pattern

Whereas a negligible improvement can be observed for the reference joints, a significant increase of joint tensile strength is present for pinned joints. Circumferential layers can only be applied to joints with a limited width and no lateral restrictions.

5.4.1.2 Progression of damage

Co-bonded hybrid pinned composite/metal joints of joint design 1 offer two basic mechanisms for load transfer between the metallic and composite joint member, adhesive bonding and form closure through pins. Due to the different nature of both joining mechanisms, a typical two-stepped failure progression can be observed for all specimens of test series 1 and 3. Figure 5-25 exemplarily illustrates the local displacement value u_x for a pinned CFRP/titanium joint of joint design 1.

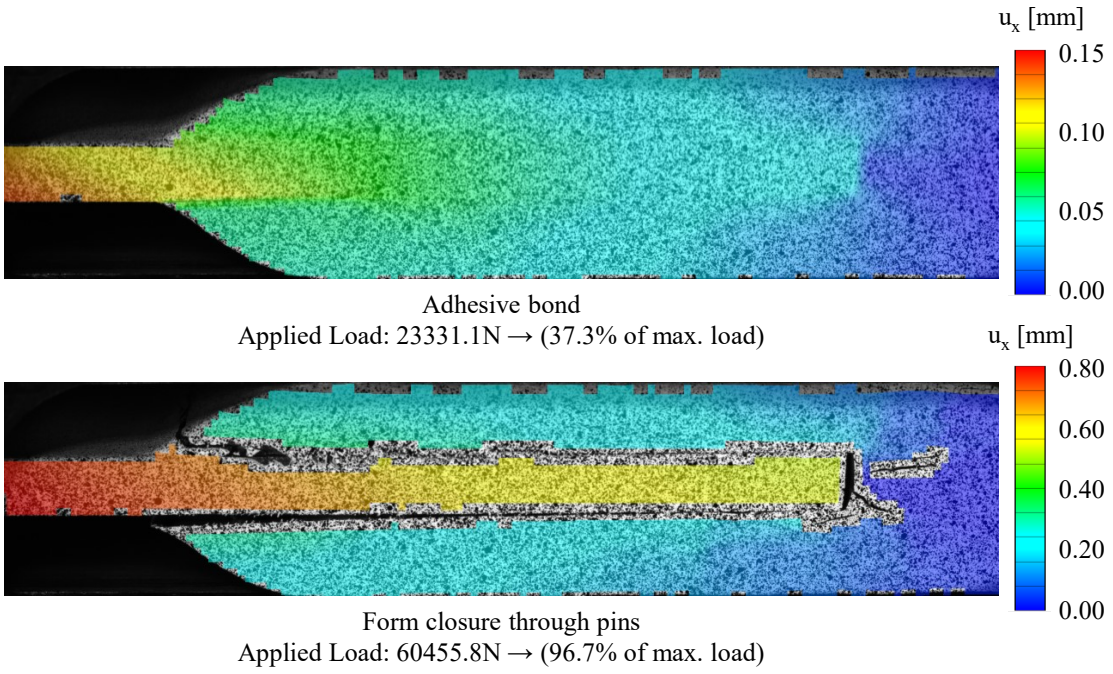

Figure 5-25: Progression of damage for a pinned CFRP/titanium joint with a 6x4 pin pattern, DIC- measurement

At a comparably lower load level of 37% of the maximum applied load, the adhesive bond between the titanium and CFRP joint member is still intact. The DIC measurements also indicate a high stiffness of the adhesive bond as the distribution of u_x shows a similar deformation for CFRP and titanium joint member. An increase of the applied tensile load leads to a crack initiation located at the front edge of the CFRP joint member (CFRP taper) and further to delamination within the interface between CFRP and titanium joint member.

This is referred to as the first failure. Afterwards, the pins are exclusively responsible for load transfer. Local displacement values u_x for the titanium joint member are significantly higher in comparison to the CFRP joint member. This kind of damage progression meets the requirements of a fail-safe design, as the ultimate load is above the load at initial damage.

5.4.1.3 Variation of pin pattern

In order to reduce deflection of the composite laps towards thickness direction but still enable the observation of the lateral surface by the DIC-system, a clamping device was designed, see Figure 5-26.

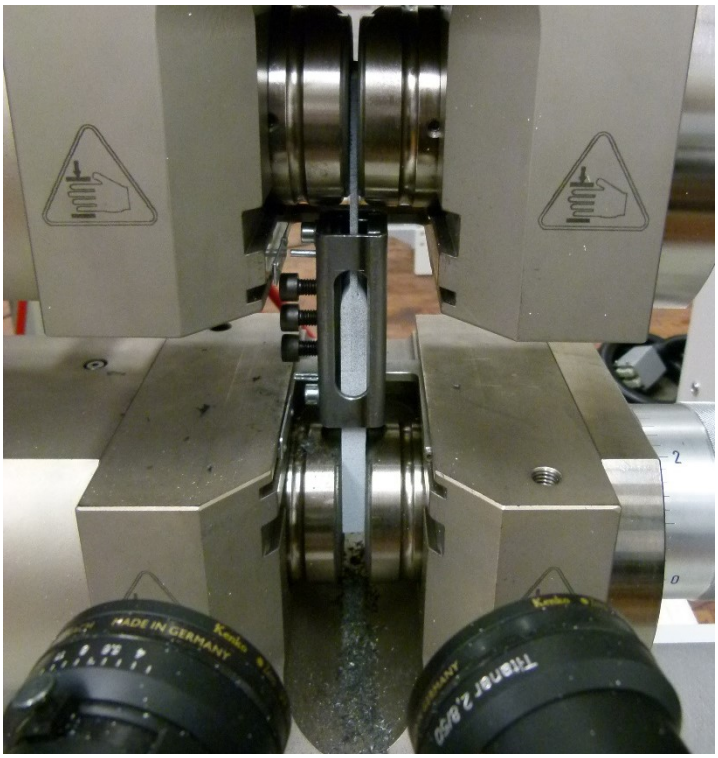

Figure 5-26: Testing setup with clamp for CFRP/titanium joints of joint design 1

Clamping the specimens is necessary in order to prevent the deflection of composite layers towards z-direction. Each of the three screws were tightened with a torque of 0.5Nm prior to testing. This torque was adjusted in a way that the frictional force between the specimen and the clamping device compensated for the gravity of the clamping device. Therefore, the clamping device could be kept in position while minimum force was introduced into the specimen by the screws. However, it has to be noted that the clamping is able to reduce, but cannot completely inhibit the expansion of the specimen in thickness direction.

As opposed to the reference joints described, none of the titanium joint members of the pinned configurations were acid etched nor treated with a primer. Hence, in order to estimate the load carrying capability of the adhesive bond between the titanium and CFRP joint member, reference joints without surface treatment were manufactured and tensile tested. In addition, several configurations with different pin patterns were investigated, see Figure 5-27.

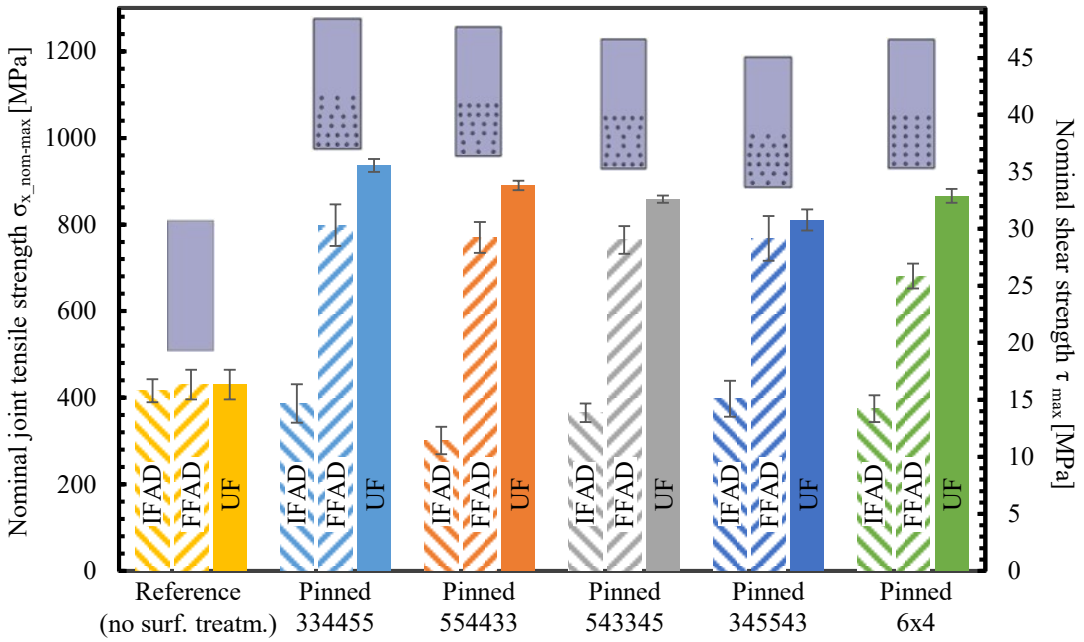

Figure 5-27: Comparison of joint strength for CFRP/titanium joints, co-bonded reference vs. pinned joints with various pin patterns
Initial Failure of ADhesive bond (IFAD); Final Failure of ADhesive bond (FFAD); Ultimate joint Failure (UF)

All pinned configurations are characterized by the same total number of pins. Load between the titanium and composite joint member is transferred via an adhesive bond as well as a form closure mechanism provided by pins, as described in Chapter 5.4.1.2. In order to analyze the adhesive bond for the pinned configurations, the load at failure of the adhesive bond is plotted in Figure 5-27. A distinction is made between the Initial Failure of the ADhesive bond (IFAD) and the Final Failure of the ADhesive bond (FFAD).

IFAD describes the load state when crack initiation occurs between the titanium and composite joint member. It was found that inserting pins in the joint leads to a lower load at IFAD in comparison to the co-bonded reference. The configurations with five pins in the first row (pinned 554433 and pinned 543345) are characterized by the lowest load at IFAD, whereas the configuration with three pins in the first row almost reach the reference's IFAD-load. For pinned specimens, failure of the adhesive bond is not characterized by sudden failure, but by gradual crack propagation between the titanium and composite joint members.

FFAD describes the load state right before final failure of the adhesive bond. At the FFAD-state, the crack tip reaches the metallic joint member's edge, which is embedded in between both composite laps. After FFAD, pins are exclusively responsible for load transfer. For all pinned configurations, the applied load at FFAD is significantly higher, when compared to the co-bonded reference joint. This observation therefore raises the question whether pins are responsible for decelerating crack propagation between the

metallic and composite joint member. This question is discussed further in Chapter 5.4.2.

It was also found that the specific pin pattern does not have a major impact on the joint tensile strength at ultimate load (UF). However, all of the pinned configurations reach a joint tensile strength around two times higher than the reference joints. Furthermore, the variation coefficient for UF is significantly lower for pinned configurations in comparison to the co-bonded reference. Similar observations were also made for the tests described in Chapter 5.4.1.1. The failure modes at ultimate load (UF) for all configurations described above, are illustrated in Figure 5-28.

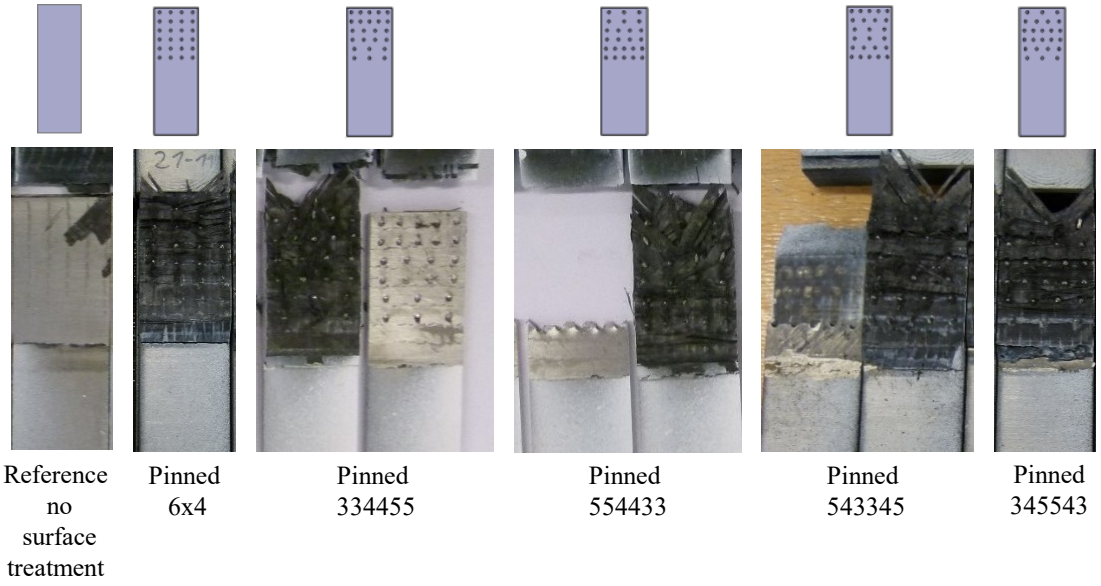

Figure 5-28: Failure modes for CFRP/titanium joints, co-bonded reference and joints with various pin patterns

Adhesive failure at ultimate load between the titanium and CFRP joint member can be observed for the reference joints with no surface treatment. Interlaminar delamination within the composite joint member is a possible failure mode for all pinned configurations. This type of delamination exclusively occurs between a 90°- and 0°-layer located close to the top of the pins. An explanation for this failure mode is given in Chapter 5.4.2.2. Pin failure can be observed for the "334455" pinned configuration. Because of the reduced cross section through hole drilling (inserted pinning), net section failure within the titanium joint member is responsible for final failure for some of the pinned joints with a "554433" and "543345" pattern. Pin failure und titanium net section failure is further described in Chapter 5.4.2.5.

5.4.2 Simulation results

This chapter presents the FE-results for test series 3. In order to validate the FEA, a direct comparison is made between FE- and testing results by means of stress-strain

curves for all configurations tested. In addition, the FEA aims to further analyze the stress state within and the interaction between the composite and metallic joint member and pins.

5.4.2.1 Co-bonded reference

To validate the input parameters for the cohesive elements in the interface between composite and titanium joint member, a FE-model of the reference CFRP/titanium joint of joint design 1 was set up. The values for Mode I and Mode II fracture toughness, determined within test series 2, see Chapter 5.2.3.2 and Chapter 5.2.4, are used as material input parameters for the cohesive zone between CFRP and titanium joint member. The critical stresses for damage initiation in normal and transversal direction are estimated with the help of parametric studies. The chosen values can be found in the Appendix, see Table A-1. Figure 5-29 displays the stress-strain curves for FE- and mechanical testing, as wells as a visualization of the damage degradation value *D* for all cohesive zones.

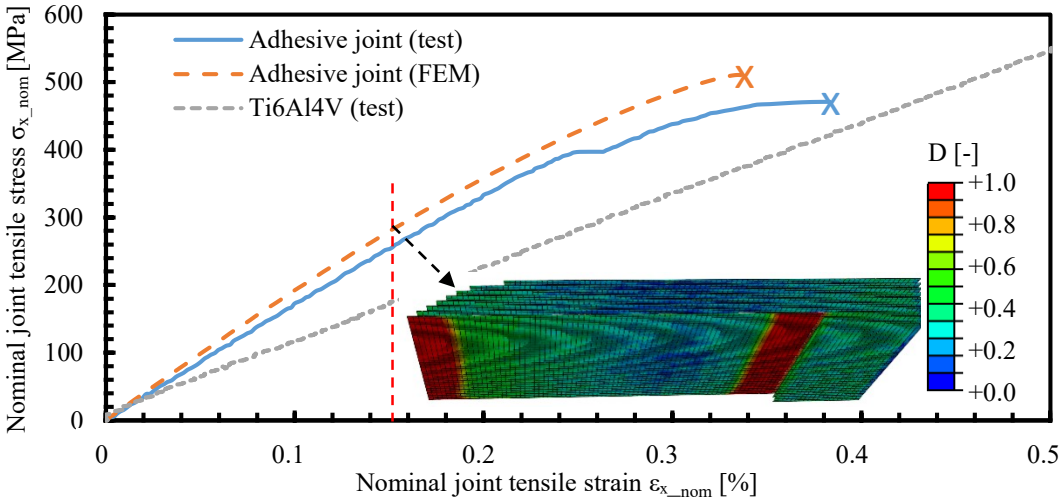

Figure 5-29: Stress-strain behavior, testing vs. FEM for a co-bonded CFRP/titanium reference joint

Maximum values for *D* can be observed at the front and back end of the adhesive bond. Crack initiation starts almost simultaneously at both ends followed by a crack propagation towards the center of the joining area.

As stated in Chapter 5.2.3.1, the correct choice for the interlaminar Mode I fracture toughness value within the composite joint member is critical due to the alternating fiber angles and stitching patterns. Two mean G_{Ic}-values for the NCF/PR520 configuration were measured within test series 2. The lower G_{Ic}-value (417J/m²) is here denoted as "G_{Ic_1}" and the higher G_{Ic}-value as "G_{Ic_2}" (952J/m²). As delamination occurs between titanium and CFRP joint member and not in between the CFRP layers, both G_{Ic}-values, G_{Ic_1} and G_{Ic_2} lead to comparable results.

5.4.2.2 Choice of G_{Ic}-value

However, the choice of the G_{Ic}-value for inter-ply behavior between the different NCF-layers influences the behavior of pinned joints. Therefore, FEA of the entire pinned CFRP/titanium joint with a 6x4 pin pattern was conducted for both G_{Ic}-values and compared to testing results, see Figure 5-30.

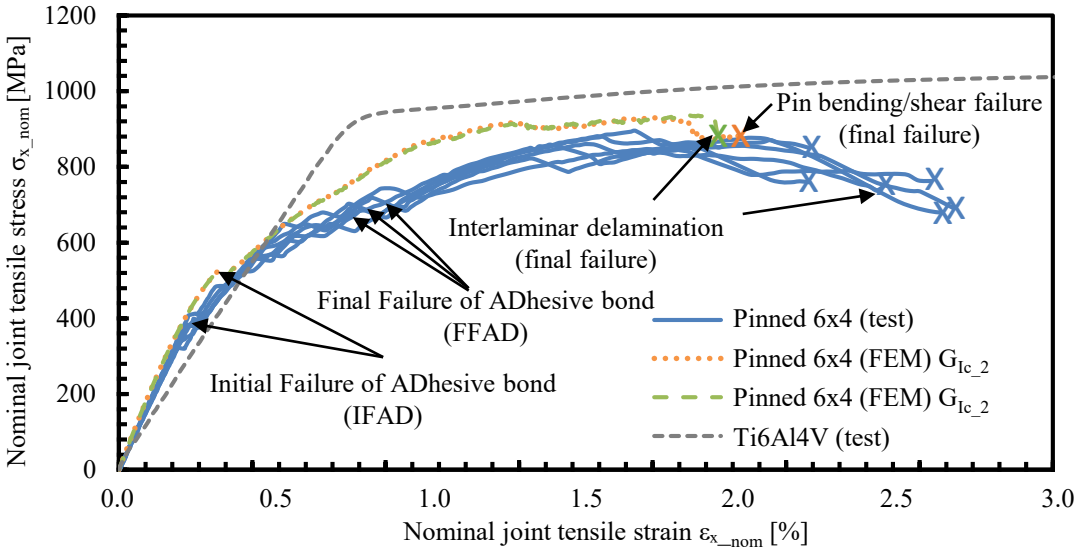

Figure 5-30: Stress-strain behavior, testing vs. FEM for a pinned CFRP/titanium joint with a 6x4 pin pattern

First failure is identified by a small load drop within the stress-strain curve. Whereas the FE-model is based on a symmetry towards the mid-*x*-*y*-plane, real test specimens are not completely symmetrical. Therefore, failure of the tested adhesive bond does not occur simultaneously at both interfaces between CFRP and titanium joint member. After first failure of the adhesive bond (IFAD), crack propagation between the metallic and composite joint members occurs. The crack runs from the adhesive area's left end (taper of composite joint member) towards the metallic joint member's right edge, which is embedded in between both composite laps. FFAD describes the state of ultimate adhesive bond failure. At load states above FFAD, pins exclusively take over the load until final failure of the joint at ultimate load (UF).

The analysis of the FE-results indicates that by choosing the lower G_{Ic}-value "G_{Ic_1}", interlaminar delamination within the CFRP joint member is responsible for final failure, similar to all tested specimens of configuration "pinned 6x4". Therefore, the G_{Ic}-value "G_{Ic_1}" is used for successive FE analysis. Figure 5-31 illustrates the cohesive zone affected by this interlaminar delamination for both FE-models with input parameters "G_{Ic_1}" and "G_{Ic_2}" shortly after final failure.

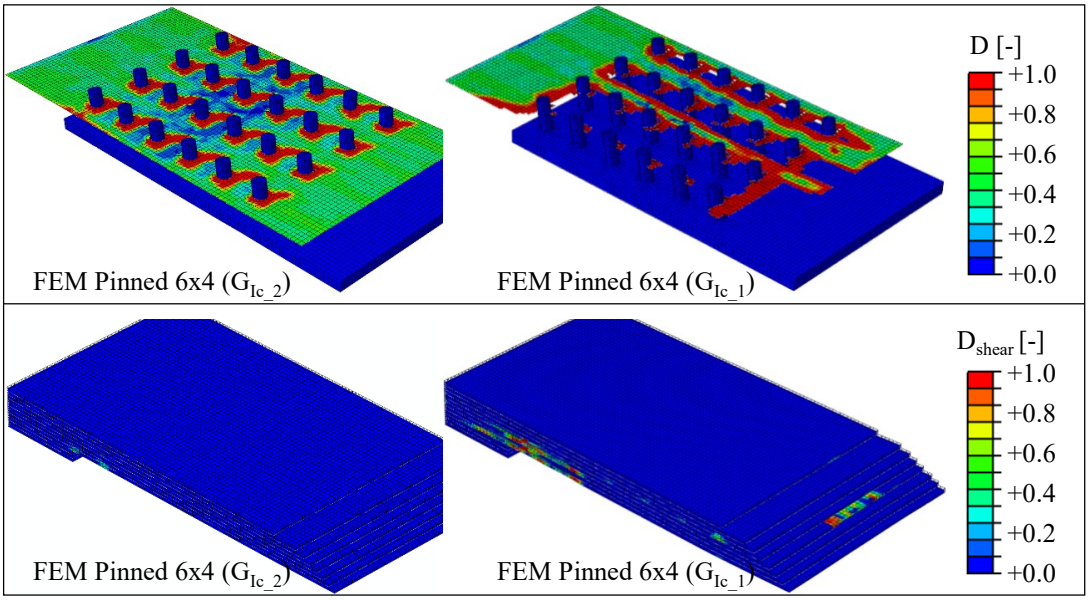

Figure 5-31: Choice of G_{Ic}-value and its effect on interlaminar delamination failure, simulative approach

After delamination occurs, the CFRP layers located outside the delamination plane are no longer connected to the inner layers, the pins and titanium joint member. As the inner layers are not able to withstand the high tensile load, net section failure within these layers occurs immediately after delamination. This net section failure behind the last pin row is visualized in Figure 5-31 on the bottom right. D_{shear} describes the damage degradation value for shear failure. These observations indicate that pinning, in comparison to adhesive joints, is an effective method to transfer load into the outer composite layers of the DLS-joint.

5.4.2.3 Pin quantity

Besides the adjustment of pins, the total amount of pins also has an impact on the stiffness and especially on the joint's tensile strength. In order to determine the number of pins that lead to a maximum joint tensile strength, several rectangular pin patterns are further investigated. The spacings s_x and s_y between the pins are defined, according to the following formulae:

$$s_x = 30.5[mm]/n_x \tag{5-4}$$

$$s_y = 25.4[mm]/n_y \tag{5-5}$$

Where s_x and s_y are the spacings in x (length) and y (width) direction, respectively. The values n_x and n_y describe the number of pins in x and y direction. Edge spacings were chosen to be 50% of s_x and s_y.

Whereas mechanical testing was performed for specimens of configurations "5x4" and "6x4", joints of configuration "4x3", "5x4", "6x4" and "6x5" were numerically examined with the help of FEA, see Figure 5-32.

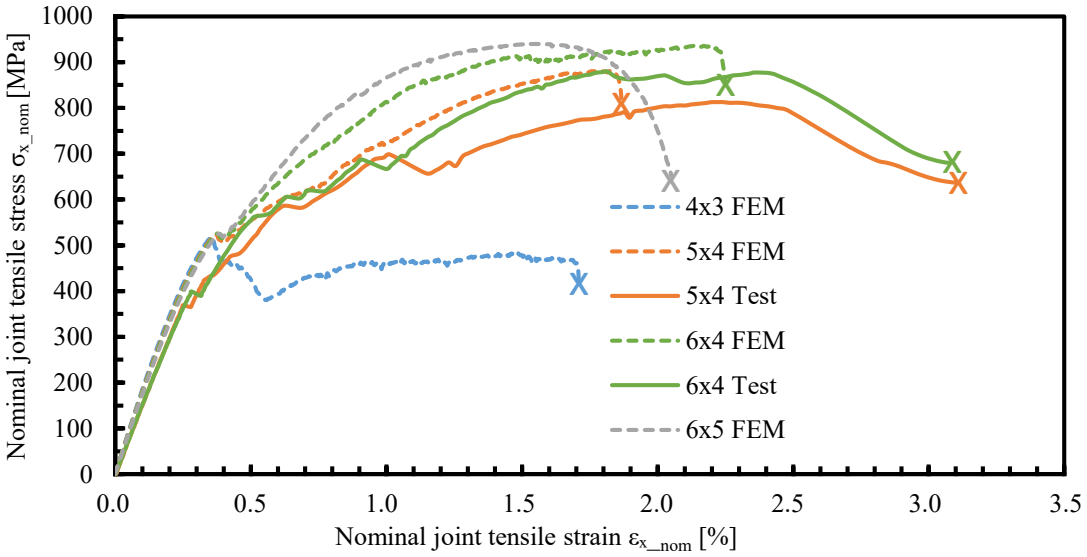

Figure 5-32: Influence of pin quantity on joint performance for CFRP/titanium joint design 1

The FE-results show that joints with a 4x3 pin pattern fail at a low load level due to pin shear failure. FEA and mechanical tests confirm that pin failure is also the reason for failure of the joints with a 5x4 pin pattern. Joints with a 6x4 pin pattern fail as a result of interlaminar delamination. Titanium net section failure is identified by FEA to be responsible for final failure of the joint with a 6x5 pin pattern. Mechanical testing also shows that joints with 5 pins in the first pin row are likely to fail by titanium net section failure, see Chapter 5.4.1.3.

These investigations indicate that, in terms of maximum joint tensile strength, the amount of 24 pins on each side of the titanium joint member leads to the maximum joint strength. It has to be noted that the effect of fiber undulation around the pins and a locally increased fiber volume fraction is not considered in the FE-model for joint design 1. It can be assumed that a high pin density and pin diameter results in a weakening of the composite joint member. Furthermore, pin insertion becomes more difficult with an increasing pin diameter and pin density.

5.4.2.4 Pin pattern

The influence of the pin pattern on the joint tensile strength was already analyzed in Chapter 5.4.1.3. This chapter now presents stress-strain curves of the FE-results and representative test specimens, see Figure 5-33.

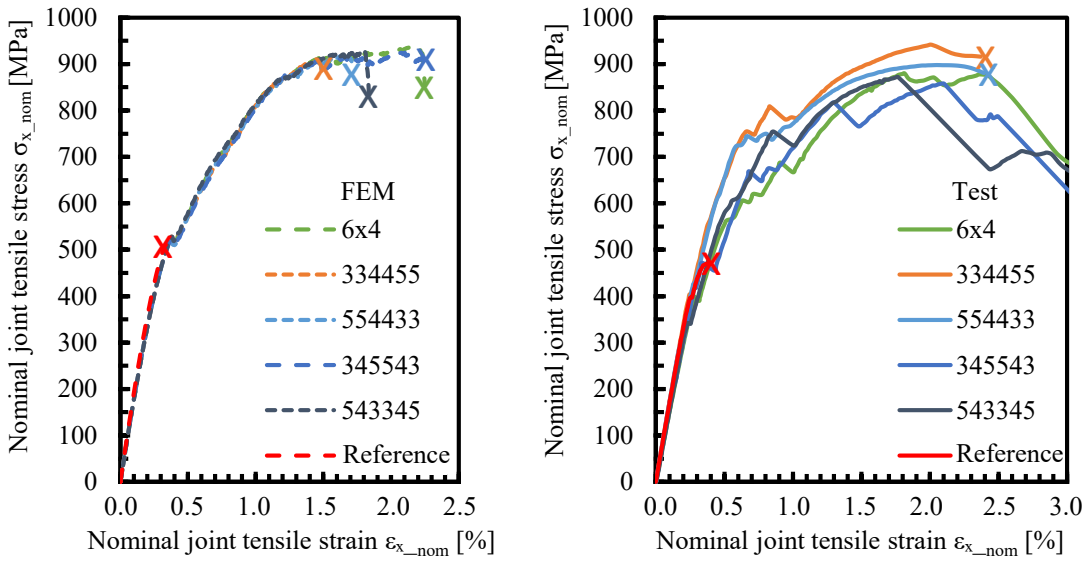

Figure 5-33: Influence of pin pattern on joint performance for CFRP/titanium joint design 1

The pin pattern has a negligible influence on the joint tensile stiffness in the linear elastic region as demonstrated by FE- and testing results. Furthermore, FE-results show an almost identical stress-strain behavior after first failure. Only the strain at final failure is dependent on the specific pin pattern. A stiffness variation after first failure can be observed for the different configurations. The specific modes for final failure are listed in Table 5-3.

Table 5-3: Reasons for final failure of different pin patterns

Configuration	FEA	Testing
6x4	Interlaminar delamination	Interlaminar delamination
334455	Interlaminar delamination	Interlaminar delamination & Pin failure
554433	Interlaminar delamination	Interlaminar delamination & Titanium net section
345543	Pin failure	Interlaminar delamination
543345	Interlaminar delamination	Interlaminar delamination & Titanium net section

With an exception of configuration "345543", interlaminar delamination is indicated by the FEA to be responsible for final failure. The following chapter analyzes the other two failure modes, titanium net section and pin failure in detail.

5.4.2.5 Analysis of failure modes - titanium net section and pin shear/bending

Hole drilling reduces the cross-sectional area of the titanium joint member and furthermore creates stress peaks around the holes. Because of ductile material behavior of Ti6Al4V, stress peaks decrease once plasticity occurs at high stresses, see Chapter 2.2. Four tensile tested specimens failed due to titanium net section. The average applied tensile load was 67107.5N (±1048.8N). Hence, the mean nominal joint tensile strength for these specimens can be calculated as follows:

$$\bar{\sigma}_{x\_nom} = \frac{\sum_{i=1}^{4} \frac{F_{x_i}}{w_{m_i} * t_{m_i}}}{4} = 877.75 N/mm^2 \tag{5-6}$$

The joint tensile strength is referenced to the width w_m and thickness t_m of the titanium joint in front of the joining area and therefore does not account for the reduced cross section within the first pin row - where net section failure occurs. The mean stress within the remaining cross section can be calculated by decreasing the width w_m by 5 times the diameter of the hole:

$$\bar{\sigma}_{x\_nom\_red} = \frac{\sum_{i=1}^{4} \frac{F_{x_i}}{(w_{m_i} - 5 * d) * t_{m_i}}}{4} = 1243.8 N/mm^2 \tag{5-7}$$

This consideration does not account for stress peaks around the holes, which exist in reality and result in a weakening of the metallic insert towards tensile direction, see Chapter 2.2. However, the tensile strength of Ti6Al4V was only measured to 1054.4N/mm², see Chapter 5.2.1. FEA helps to understand the deviation between the mean tensile stress within the remaining cross section at ultimate load $\bar{\sigma}_{x\_nom\_red}$ and the tensile strength of Ti6Al4V measured by tensile testing of titanium dog-bone shaped specimens σ_{nom_max}. An explanation for this phenomenon is presented in Figure 5-34.

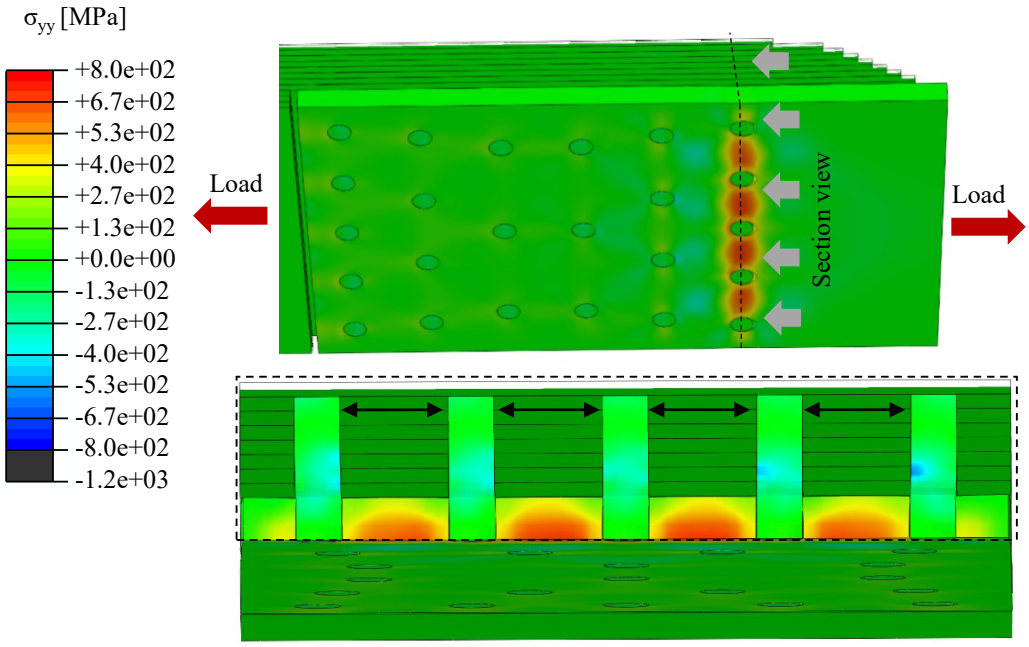

Figure 5-34: Analysis of the titanium joint member's net section failure

This figure illustrates the stress value σ_{yy} in the direction of the specimen's width prior to final failure. Plastic deformation takes place within the titanium joint member. The 90°-layers are primarily responsible for a high transverse stiffness, therefore low transverse contraction of the composite joint member. As both joint members are connected by pins, necking cannot occur over the entire width of the specimen. Consequently, a distinct three-dimensional stress state is created within the first pin row in between the pin, partially compensating the weakening of the titanium joint member through hole drilling.

Besides net section failure of the titanium joint member and interlaminar delamination within the composite joint member, pin failure was observed to be responsible for final joint failure. Pins are exposed to two different loading conditions, bending around the *y*-axis and *x*-axis and shear within the *x*-*y* plane. The stress state within the pin is highly dependent on the hole bearing behavior of the CFRP joint member, see Figure 5-35.

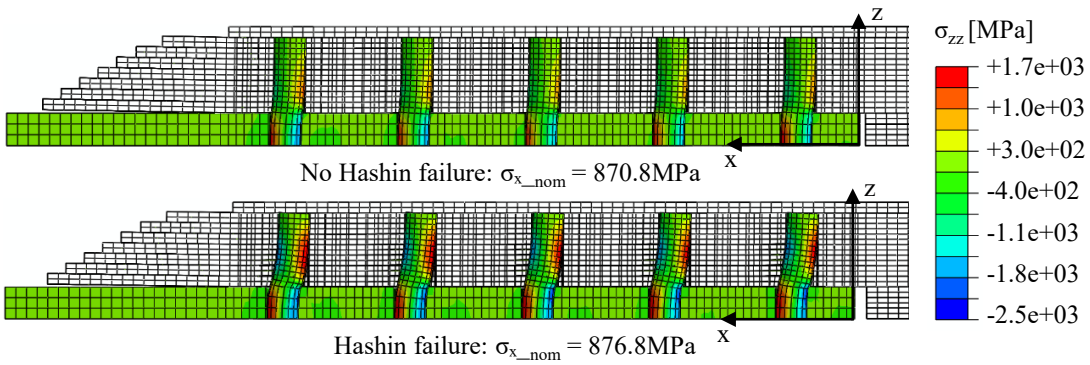

Figure 5-35: Analysis of pin shear and bending behavior

The figure above illustrates the pin's stress distribution in *z*-direction. The form closure between the pin and CFRP joint member leads to high compressive stresses within the composite elements, which are located adjacent to the joint face in front of the pin. Within the linear elastic state of the composite material and low pin bending, the compressive stresses are only dependent on the fiber direction and in-plane location, not on the vertical location of the elements.

However, if a Hashin failure criteria is applied for the CFRP joint member, element stiffness degradation occurs after damage initiation for high compressive stresses. This leads to an expansion of the hole, especially within the layers which are located close to the titanium surface. As a consequence, the contact area between pin and composite joint member is no longer vertically oriented. In addition, damage evolution and therefore stiffness degradation is higher for the inner composite layers. The resulting leverage effect further increases pin bending. The analysis of the FE-models with an implemented Hashin failure criteria shows that pins ultimately fail due to high stresses σ_{zz}, not due to transversal shear within the *x*-*y* plane. These observations emphasize the need for a proper modelling of the composite joint member's material behavior in the area around the pin.

Both FE-models, with and without Hashin failure, show that pins slow down crack propagation within the adhesive bond between metallic and composite joint member. Due to their great resistance to shear, shear stresses are partially absorbed by the pins. This relieves the stress within the remaining adhesive zone. It also explains the increased load at FFAD when comparing the pinned to the co-bonded reference joints, see Figure 5-27.

The FE analysis presented in this chapter is based on the assumption that there are no fiber undulations around the pins and that the fiber volume fraction is evenly distributed throughout the entire composite joint member with a constant value of 60%, see Chapter 3.4.2. In order to set up a more detailed FE-model and to account for fiber undulations around the pins, these undulations first have to be measured.

5.5 Measurement of fiber undulation

The following chapter describes the results of the fiber undulation measurement around the pins. For further information regarding the measurement method and procedure, please refer to Chapter 3.3. Figure 5-36 further helps to understand the following fiber angle measurement results.

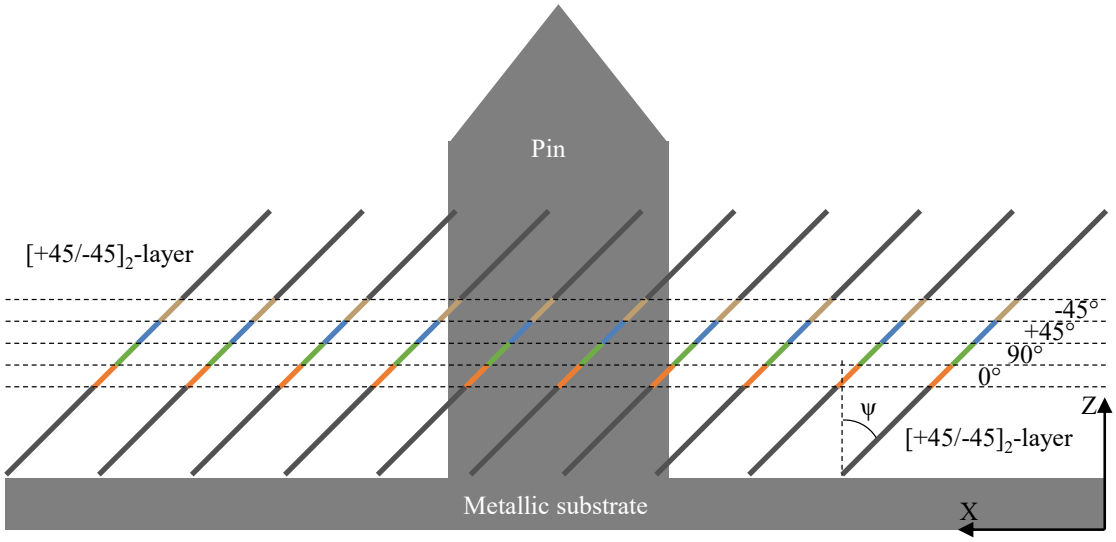

Figure 5-36: Illustration of technique for fiber angle measurements

As explained in Chapter 3.3.1.2, the entire layup consists of 12 single prepreg plies. $[+45/-45]_2$-stacks are placed on the top and the bottom in order to protect the inner plies during manufacturing. The inner section consists of a 0°, 90°, +45° and -45° ply. The spacing between the pins is similar for 0° and 90° principal fiber direction, therefore measurement results can be directly transferred from 0° to 90°. The same applies for the +45° and -45°-direction. As microscopy inspection and subsequent image recognition is time-consuming, only the 0°- and -45°-ply were analyzed. Figure 5-36 shows the measurement planes in the *X*-*Z*-plane, which are tilted towards the pin's longitudinal axis, by the tilting angle ψ. The figures in the next chapters show measurement results in the *X*-*Y*-plane. However, it is important to note, that this measurement technique includes measurement points in both the 2-dimensional *X*-*Y*-plane and also in the thickness (*Z*-) direction. For the fiber angle measurements, the global coordinate system is denoted with capital letters *X*, *Y*, *Z* to prevent from ambiguity. However, the directions *X*, *Y* and *Z* of the global coordinate system from fiber angle measurements coincide with the directions *x*, *y* and *z* in Figure 3-5 and Figure 3-12.

5.5.1 Undulation in 0° and 90°- direction

As described in Chapter 3.3, the pin's distance in regard to the principal fiber direction significantly influences the fiber undulations and geometry of the resin pockets. Undulations were measured separately for 0° and -45° principal fiber direction. Figure 5-37 illustrates measurement points and the mean fiber direction for a cuboid element of approximately 8*8*0.137 mm³ (*X*-*Y*-*Z*).

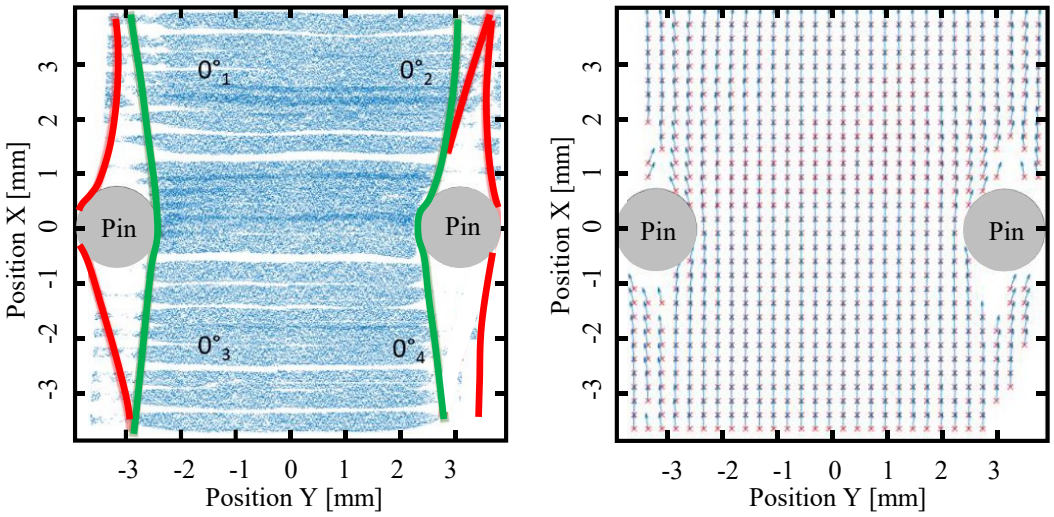

Figure 5-37: Fiber direction measurement points (left), principal fiber direction 0° (right)

The plot on the left shows each measurement point in blue color and a trend for the resin pockets. The plot on the right illustrates the averaged fiber direction of the single cuboid cell. This analysis indicates that in the case of 0° and 90° principal fiber direction, large areas in between the pins are not affected by fiber displacement caused by pin insertion. Fiber angle analysis along a section in *Y*-direction confirms this result, see Figure 5-38.

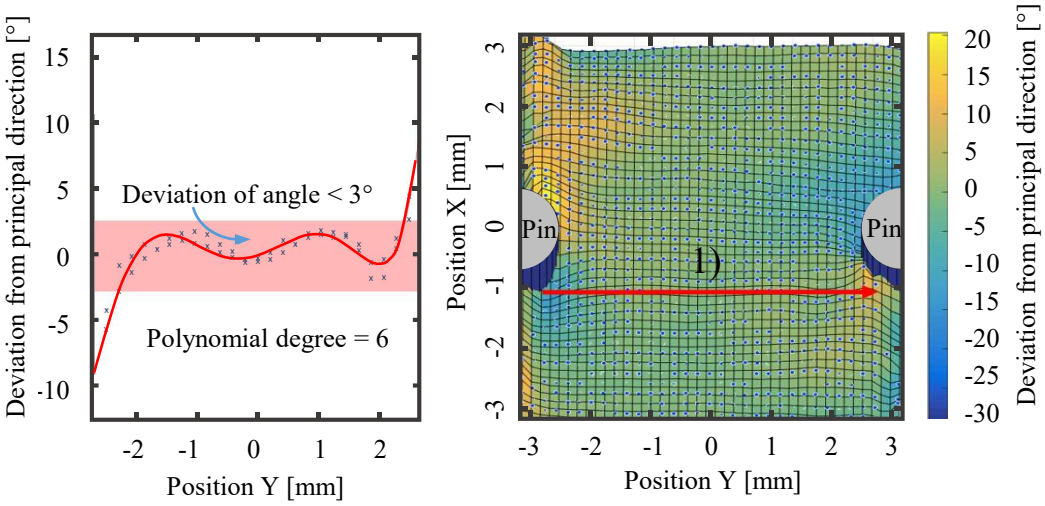

Figure 5-38: Fiber angle along section (left), deviation from principal fiber direction 0° (right)

The position of this section, marked with a red arrow, is located 1mm below the pin's center. Maximum deviations of the fiber angles from the principal direction are observed in this region. However, Figure 5-38 still shows local fiber angle deviations from the principal angle in a range of only ±3° for *Y*-positions of -2.30mm to +2.35mm. The dark blue colored areas around the pins are characterized by a low precision. In order to further simplify the visualization of the fiber angle deviation from principal direction, deviations within a range of -3° to +3° are in blue color, see Figure 5-39.

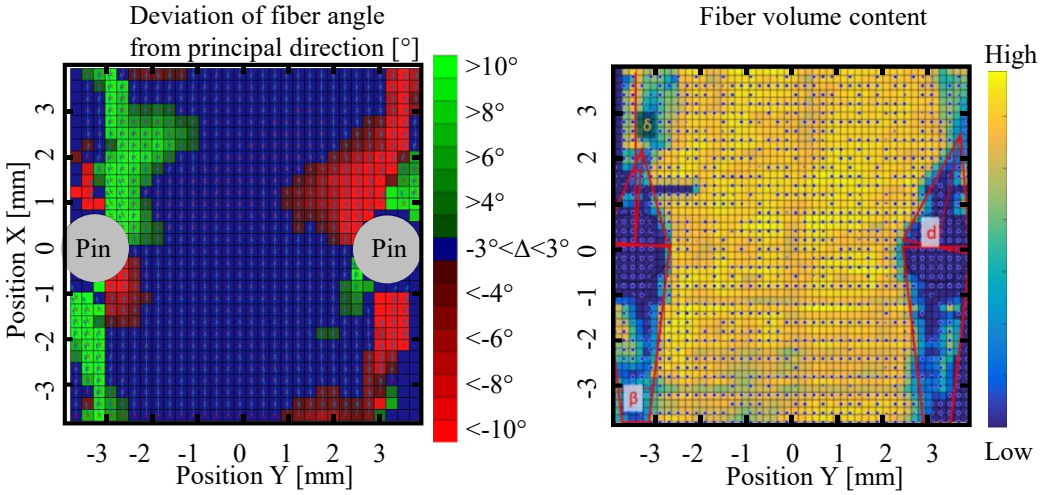

Figure 5-39: Trend of fiber angle (left) and fiber volume fraction for a unit cell (right), principal direction 0°

This figure also illustrates the local fiber volume fraction distribution. Assuming that the fiber undulations are identical around different pins, the fiber angle deviation from principal direction and local fiber volume content would be symmetrical to the *X*-*Z* (*Y*=0) and *Y*-*Z* plane (*X*=0). However, Figure 5-39 indicates that in the case of 0°/90° principal fiber direction, the influence of fiber displacement by the pins can be measured, but is rather randomly distributed and not repeated for different unit cells. Analyzing local fiber volume content is the most appropriate method to describe the shape of resin rich zones. It was found that resin rich zones form into resin pockets, which are not connected to the resin pocket of the adjacent pin. They also form into resin channels, which describe an area of low fiber volume content in between two adjacent pins.

5.5.2 Undulation in ±45°- direction

According to the measurements for the 0°/90°-principal fiber direction, the fiber undulation was also evaluated for the ±45°-principal fiber direction.

Figure 5-40 illustrates the measurement points and the average in-plane fiber direction for a -45° unit cell.

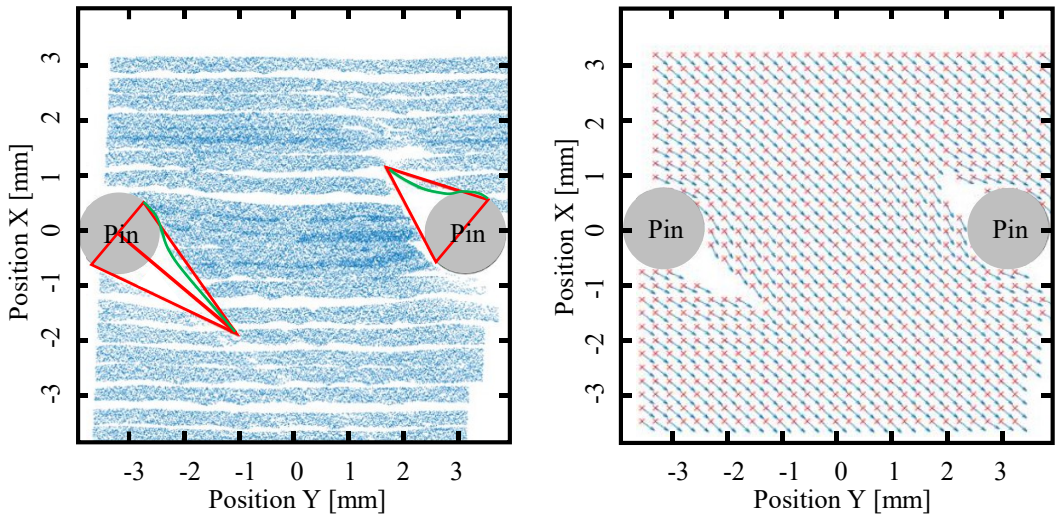

Figure 5-40: Fiber direction measurement points (left), principal fiber direction -45° (right)

The distance between two pins in principal fiber direction is 1.41 times higher in comparison to the 0°/90°-direction. Therefore, fibers converge in a region behind the pins. The deviation of the fiber angle from the principal fiber angle is displayed in Figure 5-41.

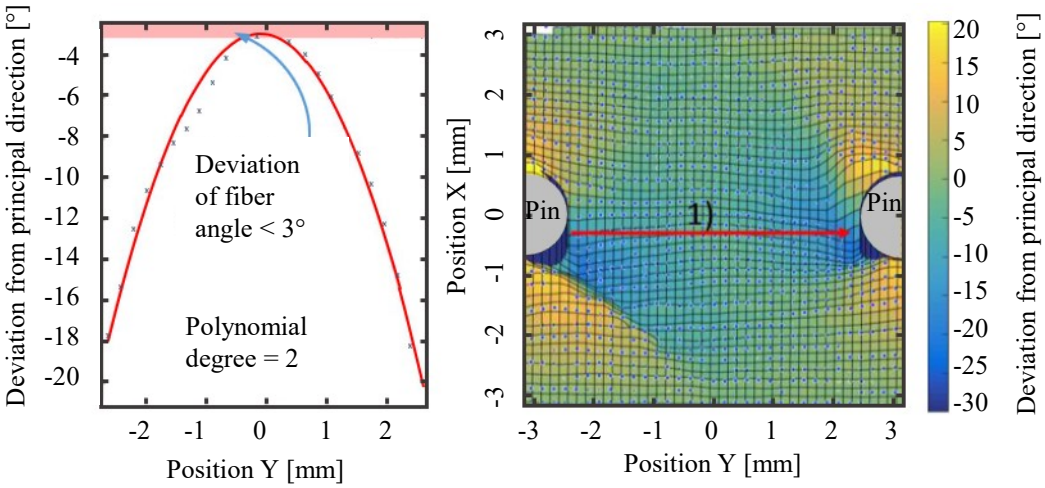

Figure 5-41: Fiber angle along section (left), deviation from principal fiber direction -45° (right)

As opposed to the 0°/90°-principal direction, fiber undulation is more pronounced for the ±45°-principal direction in the region between the pins. This becomes more apparent in Figure 5-42.

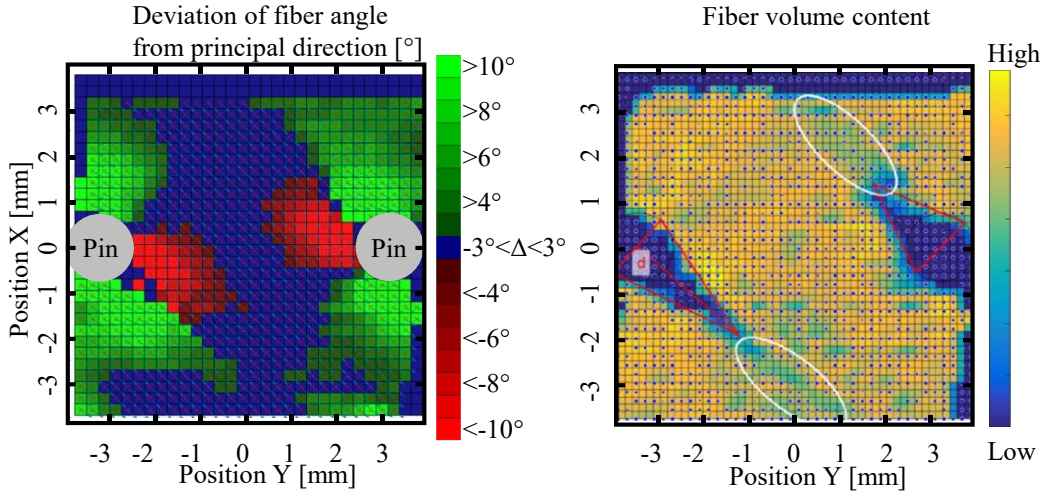

Figure 5-42: Trend of fiber angle (left) and fiber volume fraction for a unit cell (right), principal direction -45°

In contrast to the 0°/90°-principal fiber direction, measurements for the ±45° principal direction show a similar behavior of fiber course around both pins. Therefore, it can be assumed that the measurements for this unit cell are also representative for other unit cells. Resin pockets are clearly defined and the local fiber volume fraction is more evenly distributed in comparison to the 0°/90°-direction. An increase of distance between the pins in *X*- and *Y*-direction and/or a decrease of pin diameter would result in a more defined fiber course. However, the measurement results can be also transferred to neighboring sections.

The FE-model, described in Chapter 3.4.3 is based on the measurements presented above. In the case of ±45° principal fiber direction, fiber undulations measured around both pins were averaged and one pattern for fiber undulation and volume fraction was derived for the FE-model. For the 0°/90°-principal fiber direction, two patterns were taken into consideration for the FE-model. The fiber undulation measurements indicate that resin pockets and resin channels can occur between adjacent pins. Therefore, two different FE-models were created, including either resin pockets or resin channels, see Chapter 5.6.2.3.

5.6 Test series 4: CFRP/titanium joint design 2

The goal of test series 4 is to further investigate the load carrying capability of the CFRP joint member. By adapting the joint design, failure within the titanium joint member and pins could be prevented, see Chapter 3.2.5.2.

5.6.1 Tensile testing

This chapter describes the results of mechanical tensile testing. Three different composite layups, $[\pm 45]_2$, quasi-isotropic [0/90/-45/+45], and $[0/90]_2$, were used to investigate

the influence that fiber orientation had on the mechanical performance. In contrast to specimens of test series 1 and 3 which were produced using NCF material, the composite joint member for test series 4 is made from Prepreg, see Chapter 3.2.5 and Chapter 4.4. Two different types of joints were tested. Whereas joints of configuration "dh" were manufactured by hole drilling into the cured composite joint member, a special pin insertion process was used for the "fh" specimens, which are characterized by fiber undulation around the pins, see Chapter 3.3.

5.6.1.1 Preliminary testing

Preliminary testing with "dh" specimens indicated failure due to the composite layers' bending toward the *z*-direction rather than bearing failure, see Figure 5-43.

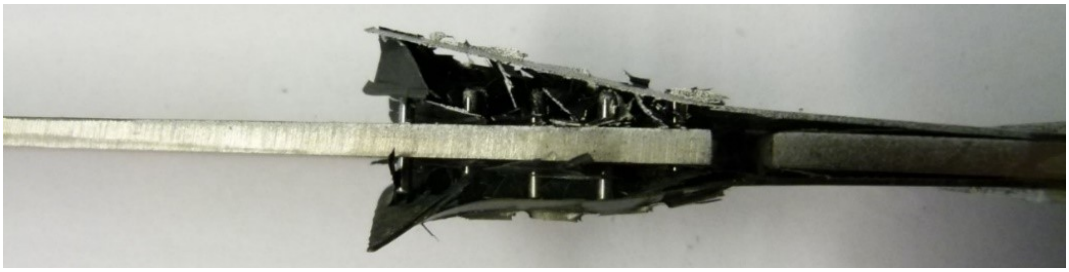

Figure 5-43: Failure analysis for an unclamped specimen

A metallic clamp was installed at the composite joint member's front edge to exclude this failure mode. The clamping device consists of two metal plates, which are kept together by two screws. The tightening torque was adjusted to 0.3Nm for successive testing. Figure 5-44 illustrates the influence of this restriction of movement in the *z*-direction.

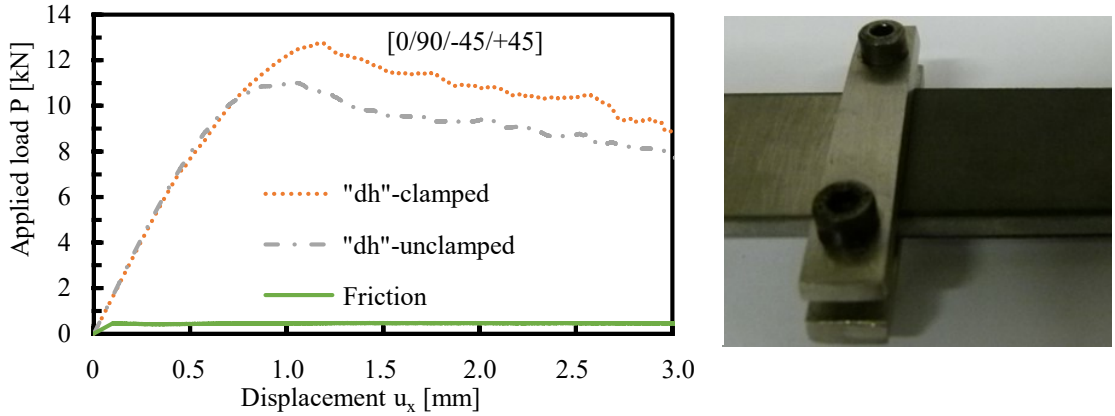

Figure 5-44: Influence of clamping on joint performance, stress-strain behavior

According to Chapter 4.4.1, there is no adhesive bond between the composite and titanium joint member. The load-displacement curves for both the "dh"/unclamped and the "dh"/clamped specimens reveal simultaneous linear elastic behavior up to an applied

tensile load of 6kN followed by a slight reduction in tensile stiffness until 10kN. Whereas the "dh"/unclamped specimen failed at a maximum load of 11.0kN, the "dh"/clamped specimen was able to withstand a 12.6kN load before successive bearing failure in all pin rows. A friction test was performed to investigate friction behavior between the composite and titanium joint members. A joint with a cured, unnotched composite joint member was tested for this purpose. The frictional forces can be calculated to be as low as 3.7% of the maximum load on the quasi-isotropic "dh"/clamped joint.

5.6.1.2 Strength and failure modes

Figure 5-45 compares the nominal joint tensile strength $\sigma_{x\_nom\text{-}max}$ for all configurations.

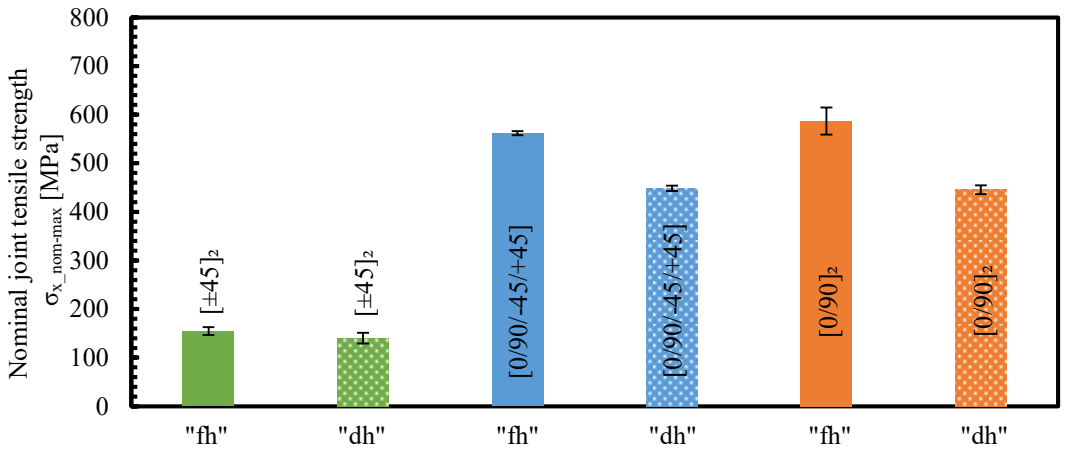

Figure 5-45: Joint strength for different prepreg layups, formed hole vs. drilled hole

Specimens with formed holes of configuration $[\pm45]_2$-"fh" reached a mean joint strength of 154.6MPa (±8.1MPa) and $[\pm45]_2$-"dh" specimens a mean joint strength of 140.1MPa (±11.2MPa). An increase of 10.3% in joint strength can thus be calculated for the "fh"-joints. The quasi-isotropic "fh"-specimens were able to withstand a mean joint tensile stress of 561.7MPa (±4.2MPa), 25.3% greater than that of the "dh"-specimens, which were measured at 448.4MPa (±5.8MPa). $[0/90]_2$-"fh"-specimens (587.0±28.0MPa) manifest an even greater increase (31.8%) in mean joint tensile strength than their counterparts (445.5±9.2MPa).

Figure 5-46 presents the failure modes for all tested configurations.

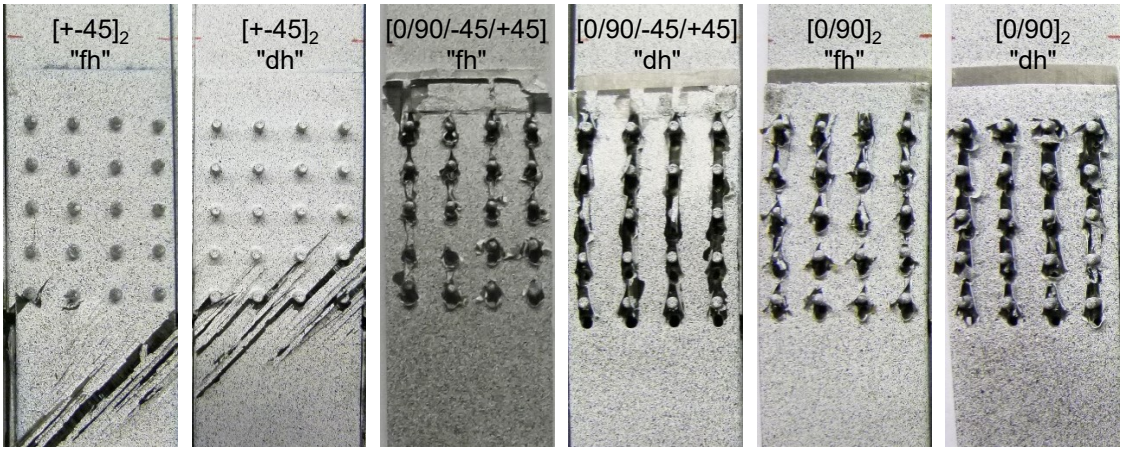

Figure 5-46: Failure modes for different composite layups, formed hole vs. drilled hole

The $[\pm 45]_2$-"fh"-specimens failed due to shear behind the joining area. This failure mode emphasizes the importance of using the release foil, see Chapter 3.2.5.2. An adhesive bond between the spacer and the composite joint member would prevent pure shear failure in the composite behind the joining area, as load transfer to the metallic spacer would be possible. The undulations around the pins create a locking effect between adjacent fibers, producing greater shear strength. That is why the $[\pm 45]_2$-"fh"-specimens failed behind the joining area, where undulations are absent. The opposite can be observed for the $[\pm 45]_2$-"dh"-specimens: the absence of undulations enables crack propagation due to in-plane shear within the joining area, see Figure 5-47.

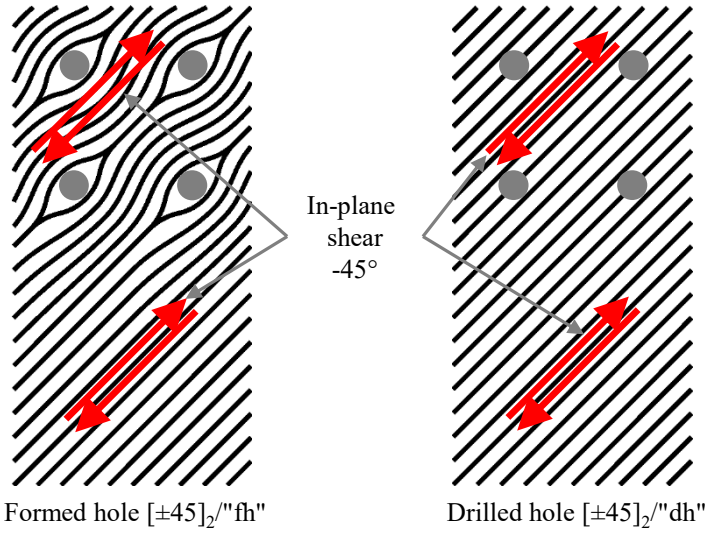

Figure 5-47: Schematic illustration of the locking effect for ±45°-plies with formed holes

In contrast to the $[\pm 45]_2$ specimens, all of the "fh" and "dh" quasi-isotropic and $[0/90]_2$ cross-ply specimens failed due to hole bearing.

5.6.1.3 Stress-strain behavior

Representative stress-strain curves for all configurations are shown in Figure 5-48.

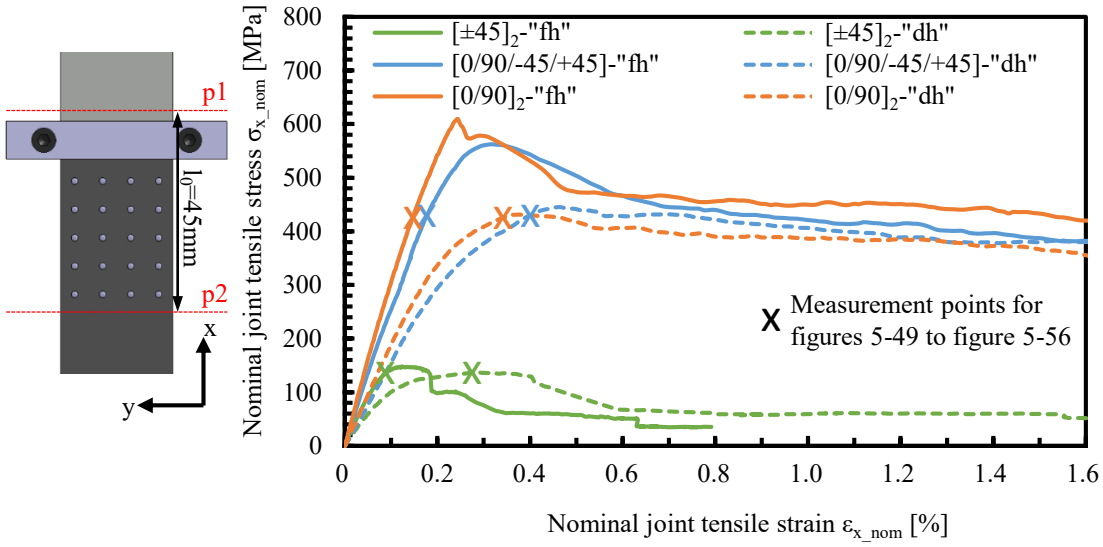

Figure 5-48: Stress-strain behavior for different composite layups, formed hole vs. drilled hole

Approximately linear elastic behavior characterizes all "fh"-configurations almost until initial failure at maximum joint tensile stress. The [0/90]$_2$-"fh"-specimen consists of two stiff 0°-plies per lap and, therefore, has the greatest stiffness of all configurations. Joint tensile stiffness for the [0/90/-45/+45]-"fh"-specimen is lower in comparison to the [0/90]$_2$-"fh"-specimen, yet still higher than for the [±45]$_2$-"fh"-specimen. The [0/90]$_2$-"fh"-specimen exhibits the strongest joint followed closely by the quasi-isotropic "fh"-specimen, whereas the [±45]$_2$-"fh"-specimen is much weaker due to the lack of load-carrying 0°-fibers. The counterparts of configuration "dh" are characterized by a lower initial joint stiffness unlike their corresponding "fh"-configurations, followed by decreasing joint stiffness until maximum joint stress is reached. Furthermore, it can be stated that the joint tensile strength of the "dh"-joints is lower than of the "fh"-joints for all three laminates. None of the tested specimens showed sudden failure. However, residual joint strength in relation to maximum joint stress at ultimate load is highest for the [0/90]$_2$-"dh"-specimen and [0/90/-45/+45]-"dh"-specimen, closely followed by their counterparts with formed holes. The reason for this behavior is bearing failure, see Figure 5-46.

5.6.1.4 Local distribution of strain

The Digital Image Correlation technique allows detailed analysis of local strains for all specimens tested.

Figure 5-49 displays the distribution of nominal strain ε_{x_nom} for a $[\pm45]_2$-"dh"-specimen and a $[\pm45]_2$-"fh"-specimen at a comparable load level prior to maximum tensile load.

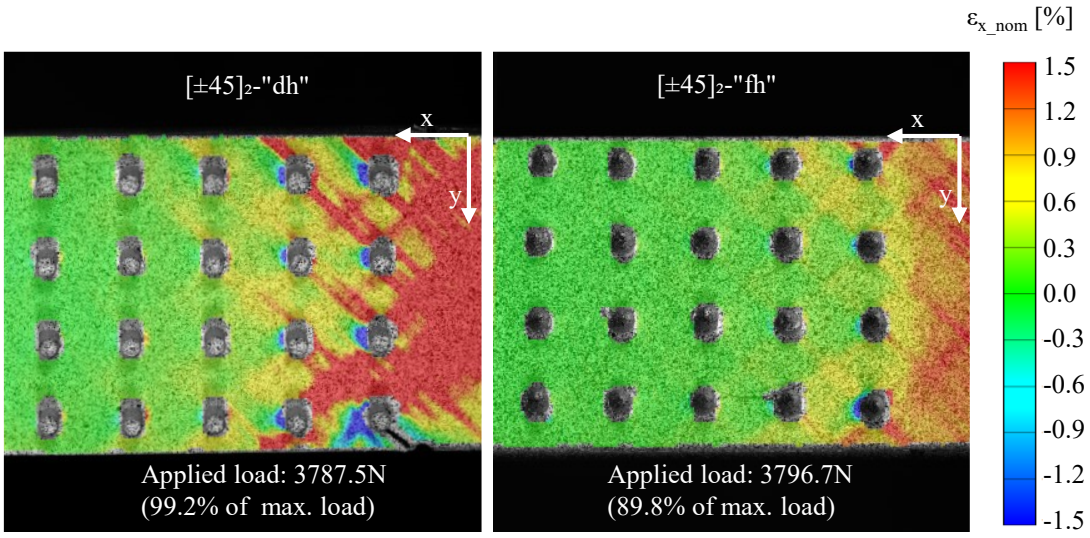

Figure 5-49: Distribution of ε_{x_nom} for a [+-45]$_2$ layup, formed hole vs. drilled hole

Two principle findings emerge from these measurements. First, the last pin row occupies the area where the laminate is exposed to greater strain than it is in other pin rows. Second, local strains ε_{x_nom} inside the joining area, especially those near the ultimate pin row, are smaller for $[\pm45]_2$-"fh" than for $[\pm45]_2$-"dh"-specimens. Since the $[\pm45]_2$-"fh"-specimens failed outside of the inspected area, failure could not be analyzed by DIC measurements. Figure 5-50 shows the distribution of nominal strain ε_{x_nom} for the quasi-isotropic configurations.

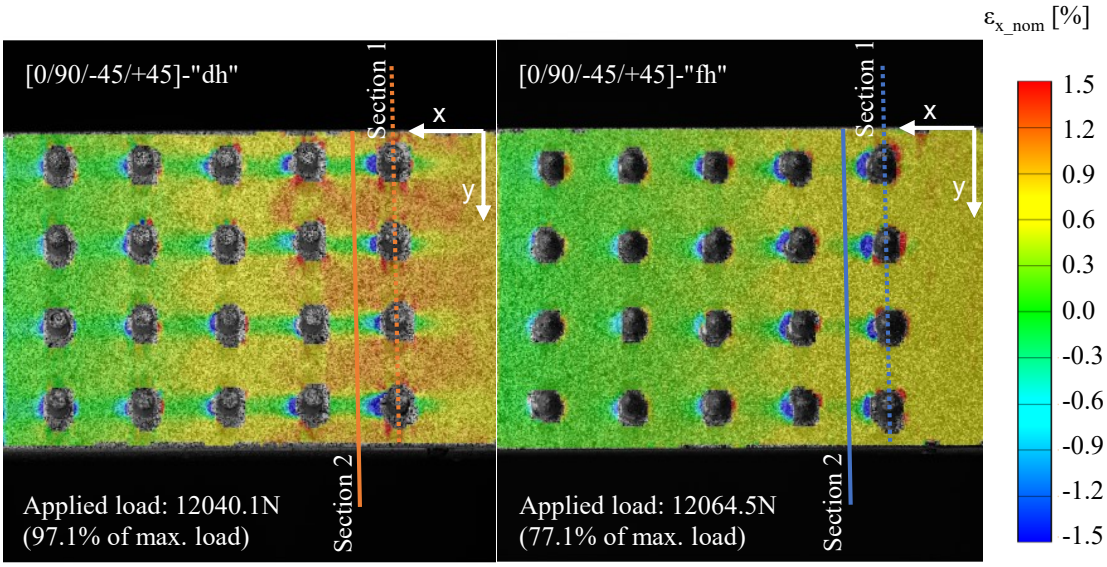

Figure 5-50: Distribution of ε_{x_nom} for a [0/90/-45/+45] layup, formed hole vs. drilled hole

Greater strains are observed in the bypass region between the fasteners for the "dh"-specimen than for the counterpart with formed holes. Furthermore, the "fh"-specimen's strain distribution is more homogeneous than the "dh"-specimens'.

To quantify local strains ε_{x_nom}, two sections are drawn along the y-direction. Section 1 runs through the center points of the fasteners in the last row. Section 2 is located halfway between the last and penultimate row of fasteners. Consequently, ε_{x_nom} values along these sections can be plotted for the "dh" and "fh"-specimens, see Figure 5-51.

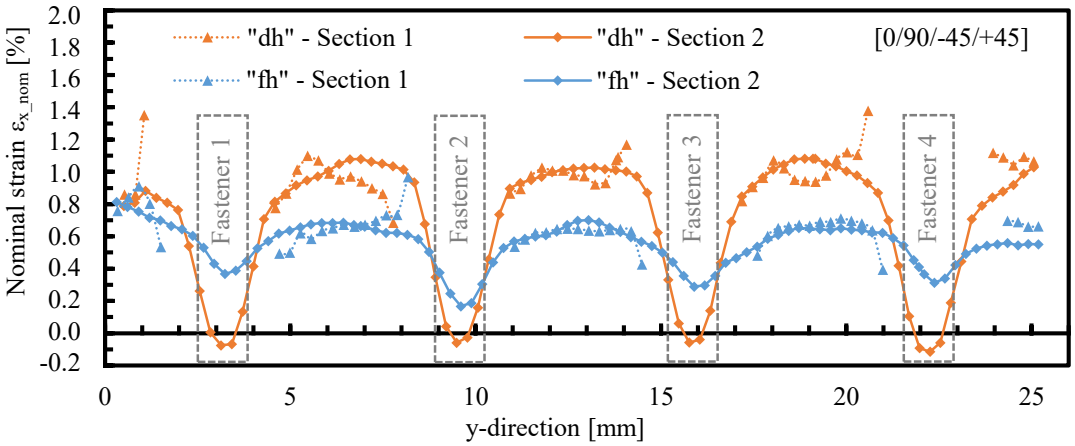

Figure 5-51: ε_{x_nom} along Section 1 and Section 2 for a [0/90/-45/+45] layup, formed hole vs. drilled hole
Applied load: 12040.1N ("dh") and 12064.5N ("fh")

Furthermore, Section 1 can be divided into five segments. The mean value of ε_{x_nom} across Section 1 can be calculated based on the following relation:

$$\bar{\varepsilon}_{x\_nom\_Section1} = \sum_{o=1}^{5}\left(\bar{\varepsilon}_{x_o} * \Delta y_o\right) \Big/ \sum_{o=1}^{5} \Delta y_o$$

$$\bar{\varepsilon}_{x\_nom\_Section1} = \sum_{o=1}^{5}\left(\sum_{p=1}^{r-1} \frac{\left(\varepsilon_{x_{o_p}} + \varepsilon_{x_{o_{p+1}}}\right) * \left(y_{o_{p+1}} - y_{o_p}\right)}{2}\right) \Big/ \sum_{o=1}^{5}\left(y_{o_r} - y_{o_1}\right) \tag{5-8}$$

Where the control variable, o, describes segments 1 to 5 and p labels the measurement point in each segment. In addition, r describes the number of measurement points for the corresponding segment and y the distance of the corresponding measurement point from the specimen's edge ($y=0$). Consequently, $\bar{\varepsilon}_{x\_nom\_Section1}$ can be calculated for the "dh" and "fh"-specimens. By comparing both values for the quasi-isotropic layup, it can be observed that the mean nominal strain for the "fh"-specimen in Section 1 is 34.6% lower than for the "dh"-specimen. Moreover, under the assumption that the pin-insertion process does not lead to fiber breakage, the number of 0°-fibers along Section 1 is also 30.9% greater for the "fh"-specimen. These observations are reasonable when taking

into account the fact that the 0°-fibers are mainly, although not exclusively, responsible for load transfer in *x*-direction. However, it needs to be emphasized that the shadow impact and edge effects described in Chapter 3.2.5.3 prevent strain values from being determined close to the fasteners, leading to possible inaccuracy in this measurement.

The formula for mean strain in *x*-direction along Section 2 is a simplified version of the formula for Section 1, as Section 2 is uninterrupted by fasteners.

$$\bar{\varepsilon}_{x\_nom\_Section2} = \sum_{p=1}^{r-1} \frac{\left(\varepsilon_{x_p} + \varepsilon_{x_{p+1}}\right) * \left(y_{p+1} - y_p\right)}{2 * \left(y_r - y_1\right)} \tag{5-9}$$

The distribution of $\bar{\varepsilon}_{x\_nom\_Section2}$ for the "dh" and "fh" quasi-isotropic specimens indicates that gradients are shallower for the "fh"-specimen. The mean strain in *x*-direction along Section 2, $\bar{\varepsilon}_{x\_nom\_Section2}$ was calculated to 0.70% for the "dh" and 0.55% for the "fh" specimen. Furthermore, the corresponding variation coefficient was computed to 55% ("dh"-specimen) and 24% ("fh"-specimen). Assuming linear-elastic material behavior, it can be stated that fiber undulation is reducing peak stresses in the areas around Section 2. In addition, the effect of local softening around the pins is responsible for homogenization of the load that different pin rows introduce into the 0°-plies. Resin pockets are characterized by less stiffness than the straight 0°-fibers in the case of "dh"-specimens with drilled holes. Softening inserts for multi rowed riveted and bolted joints have been investigated [34] and proven to reduce notch factors and improve joint strength. However, increased DIC-measurement resolution and reduced shadowing and edge effects are necessary to measure these effects in pinned specimens. Similar investigation was conducted for a $[0/90]_2$-"dh" and "fh"-specimen, see Figure 5-52.

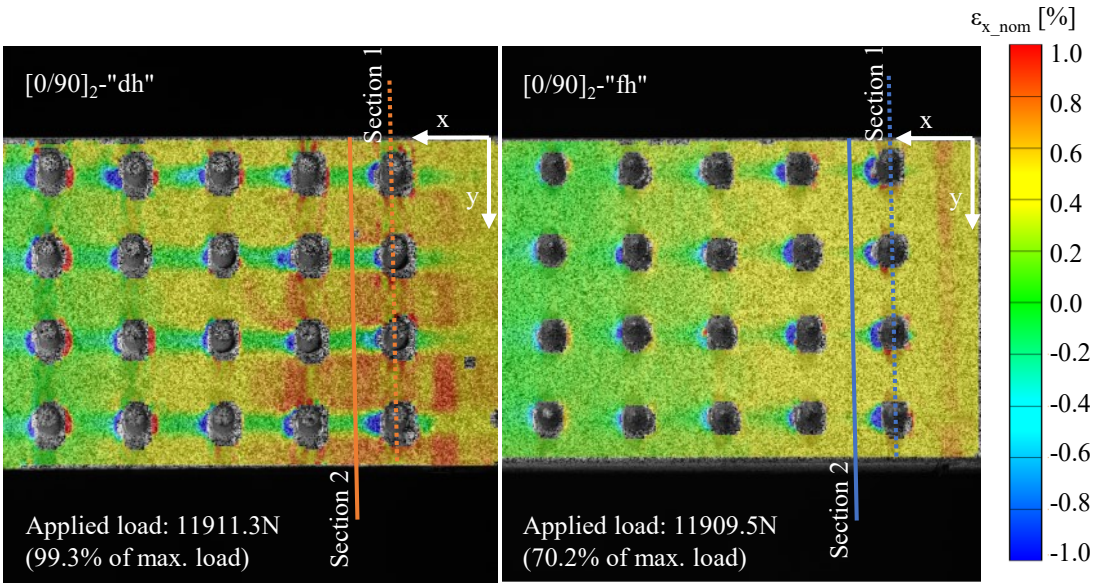

Figure 5-52: Distribution of ε_{x_nom} for a $[0/90]_2$ layup, formed hole vs. drilled hole

Similar to the quasi-isotropic specimens, the local nominal strain along Section 1 and Section 2 can be also plotted for the $[0/90]_2$-"dh" and $[0/90]_2$-"fh"-specimens, see Figure 5-53.

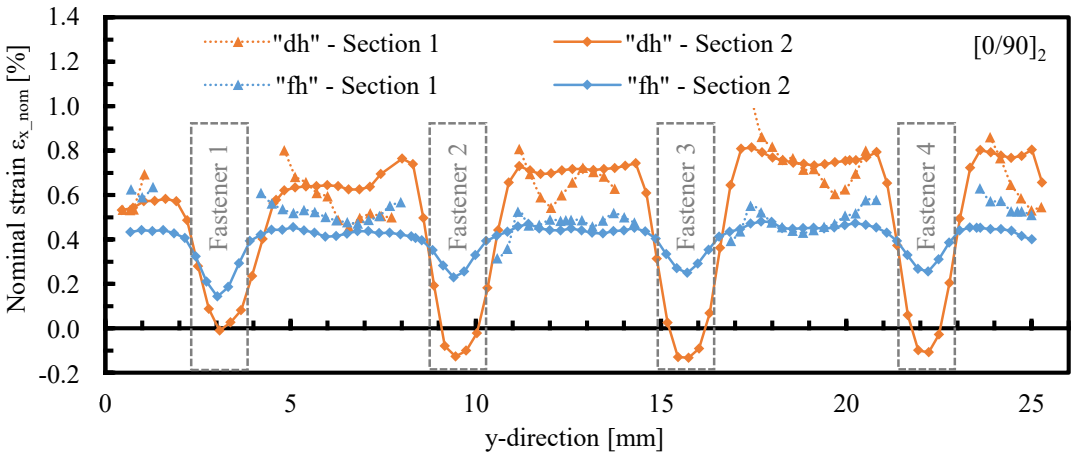

Figure 5-53: ε_{x_nom} along Section 1 and Section 2 for a $[0/90]_2$ layup, formed hole vs. drilled hole
Applied load: 11911.3N ("dh") and 11909.5N ("fh")

A 23.8% reduction for the "fh"-specimen relative to the "dh"-specimen could be calculated for the mean nominal strain in *x*-direction $\bar{\varepsilon}_{x\_nom\_Section1}$. In addition, homogenization of the strain distribution in Section 2 can be observed for the "fh"-specimen. The strain $\bar{\varepsilon}_{x\_nom\_Section2}$ was computed at 0.51% and 0.40% for the "dh" and "fh"-specimens, respectively. Like the quasi-isotropic specimen, the variation coefficient of the nominal strain $\bar{\varepsilon}_{x\_nom\_Section2}$ for the $[0/90]_2$ specimen is also smaller for the "fh"-specimen (18%) than for the "dh"-specimen (60%). Due to the additional 0°-layer, strain values in loading direction are generally smaller for the $[0/90]_2$ than for the quasi-isotropic setup.

5.6.1.5 Local direction of strain

Since the strain values, ε_{x_nom} and ε_{y_nom} are defined as being dependent on the coordinate system, strain direction cannot be described using them. However, this disadvantage can be eliminated by using major strain, ε_{I_nom} and minor strain, ε_{II_nom} measures. The stretch tensor,

$$U = \begin{pmatrix} 1+\varepsilon_{x\_nom} & \varepsilon_{xy\_nom} \\ \varepsilon_{xy\_nom} & 1+\varepsilon_{y\_nom} \end{pmatrix} \tag{5-10}$$

can be transformed into the diagonal form. Its eigenvalues, λ_I and λ_{II} are calculated as

$$\lambda_{I,II} = 1 + \frac{\varepsilon_{x\_nom}+\varepsilon_{y\_nom}}{2} \pm \sqrt{\left(\frac{\varepsilon_{x\_nom}+\varepsilon_{y\_nom}}{2}\right)^2 - \left(\varepsilon_{x\_nom} * \varepsilon_{y\_nom} - \varepsilon_{xy\_nom}^2\right)} \tag{5-11}$$

The major strain, ε_{I_nom} and minor strain, ε_{II_nom} can be determined, based on the larger eigenvalue λ_I and smaller eigenvalue λ_{II}, respectively. Furthermore, the eigenvectors indicate the direction of the corresponding strain measures.

To evaluate the course of strain for "dh" and "fh"-quasi-isotropic and cross-ply $[0/90]_2$ specimens, local values of major strain and their corresponding direction are analyzed for a region of interest, see Figure 5-54.

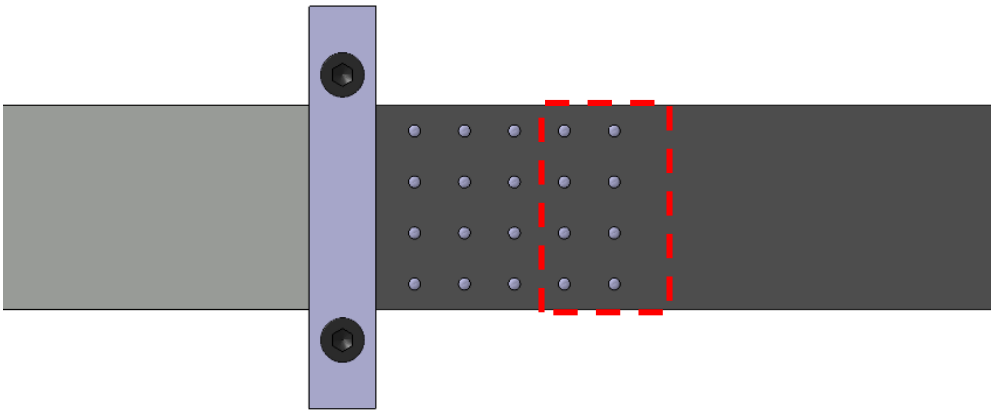

Figure 5-54: Region of interest for the analysis of strain direction

Figure 5-55 and Figure 5-56 show the results from DIC measurements for representative specimens at a load level similar to Figure 5-50 and Figure 5-52.

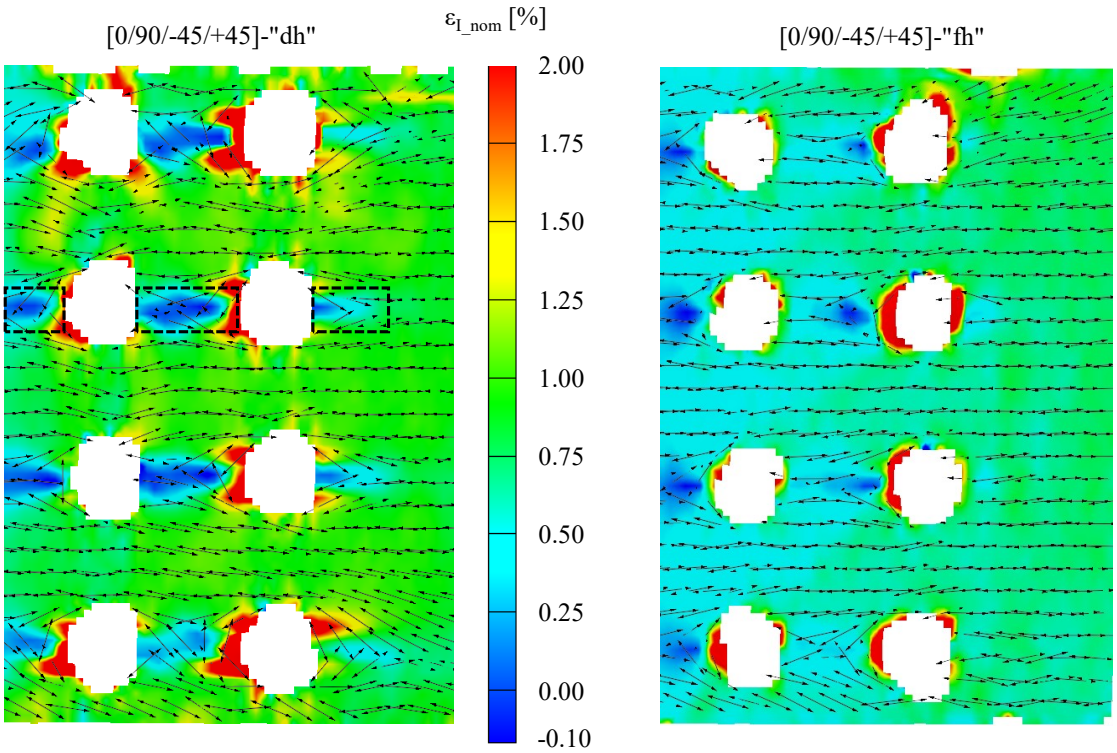

Figure 5-55: Strain direction for a [0/90/-45/+45] layup, formed hole vs. drilled hole
Applied load: 12040.1N ("dh") and 12064.5N ("fh")

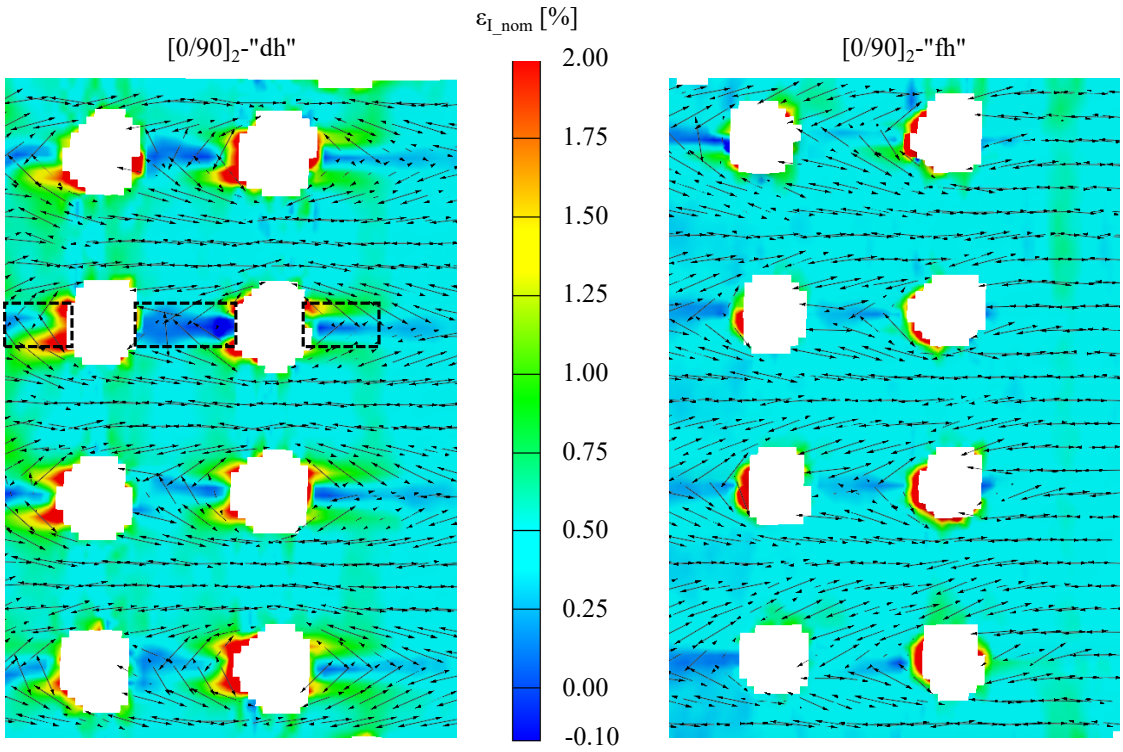

Figure 5-56: Strain direction for a [0/90]$_2$ layup, formed hole vs. drilled hole
Applied load: 11911.3N ("dh") and 11909.5N ("fh")

The "dh"-joints are first analyzed in more detail. Great stiffness in tensile direction by non-undulated 0° fibers characterizes the regions in front and behind the fasteners, marked by the black boxes. The course of major strain in these regions deviates significantly from the tensile direction for both layups. It can therefore be concluded that a high in-plane shear stress level prevails in the 0°-plies, especially at the upper and lower borderlines of the boxes. Only in-plane or interlaminar shear can transfer stresses from adjacent plies into the load-carrying endless 0° fibers. Inspection of the area behind the last fastener row for the quasi-isotropic and [0/90]$_2$ specimens highlights another remarkable detail. Major strain converges with tensile direction closer to the fastener for the quasi-isotropic specimen. This can be explained by the presence of ±45° plies. These plies ensure better load transfer from the regions in front and behind the fasteners into the bypass region than one 0° and 90° layer. However, for the "fh"-configurations, fiber undulations are present in every layer. Figure 5-55 and Figure 5-56 illustrate that in the case of "fh"-specimens, the course of major strain follows the fiber direction, leading to better load transfer from the regions in front and behind the pins into the bypass region. The result is a stiffer joint and more homogeneous distribution of ε_{x_nom} for joints with formed holes than for joints with drilled holes.

5.6.2 Modelling results

Pinned composite/titanium joints were previously investigated via FEA in Chapter 5.4.2. However, two issues occurred in the first approach for the joint's FE-modelling:

- Titanium joint members, pins and composite joint member are simultaneously subjected to damage degradation under great tensile loads. Hence, an isolated investigation of the composite joint member is challenging, as the joint's stress-strain behavior is influenced by composite and titanium joint member and pins.
- Fiber undulations around the pins were ignored and the fiber volume fraction was set to 60% throughout the entire composite joint member. However, mechanical testing, presented earlier, indicated that undulations significantly influence the mechanical performance of the pinned composite/titanium joint.

The FE-model for test series 4 is based on the measurement results of fiber undulation, presented in Chapter 5.5. However, in the case of the 0° and 90° principal fiber direction, the presence of resin pockets and resin channels was observed. Chapter 5.6.2.3 directly compares the joint's mechanical performance of those only with resin pockets against a joint characterized exclusively by resin channels within the 0° and 90° predominant fiber direction.

5.6.2.1 FEA vs. testing

To validate the simulation, a representative pinned specimen with a quasi-isotropic layup and formed holes was chosen for the comparison to the FE-results, see Figure 5-57.

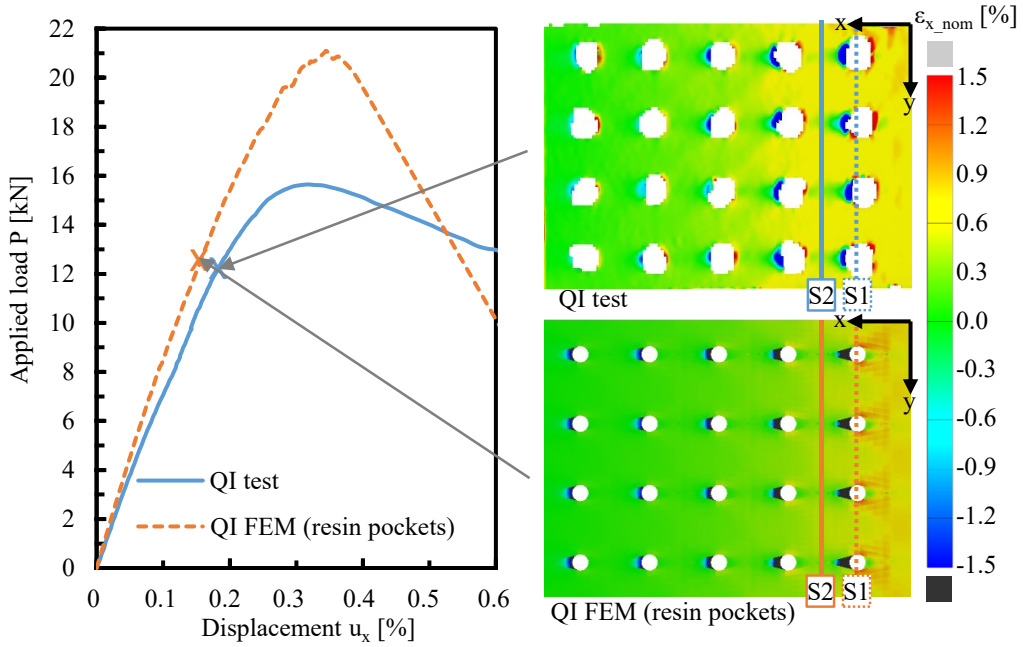

Figure 5-57: FEA vs. testing for a [0/90/-45/+45] layup, load-displacement curve and distribution of strain

Strong correlation between mechanical testing and simulation results can be found for low tensile loads. However, by increasing the tensile load, the FEA overestimates the joint's tensile stiffness. Furthermore, the joint tensile strength predicted by FEA is 33% higher than that measured by mechanical testing. In accordance to the testing results, hole bearing was found to be responsible for final failure of the joint.

To study the cause of this mismatch in joint tensile stiffness, the local nominal strain ε_{x_nom}, is analyzed in detail. Several aspects are simplified within the FE-model and are likely to be responsible for the discrepancy between FE- and testing results. These aspects are as follows:

- no fiber breakage through pin insertion
- no failure criteria for fibers in tension
- clearly defined fiber undulation and resin pockets
- all unit cells are identical in geometry and mechanical properties
- no plasticity within 90° and ±45°-plies
- no porosity considered
- material models (especially neat resin compression) are not accurate

In accordance with the strain measurements presented in Chapter 5.1.4, the strain distribution along Section 1 and Section 2 can be also visualized for the FE-results. Figure 5-58 refers to a joint with resin pockets and quasi-isotropic layup at a load level of 12kN, similar to Figure 5-57.

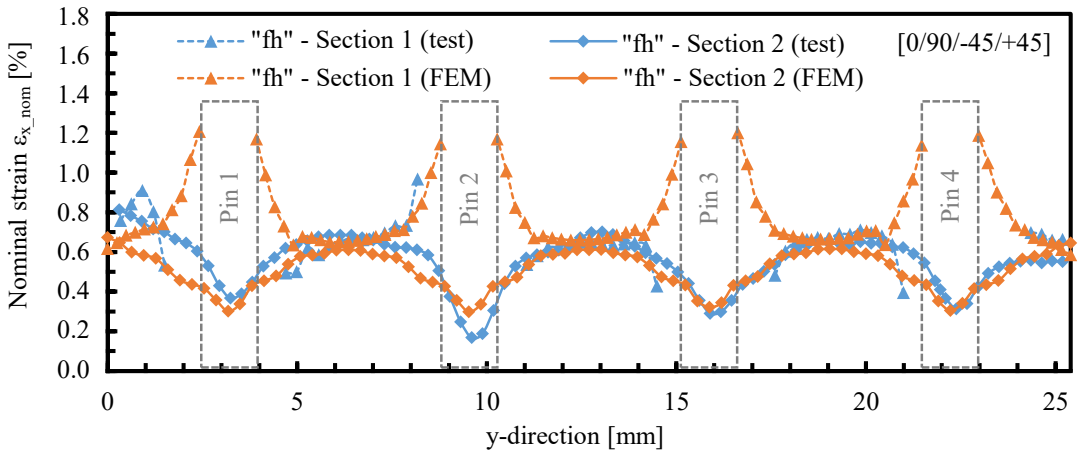

Figure 5-58: ε_{x_nom} along Section 1 and Section 2 for a [0/90/-45/+45] layup with formed holes and resin pockets, Testing vs. FEA

The evaluation of FE-results also allows for the investigation of the areas close to the pins. The distribution of nominal strain ε_{x_nom} along Section 1 is characterized by local stress peaks close to the pins. The course of strain along Section 2 shows minimum strains ε_{x_nom} at the locations where fiber bundles converge behind and in front of the resin pockets and slightly curved stress peaks.

5.6.2.2 Load transfer into pins

As opposed to the DIC measurements presented in the previous chapter, logarithmic stress measures are now used instead of nominal stress measures. To evaluate the load transfer from the composite joint member into the pins, Figure 5-59 shows the distribution of logarithmic stress in tensile (x-) direction σ_{xx} of pins and titanium joint member at a tensile load of 12kN.

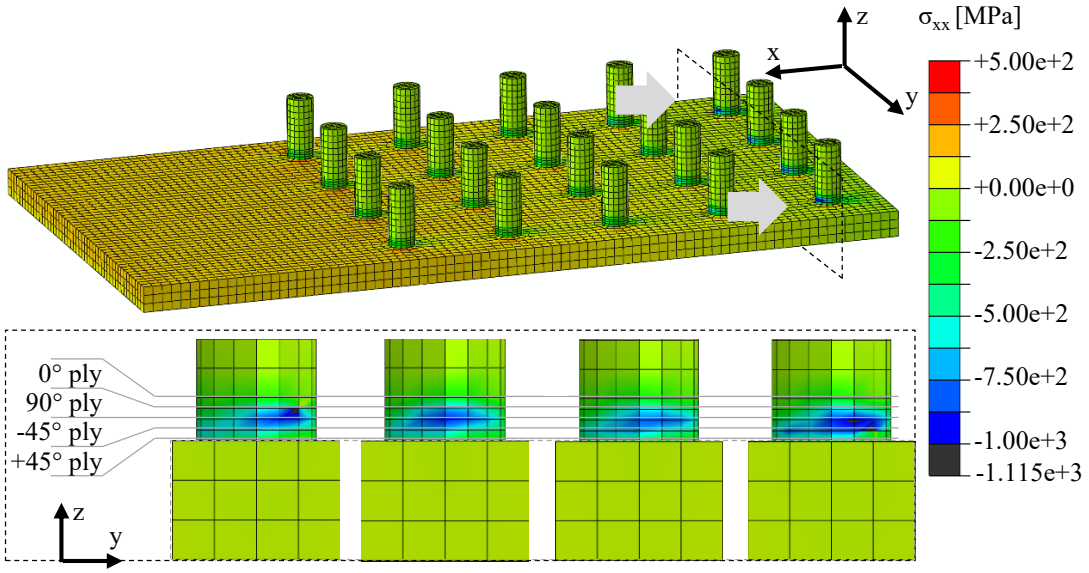

Figure 5-59: Load transfer from composite joint member into pins for a [0/90/-45/+45] layup, formed holes and resin pockets

Special focus is given to the pins as they are exposed to the greatest loads. 90°-plies are characterized by a compressive transversal stiffness 3.45 times greater than the resin pockets of the 0°-plies. Therefore, load transfer from the composite joint member into the pins primarily takes place through the 90°-plies. This raises the question whether the presence of either resin pockets or resin channels is more beneficial for the overall joint tensile strength.

5.6.2.3 Resin pocket vs. resin channel

The measurements of fiber undulation, presented in Chapter 5.5, indicated that the presence of resin channels is most probable within the 0° and 90°-plies. This is because of the smaller pin distance in principal fiber direction compared to the ±45°-plies. Therefore, a FE-model was set-up, containing resin channels with a constant width. The geometries chosen for the resin pockets and channels are a theoretical example. In reality, interim stages of both solutions are more likely to occur and the geometry of a single unit cell is not completely identical to other unit cells.

Figure 5-60 presents a comparison of load-displacement behavior for a joint with quasi-isotropic layup with either resin pockets or resin channels. In addition, the logarithmic stress σ_{xx} in tensile direction is shown for the 0°, 90° and ±45° plies.

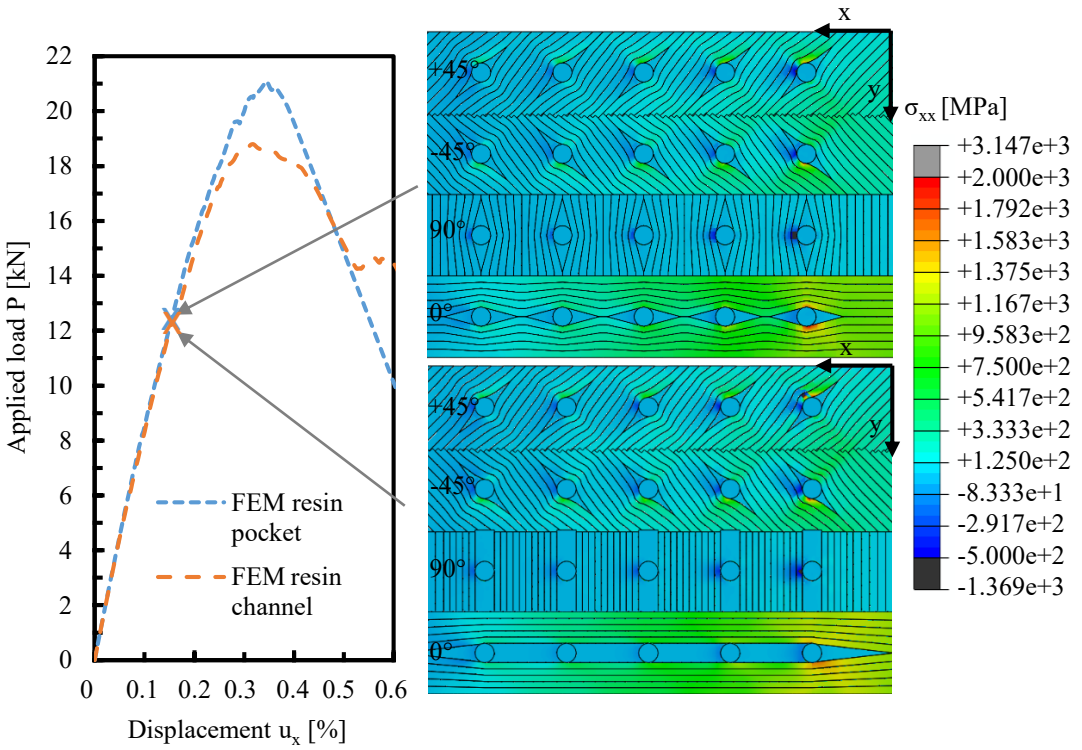

Figure 5-60: Resin pocket vs. resin channel for a [0/90/-45/+45] layup, load-displacement behavior and distribution of strain

Locations in front of the pins are exposed to compressive stresses. Especially within the 90°-plies and, to a lesser extent, also within the ±45°-plies, which further confirms the investigations made when analyzing Figure 5-59. In the case of the quasi-isotropic joint with resin pockets, first intra-laminar delaminations can already be observed located close to the last pin row within the +45°-ply. However, the 0°-plies are primarily responsible for load transfer in tensile direction. Stress peaks can be found near the pins where fiber bending is greatest.

To further assess the influence of fiber bending on the joint's tensile performance, the stress in longitudinal fiber direction σ_{11} is analyzed in more detail for joints with quasi-isotropic layup and resin pockets or resin channels.

Figure 5-61 illustrates the distribution of σ_{11} for the 0°-ply of a joint with quasi-isotropic laminate and resin pockets under a tensile load of 12kN.

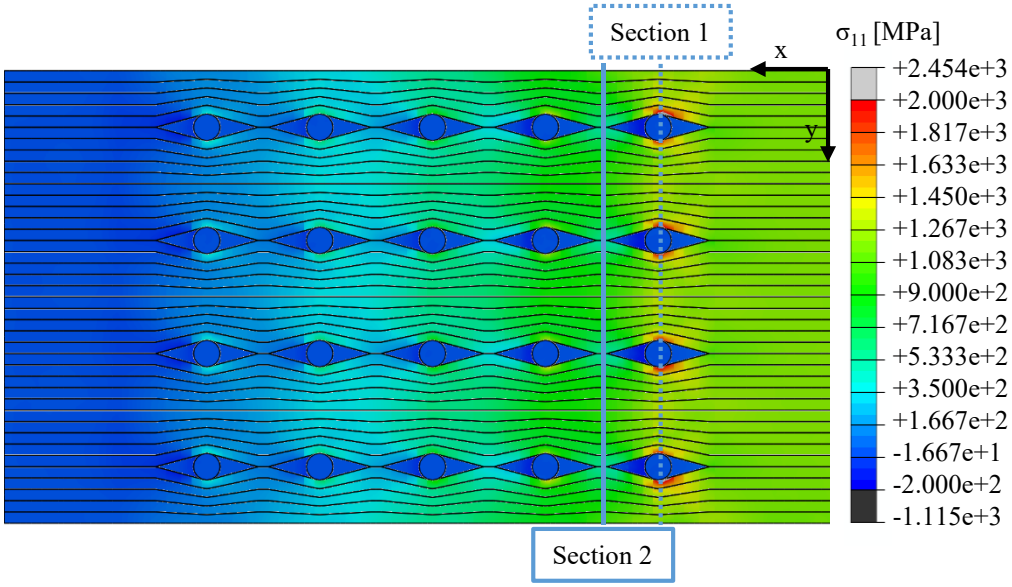

Figure 5-61: Distribution of stress σ_{11} for a [0/90/-45/+45] layup with formed holes and resin pockets

Maximum values for σ_{11} of almost 3000MPa are predicted by FEA at the location next to the pin. The tensile strength for a unidirectional Cycom 5320-1 prepreg layup with 60% FVF is specified as 2428MPa in the data sheet. However, in order to completely describe the joint's failure under tension and properly predict the joint strength, fiber tension failure at higher fiber volume fractions also has to be included into the analysis. Under the assumption that the tensile strength in 0°-direction is dependent on the number of filaments per cross sectional area, the tensile strength for different fiber volume fractions can be estimated as follows:

$$X^T(\varphi) = \frac{X^T{}_{60\%}}{0.6} * \boldsymbol{\varphi} \tag{5-12}$$

where $X^T{}_{60\%}$ is the tensile strength of a unidirectional layer with 60% FVF taken from the datasheet. Therefore, $X^T(\varphi)$ is in a range of 2518MPa for 60% FVF to 3273MPa for 78% FVF, respectively. However, this can only serve as a rough estimation, as test results for higher fiber volume fractions are unknown. Figure 5-62 illustrates the distribution of σ_{11} along Section 1 and Section 2.

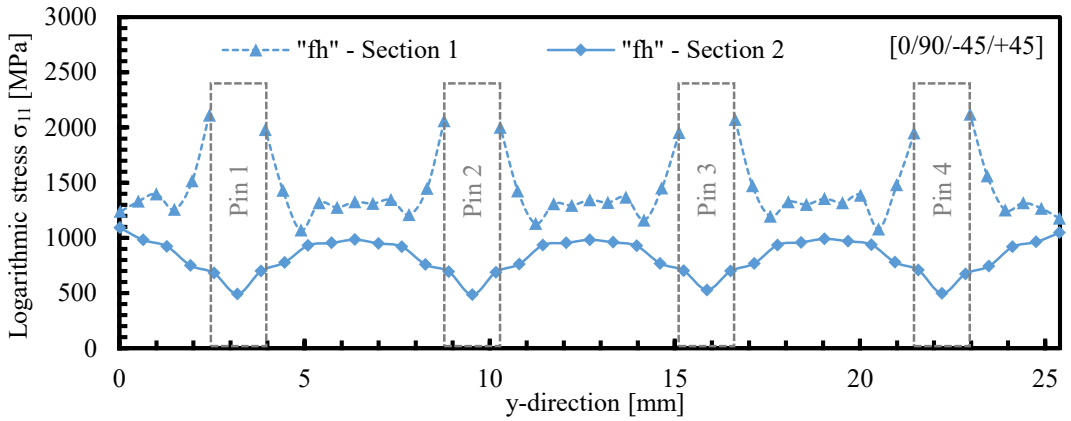

Figure 5-62: σ_{11} along Section 1 and Section 2 for a [0/90/-45/+45] layup with formed holes and resin pockets

Stress peaks close to the pins are present along Section 1, whereas the stress at the remaining locations between the pins is rather constant. The stress distribution along Section 2 is characterized by local minima located between the pins with respect to the *x*-direction. Slightly curved stress peaks are present where fiber bundles converge behind and in front of the resin pockets. Greatest values for σ_{11} along Section 2 are predicted for the upper edge of the specimen. According to Figure 5-60, first delaminations already occur at this load level within the +45°-ply at this location. As a consequence, σ_{11} within the 0°-ply is generally higher in the upper edge region than in the lower edge region. A similar analysis was performed for a FE-model which contained resin channels instead of resin pockets between the pins in *x*-direction (0°-ply) or *y*-direction (90°-ply). Figure 5-63 shows the distribution of σ_{11} on the 0°-layer for the FE-model with resin channels.

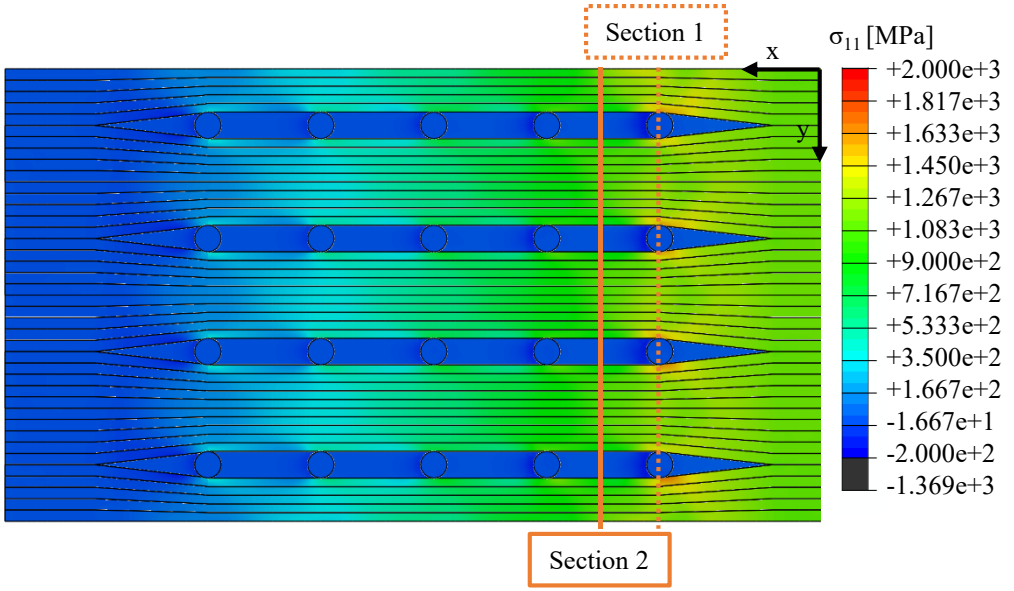

Figure 5-63: Distribution of stress σ_{11} for a [0/90/-45/+45] layup with formed holes and resin channels

The bending angle of the fibers next to the pins in Section 1 reduces from 22.5° (FE-model with only resin pockets) to 11.25° (FE-model with resin channels). As a consequence, σ_{11} stress peaks next to the pins in the last row are also lower for the FE-model with resin channels than for the FE-model with resin pockets within the 0° and 90°-ply. Similar to Figure 5-61, the two sections were also analyzed for the FE-model with resin channels, see Figure 5-64.

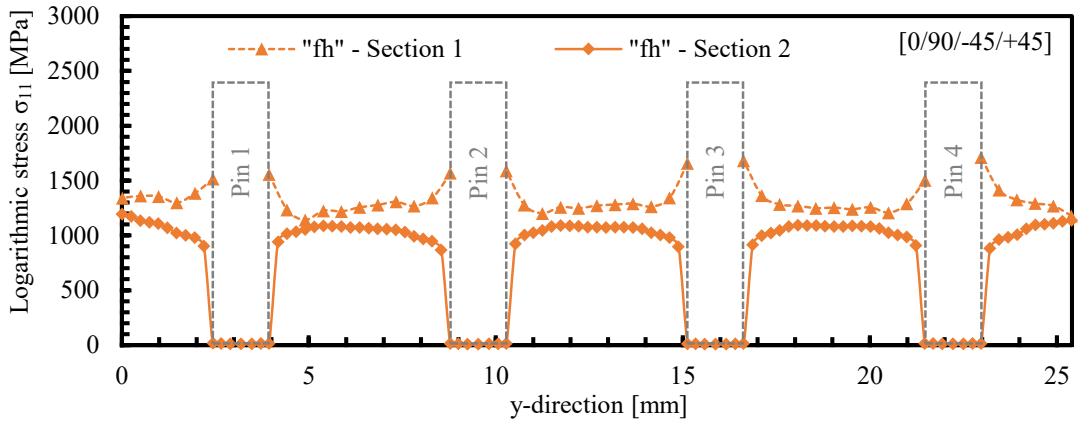

Figure 5-64: σ_{11} along Section 1 and Section 2 for a [0/90/-45/+45] layup with formed holes and resin channels

Stresses in longitudinal fiber direction σ_{11} along Section 2 are characterized by relatively constant plateaus between the resin channels and minimum stresses within the resin channels. As the neat resin's material behavior is defined to be isotropic, the $_{11}$-direction of resin pockets and resin channels is identical with tensile direction. These observations emphasize that resin channels are not exposed to tensile stresses and therefore are not involved in the load transfer from the laminate into the pins. Figure 5-65 illustrates FE-results of the load-displacement behavior for a joint with quasi-isotropic layup and either resin pockets or resin channels incorporating fiber tension failure (FTF). Furthermore, failure modes for both models are illustrated in this figure.

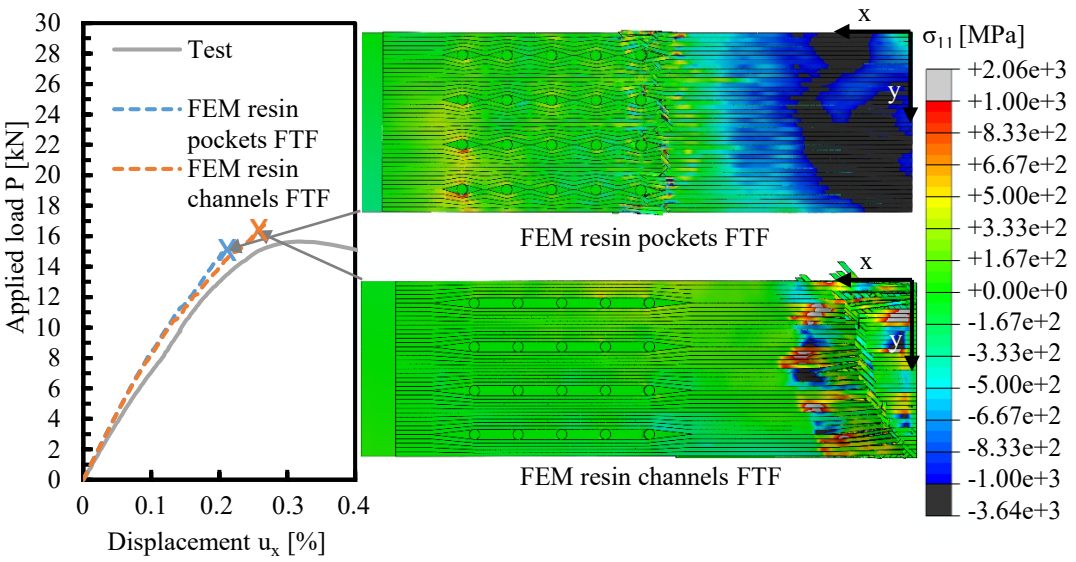

Figure 5-65: Resin pocket vs. resin channel for a [0/90/-45/+45] layup with formed holes, fiber tension failure (FTF)

The tensile strengths predicted for both setups is similar to the tensile strength of the tested specimens. The failure modes for the FE-results are either net section failure in the last pin row for resin pockets or net section failure far behind the joining area for resin channels. Therefore, it can be stated that extensive fiber bending around the pins reduces the tensile strength of pinned composite/metal joints. However, in comparison to joints with drilled holes, pinned joints with formed holes are still superior in terms of joint tensile strength as evidenced by mechanical testing in Chapter 5.6.1.2.

6 Classification of pinned joints

This chapter compares pinned joints to co-bonded and state-of-the-art Hi-lock riveted composite/titanium joints in terms of joint efficiency, specific joint tensile strength and lightweight efficiency. In addition, design rules for pinned composite/metal joints are presented.

6.1 Joint efficiency and specific joint tensile strength

The comparison of different joining technologies is based on joint geometries, which are displayed in Figure 6-1.

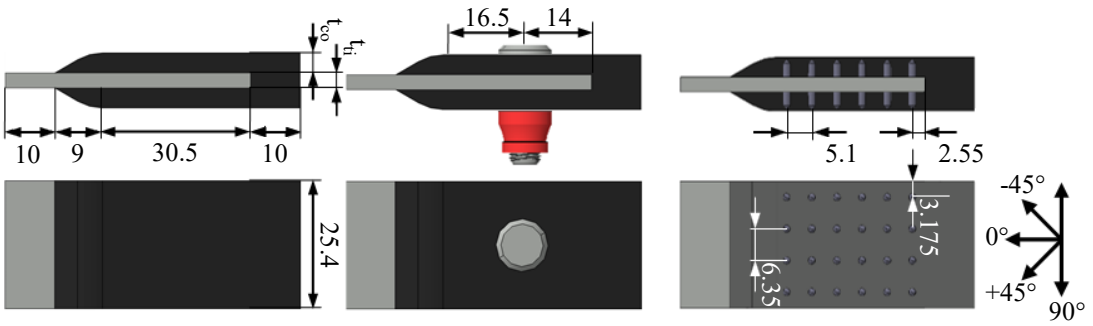

Figure 6-1: Joint geometries for co-bonded, riveted (Hi-lock) and pinned joints
For better visibility, the composite joint member for the pinned configuration is transparent; all dimensions in [mm]

The area that is analyzed is extended by 10mm in front and behind the joining area, to account for the connecting areas. A co-bonded joint with a titanium surface, treated by acid etching and primer, is used as a reference. For the pinned configuration, a 6x4 pin pattern is chosen. Whereas testing results for co-bonded and pinned joints are directly taken from Chapter 5, Hi-lock riveted joints are not investigated within the scope of this thesis. Therefore, ultimate tensile loads for Hi-lock joints have to be estimated based on literature.

Fiber-Metal-Laminates, see Chapter 2.2, are characterized by a higher bearing strength than pure composite laminates [34, 38]. Two different configurations for Hi-lock joints are analyzed: a joint with a quasi-isotropic CFRP joint member and a joint with a hybrid CFRP/titanium laminate. Edge to fastener diameter (e/d) and width to fastener diameter (w/d) values coincide with recommendations available in literature [38, 98]. All material

parameters which are necessary for the estimation of the load carrying capability for both Hi-lock configurations are listed in Table 6-1.

Table 6-1: Input for estimation of joint efficiencies and specific joint tensile strengths

Input	Ti6Al4V tensile strength	CFRP 25/50/25 [0°/±45°/90°] tensile strength	FML CFK/Ti 45.5/54.5Ti [0°/Ti] tensile strength	Ti6Al4V ultimate bearing strength	CFRP 25/50/25 [0°/±45°/90°] ultimate bearing strength	FML CFK/Ti 45.5/54.5Ti [0°/Ti] ultimate bearing strength	Hi-lock HL10 ¼" double shear load
[-]	[MPa]	[MPa]	[MPa]	[MPa]	[MPa]	[MPa]	[N]
Value	1050	730	1440	1875	670	1574	41368
Source	Figure 5-10	estimated	[38]	[38]	[98]	[38]	[114]

Table 6-2 lists the ultimate loads for the Ti6Al4V and CFRP/FML joint member which were measured during tensile testing of pure titanium or given in literature for CFRP/FML specimens.

Table 6-2: Ultimate loads and thicknesses for CFRP/FML and Ti6Al4V joint member; non-adapted geometries

Joining technology	Ultimate load titanium joint member	Ultimate load CFRP or FML joint member	Ultimate load CFRP or FML bearing	Ultimate load titanium joint member bearing	Ultimate load Hi-lock double shear	Ultimate load at joint failure	Thickness CFRP or FML t_{co}	Thickness Ti6Al4V t_{ti}
[-]	[N]	[N]	[N]	[N]	[N]	[N]	[mm]	[mm]
Co-bonded CFRP/Ti	80010	148336	-	-	-	42267	4	3
Hi-lock CFRP/Ti	80010	148336	34036	35719	41368	34036	4	3
Hi-lock FML/Ti	80010	292547	79959	35719	41368	35719	4	3
Pinned CFRP/Ti	80010	148336	-	-	-	52782	4	3

In addition, estimated ultimate loads based on the bearing strength are given. The double shear load for a ¼" HL10 Hi-lock rivet is taken from literature. These values apply for

joints with a 4mm thickness for the CFRP or FML joint member (t_{co}) and a 3mm thickness for the titanium insert (t_{ti}). The pinned CFRP/Ti6Al4V joint is not wrapped with circumferential UD-layers. The joint efficiency is calculated with the following formula:

$$Joint\ efficiency = \frac{Ultimate\ load\ at\ joint\ failure}{Ultimate\ tensile\ load\ of\ joint\ member^{1}} \tag{6-1}$$

It can be related either to the titanium or CFRP or FML joint member. The joint efficiency serves as an indicator for the joint member's utilization factor. In order to also account for the joint's weight, the specific joint tensile strength can be calculated:

$$Specific\ joint\ tensile\ strength = \frac{Ultimate\ load\ at\ joint\ failure}{Cross\ section\ of\ joint\ member^{2}} * \frac{1}{Averaged\ joint\ density} \tag{6-2}$$

It can also be related either to the titanium or CFRP or FML joint member. The joint efficiencies and specific joint tensile strengths are shown in Figure 6-2.

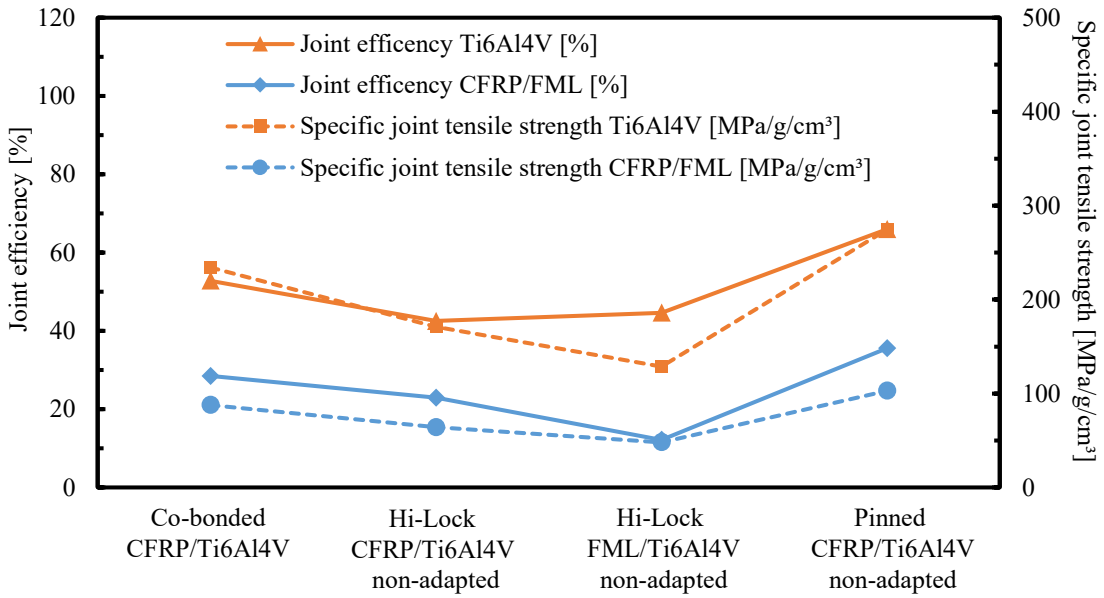

Figure 6-2: Joint efficiencies and specific joint tensile strengths for different joining technologies/non-adapted geometries

Joint geometries are based on joint design 1, see Figure 6-1 and Table 6-2. Table 6-2 lists the ultimate loads for the Ti6Al4V and CFRP or FML joint member which were measured during tensile testing of pure titanium or CFRP or FML specimens; no circumferential layers for pinned joint, see Figure 5-23 and Figure 5-24

[1] Ultimate tensile load measured during tensile testing of a pure Ti6Al4V, CFRP or FML specimen i.e. Figure 5-10; Figure 5-12

[2] Cross section of joint member; t_{ti} * 25.4mm (Ti6Al4V) or t_{co} * 25.4mm (CFRP or FML)

Pinned joints indicate the highest joint efficiencies and specific joint tensile strengths, closely followed by the co-bonded joint. However, the Hi-lock riveted joints are not yet optimized in terms of maximum tensile load. The CFRP/Ti6Al4V Hi-lock configuration fails due to bearing within the CFRP joint member. The FML/Ti6Al4V Hi-lock joint fails due to bearing within the titanium joint member. By adapting both joint members' thicknesses, t_{co} and t_{ti}, the estimated ultimate joint tensile loads for both Hi-lock configurations can be increased, see Table 6-3.

Table 6-3: Ultimate loads and thicknesses for CFRP/FML and Ti6Al4V joint member; adapted geometries

Joining technology	Ultimate load titanium joint member	Ultimate load CFRP or FML joint member	Ultimate load CFRP or FML bearing	Ultimate load titanium joint member bearing	Ultimate load Hi-lock double shear	Ultimate load at joint failure	Thickness CFRP or FML t_{co}	Thickness Ti6Al4V t_{ti}
[-]	[N]	[N]	[N]	[N]	[N]	[N]	[mm]	[mm]
Co-bonded CFRP/Ti	80010	148336	-	-	-	42267	4	3
Hi-lock CFRP/Ti	92665	180414	41396	41368	41368	41368	4.865	3.4745
Hi-lock FML/Ti	92665	151393	41379	41368	41368	41368	2.07	3.4745
Pinned CFRP/Ti	80010	148336	-	-	-	59701	4	3

The pinned joint is now wrapped with circumferential layers. Adding circumferential layers to the co-bonded joint without pins does not lead to an increased joint tensile strength, see Chapter 5.4.1.1. Therefore, the co-bonded configuration stays unchanged. The joint efficiencies and specific joint tensile strengths are plotted for the four configurations that are investigated. The results are shown in Figure 6-3.

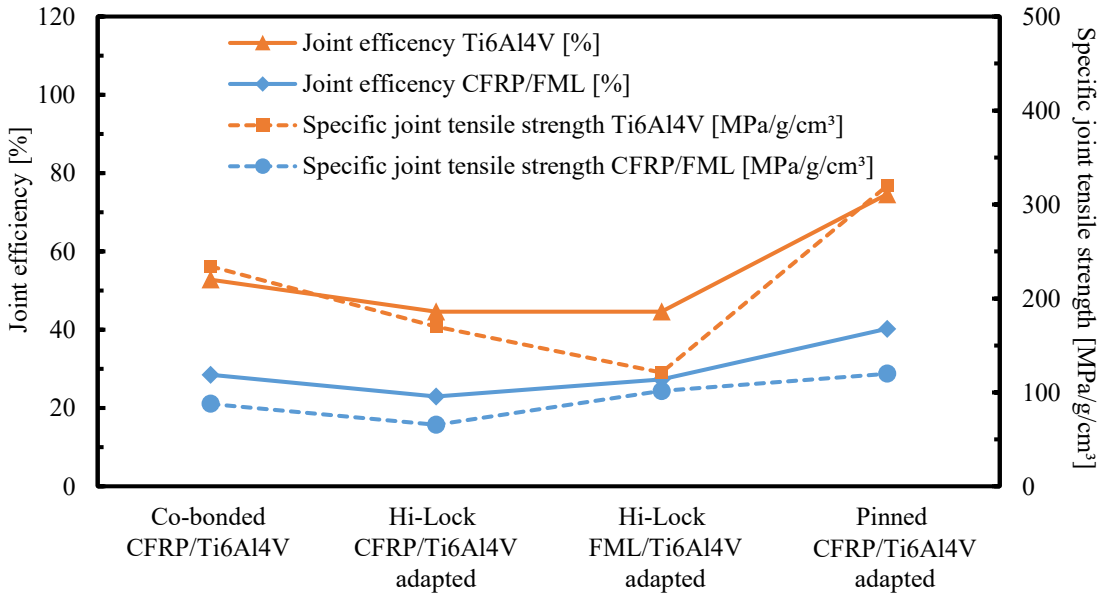

Figure 6-3: Joint efficiencies and specific joint tensile strengths for different joining technologies/adapted geometries
Joint geometries are adapted in order to reach maximum joint tensile strengths, see Figure 6-1 and Table 6-3; circumferential layers for pinned joint, see Figure 5-23 and Figure 5-24

The joint efficiencies for the Hi-lock riveted joint with a pure CFRP joint member differ slightly from the non-adapted geometry. Due to the FML laminate's higher bearing strength in comparison to the pure CFRP laminate, the CFRP or FML joint member's joint efficiency is also higher for the FML/Ti6Al4V Hi-lock joint.

However, fiber-metal-laminates are characterized by an increased density when compared to pure CFRP laminates, which is disadvantageous for lightweight applications. A transition zone is required to join a FML with a CFRP structure, see Chapter 2.2. This transition zone is not considered within these calculations.

In order to evaluate the entire joint in terms of eligibility for lightweight applications, the lightweight efficiency is introduced:

$$Lightweight\ efficiency = \frac{Ultimate\ load\ at\ joint\ failure}{Averaged\ joint\ weight} \tag{6-3}$$

The lightweight efficiencies for the four joining technologies are presented in Figure 6-4.

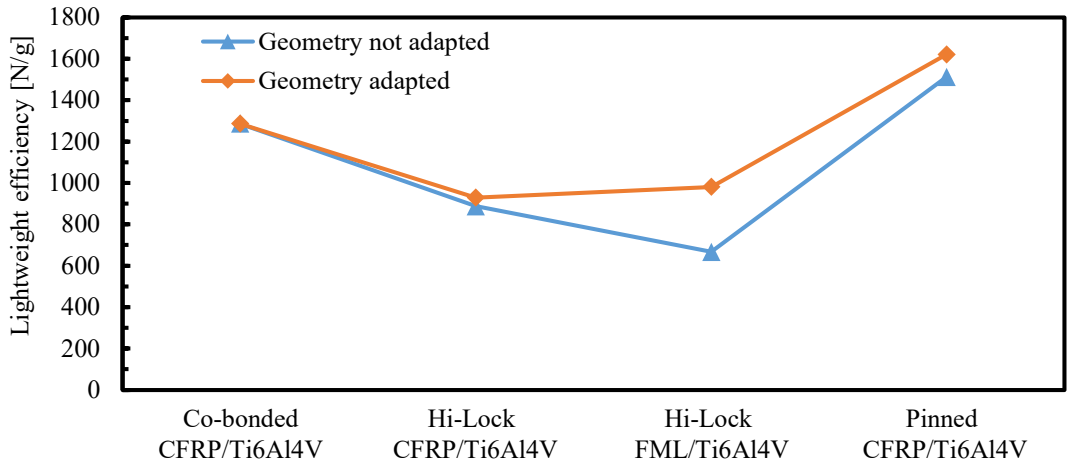

Figure 6-4: Lightweight efficiencies for different joining technologies

Due to its high joint strength and low weight, the co-bonded reference shows strong lightweight efficiency. The CFRP laminate is characterized by a low bearing strength when compared to fiber-metal-laminates or Ti6Al4V. As a result, it is necessary to increase the composite joint member's thickness, which leads to a low lightweight efficiency.

Hi-lock riveted FML/Ti6Al4V joints with an adapted geometry show a higher lightweight efficiency than the CFRP/TiAl4V Hi-lock joints. Although the FML laminate is characterized by a higher density in comparison to the pure CFRP laminate, the bearing strength is increased.

Pinned joints show the highest joint efficiencies for the following reasons:

1. Pins have a much lower weight in comparison to Hi-lock rivets
2. The load introduction into the composite joint member is more efficient as load-carrying fibers are not cut by hole drilling, see also Chapter 5.6
3. The titanium joint member is also reinforced by the pins, as transverse contraction is reduced, see Chapter 5.4.2.5

However, it is important to note that these results only apply for the specific joint geometries displayed in Figure 6-1.

6.2 Influencing parameters

This chapter describes the influence different parameters have on the categories joint stiffness, load at first failure, load at ultimate failure (or joint strength) and manufacturability. These parameters are classified into three evaluation criteria:

- "0" —> no influence
- "+" —> minor influence
- "++" —> major influence

Table 6-4 lists different parameters and evaluates their influence on the four categories. The evaluation is based on testing and simulation as well as literature research. It is only valid for the specific joint configurations investigated within the scope of this thesis.

Table 6-4: Influencing parameters for pinned composite/metal joints

	Parameter	Influence on:			
		Joint stiffness (linear elastic)	Load at first failure	Load at ultimate failure	Manufacturability
a)	Pin head shape	+	n/a	+	++
b)	Pin diameter	+	n/a	++	++
c)	Pin length	+	n/a	++	+
d)	Pin density	+	n/a	++	++
e)	Pin pattern	0	+	0	0
f)	Pin material	0	n/a	++	0
g)	Pinning technology	+	n/a	++	++
h)	Stiffness relation of joint members	++	++	0	0
i)	Fiber undulation around pins vs. drilled holes	+	n/a	++	+
j)	Composite layup [0/90/-45/+45] vs. $[0/90]_2$	+	n/a	+	0
k)	Surface treatment of metallic joint member	0	++	0	++

a) The use of spiky pin head shapes reduces out-of-plane fiber undulations and facilitates pin insertion into the uncured composite material. Utilizing pin head shapes that provide

undercuts, i.e. ball head shaped pin heads, reduce bending of the composite laps towards z-direction. It complicates pin insertion into the uncured composite material, due to an increased pin head diameter.

b) Increasing the pin diameter leads to more distinct fiber undulations, therefore reduces the composite joint member's stiffness. It provides greater pin shear strength and bending stiffness, which can increase the load at ultimate joint failure. Inserting pins into the uncured composite joint member becomes more challenging with larger pin diameters.

c) Using longer pins increases fiber undulations, therefore reduces the composite joint member's stiffness. As pinned joints can fail by interlaminar delamination located close to the pin heads, increasing the pin length can lead to enhanced joint strength.

d) High pin densities result in more distinct fiber undulations, therefore reduce the composite joint member's stiffness. A large number of pins leads to a high overall pin shear strength, which can enhance the overall joint strength. It also increases the fiber volume content and depicts the limiting factor for pin density.

e) Assuming that the mean pin density remains unchanged, altering the pin pattern has no influence on the initial joint stiffness, but on the load at first failure. Decreasing the number of pins in the first pin row increases the load at first failure, see Chapter 5.4.1.3. The pin pattern only shows little impact on the load at ultimate joint failure.

f) As the adhesive bond between the metallic and composite joint member is responsible for load transfer within the linear elastic state, altering the pin material has no influence on the initial joint stiffness. However, using spring steel pins leads to a very high pin shear strength and therefore can result in a high ultimate load at joint failure.

g) The type of pinning technology selected highly influences the pin's shear strength and, depending on the pin diameter and density, also the load at ultimate joint failure. It has a direct impact on the manufacturing effort required. Utilizing inserted pins requires holes to be drilled into the metallic joint member, which reduces its stiffness and load carrying capability.

h) Stiffness balanced double-lap joints provide a greater adhesive joint strength in comparison to unbalanced joints. The joint members' tensile stiffness also influences the magnitude of stress peaks due to thermal variations. Increasing the stiffness of one joint member (metallic or composite) results in greater peak stresses and vice versa.

i) Testing and simulation results presented in Chapter 5.6 show that joints with formed holes (fiber undulations around pins) are characterized by a higher load at ultimate joint failure in comparison to their counterparts with drilled holes within the composite joint member. No information is available in terms of initial joint stiffness as these joints do not include an adhesive bond between the composite and titanium joint member. Inserting the pins into uncured composite laminate increases the manufacturing effort prior to the curing step. However, hole drilling is not necessary.

j) Comparing a joint with a [0/90/-45/+45] layup to a $[0/90]_2$ layup revealed that the layup has little influence on the joint strength. However, joints with a $[\pm45]_2$ showed low joint strength due to the lack of load carrying 0°-layers.

k) Proper surface treatment of the metallic joint member increases the adhesive bond strength, therefore load at first failure. However, it also results in a higher manufacturing effort when compared to joints with untreated metallic surface.

6.3 Intended range of application and design guidelines

The pinning technology should be considered for composite/metal joints under tension if the following requirements are met and boundary conditions are present:

- lightweight efficiency is important
- joint disassembly is not required
- the joint should provide a great ultimate joint strength
- the fail-safe criterion has to be met
- a high energy absorption capacity is key
- the joining area's length is small
- the composite layup includes several fiber directions (0° are essential, 90° and/or ±45° are also necessary; other layups were not investigated within the scope of this thesis)
- the composite joint member consists of prepreg material or NCF and RTM resin (the use of weave material was not investigated within the scope of this thesis)
- a closed rigid tooling facilitates the pin insertion. However, joints can also be manufactured using a semi-rigid tooling, including a rigid bottom tool and vacuum foil

Within the scope of this thesis, 1.5mm diameter spring steel pins combined with a pin density of 5.5% showed good shear strength and bending stiffness. This setup results in an averaged fiber volume fraction of 63.5% within the joining area (60% outside the joining area). Utilizing spiky pins facilitates the insertion into the uncured composite joint member. Adding circumferential layers significantly improves the joint strength, but also limits the possible application cases. Pinned joints showed greater joint strength in comparison to the co-bonded reference, because pins are able to transfer load into the outer composite layers. Co-bonded joints failed due to interlaminar delamination in between the inner composite layers. These investigations only apply for the configurations and geometries tested within the scope of this thesis and might differ for other joint geometries and/or materials.

7 Conclusion

This chapter summarizes the work content of this thesis. However, several topics regarding pinned composite/metal joints are still not fully understood, whereas suggestions for further work are also presented in this chapter.

7.1 Summary

This thesis investigates the mechanical performance of pinned composite/metal joints under quasi-static tension. To gain insight into the strain and stress state within the pinned composite/metal joint, numerous mechanical tests and FE-simulations were performed.

Chapter 1 provides a general background of composite/metal structures, highlights the need for various industrial applications and also explains the challenges that arise when joining carbon fiber composites to metals. In addition, it describes the goal and structure of this work.

The two conventional joining technologies, adhesive bonding and joining through form closure, like riveting or bolting, are first described in Chapter 2. The pinning technology represents a combination of these two joining mechanisms. Former research studies present three technologies for pin creation on the metallic joint member's surface. These technologies are Surfi-Sculpt^{TM}, cold metal transfer (CMT) pinning and additive layer manufacturing (ALM). Chapter 2 focuses further on the state of the art regarding pinned composite/metal joints and also describes mechanical test and simulation results found in former studies. However, these studies differ in terms of joint geometry, material selection and test implementation. Therefore, the need for a comparative study underlying similar conditions becomes apparent. Furthermore, the load introduction from the pins into the composite joint member as well as the impact of fiber undulations on the joint's mechanical performance have not been adequately investigated.

Chapter 3 provides insight into the methods and procedures utilized in this thesis. First, basic requirements for pinned composite/metal joints are explained, followed by a description of the standards, equipment and methods used for destructive testing. A double lap joint specimen design was chosen for the pinned composite/metal joint. However, two different DLS-geometries, differing in thickness of the composite joint member, are used. The joint geometry with thick composite laps (joint design 1) helps to determine the overall load carrying capability of the pinned composite/metal joint. The joint geometry with thin composite laps (joint design 2) serves to evaluate the impact of fiber undulation around the pins on the tensile strength of the composite joint member. Tensile

testing of the pinned composite/metal joints was performed with the help of digital image correlation (DIC) techniques to capture the deformation state on the specimen's surface. All pinned joints were tested with an identical free crosshead speed. In addition to mechanical testing, FE-modelling was conducted to investigate the stress state within the joint and the mechanical interaction between composite and metallic joint member and pins. However, proper FE-modelling requires correct material input parameters. Therefore, several mechanical tests were performed on coupon level:

- metal tension
- CFRP tension
- Mode I fracture toughness
- Mode II fracture toughness
- neat resin tension
- neat resin compression

Measurement of the fiber undulation, depending on the predominant fiber direction, is necessary to set up a detailed FE-model. Based on the two different joint geometries mentioned above, FE-models for the pinned composite/metal joint were created. On the one hand, the FE-model for joint design 1 does not cover fiber undulation, but is less computationally intensive than the model for joint design 2. On the other hand, the FE-model for joint design 2 includes fiber undulation and allows for a detailed analysis of the in-plane load transfer from pins to the composite joint member. The mechanical behavior of the metallic joint member and pins is computed using a material model which covers plasticity and ductile damage with linear damage degradation. Interlaminar and - in the case of joint design 2 -, intra-laminar delamination is taken into account by utilizing cohesive elements. A Hashin-failure criterion helps to describe in-plane failure for the FE-model of joint design 1 and fiber tension failure for joint design 2.

Chapter 4 describes the methods, procedures and technologies used for specimen manufacturing. The manufacturing chain consists of six steps:

1. Pin creation/insertion onto or into the metallic joint member
2. Preforming of NCF or prepreg material
3. Pin insertion into the uncured composite joint member
4. Resin infusion (NCF) or dwell phase (prepreg)
5. Resin cure
6. Cutting and trimming

First, the pinned metallic sheets created via laser pinning, similar to Surf Sculpt^{TM} technology, CMT pinning and inserted pinning are presented. Pin insertion into the uncured composite joint member represents a key aspect within the manufacturing chain of pinned composite/metal joints. In order to minimize fiber breakage, correct positioning of the fibrous material (NCF or prepreg) in relation to the pinned metal sheet and the right selection of the supporting material is essential. In the case of joint design 1, the dry NCF-material is impregnated with RTM-resin in a closed mold, mounted on a press.

The pressure difference between resin inlet and outlet was adjusted with an estimation based on Darcy's law. Therefore, the mold geometry, resin viscosity, permeability of the NCF material, fiber volume fraction and maximum possible infusion time have to be taken into consideration. To assure complete preform filling and minimum void content, an adapted infusion approach was developed. Prepreg processing also took place within a closed mold under the pressure of a press. Cutting and trimming of the composite/metal panels was performed with a waterjet cutting and grinding machine, respectively.

All testing and simulation results are presented in Chapter 5. First, the appropriate pinning technology had to be chosen. Tensile testing results show that CMT-pinned specimens and specimens with inserted pins could reach a joint tensile strength at a comparable level. A lower joint tensile strength is observed for laser pinned specimens as laser pins are not able to provide sufficient pin bending stiffness and shear strength. Due to a more uniform material structure, hence mechanical properties, inserted pins were chosen for further investigation. The material input data for the metallic joint member was determined with the help of tensile testing. Whereas mechanical tensile testing of [0/90] and [±45] is used to identify the linear elastic in-plane material behavior and strength of the NCF/PR520 combination, material data for the 5320-1 prepreg material is taken from the data sheet. Mechanical testing for Mode I fracture toughness indicates that the stitching pattern of the NCF material has a high influence on the G_{Ic}-value. A stitching pattern, oriented perpendicular to the direction of crack propagation leads to a G_{Ic}-value more than two times as great as the stitching pattern oriented at 45° in respect to the direction of crack propagation. To evaluate the Mode I fracture toughness between metallic and composite joint member, hybrid Ti/NCF/PR520 DCB-specimens were also tested. Fiber-bridging was observed and the initial value of G_{Ic} reached high values around 1100J/m². In addition to the configurations with NCF material, Mode I fracture toughness was also investigated for Prepreg 5320-1. To evaluate the Mode II fracture toughness, ENF-specimens were tested for the configurations mentioned above. Neat resin testing, tension and compression, are necessary to obtain material input data for the FE-modelling of resin rich zones adjacent to the pins.

Several configurations were tested to investigate stiffness and strength properties of hybrid composite/titanium joints of joint geometry 1:

- co-bonded reference with surface treatment of titanium (acid etched + primer)
- pinned with 6x4 pin pattern
- co-bonded reference with surface treatment of titanium and circumferential layers
- pinned with 6x4 pin pattern and circumferential layers
- co-bonded reference, no surface treatment of titanium - clamped
- pinned with 5x4 pin pattern - clamped
- pinned with 6x4 pin pattern - clamped
- pinned with 334455 pin pattern - clamped
- pinned with 554433 pin pattern - clamped

- pinned with 345543 pin pattern - clamped
- pinned with 543345 pin pattern - clamped

Co-bonded reference hybrid composite/titanium baseline joints with surface treatment reach a mean joint tensile strength of 555MPa, referenced to the cross section of the titanium joint member. An increase of 25% in tensile strength can be observed for the pinned joints with six pin rows and four pins each row. These pinned joints failed due to a deflection of the composite laps towards the thickness direction, as already observed for the pinned composite/steel joints. To prevent this failure mode, circumferential unidirectional prepreg layers were winded around the composite and titanium joint member. Whereas these circumferential layers have only a negligible influence on the joint strength of the co-bonded reference joint, the joint strength of the pinned configuration reaches values 35% greater than those of the co-bonded reference joints.

A clamping device was developed, preventing deflection of the composite layers towards the thickness direction, while still enabling inspection of the lateral surface of the joining area by the DIC-system. None of the pinned joints were subjected to a special surface treatment of the titanium insert. Therefore, a co-bonded reference joint without surface treatment was clamped inside the device and tested, resulting in a mean joint tensile strength of 430MPa. Mean joint tensile strength is 90% greater (799MPa) for a joint with a rectangular 5x4 pin pattern (20 pins) and 101% greater (866MPa) for a 6x4 pin pattern with 24 pins. Pinned composite/titanium joints with 30 pins and different pin patterns reach mean tensile strengths ranging from 810MPa to 936MPa, whereas the greatest values were measured for the 334455 pin pattern.

First failure of the pinned joints is always characterized by adhesive failure in the interface between titanium and composite joint member. However, after adhesive failure, pins take over the load which results in a degradation of joint stiffness. If the pins' shear strength is sufficient, ultimate failure occurs at a higher joint tensile load than first failure. Different failure modes can be observed for the pinned configurations. Specimens finally fail due to titanium net section failure in the first pin row, pin shear failure and interlaminar delamination in the composite. The comparison of a surface treated co-bonded reference joint and a pinned joint with 24 pins indicate that a growth of 62% in joint tensile strength is possible.

FE-analysis was conducted for all configurations of joint design 1. Whereas the joint stiffness until first failure can be accurately predicted, the joint stiffness after first failure is overestimated by the FE-analysis. The joint strength is only slightly overrated by the simulation. However, no fiber undulations are implemented into the FE-model for joint design 1. Therefore, the tests and FE-analyses for pinned composite/titanium joints of joint design 2 aim to determine the impact of fiber undulation on the joints' tensile behavior. Measurement of fiber undulation show that resin pockets form for the ±45° plies, whereas resin pockets and resin channels can be observed for the 0° and 90°-direction.

To evaluate the impact of fiber undulation on the joint behavior, joints with formed holes were tensile tested against joints with drilled holes in the composite laminate. Whereas the joints with drilled holes were produced by means of drilling holes into the cured laminate, the pins for the configurations with formed holes were inserted into the uncured laminate. As a result, fibers are cut for the configuration with drilled holes, but undulate for the configuration with formed holes. The load carrying capability of the joints with formed holes is 25% and 32% greater for a quasi-isotropic and 0°/90° cross-ply laminate when comparing to their counterparts with drilled holes. A detailed analysis of local strain distribution on the surface of the outer 0°-plies, measured by the DIC system, indicate that a more homogeneous strain distribution is present for the specimens with formed holes than for their counterparts with drilled holes.

As inspection of areas close to pins is not possible due to restrictions of the DIC-technique, investigation of these areas was done with the help of FEA. Two FE-models containing only resin pockets or only resin channels within the 0° and 90°-plies were set up. Local stress peaks, located adjacent to the pins, lead to fiber tension failure. Therefore, the joint efficiency does not reach a value of 100%.

It can be stated that the increase in joint tensile strength of joints with formed holes in comparison to the joints with drilled holes is primarily because of the minimization of fiber breakage of load-carrying 0°-fibers. Pinned composite/metal joints with formed holes reached a joint tensile strength up to 89% of the tensile strength of the titanium joint member (Ti6Al4V) or approximately 75% of the composite joint member (Prepreg 5320-1 quasi-isotropic layup). These values only apply for the configurations tested within the scope of this thesis. The maximum obtained shear strength, referred to as the adhesively bonded area (2*25.4mm*39.5mm), can be calculated to 35.6MPa. When referring to the pinned area (2*25.4mm*30.5mm), the shear strength calculates to 46.0MPa. In addition, as a result of their multi-stepped damage progression, pinned joints fulfill the requirements of the fail-safe design philosophy.

7.2 Future work

To further investigate the mechanical behavior of pinned composite/metal joints in a quasi-isotropic tensile stress state, several studies are plausible. Telecentrical illumination and objectives could eliminate the shadowing impact around the pins in test series 4 and therefore enlarge the inspected area. However, edge effects, mentioned in Chapter 3.2.5.3, cannot be completely suppressed. Within the past few years, several advanced imaging technologies have been developed, which could help to not only inspect the surface of the specimen, but also the entire volume. Modern Computed Tomography scanners, Confocal Imaging Microscope architectures or Magnetic Resonance Imaging could be used to capture the volumetric image data during testing. Volumetric Digital Image Correlation techniques could visualize the strain state within all composite plies and further help to measure the fiber orientation during testing.

Refining the FE-modelling input data and improving the material models, especially for neat resin under compression, could increase the predictability of the pinned composite/metal joint's mechanical behavior via FE-methods.

This thesis primarily focused on the mechanical behavior of the composite joint member and the effects of fiber undulation around the pin. Improving technologies for pin creation was not the goal of this research. Further development of CMT or additive layer manufacturing technology could increase the joint stiffness and strength of pinned composite/titanium joints, as drilling holes into the metallic joint member was not necessary. However, both technologies have to be able to provide high pin shear strength and bending stiffness.

The use of circumferential layers was proven to be an effective method to suppress deflection of the composite laps in z-direction, but also leads to restrictions for possible joint designs. Undercuts on the top of the pins help to reduce this deflection behavior. However, a technology which could enable the creation of these undercuts after curing of the resin on top of the pins would facilitate the pin insertion. Due to a low pin diameter, the force necessary for pin insertion and the risk of fiber breakage within the dry fiber or uncured prepreg material would be reduced.

The mechanical response of these structures under compressive and torsional loading or bending around the *y*- or *z*- axis is still inadequately researched and therefore another topic to investigate.

References

[1] Mouritz A P, *Introduction to Aerospace Materials*. Cambridge, UK: Elsevier Science, 2012.

[2] Litchfield R E, Critchlow G W, Wilson S, "Surface cleaning technologies for the removal of crosslinked epoxide resin", *International Journal of Adhesion and Adhesives*, vol. 26, no. 5, pp. 295–303, 2006.

[3] Bardis J, Kedward K, *Effects of Surface Preparation on the Long-Term Durability of Ahesively Bonded Composite Joints*. Springfield, Virginia/USA: Department of Mechanical & Environmental Engineering, University of California Santa Barbara, CA 93106, 2004.

[4] Hart-Smith L J, Ed., *The critical Factors controlling the Durability of bonded Composite Joints: Surface Preparation and the Presence or Absence of pre-bond Moisture*. Seattle, Washington/US, 2004.

[5] Arenas J M, Alía C, Narbón J J, Ocaña R, González C, "Considerations for the industrial application of structural adhesive joints in the aluminium–composite material bonding", *Composites Part B: Engineering*, vol. 44, no. 1, pp. 417–423, 2013.

[6] Critchlow G W, Brewis D M, "Review of surface pretreatments for titanium alloys", *International Journal of Adhesion and Adhesives*, vol. 15, pp. 161–172, 1995.

[7] Critchlow G W, Cottam C A, Brewis D M, Emmony D C, "Further studies into the effectiveness of C02-1aser treatment of metals for adhesive bonding", *International Journal of Adhesion and Adhesives*, vol. 17, pp. 143–150, 1997.

[8] Ingram C, Ramani K, "The effect of sodium hydroxide anodization on the durability of poly(etherketonetherketoneketone) adhesive bonding of titanium", *International Journal of Adhesion and Adhesives*, vol. 17, pp. 39–45, 1997.

[9] Molitor P, Barron V, Young T, "Surface treatment of titanium for adhesive bonding to polymer composites: a review", *International Journal of Adhesion and Adhesives*, vol. 21, no. 2, pp. 129–136, 2001.

[10] Bowditch M R, "The durability of adhesive joints in the presence of water" *International Journal of Adhesion and Adhesives*, vol. 16, pp. 73–79, 1996.

[11] Hart-Smith L J, *Adhesive-bonded Douple-Lap Joints*. Hampton, Virginia/USA: National Aeronautis and Space Administration, 1973.

[12] Mubashar A, Ashcroft I A, Critchlow G W, Crocombe A D, "Moisture absorption–desorption effects in adhesive joints", *International Journal of Adhesion and Adhesives*, vol. 29, no. 8, pp. 751–760, 2009.

[13] Hart-Smith L J, *Analysis and design of advanced composite joints*. Washington D.C./USA: National Aeronautis and Space Administration, 1974.

[14] Wang C H and Gunnion A, *Design Methodology for Scarf Repairs to Composite Structures*. Fishermans Bend, Victoria/Australia: DSTO 0H Defence Science and Technology Organisation, 2006.

[15] Volkersen O, “Die Nietkraftverteilung in Zugbeanspruchten Nietverbindungen mit Konstanten Laschenquerschnitten”, *Luftfahrtforschung*, vol. 15, pp. 4–47, 1938.
[16] de Bruyne N A, “The strength of glued joints”, *Aircraft Engineering*, vol. 16, pp. 115–118, 1944.
[17] Tsai M Y, Morton J, “An investigation into the stresses in double-lap adhesive joints with laminated composite adherends”, *International Journal of Solids and Structures*, vol. 47, pp. 3317–3325, 2010.
[18] Schürmann H, Elter A, “Beitrag zur Gestaltung von Schraubverbindungen bei Laminaten aus Faser-Kunststoff-Verbunden”, *Konstruktion*, vol. 1-2, no. 62-66, 2013.
[19] Department of Defence - United States of America, *Composite Materials Handbook - MIL-HDBK-17-3F: Volume 3. Polymer Matrix Composites - Materials Usage, Design, and Analysis*: Department of Defence - United States of America, 2002.
[20] *Cycom PR520 RTM resin - data sheet*.
[21] Callister W D, Rethwisch D G, *Materials Science and Engineering: an Introduction - eighth edition,* 8th ed. New York/USA: John Wiley & Sons, 2010.
[22] Oberg E, Jones F D, Horton H L, Ryffel H H, *Machinery's Handbook: 29th Edition*. New York/USA: Industrial Press, 2012.
[23] Chen W T, Nelson C W, “Thermal Stress in Bonded Joints”, *IBM Journal of Research and Development*, vol. 23, no. 2, pp. 179–188, 1979.
[24] Schürmann H, *Konstruieren Mit Faser-Kunststoff-Verbunden,* 2nd ed. Berlin/Germany: Springer-Verlag Berlin and Heidelberg GmbH & Co. KG, 2008.
[25] Heslehurst L B, Hart-Smith L J, “The science and art of structural adhesive bonding”, *SAMPE Journal*, vol. 38, pp. 60–71, 2002.
[26] Thoppul S D, Finegan J, Gibson R F, “Mechanics of mechanically fastened joints in polymer–matrix composite structures – A review”, *Composites Science and Technology*, vol. 69, pp. 301–329, 2009.
[27] Tserpes K I, Labeasb G, Papanikosb P, Kermanidisa T, “Strength prediction of bolted joints in graphite/epoxy composite laminates”, *Composites Part B: Engineering*, vol. 33, pp. 521–529, 2002.
[28] Wilmes H, Herrmann A S, Kolesnikov B, Kröber I, *Festigkeitsanalysen von Bolzenverbindungen für CFK-Bauteile mit dem Ziel der Erstellung von Dimensionierungsrichtlinien*. Braunschweig/Germany.
[29] Tong L, Soutis C, *Recent Advances in Structural Joints and Repairs for Composite Materials*. Dordrecht/Netherlands: Springer-Science+Business Media B.V., 2003.
[30] Camanho P P, Matthews F L, “Stress analysis and strength prediction of mechanically fastened joints in FRP: a review”, *Composites Part A: Applied Science and Manufacturing*, vol. 28A, pp. 529–547, 1997.

[31] Gay D, Hoa S H, Tsai S W, *Composite Materials: Materials Design and Applications*. Boca Raton, Florida/US: CRC Press LLC, 2003.
[32] Heslehurst R B, "Composite Structures Joint Design Technology", Dallas, Texas/US, 10/2015.
[33] Crothers P J, Drechsler K, Feltin D, Herszberg I, Kruckenberg T, "Tailored fibre placement to minimise stress concentrations", *Composites Part A: Applied Science and Manufacturing*, vol. 28A, pp. 619–625, 1997.
[34] Kolesnikov B, Herbeck L, Fink A, Ed., *Fortschrittliche Verbindungstechniken von Faserverbundstrukturen*. Dresden/Germany, 2004.
[35] Fink A, Camanho P P, Andrés J M, Pfeiffer E, Obst A, "Hybrid CFRP/titanium bolted joints: Performance assessment and application to a spacecraft payload adaptor", *Composites Science and Technology*, vol. 70, pp. 305–317, 2010.
[36] Wittenberga T C, van Batena T J, de Boerb A, "Design of fiber metal laminate shear panels for ultra-high capacity aircraft", *Aircraft Design*, vol. 4, pp. 99–113, 2001.
[37] Camanho P P, Fink A, Obst A, Pimenta S, "Hybrid titanium–CFRP laminates for high-performance bolted joints", *Composites Part A: Applied Science and Manufacturing*, vol. 40, no. 12, pp. 1826–1837, 2009.
[38] Fink A, Kolesnikov B, Wilmes H, *CFRP/Titanium hybrid material improving composite structure coupling*. Braunschweig/Germany.
[39] Both J C, "Tragfähigkeit von CFK-Metall-Laminaten unter mechanischer und thermischer Belastung", PhD, Lehrstuhl für Leichtbau, Technische Universität München, Munich/Germany, 2014.
[40] Havar T, "Beitrag zur Gestaltung und Auslegung von 3D-verstärkten Faserverbundschlaufen", PhD, Institut für Flugzeugbau, Universität Stuttgart, Stuttgart/Germany, 2007.
[41] Byrd L W, Birman V, "Effectiveness of z-pins in preventing delamination of co-cured composite joints on the example of a double cantilever test", *Composites Part B: Engineering*, vol. 37, no. 4-5, pp. 365–378, 2006.
[42] Cartie D D R, "Effect of Z-Fibres TM on the Delamination Behaviour of Carbon Fibre I Epoxy Laminates", PhD, School of Industrial and Manufacturing Science-Advanced Materials Department, Cranfield University, Cranfield/UK, 2000.
[43] Chang P, "The Mechanical Properties and Failure Mechanisms of Z-Pinned Composites", PhD, School of Aerospace, RMIT University, Melbourne, Victoria/Australia, 2006.
[44] Chang P, Mouritz A P, Cox B N, "Properties and failure mechanisms of pinned composite lap joints in monotonic and cyclic tension", *Composites Science and Technology*, vol. 66, no. 13, pp. 2163–2176, 2006.
[45] Dantuluri V, Maiti S, Geubelle P H, Patel R, Kilic H, "Cohesive modeling of delamination in Z-pin reinforced composite laminates", *Composites Science and Technology*, vol. 67, no. 3-4, pp. 616–631, 2007.

[46] Mouritz A P, “Review of z-pinned composite laminates”, *Composites Part A: Applied Science and Manufacturing*, vol. 38, no. 12, pp. 2383–2397, 2007.
[47] Mouritz A P, “Delamination properties of z-pinned composites in hot–wet environment”, *Composites Part A: Applied Science and Manufacturing*, vol. 52, pp. 134–142, 2013.
[48] Heimbs S, Nogueira A C, Hombergsmeier E, May M, Wolfrum J, “Failure behavior of composite T-joints with novel metallic arrow-pin reinforcement”, *Composite Structures*, vol. 110, pp. 16–28, 2014.
[49] Nogueira A C, Drechsler K, Hombergsmeier E, Pacchione M, Ed., *Investigation of the Properties and Failure Mechanisms of a Damage Tolerant 3D-reinforced Joint for Lightweight Structures*. Leiden/Netherlands, 2011.
[50] Nogueira A C, Drechsler K, Hombergsmeier E, Ed., *Analysis of the static and fatigue strength of a damage tolerant 3D-reinforced joining technology on composite single lap joints*. Noordwijk/Netherlands, 2012.
[51] Jürgens M, Nogueira A C, Lang H, Hombergsmeier E, Drechler K, Ed., *Influence of an optimized 3D-reinforcement layout on the structural mechanics of co-bonded CFRP joints. In: Proceedings of the 16th European conference on composite materials*. Sevilla/Spain, 2014.
[52] Löbel T, Kolesnikov B, Scheffler S, Stahl A, Hühne C, “Enhanced tensile strength of composite joints by using staple-like pins: Working principles and experimental validation”, *Composite Structures*, vol. 106, pp. 453–460, 2013.
[53] Schierl A, “The CMT process a Revolution in welding technology”, *Welding in the World*, vol. 49, no. 9, p. 38, 2005.
[54] Ucsnik S, Scheerer M, Zaremba S, Pahr D H, “Experimental investigation of a novel hybrid metal–composite joining technology”, *Composites Part A: Applied Science and Manufacturing*, vol. 41, no. 3, pp. 369–374, 2010.
[55] Stelzer S, Ucsnik S, Pinter G, “Strength and damage tolerance of composite–composite joints with steel and titanium through the thickness reinforcements”, *Composites Part A: Applied Science and Manufacturing*, vol. 88, pp. 39–47, 2016.
[56] Stelzer S, Ucsnik S, Pinter G, “Fatigue behaviour of composite–composite joints reinforced with cold metal transfer welded pins”, *International Journal of Fatigue*, vol. 81, pp. 37–47, 2015.
[57] Stelzer S, “Optimized experimental methods for the description of the delamination and failure behavior of high performance composites and joints”, PhD, Institute of Materials Science and Testing of Polymers, Montanuniversitaet Leoben, Leoben/Austria, 2014.
[58] Di Giandomenico V, “Surface structured bonded composite-metal joint”, PhD, School of Applied Science - Advanced Materials, Cranfield University, Cranfield/UK, 2014.
[59] Graham P D, Rezai A, Baker D, Smith P A, Watts J F, *Hybrid joints: High strength multi-material joints*. Bristol/UK.

[60] Graham P D, Rezai A, Baker D, Smith P A, Watts J F, Ed., *A hybrid joining scheme for high strength multi-material joints*. Jeju Island/Korea, 2011.
[61] Joesbury A M, "New approaches to composite metal joining", PhD, School of Aerospace, Transport and Manufacturing, Cranfield University, Cranfield/UK, 2015.
[62] Smith F, Ed., *COMELD - An innovation in composite to metal joining*. Bromsgrove/UK, 2004.
[63] Tu W, "Comeld TM Joints: Optimisation of Geometric Parameters of the Protrusions", PhD, Department of Materials, Queen Mary, University of London, London/UK, 2011.
[64] Wang X, Ahn J, Kaboglu C, Yu L, Blackman, Blackman R K, "Characterisation of composite-titanium alloy hybrid joints using digital image correlation", *Composite Structures*, vol. 140, pp. 702–711, 2016.
[65] Wang X, Ahn J, Lee J, Blackman R K, "Investigation on failure modes and mechanical properties of CFRP-Ti6Al4V hybrid joints with different interface patterns using digital image correlation", *Materials & Design*, vol. 101, pp. 188–196, 2016.
[66] Bianchi F, "Numerical Modelling of Through-Thickness Reinforced Structural Joints", PhD, School of Engineering, Cranfield University, Cranfield/UK, 2012.
[67] Earl C, Hilton P, O'Neill B, "Parameter Influence on Surfi-Sculpt Processing Efficiency", *Physics Procedia*, vol. 39, pp. 327–335, 2012.
[68] Dickinson L C, Farley G L, Hinders M K, "Prediction of Effective Three-Dimensional Elastic Constants of Translaminar Reinforced Composites", *Journal of Composite Materials*, vol. 33, no. 11, pp. 1002–1029, 1999.
[69] Grassi M, Zhang X, Meo M, "Prediction of stiffness and stresses in z-fibre reinforced composite laminates", *Composites Part A: Applied Science and Manufacturing*, vol. 33, no. 12, pp. 1653–1664, 2002.
[70] Stringer L G, Hiley M J, Ed., *Through-thickness reinforcement of composites: z-pinning, stitching and 3-D weaving*. San Diego, California/USA, 2003.
[71] Partridge I K, Cartie´ D D R, Troulis M, Grassi M, Zahng X, Ed., *Evaluating the mechanical effectiveness of z-pinning*. San Diego, California/USA, 2004.
[72] Mouritz A P, "Compression properties of z-pinned composite laminates", *Composites Science and Technology*, vol. 67, no. 15-16, pp. 3110–3120, 2007.
[73] Freitas G, Magee C, Dardzinski P, Fusco T, "Fibre insertion process for improved damage tolerance in aircraft laminates", *Journal of Advanced Materials*, vol. 25, no. 4, pp. 36–43, 1994.
[74] Huang H J, Waas A M, "Modeling and predicting the compression strength limiting mechanisms in Z-pinned textile composites", *Composites Part B: Engineering*, vol. 40, no. 6, pp. 530–539, 2009.
[75] Freitas G, Fusco T, Campbell T, Harris J, Rosenberg S, Ed., *Z-Fibre technology and products for enhancing composite design*. Florence/Italy, 1996.

[76] Steeves C A, Fleck N A, “In-plane properties of composite laminates with through-thickness pin reinforcement”, *International Journal of Solids and Structures*, vol. 43, no. 10, pp. 3197–3212, 2006.
[77] Brown N W A, Worrall C M, Ogin S L, Smith P A, “Investigation into the mechanical properties of thermoplastic composites containing holes machined by a thermally-assisted piercing (TAP) process”, *AMPCS: Advanced Manufacturing: Polymer & Composite Science*, vol. 1, no. 4, pp. 199–209, 2016.
[78] Seidlitz H, Ulke-Winter L, Kroll L, “New Joining Technology for Optimized Metal/Composite Assemblies”, *Journal of Engineering*, vol. 2014, no. 9, pp. 1–11, 2014.
[79] Grassi M, “Numerical modelling of composite laminates with through-thickness-reinforcements”, PhD, College of Aeronautics, Cranfield University, Cranfield/UK, 2004.
[80] Grassi M, Zhang X, “Finite element analyses of mode I interlaminar delamination in z-fibre reinforced composite laminates”, *Composites Science and Technology*, vol. 63, no. 12, pp. 1815–1832, 2003.
[81] Song M C, Sankar B V, Subhash G, Yen C F, “Analysis of mode I delamination of z-pinned composites using a non-dimensional analytical model”, *Composites Part B: Engineering*, vol. 43, no. 4, pp. 1776–1784, 2012.
[82] Bianchi F, Zhang X, “Predicting mode-II delamination suppression in z-pinned laminates”, *Composites Science and Technology*, vol. 72, no. 8, pp. 924–932, 2012.
[83] Hart-Smith L J, Ed., *Adhesive-bonded joints for composites: Phenomenological considerations, Douglas Paper 6707.* El Segundo, California/USA, 1978.
[84] Gefu J, Ouyang Z, Guoqiang L, “Effects of bondline thickness on Mode-I nonlinear interfacial fracture of laminated composites: An experimental study”, *Composites Part B: Engineering*, vol. 47, pp. 1–7, 2013.
[85] Bruyneel M, Delsemme J P, Goupil A C, Jetteur P, Lequesne C, Naito T, Urushiyama Y, Ed., *Damage Modelling of Laminated Composites:: Validation of the intra laminar Law of SAMCEF at the Coupon Level for UD Plies*. Seville/Spain, 2014.
[86] Klug H P, Appel U, *Aramis User manual - Software*. Braunschweig/Germany: GOM mbh, 2011.
[87] Sutton M A, Orteu JJ, Schreier H W, *Image Correlation for Shape, Motion and Deformation Measurements*. New York/USA: Springer US, 2009.
[88] *ASTM D 3528-96 (Reapproved 2008), Standard Test Method for Strength Properties of Double Lap Shear Adhesive Joints by Tension Loading*.
[89] *DIN EN ISO 6892-1:2014-06, Metallische Werkstoffe - Zugversuch - Teil 1: Prüfverfahren bei Raumtemperatur (ISO/DIS 6892-1:2014); Deutsche Fassung prEN ISO 6892-1:2014*.
[90] *DIN 50125:2009-07, Prüfung metallischer Werkstoffe - Zugproben*.

[91] *ASTM D 3039/D 3039M-00, Standard Test Method for Tensile Properties of Polymer Matrix Composite Materials*.
[92] *ASTM D 3518/D 3518M - 94 (Reapproved 2001), Standard Test Method for In-Plane Shear Response of Polymer Matrix Composite Materials by Tensile Test of a +-45° Laminate*.
[93] *ASTM D 5528-01, Standard Test Method for Mode I Interlaminar Fracture Toughness of Unidirectional Fiber-Reinforced Polymer Matrix Composites*.
[94] *DIN EN 6034:2016-02, Luft- und Raumfahrt- Kohlenstofffaserverstärkte Kunststoffe- Prüfverfahren - Bestimmung der interlaminaren Energiefreisetzungsrate, Mode II - GIIc; Deutsche und Englische Fassung EN 6034:2015*.
[95] *DIN EN ISO 527-1:2012-06, Kunststoffe – Bestimmung der Zugeigenschaften – Teil 1: Allgemeine Grundsätze (ISO 527-1:2012); Deutsche Fassung EN ISO 527-1:2012*.
[96] *DIN EN ISO 527-2:2012-06, Kunststoffe - Bestimmung der Zugeigenschaften – Teil 2: Prüfbedingungen für Form- und Extrusionsmassen (ISO 527-2:2012); Deutsche Fassung EN ISO 527-2:2012*.
[97] *DIN EN ISO 604:2003-12, Kunststoffe - Bestimmung der Druckeigenschaften (ISO 604:2002); Deutsche Fassung EN ISO 604:2003*.
[98] Kelly G, Hallström S, "Bearing strength of carbon fibre/epoxy laminates: effects of bolt-hole clearance", *Composites Part B: Engineering*, vol. 35, no. 4, pp. 331–343, 2004.
[99] Blanc R, Germain C J, Baylou P, Cataldi M, "Fiber orientation measurements in composite materials", *Composites Part A: Applied Science and Manufacturing*, vol. 37, no. 2, pp. 197–206, 2006.
[100] Dassault Systèmes, *Abaqus 6.14 Documentation*: Dassault Systèmes, 2014.
[101] Hashin Z, Rotem A, "A Fatigue Failure Criterion for Fiber Reinforced Materials", *Journal of Composite Materials*, vol. 7, no. 4, pp. 448–464, 1973.
[102] Hashin Z, "Failure Criteria for Unidirectional Fiber Composites", *Journal of Applied Mechanics*, vol. 47, pp. 329–334, 1980.
[103] Lapczyk I, Hurtado J A, "Progressive damage modeling in fiber-reinforced materials", *Composites Part A: Applied Science and Manufacturing*, vol. 38, no. 11, pp. 2333–2341, 2007.
[104] Benzeggagh M L, Kenane M, "Measurement of mixed-mode Delamination Fracture Toughness of Unidirectional Glass/Epoxy Composites with mixed-mode bending Apparatus", *Composites Science and Technology*, vol. 56, pp. 439–449, 1996.
[105] Camanho P P, Davila C G, de Moura M F, "Numerical Simulation of Mixed-mode Progressive Delamination in Composite Materials", *Journal of Composite Materials*, vol. 37, no. 16, pp. 1415–1438, 2003.
[106] Earl C, Castrejón-Pita J R, Hilton P A, O'Neill W, "The dynamics of laser surface modification", *Journal of Manufacturing Processes*, vol. 21, pp. 214–223, 2016.

[107] Fuchs A N, Wirth F X, Rinck P, Zaeh M F, “Laser-generated Macroscopic and Microscopic Surface Structures for the Joining of Aluminum and Thermoplastics using Friction Press Joining”, *Physics Procedia*, vol. 56, pp. 801–810, 2014.

[108] Liu B, Bickerton S, Advanit S G, “Modelling and simulation of resin transfer moulding (RTM)-gate control, venting and dry spot prediction”, *Composites Part A: Applied Science and Manufacturing*, vol. 27A, pp. 135–141, 1996.

[109] Lebrun G, Gauvin R, Kendall K N, “Experimental investigation of resin temperature and pressure during filling and curing in a flat steel RTM mould”, *Composites Part A: Applied Science and Manufacturing*, vol. 27A, pp. 347–355, 1996.

[110] Hsiao K T, Advani S G, “Flow sensing and control strategies to address race-tracking disturbances in resin transfer molding. Part I: design and algorithm development”, *Composites Part A: Applied Science and Manufacturing*, vol. 35, no. 10, pp. 1149–1159, 2004.

[111] Jiang S, Zhang C, Wang B, “Optimum arrangement of gate and vent locations for RTM process design using a mesh distance-based approach”, *Composites Part A: Applied Science and Manufacturing*, vol. 33, no. 4, pp. 471–481, 2002.

[112] Lawrence J M, Barr J, Karmakar R, Advani S G, “Characterization of preform permeability in the presence of race tracking”, *Composites Part A: Applied Science and Manufacturing*, vol. 35, no. 12, pp. 1393–1405, 2004.

[113] *Hexcel ST15 RTM resin - data sheet*.

[114] *Lisi Aerospace Hi-lock HL10 - data sheet*.

[115] Matsuzaki R, Shibata M, Todoroki A, “Improving performance of GFRP/aluminum single lap joints using bolted/co-cured hybrid method”, *Composites Part A: Applied Science and Manufacturing*, vol. 39, no. 2, pp. 154–163, 2008.

A Appendix

a Diagrams

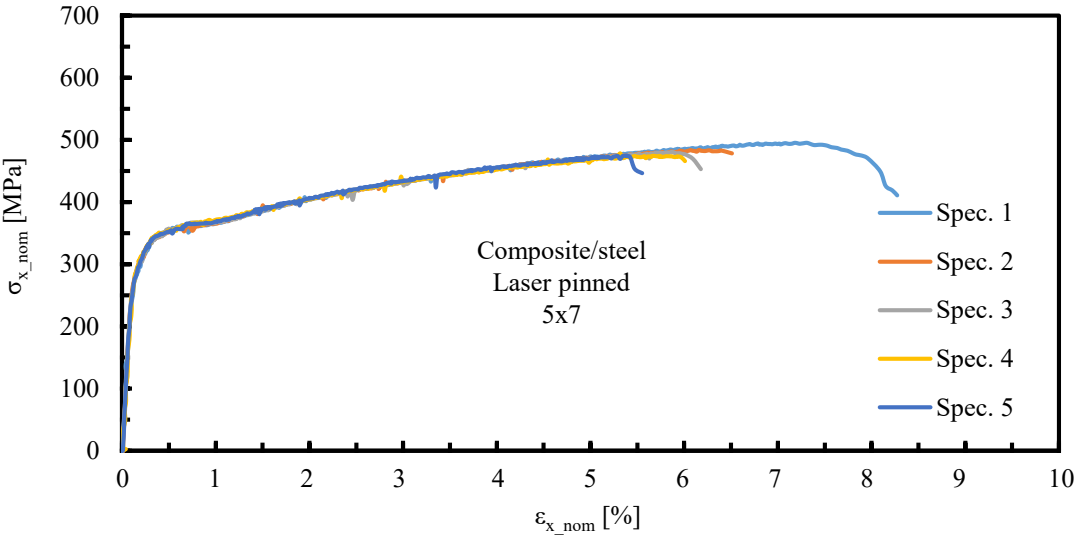

Figure A-1: Pinned composite/steel joint - laser 5x7 - joint design 1

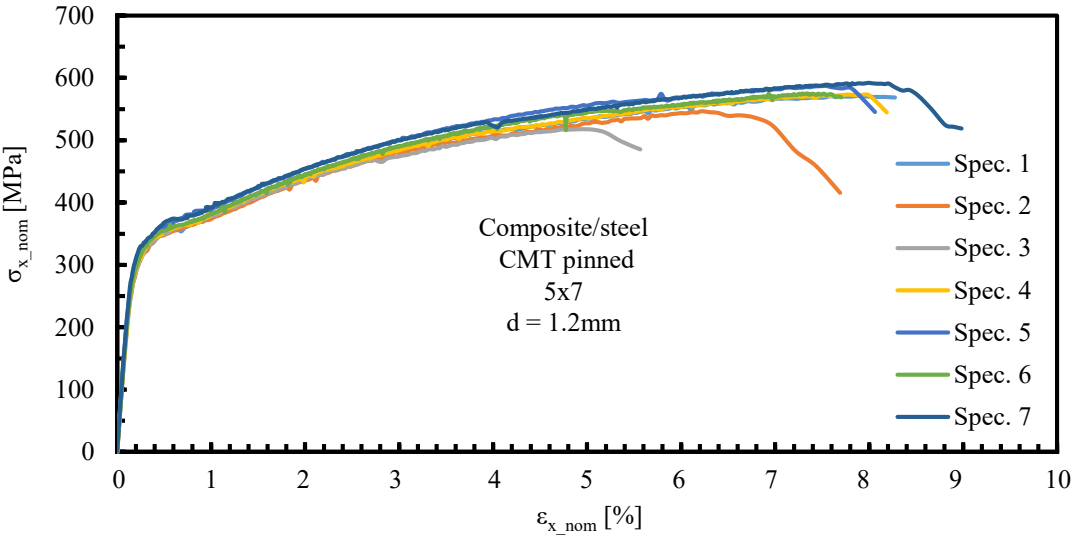

Figure A-2: Pinned composite/steel joint - CMT 5x7 d=1.2 mm - joint design 1

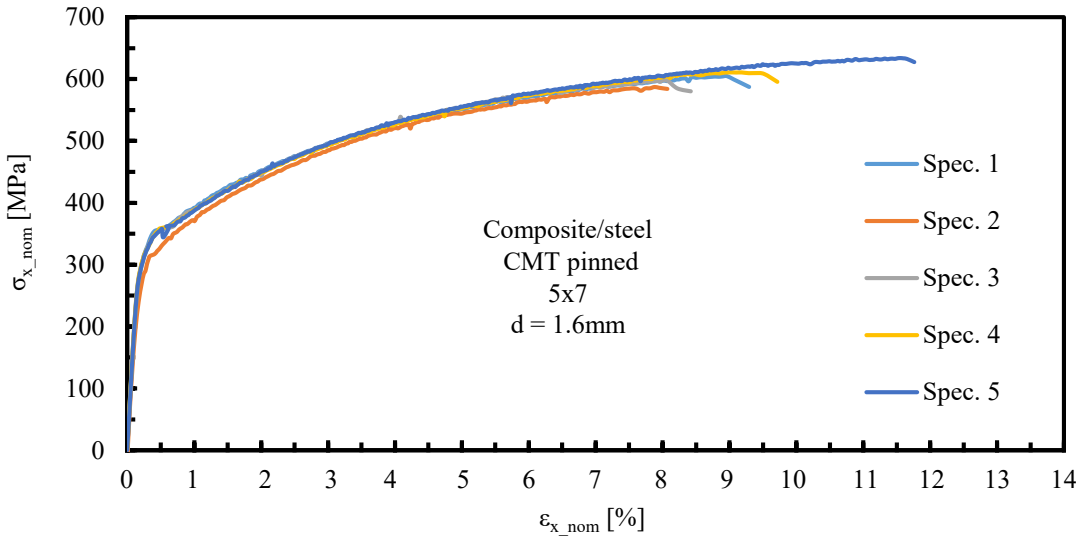

Figure A-3: Pinned composite/steel joint - CMT 5x7 d=1.6 mm - joint design 1

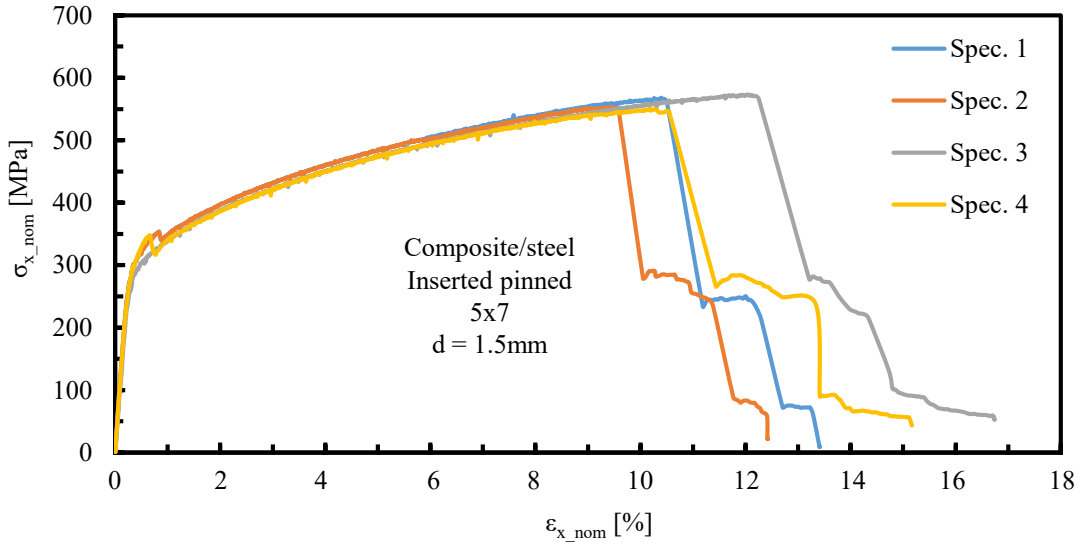

Figure A-4: Pinned composite/steel joint - inserted 5x7 d=1.5 mm - joint design 1

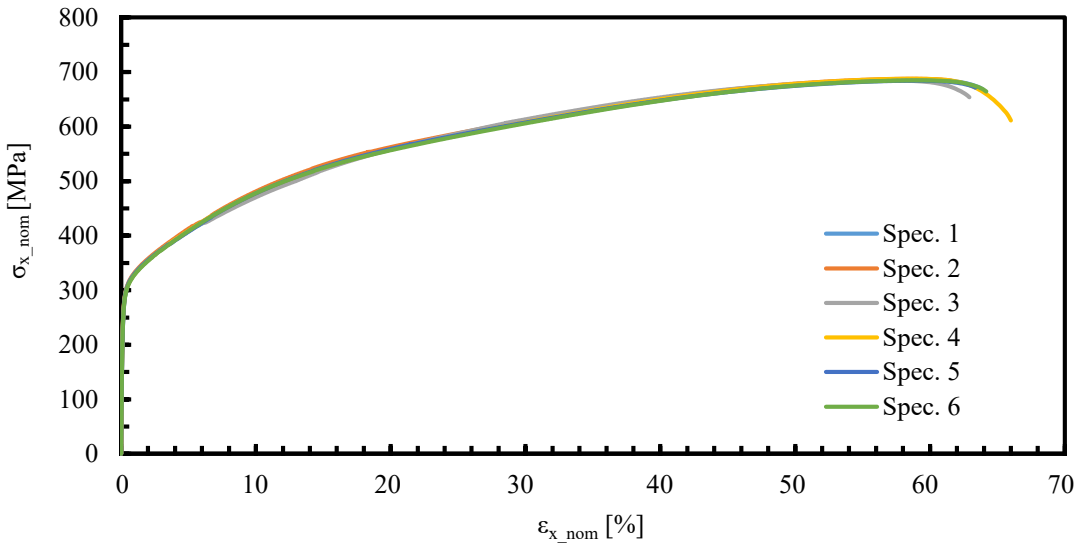

Figure A-5: Steel 1.4301 tension

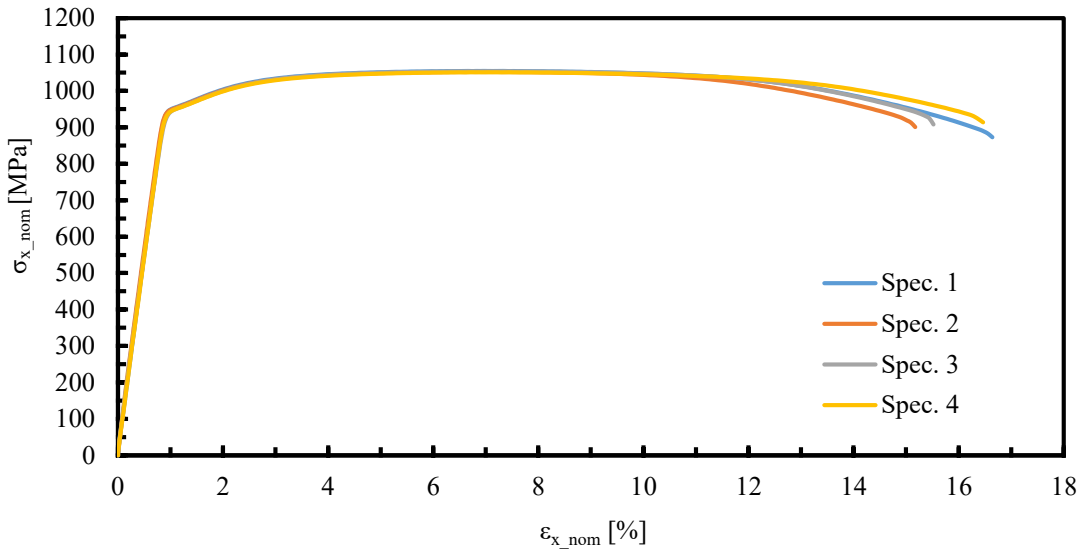

Figure A-6: Titanium Ti6Al4V tension

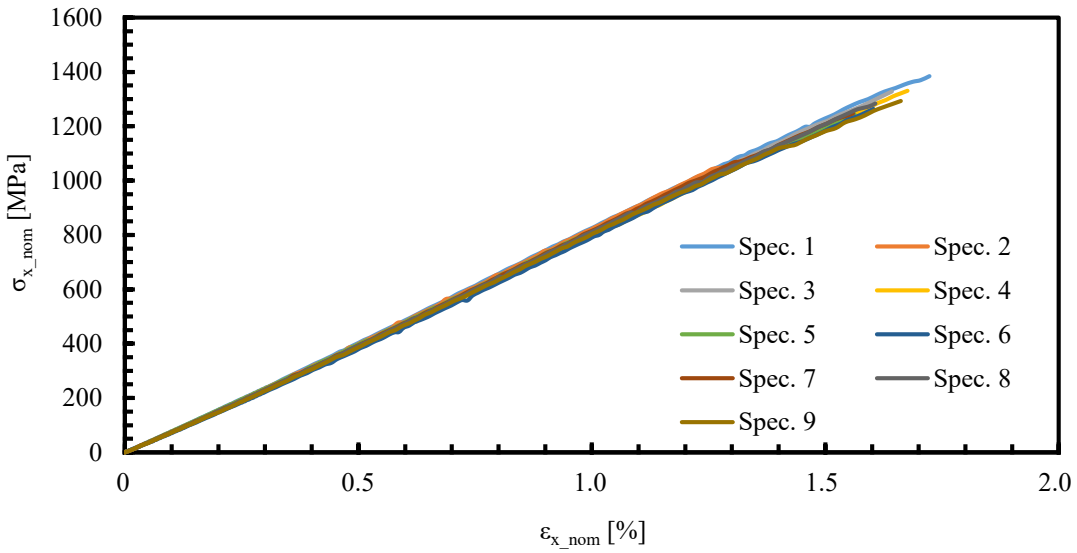

Figure A-7: CFRP [0/90] IMS60/PR520 tension

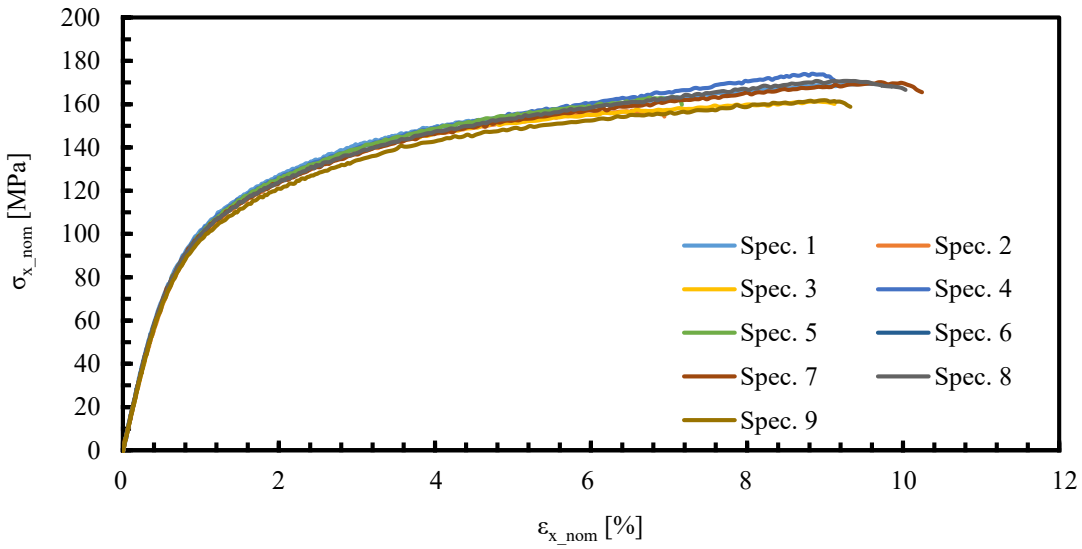

Figure A-8: CFRP [±45] IMS60/PR520 tension

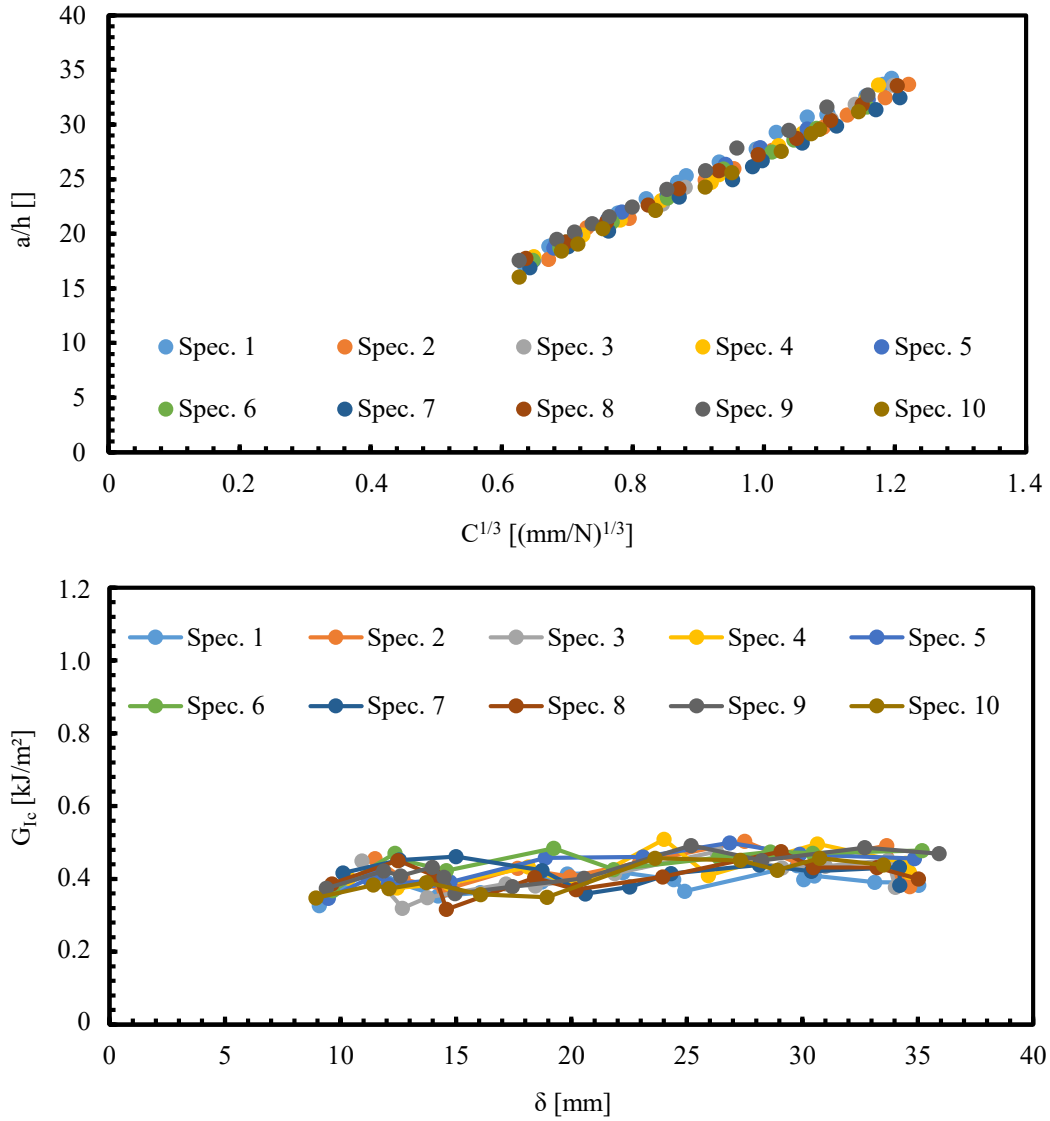

Figure A-9: ***G*$_{Ic}$-testing NCF/NCF *G*$_{Ic\_1}$**

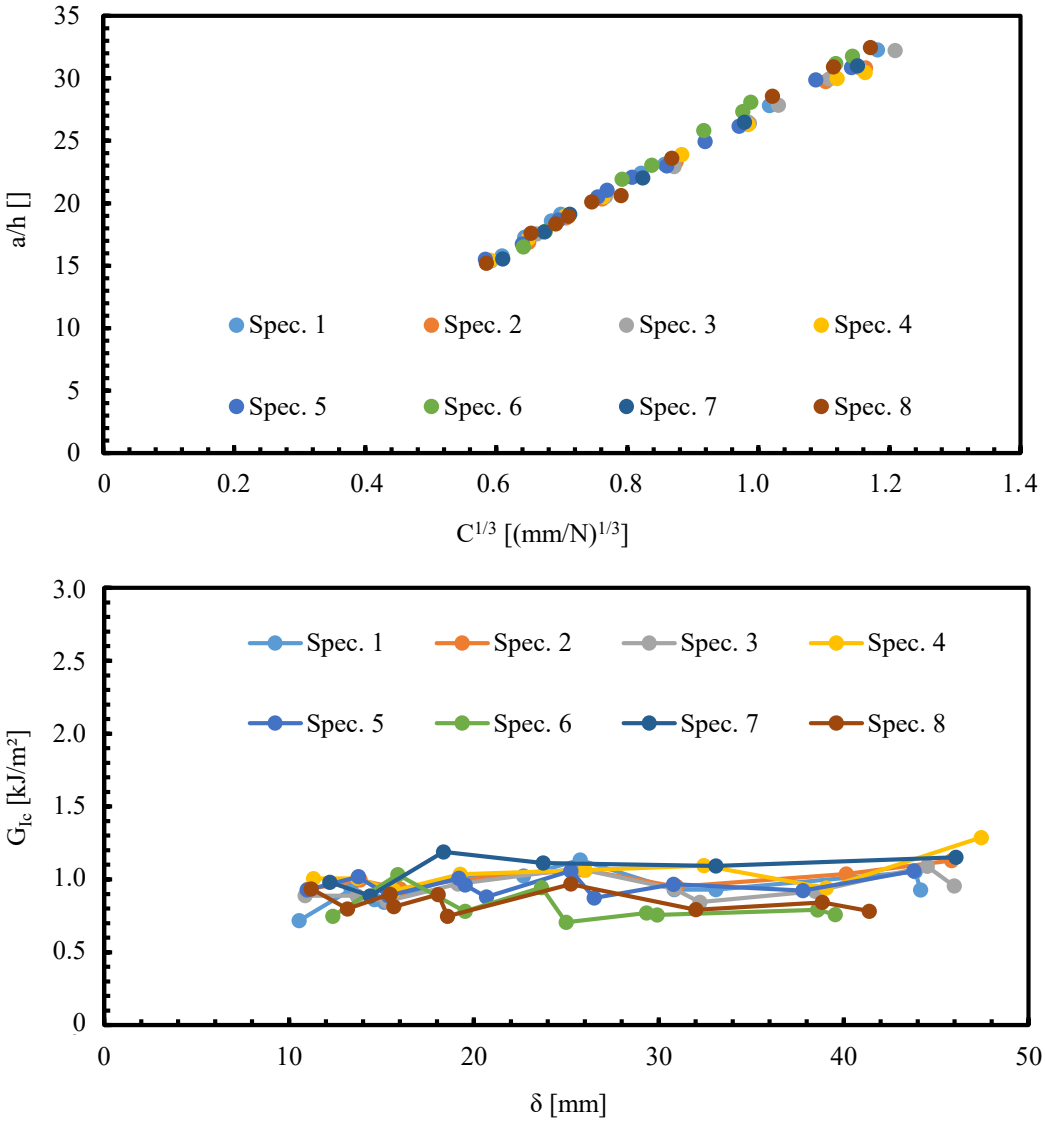

Figure A-10: G_{Ic}-testing NCF/NCF G_{Ic_2}

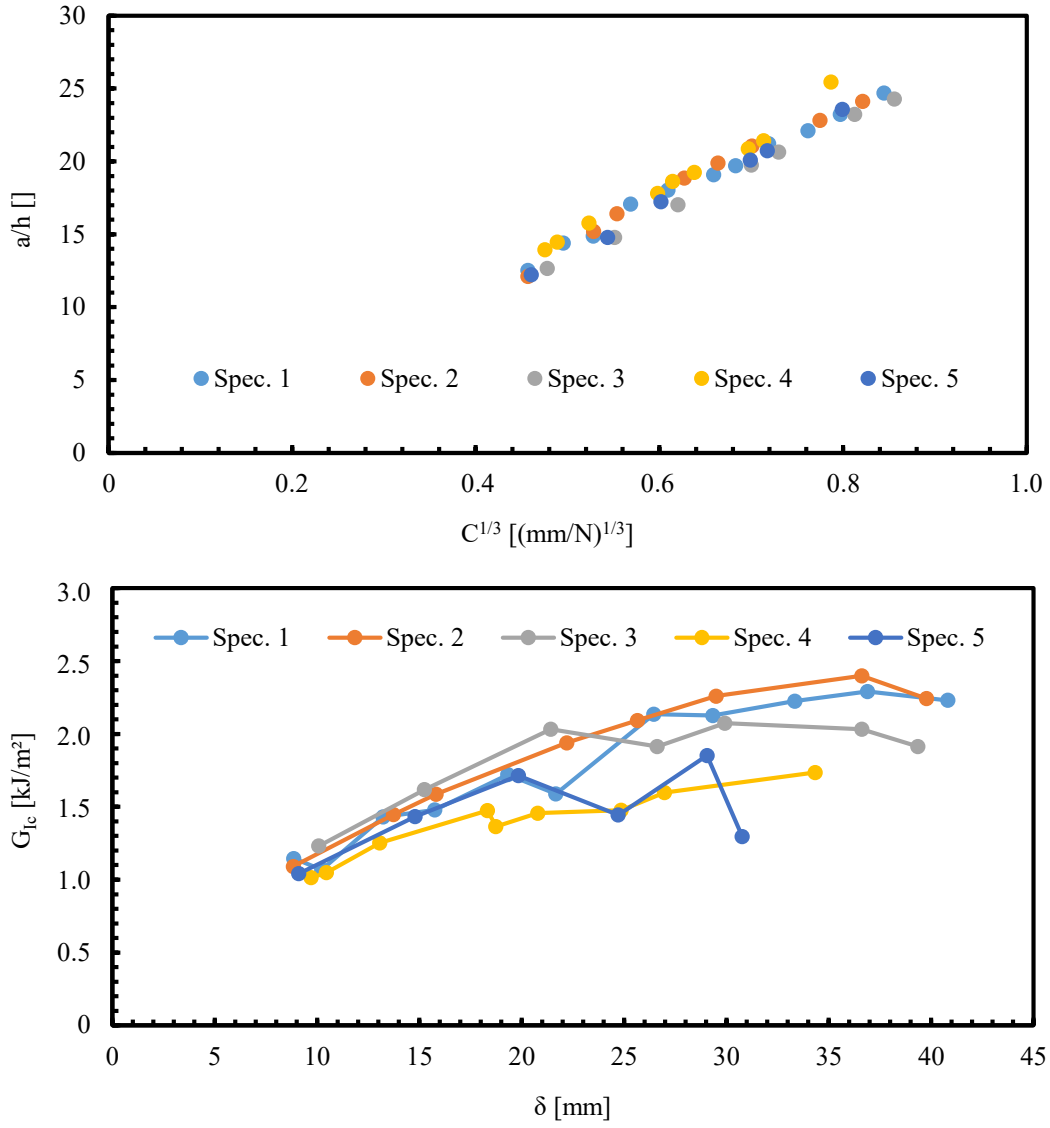

Figure A-11: G_{Ic}-testing NCF/PR520/Ti6Al4V

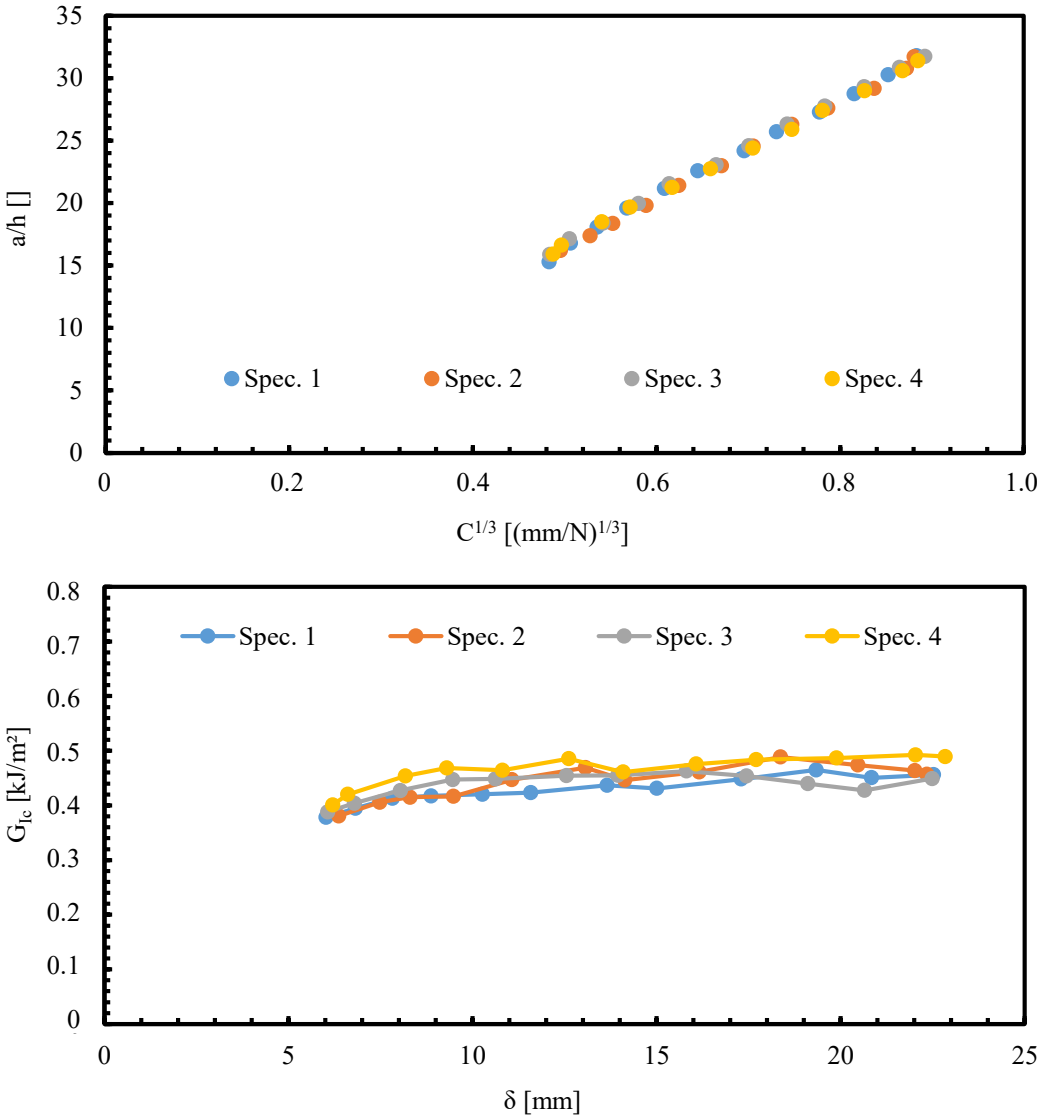

Figure A-12: G_{Ic}-testing Prepreg Cycom 5320-1

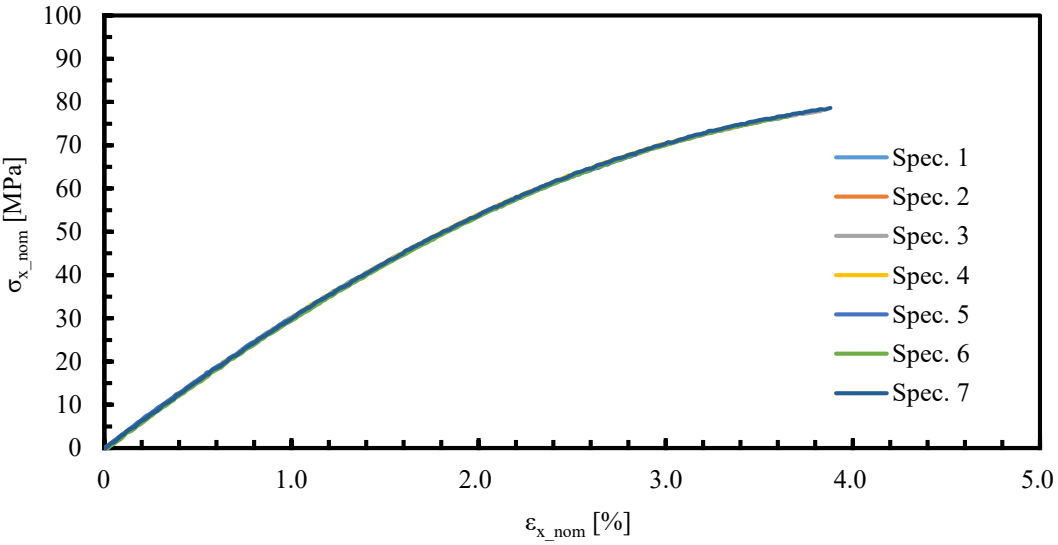

Figure A-13: PR520 neat resin testing - tension

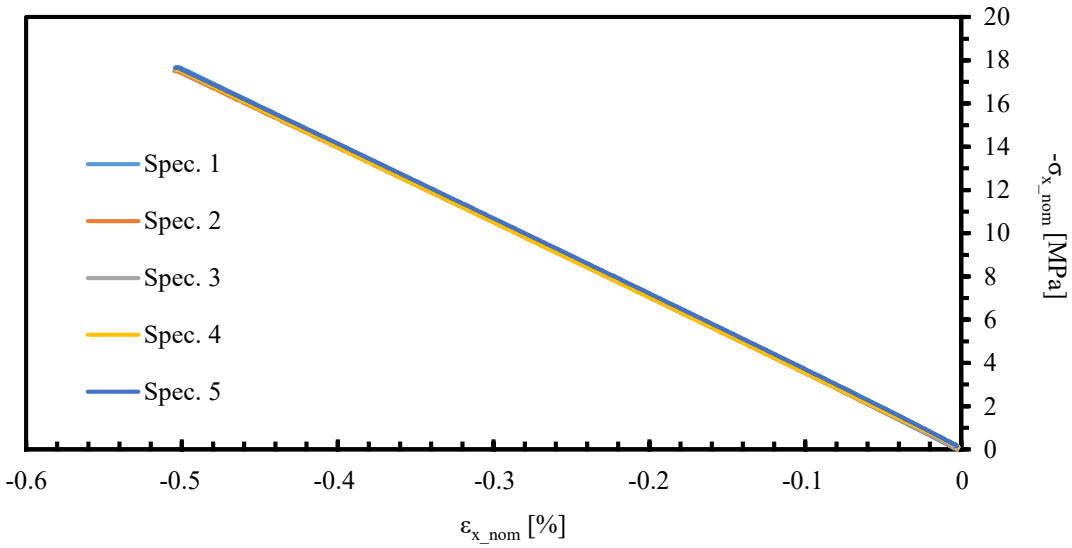

Figure A-14: PR520 neat resin testing - compression/stiffness

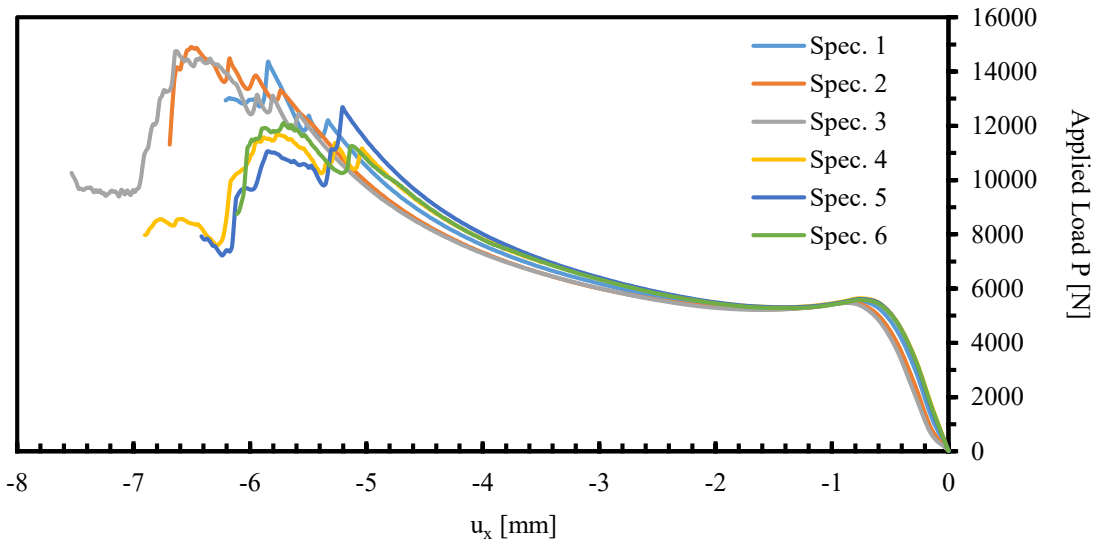

Figure A-15: PR520 neat resin testing - compression/strength

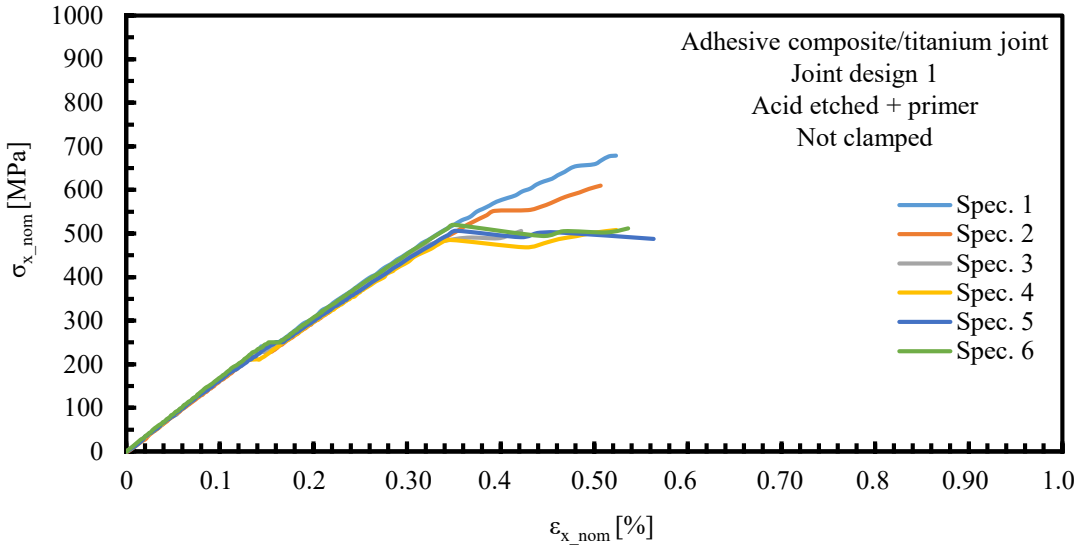

Figure A-16: Co-bonded reference composite/titanium joint - treated surface - not clamped - joint design 1

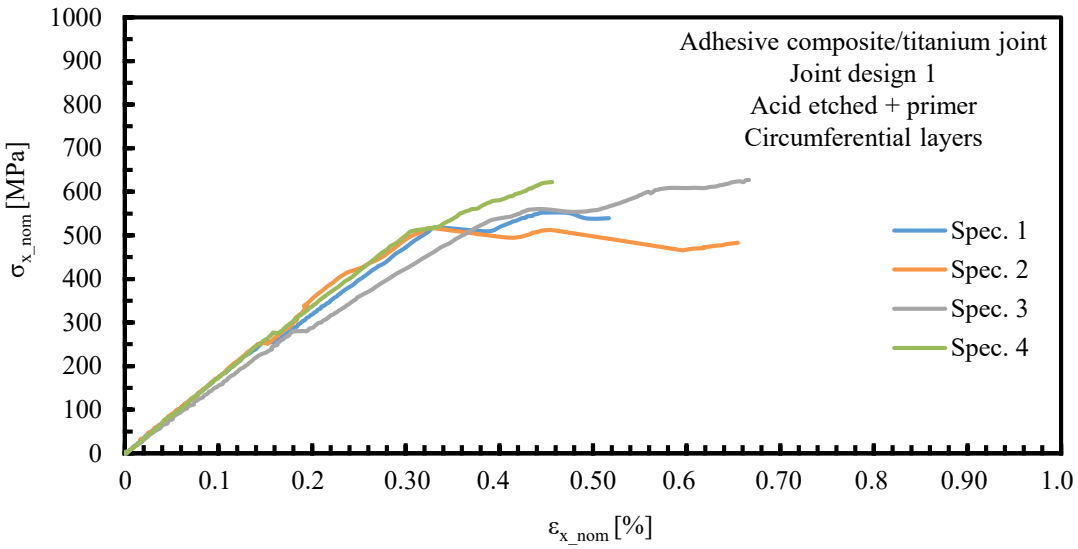

Figure A-17: Co-bonded reference composite/titanium joint - treated surface - circumferential layers - joint design 1

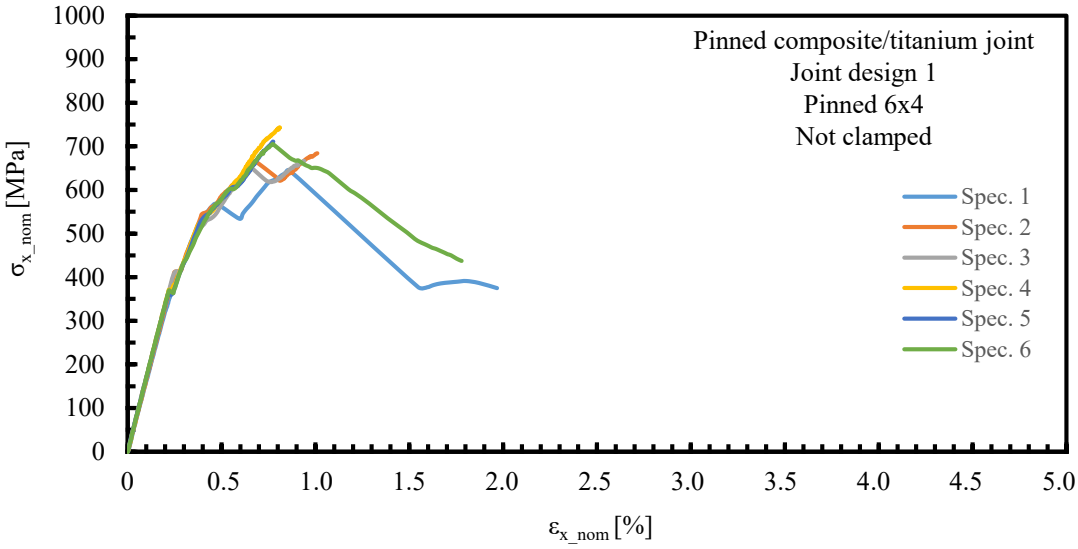

Figure A-18: Pinned composite/titanium joint - 6x4 - not clamped - joint design 1

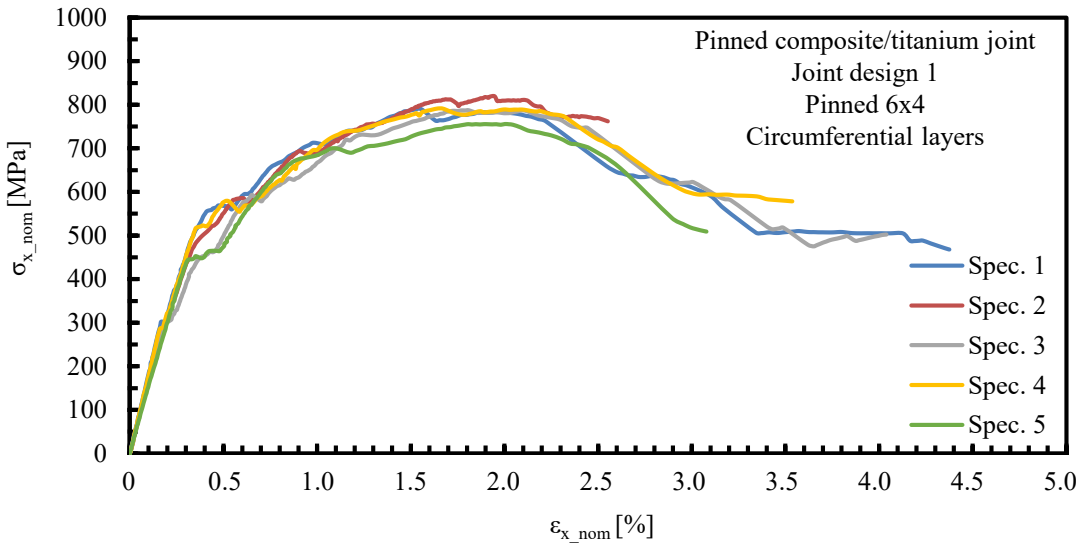

Figure A-19: Pinned composite/titanium joint - 6x4 - circumferential layers - joint design 1

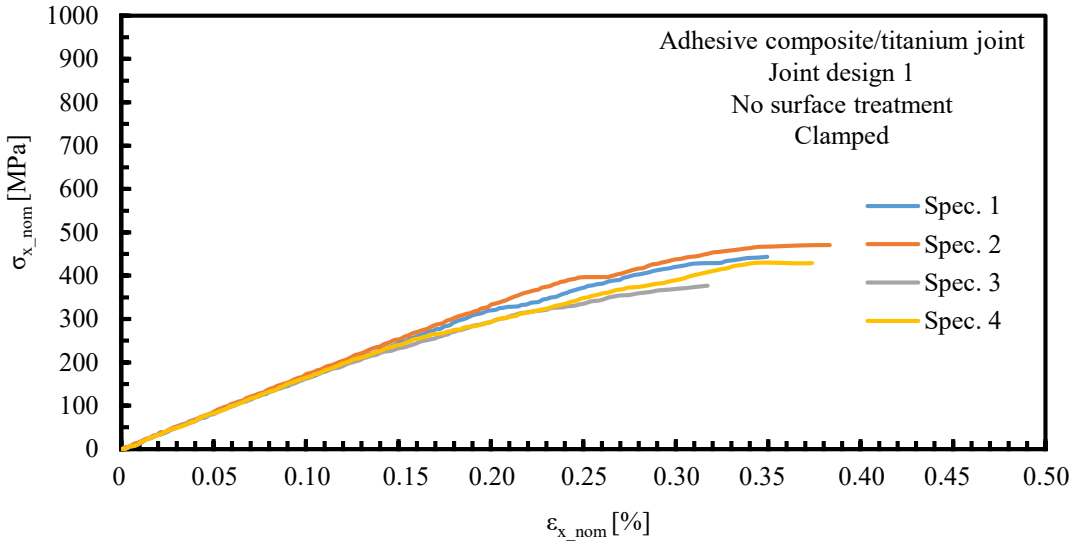

Figure A-20: Co-bonded reference composite/titanium joint - non-treated surface - clamped - joint design 1

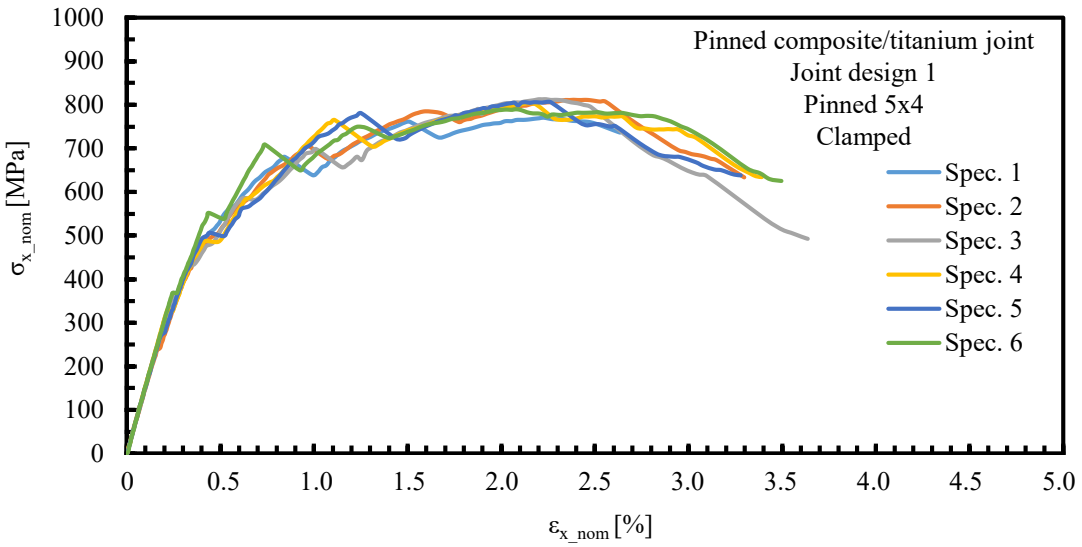

Figure A-21: Pinned composite/titanium joint - 5x4 - clamped - joint design 1

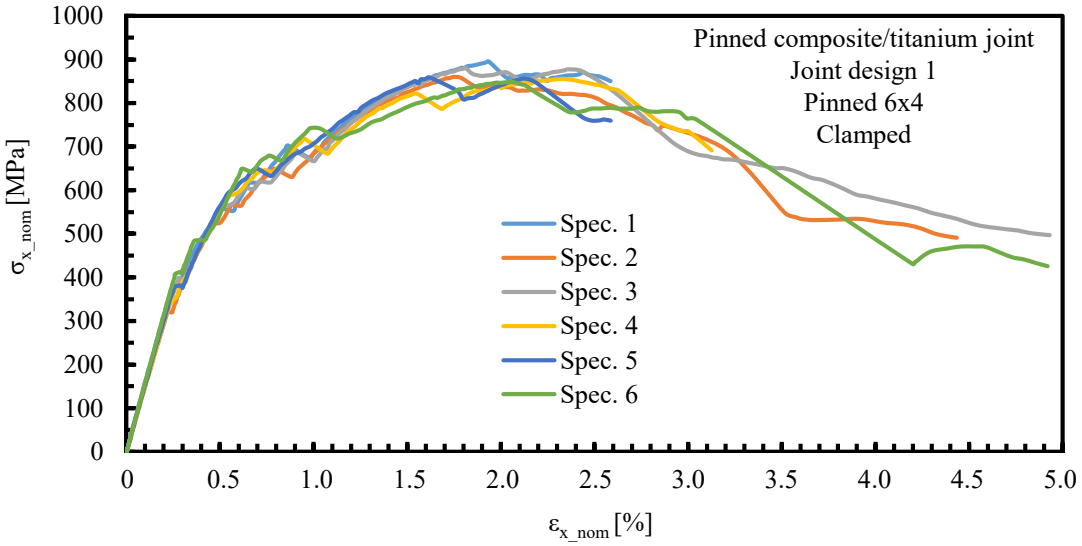

Figure A-22: Pinned composite/titanium joint - 6x4 - clamped - joint design 1

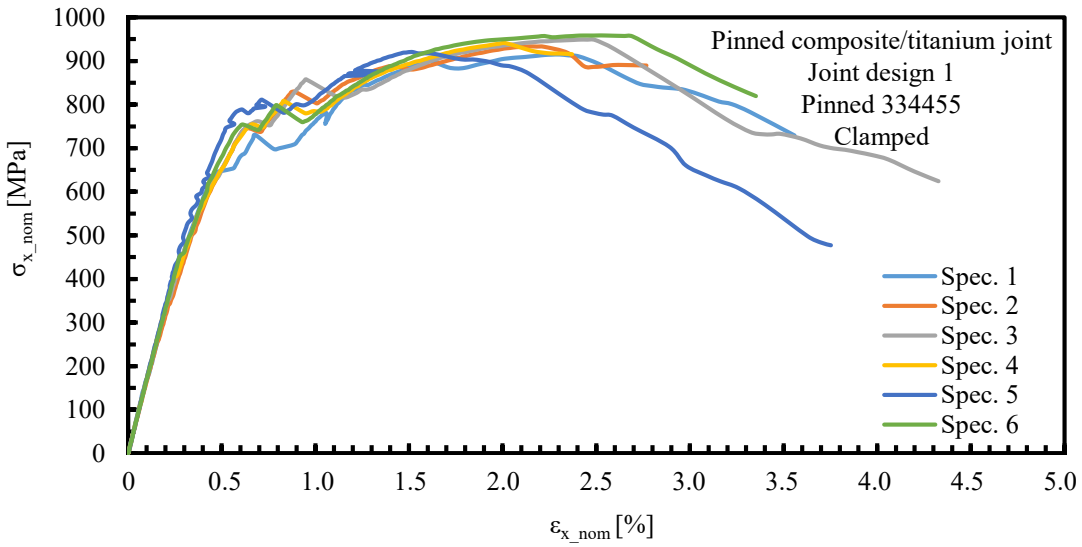

Figure A-23: Pinned composite/titanium joint - 334455 - clamped - joint design 1

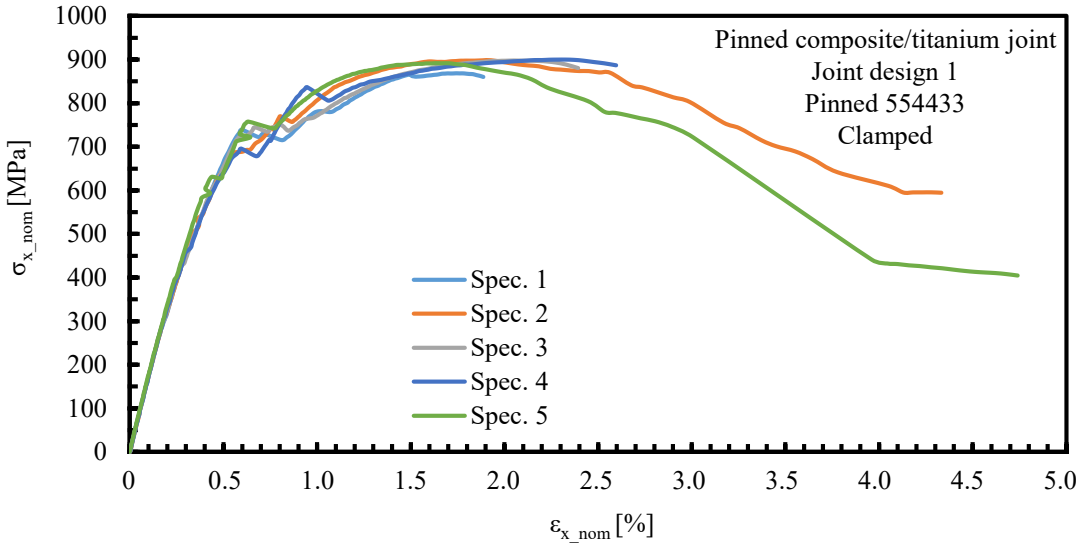

Figure A-24: Pinned composite/titanium joint - 554433 - clamped - joint design 1 [115]

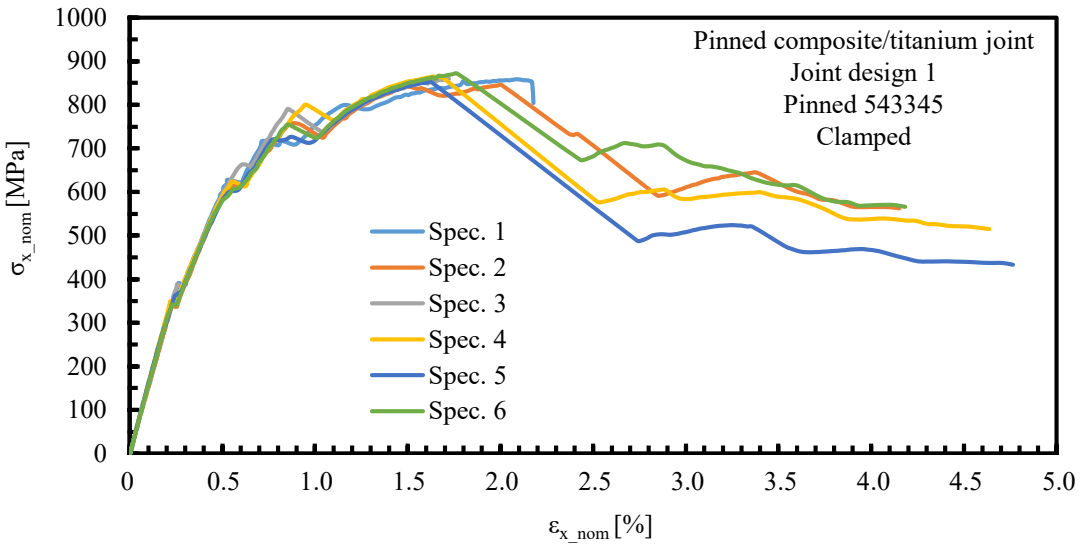

Figure A-25: Pinned composite/titanium joint - 543345 - clamped - joint design 1

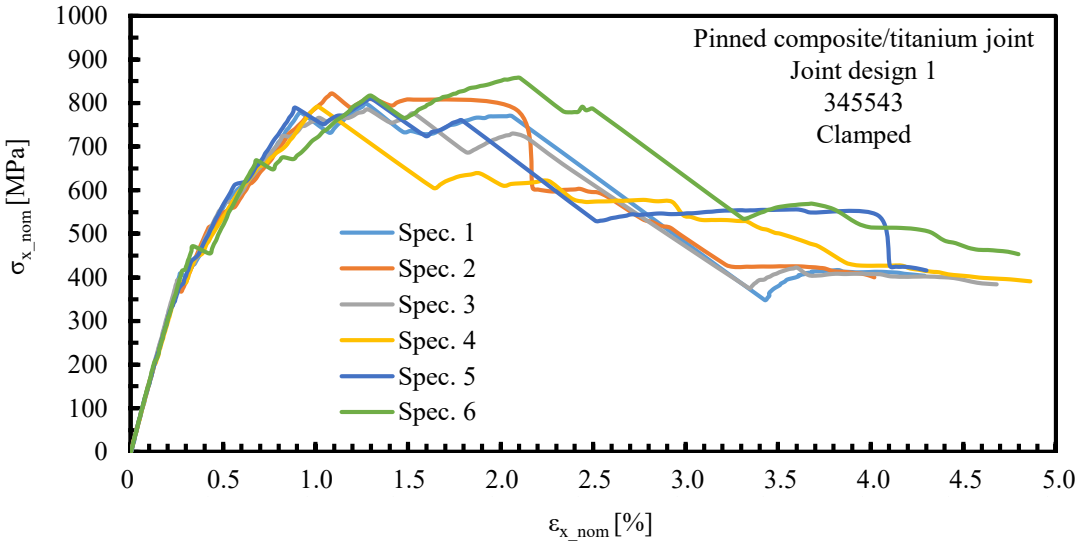

Figure A-26: Pinned composite/titanium joint - 345543 - clamped - joint design 1

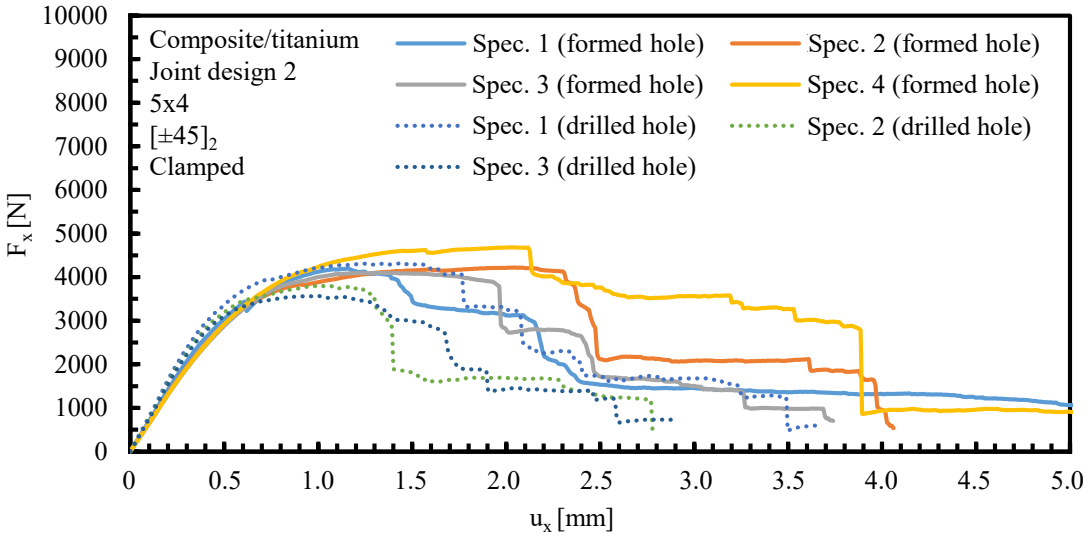

Figure A-27: Composite/titanium joint with formed/drilled hole - 5x4 - $[\pm 45]_2$ - clamped - joint design 2

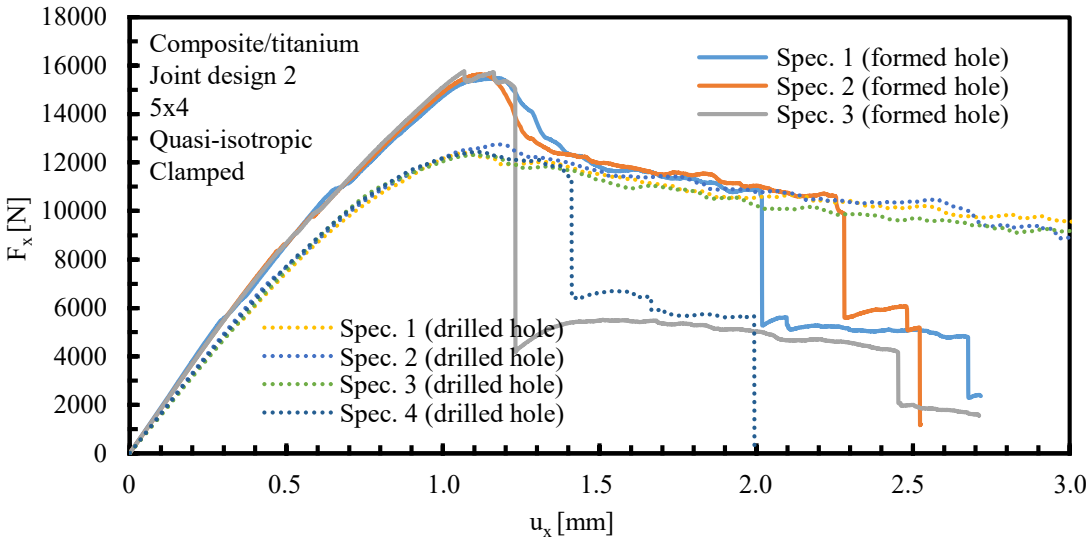

Figure A-28: Composite/titanium joint with formed/drilled hole - 5x4 - quasi-isotropic - clamped - joint design 2

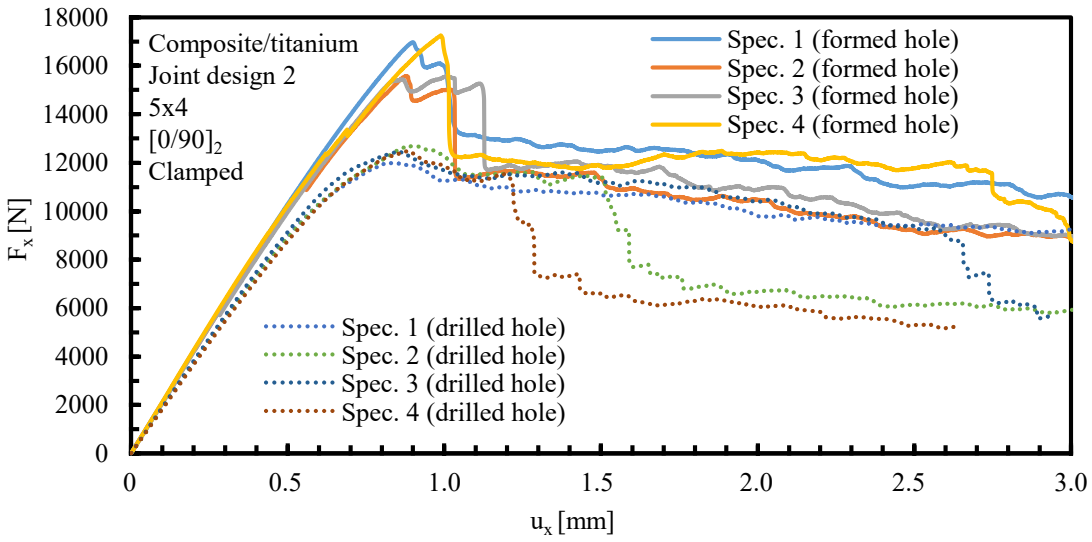

Figure A-29: Composite/titanium joint with formed/drilled hole - 5x4 - $[0/90]_2$ - clamped - joint design 2

b Data sheets

CYCOM® 5320-1 EPOXY RESIN SYSTEM

Table 2 | Lamina Level properties – Unidirectional Tape

Material: CYCOM® 5320-1 IM7 12K 145gsm 33%

Prepreg: CYCOM ®5320-1/IM7 145/33

Fiber: Hexcel IM7 12K **Resin:** CYCOM ®5320-1

Cytec – CYCOM 5320-1/IM7 12K 145/33 Unidirectional Tape Lamina Mechanical Properties Summary

Tg (dry): 386°F **Tg (wet[1]):** 321°F **Tg Method:** DMA (ASTM D7028, 35mm dual cantilever)

Processing: full vacuum, vacuum bag only room temperature for 16 hours plus integrated 200°F/350°F cure/post cure cycle with a 200°F cure for 10 hours followed immediately under the same vacuum bag by a post cure at 350°F for two hours.

Data reported as normalized (except where noted by parenthesis) by 0.0054 in. (59.9% nominal fiber volume)

Condition	-100°F Dry	75°F Dry	250°F Dry	300°F Dry	180°F Wet[1]	250°F Wet[1]
Property	Mean	Mean	Mean	Mean	Mean	Mean
0° Tensile						
ASTM D3039						
Strength (ksi)[2]	352.2	363.3	359.3		385.7	377.5
Modulus (Msi)	22.7	22.8	23.0		23.1	23.1
Poisson's Ratio	0.31	0.30	0.32		0.35	0.38
90° Tensile						
ASTM D3039						
Strength (ksi)	11.39	11.02	9.46		3.30	2.23
Modulus (Msi)	1.75	1.36	1.21		1.23	1.08
0° Compression						
ASTM D6641						
Strength (ksi)[2]	314.9	301.4	292.4		239.1	190.3
Modulus (Msi)	20.87	20.82	20.96		20.90	21.15
0°/90° Tensile						
ASTM D3039						
Strength (ksi)	189.7	192.5	189.1	185.8	203.1	197.6
Modulus (Msi)	12.30	12.08	12.24	12.07	12.38	12.18
0°/90° Compression						
ASTM D6641						
Strength (ksi)	169.6	159.7	153.9	127.6	125.9	99.6
±45° Tensile In-Plane Shear (500-3,000 µstrain chord)						
ASTM D3518						
0.2% Offset Strength (ksi)	(11.76)	(8.08)	(5.73)	(5.00)	(5.01)	(3.44)
Shear Modulus (Msi)	(0.98)	(0.80)	(0.72)	(0.70)	(0.67)	(0.53)
0° Short Beam						
ASTM D2344						
Strength (ksi)[3]		(19.4)				(8.8)

1 Wet conditioning to equilibrium at 85%RW and 160°F
2 Derived from 0°/90° strength results
3 250°F 2 hr. + 350°F 2 hr. cure

Figure A-30: Cycom 5320-1 Prepreg - lamina level properties - unidirectional tape

Neat Resin Data

Properties	RTM6	ST15
G_{Ic} (Jm^{-2})	87	1000
K_{Ic} ($MPa^{0.5}$)	0.6	1.88
Modulus (GPa)	3.3	3.3
Tg E' onset (°C) (Dry)	208	150
Tg E' onset (°C) (Wet - 72 hr boiling water)	169	136
Cured Density (gcm^3)	1.15	1.2
6 Days in MEK Uptake (%)	2.0	0.01

ST15 has high neat resin toughness

HEXCEL

4 ©2012 Hexcel – Proprietary and Confidential

Figure A-31: Hexcel ST15 RTM-resin system - neat rein properties

Viscosity Profiles

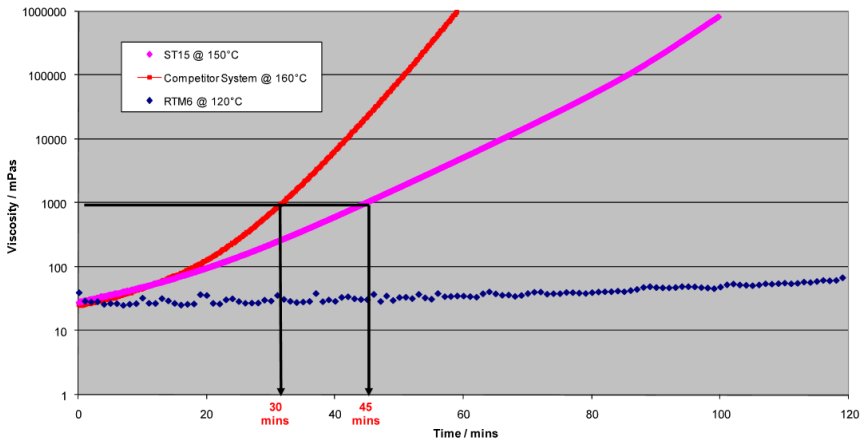

ST15 has lower injection temperature and longer injection window than competitor

HEXCEL

3 ©2012 Hexcel – Proprietary and Confidential

Figure A-32: Hexcel ST15 RTM-resin system - isothermal viscosity

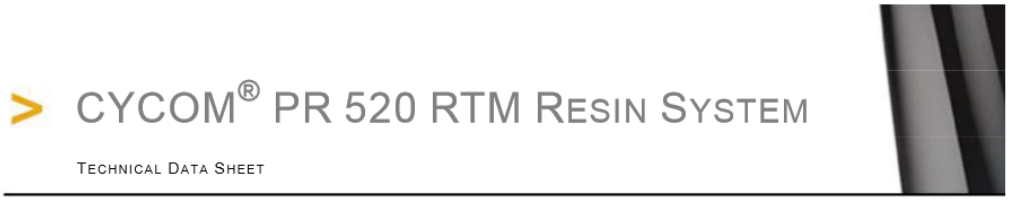

Figure 3 shows the isothermal viscosities of CYCOM PR 520 RTM at four different temperatures. Note that at 160°C (320°F) the viscosity remains below 500 cP for approximately 40 minutes.

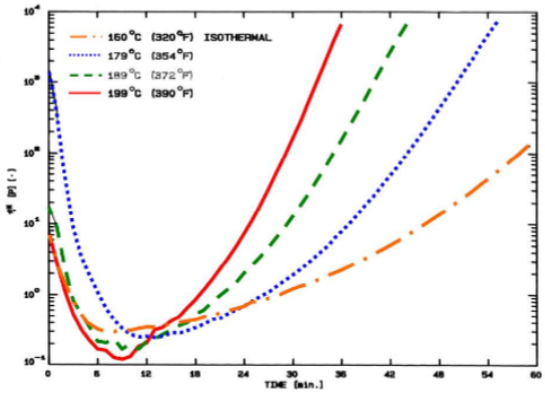

Figure 3 | CYCOM PR 520 RTM Isothermal Viscosities

Table 1 | Neat Resin Characteristics

Property [1]	Value
Cured resin density, g/cm^3	1.25
T_G by DSC, °C (°F)*	161 (322)
Tensile Strength, MPa (ksi)	82.1 (11.9)
Tensile Modulus, GPA (Msi)	4.0 (0.58)
Tensile Strain at Break, %	3.0
Poisson's Ratio	0.398
Compressive Strength, MPa (ksi)	128 (18.5)
Compressive Modulus, GPa (Msi)	3.7 (0.53)
Shear Strength, MPa (ksi)	61.4 (8.9)
Shear Modulus, GPa (Msi) [2]	0.8 (0.12)
Flexural Strength, MPa (ksi)	153.1 (22.2)
Flexural Modulus, GPa (Msi)	3.5 (0.50)
SENB KIC, MPa·m$^{1/2}$ (ksi·in$^{1/2}$)	2.2 (2.0)
SENB GIC, J/m^2 (in·lb/in^2)	1410 (8.1)
CTE by TMA, m/m·°C	52.9 x 10^{-6}

[1] All data tested at room temperature, dry conditions

[2] Minimum modulus below T_G

* NOTE: Tg data is not applicable for U.S. export control classification or licensing. For export-related information please contact us.

Figure A-33: Cycom PR520 RTM-resin system - isothermal viscosity and neat resin properties

c Material input data

Mechanical testing
Validated by simulation
Literature/Data sheet
Estimation

Figure A-34: Color code

Table A-1: Cohesive zone - material input data

Material	E/E_{nn} [MPa]	G_1/E_{ss} [MPa]	G_2/E_{tt} [MPa]	S_n [MPa]	S_s [MPa]	S_t [MPa]	G_{Ic} [J/m²]	G_{IIc} [J/m²]	η [-]
Cohesive Ti/NCF/PR520	10^6	10^6	10^6	30.15	23	23	1100	1464	1.6
Cohesive NCF/PR520 G_{Ic_1}	10^6	10^6	10^6	80.2	61.4	61.4	418	1972	1.6
Cohesive NCF/PR520 G_{Ic_2}	10^6	10^6	10^6	80.2	61.4	61.4	952	1972	1.6
Cohesive Prepreg	10^6	10^6	10^6	80.2	61.4	61.4	439	867	1.6

Table A-2: PR520 - linear elastic material input data

Material	*E* [MPa]	*v* [-]	*Plasticity*
PR520 RTM-resin	3500	0.38	see C4

Table A-3: CFRP - linear elastic material input data

Material	*FVF* [%]	E_1 [MPa]	$E_2=E_3$ [MPa]	$v_{12}=v_{13}$ [-]	v_{23} [-]	$G_{12}=G_{13}$ [MPa]	G_{23} [MPa]
IM7/PR520	60	149514[1]	8505[1]	0.3[1]	0.3	4029	3271
Prepreg 5320-1	60	157183	12065	0.31	0.31	6844	3246

[1] Derived from a [0/90]-layup in consideration of neat resin properties and IM7 fiber properties

Table A-4: CFRP - input data for damage initiation

Material	X^T [MPa]	X^C [MPa]	Y^T [MPa]	Y^C [MPa]	S^L [MPa]	S^T [MPa]
IM7/PR520	2518	1349	70	170	82	82

Table A-5: CFRP - input data for damage evolution

Material	G_{ft}^C [J/m²]	G_{fc}^C [J/m²]	G_{mt}^C [J/m²]	G_{mc}^C [J/m²]
IM7/PR520	35	52.5	5	5

Table A-6: Metals - linear elastic material input data

Material	E [MPa]	ν [-]	$\bar{\varepsilon}_D^{pl}$ [-]	η [-]	$\bar{u}_f^{pl}$ [mm]	*Plasticity*
Steel 1.4301	225000	0.3	0.50	0.3333	0.6	see C 9
Ti6Al4V	124460	0.3	0.13	0.3333	0.2	see C 10
Spring steel	56800[2]	0.3	0.15	0.3333	0.2	see C 11

Table A-7: Material input data for composite joint member – joint design 2

Material	*FVF* [%]	E_1 [MPa]	E_2=E_3 [MPa]	ν_{12}=ν_{13} [-]	ν_{23} [-]	G_{12}=G_{13} [MPa]	G_{23} [MPa]	X^T [MPa]
Prepreg 5320-1	60	157183	12065	0.31	0.31	6844	3246	2428
Prepreg 5320-1	61	159673	12176	0.31	0.31	7010	3254	2468
Prepreg 5320-1	62	162163	12289	0.31	0.31	7185	3262	2509
Prepreg 5320-1	63	164653	12404	0.31	0.31	7368	3271	2549
Prepreg 5320-1	66	172122	12763	0.30	0.30	7979	3295	2671
Prepreg 5320-1	67	174612	12888	0.30	0.30	8206	3304	2711
Prepreg 5320-1	70	182081	13276	0.30	0.30	8972	3329	2833
Prepreg 5320-1	71	184571	13411	0.30	0.30	9259	3338	2873
Prepreg 5320-1	75	194530	13978	0.29	0.29	10623	3372	3035
Prepreg 5320-1	78	201999	14436	0.29	0.29	11941	3398	3156

[2] Smeared approach, adapted to mesh size

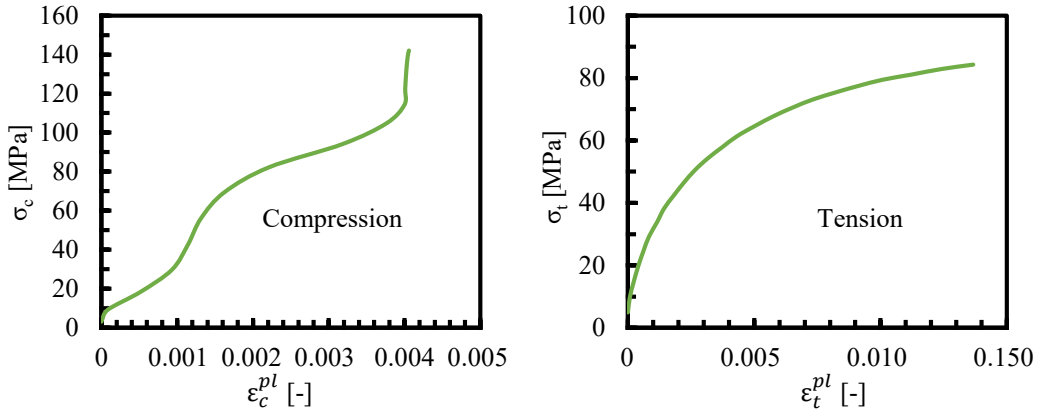

Figure A-35: PR520 - plastic material input data

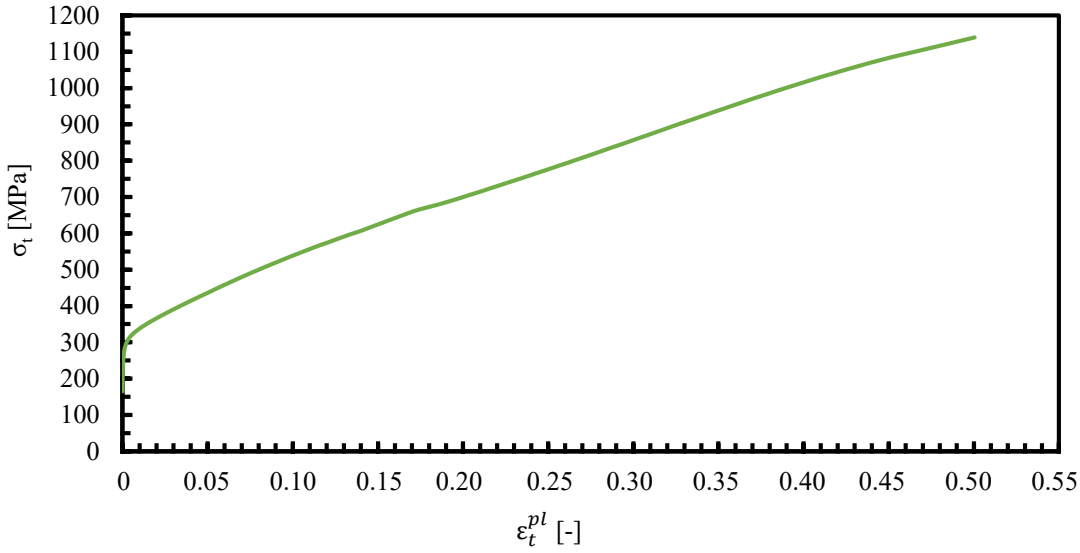

Figure A-36: Plasticity input data steel 1.4301

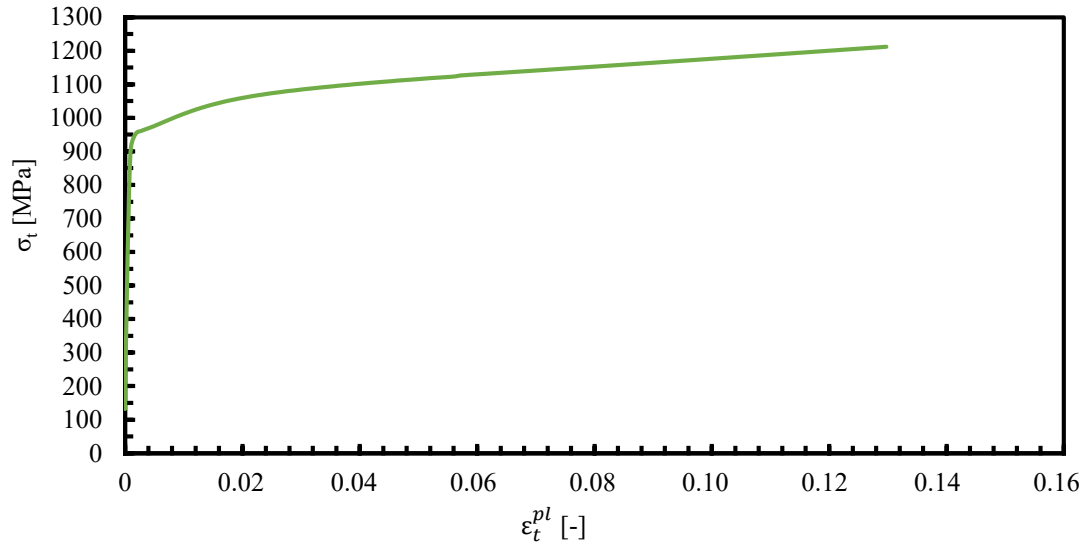

Figure A-37: Plasticity input data titanium Ti6Al4V

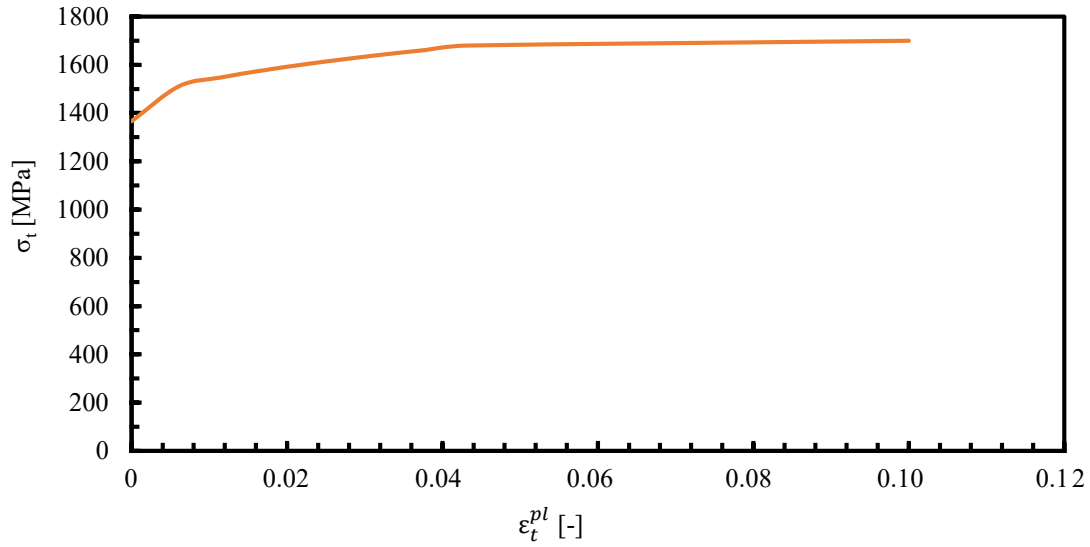

Figure A-38: Plasticity input data spring steel

B Publications

Journal paper

[P1] L. Eberl, L. Avila Gray, S. Zaremba, K. Drechsler, "The effect of fiber undulation on the strain field for pinned composite/titanium joints under tension", *Composites Part A: Applied Science and Manufacturing*, 2017; 103: 148-160.

Conference paper

[K1] L. Eberl, N. Kray, S. Zaremba, K. Drechsler, "Design of through thickness reinforced composite/metal joints - with the help of finite element analysis and quasistatic testing using digital image correlation", CAMX, Dallas, October 2015.

[K2] L. Eberl, S. Zaremba, K. Drechlser, "Through thickness reinforced composite/metal joints – the impact of the pinning technology on the joint's tensile strength", ICCM, Copenhagen, July 2015.

C Student theses

During my employment at the *Chair of Carbon Composites – Technical University of Munich* – I supervised the following student theses:

[S1] S. Sedlmeier, "Investigation of the Process Parameters and Damage Modes of a Pure Composite Joint for Implementation in CFRP", Master's Thesis in cooperation with BMW, Chair of Carbon Composites, TUM, 2013.

[S2] J. P. Beuscher, "Experimentelle Untersuchung neuartiger formschlüssiger Verbindungsmethoden zwischen metallischen Werkstoffen und kohlenstofffaserverstärkten Kunststoffen", Diploma's Thesis, Chair of Carbon Composites, TUM, 2014.

[S3] M. Steinhardt, "Untersuchung relevanter Fügetechniken zur Verbesserung der mechanischen Belastbarkeit von Hybridverbindungen in Flugzeugtriebwerken", Bachelor's Thesis, Chair of Carbon Composites, TUM, 2014.

[S4] Z. Ahec, "Development of a method for the analysis of the fibre orientation in pinned CFRP/metal joints", Semester's Thesis, Chair of Carbon Composites, TUM, 2015.

[S5] M. Krötz, "Ermittlung geeigneter Prozessparameter für thermoplastmodifizierte Harzsysteme im RTM-Prozess", Bachelor's Thesis, Chair of Carbon Composites, TUM, 2015.

[S6] M. Wimmer, "Untersuchung der Krafteinleitung bei gepinnten CFK-Metall-Probekörpern", Semester's Thesis, Chair of Carbon Composites, TUM, 2016.

[S7] F. Neuberger, "Konstruktion eines Preformtools für gestiftete CFK/Metallverbindungskonzepte", Semester's Thesis, Chair of Carbon Composites, TUM, 2016.

[S8] S. Welzenbach, "Optimierung gestifteter CFK/Titan-Hybridverbindungen", Master's Thesis, Chair of Carbon Composites, TUM, 2016.

[S9] A. Lindenmeyer, "Ermittlung der Faserondulation bei gestifteten CFK/Metallverbindungen", Bachelor's Thesis, Chair of Carbon Composites, TUM, 2016.

Parts of the following student theses contributed to the underlying PhD thesis: [S2], [S3], [S4], [S5], [S6], [S7], [S8], [S9].

The following student theses delivered significant input for the following chapters:

[S2] Chapter 5.1: Test series 1: CFRP/steel joint design 1

[S8] Chapter 5.4: Test series 3: CFRP/titanium joint design 1

[S9] Chapter 5.5: Measurement of fiber undulation

In addition, I want to thank Benedikt Streck and Laura Abram for their contribution as student assistants.